# First Row Transition Metal Complexes for Application to Dye-Sensitised Solar Cells

**Charlotte Louise Linfoot**


**Thesis submitted for the degree of PhD**

**The University of Edinburgh**

**September 2010**

## Declaration

I hereby declare that this thesis has been entirely composed by myself and that the work described herein is my own except where clearly mentioned either in acknowledgement, reference or text. It has not been submitted in whole or in part for any other degree, diploma or other qualification.

Charlotte L. Linfoot

September 2010

*Bernard Linfoot*

*Kathleen Linfoot*

*Audrey Shepherd*

*William Shepherd*

## Acknowledgements

Thanks must firstly go to Neil. I'm sure you have regretted your decision to take me on as a Masters student many times, but I have never regretted my decision to accept. The past four years have taught me more than just Chemistry; I now know how to send an email that will get a reply, from anyone, within 24 hours! Thank you.

Thank you to EaStChem for funding my research, and to the University of Edinburgh for making both my undergraduate and postgraduate student life academically and socially rewarding. A special note of thanks goes to the research group of Prof. Yersin at the University of Regensburg. They not only shared their spectroscopic expertise with me during my visit, but they also introduced me to the amazing cuisine of Bavaria.

Thank you Omar for helping me make Mr Copper One.

To Prof. Peter Tasker and Dr Andrew Smith I extend my thanks for letting me raid their old ligand samples and create Chapter Five.

The final collaboration thanks goes to a lady described on several occasions as a Goddess. Thank you Tricia for your help with emission spectroscopy and computational chemistry, but mostly for making our discussions about chemistry fun!

Now, to the Lab. Thank you Robertson members old and new. Thank you for the tea, cakes, biscuits and endless gossip. Oh and to Maxi, without you I would still be computer illiterate.

Thank you Solar Girls old and new. To my mentor Keri: The writing is over. Cool beans. To Nina: it will happen, just remember the magic words, "in sun we trust". To Martina: thank you for smiling, and thank you for tiramisu. To Tracy: I pass Cu(I) to you with both hands! Little Lush it has been a true joy working with you!!
Thank you David for the tea breaks. I love my lab, but it is always good to get away! I'm just sad that there wasn't more dancing!!!

Ben. I think the best way to thank you is to promise that I will never hug you good bye again. Rose Street has never seen such awkward English people! Tell Romain to start preparing for my visit...

Moving away from chemistry I send out my thanks to my two flatmates, Mr and Mrs Spongefoot. I hate you for Eastenders but love you for everything else! your devoted flatmate.
Well away from chemistry, my thanks go to Anna. You were there at the start of this chemistry adventure, and I'm so happy you're still my tea loving friend!!!

The most important "mate" to thank is my George. Thank you for the food, thank you for the mini-golf and thank you for Jurassic Park. You have helped keep me (almost) sane through this madness. xxx

To the Linfoots.
Thank you Johnathan and Catherine for the Sunday coffees breaks and for teaching me guitar hero. Setting the guitar to medium made me so proud!

There are no words to sum up my thanks for the next person. I am so lucky to have you as my sister...now get your clothes out of my wardrobe!!!

The biggest thanks go to my parents. You are fantastic and I am so proud to be your daughter. I love you both, but I'm sorry Dad, I did promise Mum, and let's face it, she usually does get the last word...

Thank you Mum!!!!

## Abstract

Ruthenium (II) complexes are used extensively in photoelectrochemical and photophysical devices, such as Dye-Sensitized Solar Cells (DSSCs). The use of Cu(I) as a possible replacement for Ru(II) has to date had limited exploration, but has obvious advantages in terms of low cost and high abundance. However, Cu(I) typically undergoes conformational change from tetrahedral towards square planar upon oxidation or MLCT excitation, often leading to reduced stability, reduced electron transfer rates and reduced excited state lifetime, thus impairing useful function. Typically, steric constraints are used to prevent this; however these can often be synthetically intensive, involving multi-step and low yielding synthetic pathways. In this work, we explore "blocking" functionality using two different ligands combined with a range of bipyridyl ligands with varying substituent groups.

The study has looked into the synthesis of heteroleptic Cu(I) complexes of the general formula: [Cu(POP)(bipyridyl)][$BF_4$], where POP = bis[2-(diphenylphosphanyl)phenyl] ether, and [Cu(pmppE)(bipyridyl)], where pmppE = hydrazono pyrazol-5-thiones(one). The work presented in this thesis focuses on the synthesis, and subsequent photoelectrochemical and photophysical characterisation of Cu(I) complexes, yielding results that open new avenues for design of functional Cu(I) systems. Solar cell testing also revealed photovoltages comparable to those of existing Cu(I) DSSC sensitisers.

An extensive spectroscopic study of $[Cu(POP)(dmbpy)]^+$ and $[Cu(POP)(tmbpy)]^+$ has revealed the latter to have the significantly larger quantum yield: 65 % and 4% respectively in PMMA at 300 K. A complimentary computational investigation was carried out in order to gain a better understanding of how structural rigidity affects emission properties.

# Contents



## Chapter One: Introduction

## Chapter Two: Experimental Techniques



## Chapter Three: [Cu(I)(POP)(bipyridyl)] and Related Complexes

## Chapter Five: Cu(pmppE)-based Complexes



## Chapter Six: [Ni(bipyridyl)(qdt)] Complexes

# List of Figures

## Chapter One: Introduction



## Chapter Two: Experimental Techniques



## Chapter Three: [Cu(I)(POP)(bipyridyl)] and Related Complexes

## Chapter Four: Emission Spectroscopy and Computational Study of 5 and 8



## Chapter Five: Cu(pmppE)-based Complexes

## Chapter Six: [Ni(bipyridyl)(qdt)] Complexes



## Chapter Seven: *In situ* Sensitisation

## List of Tables

## Chapter Three: [Cu(I)(POP)(bipyridyl)] and Related Complexes



## Chapter Four: Emission Spectroscopy and Computational Study of 5 and 8

## Chapter Five: Cu(pmppE)-based Complexes



## Chapter Six: [Ni(bipyridyl)(qdt)] Complexes



## Chapter Seven: *In situ* Sensitisation

# Abbreviations

| | |
|---|---|
| AM | Air mass coefficient |
| bpy | 2,2′-bipyridine |
| bpym | bipyrimidine |
| Btu | British thermal unit |
| $CDCl_3$ | Deuterated chloroform |
| CdTe | Cadmium telluride |
| Cheno | Chenodeoxycholic acid |
| CV | Cyclic voltammetry |
| D/D+ | Ground state of dye |
| D*/D+ | Excited state of dye |
| dcbpy | 4,4′-dicarboxy-2,2′-bipyridine |
| DCM | Dichloromethane |
| decbpy | 4,4′-di($CO_2$Et)-2,2′-bipyridine |
| DFT | Density functional theory |
| dmbpy | 4,4′-dimethyl-2,2′-bipyridine |
| dmphen | 2,9-dimethyl-phenanthroline |
| DMSO | Dimethyl sulfoxide |
| dpdmbpy | 4,4′-dimethyl-6,6′-diphenyl-bipyridine |
| dpdcbpy | 4,4′-dicarboxy-6,6′-diphenyl-bipyridine |
| DSSC | Dye sensitised solar cell |
| EtOH | Ethanol |
| $E_{XC}$ | Exchange/correlation functional |
| Ff | Fill factor |
| FTO | Fluorine doped tin oxide |
| GGA | Generalised gradients approximation |
| HF | Hartree-Fock |
| HOMO | Highest occupied molecular orbital |
| HTM | Hole transport material |
| $I_{SC}$ | Short circuit current |
| LDA | Local density approximation |
| LHE | Light harvesting efficiency |
| LL | ligand-ligand |
| LLCT | ligand-to-ligand charge transfer |

| | |
|---|---|
| LUMO | Lowest unoccupied molecular orbital |
| MeCN | Acetonitrile |
| MeOH | Methanol |
| MLCT | Metal-to-ligand charge transfer |
| MO | Molecular orbital |
| OLEDS | Organic light-emitting diodes |
| PCM | Polarisable continuum model |
| PES | Potential energy surface |
| PMMA | Poly(methyl methacrylate) |
| pmppE | hydrazono pyrazol-5-thiones |
| pmppO | 1-phenyl-3-methyl-4-phenylhydrazono-pyrazol-5-one |
| pmppT | 1-phenyl-3-methyl-4-phenylhydrazono-pyrazol-5-thione |
| POP | bis[2-(diphenylphosphanyl)phenyl] ether |
| qdt | 2,3-quinoxalinedithiol |
| SCRF | Self-consistent reaction field |
| TAS | Transient absorption spectroscopy |
| tcbpy | 4,4′,6,6′-tetracarboxy-2,2′-bipyridine |
| TCO | Transparent conducting-oxide electrode |
| TDDFT | Time-dependant density functional theory |
| tecbpy | 4,4′,6,6′-tetra($CO_2$Et)-2,2′-bipyridine |
| $TiCl_4$ | Titanium tetra-chloride |
| $TiO_2$ | Titanium dioxide |
| tmbpy | 4,4′,6,6′-tetramethyl-2,2′-bipyridine |
| TMs | Transition metals |
| $V_{OC}$ | Open circuit voltage |

# 1. Chapter One:

# Introduction

## 1.1 The Need for Renewable Energy

Access to a cheap energy source is a fundamental commodity for any economically developed or developing country, as quality of life is tied to the availability of useable energy. However, there are two main factors that are currently governing the future of energy production by mankind; these are climate change and energy security. The modern world is facing up to the realisation that global warming is the result of our excessive combustion of fossil fuels over the last 150 years.[1, 2] The combustion of fossil fuels produces useable energy, a process which causes extensive environmental damage due to the cumulative nature of carbon dioxide emissions in the atmosphere.[2] Around forty percent of total energy use is met by the generation of electricity (18,000 terawatt-hours of energy a year), however this results in more than 10 gigatonnes of carbon dioxide being released into the environment every year.[3] Energy security is a political concern that arises when the global distribution of fossil fuel reserves is compared to the locations of the highest fossil fuel consuming countries. The current relationship is such that threats to energy security are governed by a combination of the economic and political climate of the energy producing countries, industrial accidents and natural disasters.

The introduction of multiple energy sources, especially renewable sources, that are native to a country would reduce the threats to energy security, and be environmentally more suitable. The challenge is now to research and develop replacement energy sources capable of powering the globe. Estimates for total world energy consumption stood at $5.2 \times 10^{29}$ J in 2007, with the prediction of an increase to $6.2 \times 10^{29}$ J by 2020.[4] The United States (US) Annual Energy Review 2009[5] has stated that the US alone consumed around 95 quadrillion Btu in 2009, which breaks down to 308 million Btu of energy per person. When the rate of industrial expansion in countries such as India and China is taken alongside these numbers it becomes clear that this problem needs tackling now.

## 1.2 Alternative Energy Sources

Generating these levels of energy far exceeds that potentially available from many traditional energy sources: wind, water and bio-fuel sources.[1, 6] This does not mean that they should be ignored, in fact, there are already areas utilising these energy sources throughout the world.[3] Hyrdo-electric power plants are currently used to different extents in 160 countries worldwide, and wind power, although not on this scale currently is undergoing vast expansion.[3] The two longer term solutions are nuclear and solar power, with interest into the potential of both growing for many years due to their theoretical capabilities for generating energy.

### 1.2.1 Nuclear Power

Nuclear power holds great potential as an energy source and it currently generates 370 gigawatts a year: 15 % of the electricity generated worldwide.[3] However, can it be utilised to provide clean, safe, renewable energy?

Nuclear fission relies on a fuel source, uranium, to generate energy, which poses two problems. Firstly uranium ores have a finite lifetime, which means that the energy source is not renewable and will one day have to be replaced. Secondly, due to energy manufacturing requirements there is uncertainty over any reduction in the net carbon dioxide emissions produced compared to oil, coal and gas sources.[7] There is another significant problem that stands in the way of nuclear energy becoming the main energy source: a widespread negative public perception towards nuclear power. This exists in response to fears over whether there is adequate secure disposal of the nuclear waste produced as there are both environmental and national security concerns if it is not. When all the potential problems involved in generating and maintaining

nuclear power are considered it does not seem likely that it will be able to meet the world's requirements for a secure, clean, renewable energy source.

## 1.2.2 Solar Energy as an Answer?

Due to the physical and social limitations of the alternative energy sources that have been presented so far, it is becoming more widely believed that it will fall to solar power to generate the majority of the world's power.[1-3, 7] The sun is the Earth's largest, sustainable energy input; supplying enough energy in one hour around 100,000 TW, to fulfil mankind's energy requirements for a whole year.[1, 3, 7] Mankind would therefore only have to harvest a small fraction of daily sunlight to generate sufficient energy to satisfy global demand. Solar energy unlike nuclear energy, could also potentially provide energy with no detrimental environmental impact and no problematic waste products; in essence a secure, clean, renewable energy source.[8]

## 1.3 Current Solar Energy Capture Technologies and Research

A multitude of solar energy technologies already exists that can be broadly characterised as being either passive solar or active solar. Passive solar techniques depend in part upon architecture designed to utilise the sun's heat directly and to aid in ventilation without the need for additional power sources.[9] The vast majority of solar research ongoing today looks into developing active solar technologies as these hold the potential to produce the high volumes of energy demanded by the global community. Active solar technologies can be divided into two main families; solar thermal collectors and photovoltaic panels.[3] The work outlined in this thesis will focus on photovoltaic solar panels which are panels that convert solar radiation into direct current electricity.

In 1946, Russell Ohl patented the modern silicon solar cell, which makes up part of the first generation of solar cell technology which utilises the classic *p-n junction*. Despite these cells achieving solar-to-electrical conversion efficiencies of up to 24%, the capital cost associated with the mass production of such devices is currently too great to allow silicon solar cells to become the main generator of energy worldwide.[10] Another material in this first generation of solar cell technology is gallium arsenide. Were it not for the high cost associated with the production of this material due to the purity levels required, the material would be more commercially viable. Recent work by Rogers *et al.*[11] into gallium arsenide solar cells has yielded a major step forward to overcoming this problem but there is still some way to go.

Second generation solar cells are typically based upon direct band-gap semiconductors with the intension of producing thinner and hence cheaper devices. CdTe is classed as a second generation solar cell and makes up the largest proportion of the commercial solar cell market after silicon solar cells (~10 % and 90 % respectively). The third generation of solar cell

technology aims to couple high efficiency with low production costs. There are several technologies that fall under the heading of third generation solar cells, with the three of most relevance to this work being tandem cells, heterojunctions and dye-sensitised solar cells (DSSC). It is on the later of these that this work is primarily focussed.

## 1.4 The future of Photovoltaic Technologies

A major development in solar cell technology came from looking at how nature harnesses solar energy with great precision and efficiency. Photosynthesis gave scientists their cue to develop solar cells containing sensitiser molecules analogous to the light-absorbing chlorophyll molecule, and anchor them to a semiconducting material.[8] These devices have become known as dye-sensitised solar cells (DSSC's) and are the main focus of this thesis.

### 1.4.1 Dye-Sensitised Solar Cells

#### 1.4.1.1 The Working Principle of a Dye-Sensitised Solar Cell

High-efficiency dye-sensitised solar cells were first discovered and fabricated nearly twenty years ago by Michael Grätzel and Brian O'Regan,[12] and were the first example of a economically-competitive alternative to traditional silicon-based solar cells. DSSCs combined sufficiently high solar energy-to-electricity conversion efficiencies with the manufacturing requiring relatively low cost materials.

The working principle behind DSSC's is sub band-gap excitation;[13-15] electronic excitation of molecular dyes by sunlight gives rise to charge injection into a semiconductor material, initiating an electronic circuit. The structural layout and energy level diagram of a standard DSSC cell can be seen in Figures 1 and 2 respectively. DSSC's comprise five main elements; the Transparent-Conducting-Oxide Electrode (TCO), the metal oxide semiconducting electrode (most commonly $TiO_2$), the sensitiser dye molecule, the hole transport material (HTM) and the platinum electrode (Figure 1 and 2).[16, 17] The role of each will now be discussed briefly.

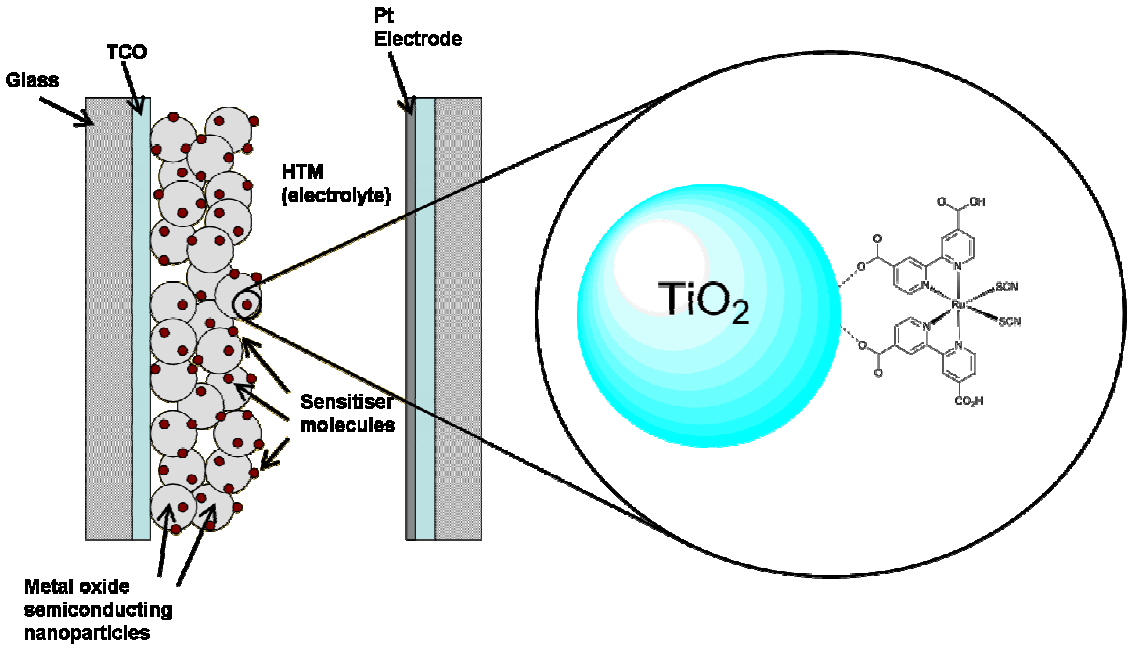


**Fig. 1** Schematic Representation of the Component Parts of a DSSC.
Note not drawn to scale and sensitser converage not depicted as a monolayer.

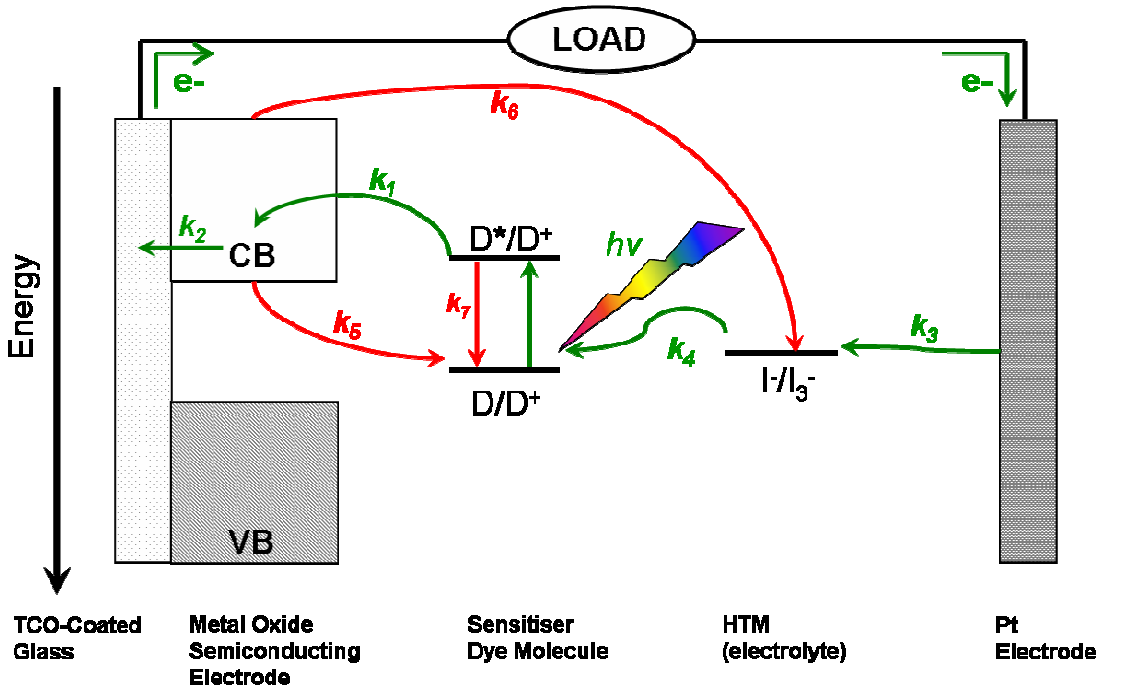


**Fig. 2** Schematic Representation of the Energy Level Diagram showing the Elemental Steps of a DSSC. D=Dye. CB=Conduction Band. VB=Valence Band. Green arrows=processes required for photovoltaic function; $hv$=incident light, $k_1$=charge injection, $k_2$=charge collection at the conducting glass electrode, $k_3$=charge collection at the Pt electrode, and $k_4$=dye regeneration. Red arrows=loss mechanisms; $k_5$=charge recombination with the oxidised dye ($D^+$), $k_6$=charge recombination with the hole-transport material (HTM), and $k_7$=decay of the excited state of the dye (D*).[17]

#### 1.4.1.1.1 TCO Electrode and Metal Oxide Semiconducting Electrode

As shown by the DSSC schematic in Figure 1, the TCO electrodes act to sandwich together the active materials of the cell, and therefore needs to allow solar radiation to pass through. The TCO electrodes are commonly made from fluorine-doped tin oxide, a transparent material which has been treated on one side to be conductive. The cell cathode is formed by coating the TCOs conductive side with platinum (Pt) (see section 1.4.1.1.3), and the anode by coating with the metal-oxide semiconducting materials.

The success of the Grätzel DSSC over previous DSSC cells came from the use of a nanoporous semiconductor in place of a thin film semiconductor. This alteration acts to exponentially increase the semiconductor surface area available for dye molecule adsorption, therefore increasing the observed photoconversion efficiencies, as quite simply more light is absorbed by the same area of solar cell.[12] The most commonly used metal-oxide semiconductor is titanium dioxide, ($TiO_2$) as research has shown it to yield the highest efficiency devices.[16]

#### 1.4.1.1.2 Sensitiser Dye Molecule

The sensitiser dye molecules acts as the active material of a DSSC by acting as a photodriven molecular electron pump: creating a current by the absorption of visible solar radiation. The energy level diagram given in Figure 2 illustrates this role and puts it into context within the complete DSSC circuit. The redox potentials of the dyes ground ($D/D^+$) and excited ($D^*/D^+$) states are vitally important in allowing the cell to function effectively. Optimisation of these two energy levels requires the consideration of multiple factors, which is an important theme throughout this thesis. Once absorption of a photon has led to the excitation of the sensitiser, electron injection into the semiconductor must be the energetically-favourable result. Therefore $D^*/D^+$ must be sufficiently negative in comparison with the conduction band of the

semiconductor (Figure 2). To allow regeneration of the dye, $D/D^+$ must be sufficiently positive in relation to the HTM energy levels (Figure 2). Alongside this, both of these processes should be met without inhibiting the amount or region of visible light absorption.

Figure 2 also demonstrates the loss mechanisms that are occurring within a working DSSC that reduce the efficiencies observed. The main problems arise from decay of the excited state before charge injection, and undesired charge recombination processes involved in the primary and secondary electron transfer processes that lead to excessive free energy loss.[13]

Sensitiser adsorption should optimally result in a monolayer coating of the semiconductor surface, therefore maximising coverage without the possibility of excess sensitiser molecules leading to undesirable processes. Adsorption of the sensitisers to the semiconductor takes place through a functional-group substituent on one of the ligands (an anchoring group) to bind with the $TiO_2$ surface. Research has shown the most successful method utilises a carboxyl group, which forms an ester linkage with the metal oxide.[18] These linkages provide intimate adsorption of the sensitisers onto the semiconductor surface creating sufficient electronic coupling between the two materials to allow charge injection to occur.[13] There are long term stability problems associated with these ester linkages due to hydrolysis of the bond causing desorption of the sensitiser from the semiconductor surface. Phosphonate groups have been tried as alternative anchoring groups as they are more stable to hydrolysis.[18] They have exhibited limited success, however charge injection efficiencies in the red region looked promising.[18]

As the result of all of these factors sensitiser dye molecule design is focused on simultaneously optimising many aspects of their chemical and photophysical properties in order to produce the highest efficiency cell. A detailed discussion of how this has been attempted will take place in section 1.4.1.2.

#### 1.4.1.1.3 Hole Transporting Material (HTM) and Platinum Electrode

The HTM and platinum (Pt) electrode act to complete the electronic circuit. The HTM re-reduces the oxidised sensitiser to its ground state, and the Pt electrode re-reduces the HTM, completing the circuit (Figure 2). The schematic representation of a DSSC given in Figure1 depicts how the HTM acts to fill any space in the device not already filled by dye or semiconductor. This means that the HTM can be a solution, solid-state or quasi-solid-state (gel) material.[17] Currently solution phase HTMs are most commonly used, with triiodide/iodide ($I^-/I_3^-$) redox electrolytes used the most extensively throughout the literature. These cells yield higher solar-to-electrical energy conversion efficiencies than those utilising a solid-state HTM (11% and 7% efficiency respectively) due to increased hole mobility.[19]

As the field advances the want to produce commercially viable solar cells is increasing, causing research to shift towards solid-state HTM solar cells.[20-23] Liquid HTMs have long-term stability problems due to the electrolyte containing volatile $I_2$, that corrodes the Pt electrode, and solvents, such as acetonitrile, that leak out of the device over time, immobilising the $I_2$. A secure hermetic seal[24] is not created which reduces the cell's performance over time. [22]

A Pt coated TCO anode completes the circuit by carrying out the two electron re-reduction of the HTM. This is achieved by the Pt electrode acting as a catalyst in the inherently slow two electron process, making completion of the circuit the more probable outcome.

#### 1.4.1.1.4 Summary

The developments made to the DSSC device have increased solar-to-electrical energy conversion efficiencies due to a combination of factors that look at optimising the photovoltaic processes involved. These include maximising light harvesting efficiency (LHE) in the visible

region, generating efficient charge separation and biasing the forward electron transfer rates over the reverse.[14-16] This last factor is achieved by sensitising the wide band-gap semiconductor (3.2 eV)[25] using sensitisers that have been designed to allow control of the interfacial and intercomponent electron transfer process kinetics.[13] Understanding the model of operation of this photoelectrochemical cell has set out design criteria for the sensitiser dye molecule that will further the evolution of DSSC's. The main focus of this thesis is the design, synthesis and characterisation of sensitiser dye molecules which will be the focus of discussion from now on.

### 1.4.1.2 Design Criteria for the Sensitiser Dye Molecule

The two functions a sensitiser should possess are the ability to absorb efficient quantities of light in the visible region, and to securely anchor via adsorption onto the surface of a semiconductor nanoparticle. The optimal dye would absorb a wide spectral range of solar radiation (400-920nm) (Figure 3) with a consistently high molar extinction coefficient as this would allow thinner devices to be constructed. Having a thin device is beneficial as the losses caused by low charge mobility and costs are minimised.

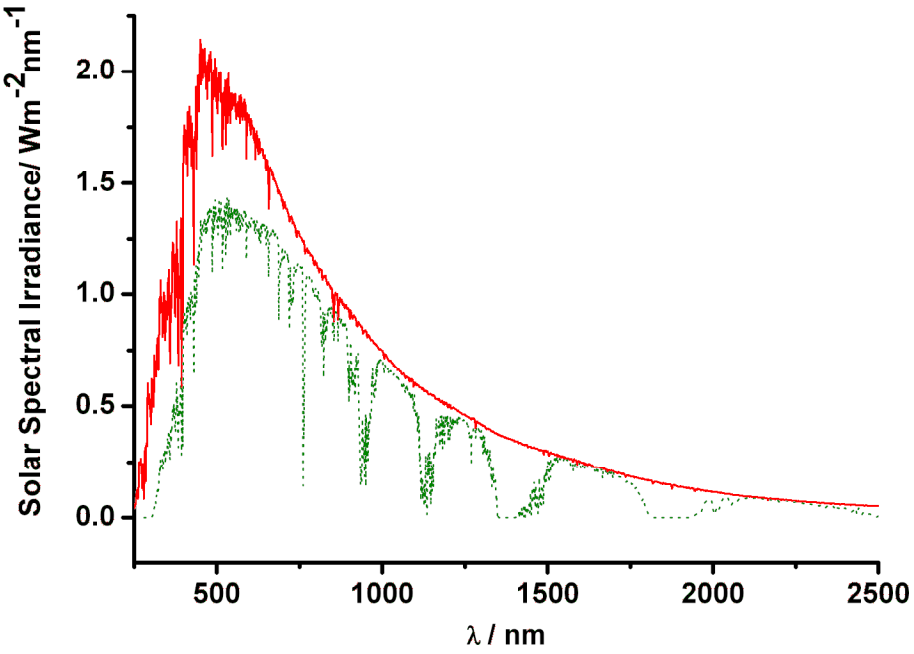


**Fig. 3** Solar Spectrum. Standard intensity AM 0 spectrum (solid red line) and AM 1.5 spectrum (dotted green line) for light incident on the Earth's surface.

Within a DSSC all reactions take place at an interface meaning that the optimisation of the interfacial interactions between solar-cell components is crucial.[14] Sensitiser design can play a significant role in affecting the rates and even the occurrence of these reactions. For example, as previously discussed, the anchoring ester linkages between the sensitiser and the semiconductor can be broken by hydrolysis. One method to prevent this is by including hydrophobic functional groups on the exterior of the sensitiser to limit water access to the semiconductor/sensitiser interface. Undesirable recombination loss processes between the semiconductor and HTM can be minimised by the inclusion of sterically bulky ligands on the sensitiser that can act to restrict semiconductor/HTM interactions.

The search to find molecules with the potential to be suitably adapted to the role of DSSC sensitiser has led to the investigation of purely organic dyes[26-28] through to complexes containing transition metals (TMs) with coordinating organic ligands. It is the later of these which will be the focus of this discussion.

#### 1.4.1.2.1 Ruthenium DSSC Sensitisers

The most successful DSSCs developed to date are based on Ru(II)-containing sensitiser molecules,[29-33] some of which are being commercially developed for niche markets.[34] Here the structures of two of the most efficient Ru(II) DSSC sensitisers (Figure 4) will be discussed to gain further insight into the chemistry behind their success. Ru(II) complexes tend to exhibit strong absorption bands in the visible light region, for example **N3** exhibits $\lambda_{max}$ = 534nm ($\varepsilon$ = 1.42 x$10^4$ $M^{-1}cm^{-1}$),[29] and the "black dye" exhibits efficient panchromatic sensitisation over the whole visible range.[30]

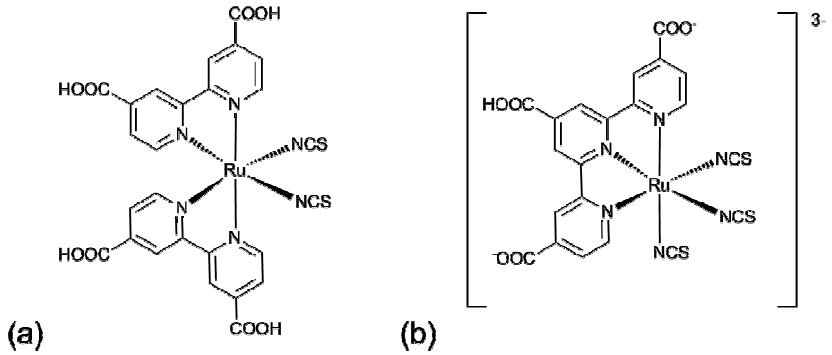


**Fig. 4** Structure of (a) **N3:** *cis*-di(thiocyanato)bis(2,2'-bipyridyl-4,4'-dicarboxlate)ruthenium(II);[29] (b) the "black dye" trithiocyanato-ruthenium(II) terpyridyl complex.[30]

The structures shown in Figure 4, and the majority of Ru(II)-sensitiser complexes, contain the same basic structural features. Polypyridine-based ligands with carboxyl-group substituents are used most extensively in Ru(II) sensitisers for several reasons. Firstly as the polypyridyl ligands are poly-dentate they provide additional stability to the molecule through the chelate effect. Secondly, as described in section 1.5.1.1.2, the carboxyl-groups act as anchoring groups and tether the sensitisers to the $TiO_2$ surface (Figure 1).[13] Lastly, coordination of polypyridyls to ruthenium gives rise to visible MLCT absorptions.

Another key structural features are the thiocyanto (NCS) ligands which are more easily oxidised than the central metal atom. Therefore the hole generated by electron injection into the $TiO_2$ is delocalised towards the NCS ligand, giving two beneficial outcomes. Firstly increased spatial charge separation which minimises the effect of charge recombination (Figure 2. $k_5$) as the electron recombination distance is increased. The second benefit is that sensitiser regeneration by the HTM (Figure 2. $k_4$) can occur more readily. The Ru(II) sensitiser will be discussed further in comparisons with the potentials of Cu(I) sensitisers in section 1.5.

#### 1.4.1.2.2 1st Row Transition Metal Sensitisers

Lower efficiency DSSCs have also been constructed using transition metal complexes of Os(II),[31, 32] Pt(II),[35, 36] Re(I),[37] Cu(I),[38-43] and Fe(II).[44-46] The use of 2nd and 3rd row transition metal as sensitisers dominates this field, due in part to their ability to display long-lived excited states following MLCT absorption in the visible region of the solar spectrum. However low abundance, and toxicity considerations could present detrimental practical implications in the long term.

Despite 1st row transition metals not presenting abundance or toxicity problems, research into 1st row transition metal sensitisers has been comparatively limited. They typically exhibit extremely short-lived excited states compared to 2nd and 3rd row transition metal complexes, arising from the low lying metal d-d excited states which allow non-radiative decay of the MLCT excited state. This is a limiting factor in terms of DSSC functionality as charge injection from the sensitiser into the $TiO_2$ is not efficiently achieved.[44, 47]

Two sensitiser design strategies have been implemented to try and overcome this problem and extend the excited state lifetime of the complex by limiting the extent of non-radiative decay of

the MLCT excited states. The first is to have a strong crystal field, aimed at raising the energy of any d-d excited states, and the second to have complexes with a full d-subshell.[45]

The first of the above strategies has been explored by Ferrere[44-46] with work on Fe(II) sensitisers designed to obtain a strong crystal field (Figure 5). The structure is analogous to a successful Ru(II) sensitiser known to exhibit strong crystal-field splitting which is believed to be the result of the inclusion of high field $CN^-$ ligands.[29]

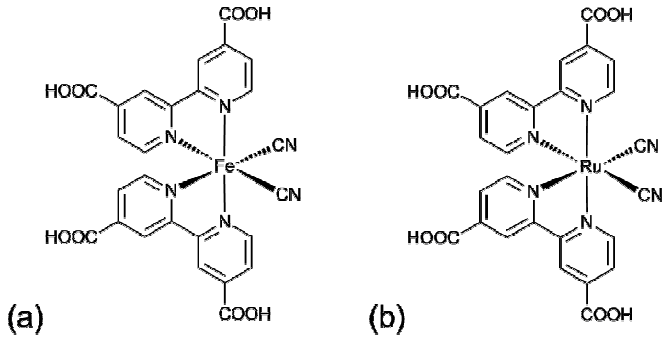


**Fig. 5** Structures of (a) $[Fe(II)(dcbpy)(CN)_2]$[44] and (b) $[Ru(II)(dcbpy)(CN)_2]$[29]

The final 1st row transition metal sensitisers to be investigated for DSSC application are Cu(I) complexes. The complexes have a full d-subshell ($d^{10}$ configuration) that prevents non-radiative decay of the MLCT excited state, and unlike Zn(II), which also has a full d-subshell, Cu(I) exhibits redox behaviour. The main focus of this thesis is to further the research into the use of Cu(I) in this role, due to the photophysical and photoelectrochemical similarities Cu(I) has with Ru(II). These properties will be discussed with respect to Cu(I) bipyridine and phenanthroline complexes, and Ru(II) bipyridine complexes.

## 1.5 A Comparison of Cu(I) with Ru(II) sensitisers

As mentioned previously, the most successful sensitiser molecules to date have Ru(II) as the central metal atom. Ru(II) polypyridines absorb light in the visible region and have reversible electrochemical behaviour.[48] Coupled with this, their excited states are long lived and they exhibit intense luminescence.[48] Promising alternatives to this expensive energy-crisis solution are Cu(I) phenanthrolines and Cu(I) polypyridines.[38, 39, 48] These complexes are the most extensively researched of the first row TM containing complexes in terms of their electrochemical and photophysical behaviour.[17, 49]

One of the main noticeable differences between the two groups of compounds is coordination number; Ru(II) complexes are 6-coordinate, whereas Cu(I) are 4-coordinate. A conformational geometry change of a Cu(I) complex takes place during the Cu(I)/Cu(II) redox process or during MLCT.[50, 51] Cu(I) complexes in the ground state observe a tetrahedral-like geometry, and in the MLCT excited state tetragonally-flattened geometries.[47] The ability to change conformation can lead to solvent attack of the excited molecule, known as exciplex quenching, and can also lead to complex degradation and decomposition. This, coupled with the slower electron transfer kinetics also induced by the conformational change, has made Cu(I) complexes less appealing for use in devices.

The extent and effect this conformational change has on the photoelectrochemical and electroluminescent properties has been investigated by designing ligands that coordinate to sterically constrain the molecule to the pseudo-tetrahedral geometry, therefore limiting the extent of the geometrical flattening.[48, 50, 51] It has been found that the degree to which the conformation flattens depends on the substituents on the ligand: their chemical nature, size, and, most importantly, the position of substitution.[47, 48, 52] The greatest effect is achieved by

substituents in the 2- and 9-positions for phenanthrolines and the 6,6′-positions for bipyridyls, due to their ability to geometrically constrain the complex (see Figure 6). In this role they have been described as “blocking groups”.

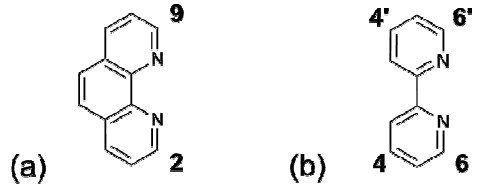


**Fig. 6** Structure and Carbon Numbering of (a) 1,10-Phenanthroline; and (b) 2,2’-bipyridine.

The extent of structural distortion achieved by oxidation allows some degree of control over the luminescence spectra observed, the emission quantum yields and the excited state lifetimes achieved by the molecules.[47, 48, 52] Hence, varying the blocking groups plays a key role in the control over the photophysical and electrochemical properties of the complexes.[48] The restriction of geometric relaxation induced by the blocking groups will also reduce the extent to which solvent attack of the excited molecule can occur.[44, 47] Therefore, the lifetime of the excited state can be extended by conformational limitation, also reducing degradation and decomposition of the complex.

Simple homoleptic complexes, such as Cu(I)(1,10-phenanthroline)$_2$ and Cu(I)(2,2′-bipyridine)$_2$, were looked at initially with comparisons with Ru(II) complexes to determine if Cu(I) could be a viable alternative electroluminescent active material for device application. Simple aryl and alkyl substituents groups were located on the 2,9- and 6,6′-position respectively, to act as “blocking” groups to sterically constrain the molecule and therefore maintain the pseudo-tetrahedral geometry.[53-62] 4,4′,6,6′-Substitutened bipyridine ligands have also been coordinated to Cu(I) to form bis-complexes.[51, 63] Probing of these complexes saw no noticeable alteration in the photophysical properties observed compared to the phenanthroline analogues, but allowed the possibility of Cu(I) complexes being exploited in DSSCs to be explored.[38-41]

Initial studies into the ability of homoleptic Cu(I) phenanthroline and bipyridine complexes to act as spectral sensitisers of wide-band gap semiconductors have been encouraging.[38, 39] The structures of the ligands used in these homoleptic complexes are shown in Figure 7.

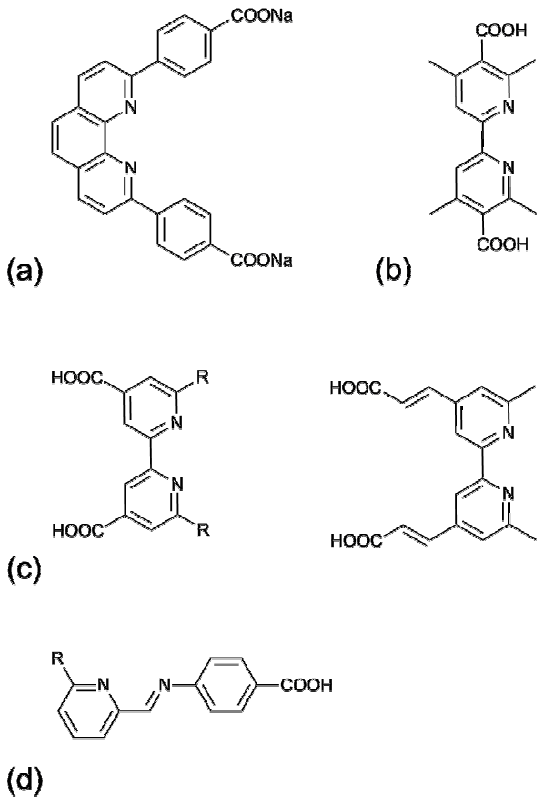


**Fig. 7** Ligands used in Homoleptic Cu(I) Sensitisers.[38-41, 43]

Sauvage et al.[38] explored the possibility of homoleptic Cu(I)-phenanthroline complexes applied as DSSC sensitisers (Figure 7 (a)), while Hamada et al.[39] looked into homoleptic Cu(I)-bipyridine based complexes (Figure 7 (b)). Although charge injection was observed when these dyes were used to sensitise colloidal semiconductor films, the overall cell efficiencies were significantly less than those observed for Ru(II) dyes. This reduction in efficiency may be explained by previous studies which have shown that for the bipyridyl ligand (Figure 7 (b)), having the anchoring group in the 5,5′-position considerably lowers the efficiency of a DSSC cell compared to having them in the 3,3′- or 4,4′-positions.[35, 64-67]

Recent work carried out by Constable *et al.*[40-42] has produced promising results, with device efficiencies reaching 2.6%. The research concentrates on complexes with anchoring groups in the 4,4'-positions and additional groups substituted in the 6,6′-positions to maintain the Cu(I) pseudo-tetrahedral geometry (Figure 7 (c)). Constable *et al.*[43] have now expanded their research to explore complexes that do not contain a bipyridyl ligand as the anchoring ligand but an iminopyridine which is electronically similar to a bipyridyl (Figure 7 (d)). The complexes investigated by Constable *et al.* yield results which highlight the potential of Cu(I) sensitisers, but the device performances are still significantly less than those of Ru(II) sensitsers. One possible explanation is that Cu(I)-bipyridine complexes generally exhibit lower molar extinction coefficients than the Ru(II) analogues. One possibility to address this has been explored by Constable *et al.*[41] is to include ligands that contain large conjugated systems so as to allow more light to be absorbed.

To date only homoleptic Cu(I) complexes have been explored in this role due to the synthetic difficulties associated with heteroleptic Cu(I) complexes. Here we hope to investigate heteroleptic Cu(I) complexes in this role, which will be discussed in more detail in section 1.7.

## 1.6 Cu(I) Photoelectrochemical and Photophysical Materials

The photophysical and electrochemical properties of phenanthroline- and bipyridine-based Cu(I) complexes have been utilised in many different areas of chemistry, and have the potential to be utilised in many more. Their ability to interact with other species, and the corresponding effect this has on their previously-described photophysical and electrochemical properties, means that bimolecular photoinduced energy- and electron-transfer processes, DNA interactions, photochemically driven molecular machines, and use as potential molecular receptors, are all areas where these molecules could play a role.[48] However, the most interesting of these applications, in terms of the work presented here, are the electron-transfer processes which can be influenced by structural variation and it is these which will be the main focus of this report.

The work presented in this thesis concentrates on the application of Cu(I) coordination complexes to DSSC technology. However, as luminescence is the most extensively investigated electronic property of these Cu(I)-complexes this will be discussed in Chapters Three and Five, with a detailed investigation of two complexes being the focus of Chapter Four. In this context Cu(I) complexes have been described as electroluminescent coordination compounds[56, 68] The colour of emission can be tuned in the same manner as the lifetime of the excited state can be adjusted; by variation of the chemical structure of the ligands used.[49] Due to this ability to control the emission colour there is growing interest in electroluminescent complexes being used as the active material in organic light-emitting diodes (OLEDs).[49, 68] The working principle of an OLED is outlined in Figure 8.

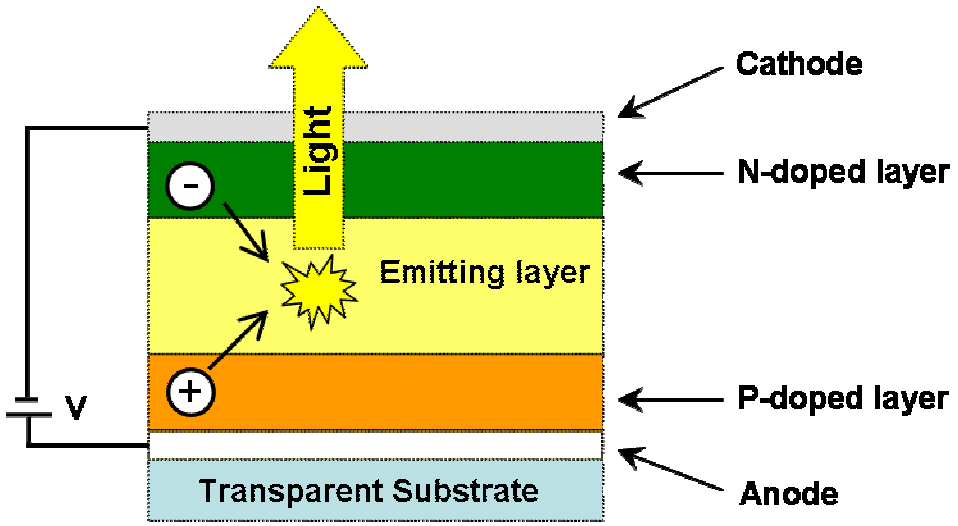


**Fig. 8** Schematic Representation of an OLED. Electrons and holes which are generated at opposite electrodes meet to form Excitons. The formed excitons then relax to the ground state and emit light. The colour emitted is dependent on the HOMO-LUMO gap.

## 1.7 Proposed Research

The main aim of this research is to synthesise heteroleptic Cu(I)-bipyridine based-complexes for use in photoelectrochemical and photophysical materials. They are suited to this role due to their extensive photophysical and electrochemical properties being adaptable and thus tuned by structural modifications of their ligands. It is widely believed that the most efficient sentitisers will be based on heteroleptic complexes, as they should achieve the desired directional charge transfer in the direction of the $TiO_2$. In a heteroleptic complex the ligands can be designed so that the non-attaching ligand is charge donating, and therefore it is hoped directional charge transfer across the complex is achieved.

There are two investigations taking place during this work. Firstly, the development of first row transition metal DSSC sensitisers: Chapters Three, Five and Seven look at heteroleptic Cu(I) senstisers, and Chapter Six looks at utilising Ni(II) in this role. The second is an exploration into how structural behaviour can effect the photoluminescent properties of Cu(I) complexes: Chapter Four. Each chapter of this thesis contains a detailed introduction outlining its particular aims and puts the work into context with respect to the literature.

## 1.8 References


1. R. Eisenberg and D. G. Nocera, *Inorganic Chemistry*, 2005, **44**, 6799-6801.
2. N. S. Lewis and D. G. Nocera, *Proceedings of the National Academy of Sciences*, 2006, **103**, 15729-15735.
3. Q. Schiermeier, J. Tollefson, T. Scully, A. Witze and O. Morton, *Nature*, 2008, **454**, 816-823.
4. http://www.eia.doe.gov/oiaf/ieo/highlights.html.
5. http://www.eia.doe.gov.
6. K. Zweibel and P. Singh, *American Journal of Physics*, 1993, **61**, 286-287.
7. K. W. J. Barnham, M. Mazzer and B. Clive, *Nature Materials*, 2006, **5**, 161-164.
8. M. K. Nazeeruddin, *Coordination Chemistry Reviews*, 2004, **248**, 1161-1164.
9. E. Mazria, *Passive Solar Energy Book*, 1979.
10. M. A. Green, *Progress in Photovoltaics: Research and Applications*, 2001, **9**, 123-135.
11. J. Yoon, S. Jo, I. S. Chun, I. Jung, H.-S. Kim, M. Meitl, E. Menard, X. Li, J. J. Coleman, U. Paik and J. A. Rogers, *Nature*, **465**, 329-333.
12. B. O'Regan and M. Gratzel, *Nature*, 1991, **353**, 737-740.
13. C. A. Bignozzi, R. Argazzi and C. J. Kleverlaan, *Chemical Society Reviews*, 2000, **29**, 87-96.
14. B. A. Gregg, *Coordination Chemistry Reviews*, 2004, **248**, 1215.
15. J. A. McCleverly and T. J. Meyer, *Comprehensive Coordination Chemistry II*, Elsevier, 2003.
16. G. J. Meyer, *Journal of Chemical Education*, 1997, **74**, 652-null.
17. N. Robertson, *Angewandte Chemie International Edition*, 2006, **45**, 2338-2345.
18. S. M. Zakeeruddin, M. K. Nazeeruddin, P. Pechy, F. P. Rotzinger, R. Humphry-Baker, K. Kalyanasundaram, M. Gratzel, V. Shklover and T. Haibach, *Inorganic Chemistry*, 1997, **36**, 5937-5946.
19. P. Wang, Q. Dai, S. M. Zakeeruddin, M. Forsyth, D. R. MacFarlane and M. Grätzel, *Journal of the American Chemical Society*, 2004, **126**, 13590-13591.
20. N. C. Greenham, X. Peng and A. P. Alivisatos, *Physical Review B*, 1996, **54**, 17628.
21. G. Yu and A. J. Heeger, *Journal of Applied Physics*, 1995, **78**, 4510-4515.
22. K. Murakoshi, R. Kogure, Y. Wade and Y. S., *Solar Energy Materials and Solar Cells*, 1998, **55**, 113.
23. H. J. Snaith, S. M. Zakeeruddin, L. Schmidt-Mende, C. Klein and M. Grätzel, *Angewandte Chemie International Edition*, 2005, **44**, 6413-6417.
24. P. Wang, S. M. Zakeeruddin, J. E. Moser, M. K. Nazeeruddin, T. Sekiguchi and M. Gratzel, *Nat Mater*, 2003, **2**, 402-407.
25. M. Gratzel, *Nature*, 2001, **414**, 338-344.
26. K. Hara, Z.-S. Wang, T. Sato, A. Furube, R. Katoh, H. Sugihara, Y. Dan-oh, C. Kasada, A. Shinpo and S. Suga, *The Journal of Physical Chemistry B*, 2005, **109**, 15476-15482.
27. T. Horiuchi, H. Miura, K. Sumioka and S. Uchida, *Journal of the American Chemical Society*, 2004, **126**, 12218-12219.

28. Y.-S. Chen, C. Li, Z.-H. Zeng, W.-B. Wang, X.-S. Wang and B.-W. Zhang, *Journal of Materials Chemistry*, 2005, **15**, 1654-1661.
29. M. K. Nazeeruddin, A. Kay, I. Rodicio, R. Humphry-Baker, E. Mueller, P. Liska, N. Vlachopoulos and M. Graetzel, *Journal of the American Chemical Society*, 1993, **115**, 6382-6390.
30. M. K. Nazeeruddin, P. Pechy and M. Gratzel, *Chemical Communications*, 1997, 1705-1706.
31. R. Argazzi, C. A. Bignozzi, T. A. Heimer, F. N. Castellano and G. J. Meyer, *Inorganic Chemistry*, 1994, **33**, 5741-5749.
32. T. A. Heimer, C. A. Bignozzi and G. J. Meyer, *The Journal of Physical Chemistry*, 1993, **97**, 11987-11994.
33. O. Kohle, S. Ruile and M. Gratzel, *Inorganic Chemistry*, 1996, **35**, 4779-4787.
34. http://www.g24i.com/.
35. E. A. M. Geary, L. J. Yellowlees, L. A. Jack, I. D. H. Oswald, S. Parsons, N. Hirata, J. R. Durrant and N. Robertson, *Inorganic Chemistry*, 2004, **44**, 242-250.
36. A. Islam, H. Sugihara, K. Hara, L. P. Singh, R. Katoh, M. Yanagida, Y. Takahashi, S. Murata, H. Arakawa and G. Fujihashi, *Inorganic Chemistry*, 2001, **40**, 5371-5380.
37. G. M. Hasselmann and G. J. Meyer, *Z. Phys. Chem.*, 1999, 39.
38. N. Alonso-Vante, J.-F. Nierengarten and J.-P. Sauvage, *J. Chem. Soc., Dalton Trans. FIELD Full Journal Title:Journal of the Chemical Society, Dalton Transactions: Inorganic Chemistry (1972-1999)*, 1994, 1649-1654.
39. S. Sakaki, T. Kuroki and T. Hamada, *Journal of the Chemical Society, Dalton Transactions*, 2002, 840-842.
40. T. Bessho, E. C. Constable, M. Graetzel, A. H. Redondo, C. E. Housecroft, W. Kylberg, M. K. Nazeeruddin, M. Neuburger and S. Schaffner, *Chemical Communications*, 2008, 3717-3719.
41. E. C. Constable, A. H. Redondo, C. E. Housecroft, M. Neuburger and S. Schaffner, *Dalton Transactions*, 2009, 6634-6644.
42. A. H. Rendondo, E. C. Constable and C. E. Housecroft, *CHIMIA International Journal for Chemistry*, 2009, **63**, 205-207.
43. B. Bozic-Weber, E. C. Constable, C. E. Housecroft, M. Neuburger and J. R. Price, *Dalton Transactions*, 2010, **39**, 3585-3594.
44. S. Ferrere and B. A. Gregg, *Journal of the American Chemical Society*, 1998, **120**, 843-844.
45. S. Ferrere, *Chemistry of Materials*, 2000, **12**, 1083-1089.
46. S. Ferrere, *Inorganica Chimica Acta*, 2002, **329**, 79-92.
47. S.-M. Kuang, D. G. Cuttell, D. R. McMillin, P. E. Fanwick and R. A. Walton, *Inorganic Chemistry*, 2002, **41**, 3313-3322.
48. N. Armaroli, *Chemical Society Reviews*, 2001, **30**, 113-124.
49. A. Barbieri, G. Accorsi and N. Armaroli, *Chemical Communications*, 2008, 2185-2193.
50. N. Armaroli, G. Accorsi, F. Cardinali and A. Listorti, *"Photochemistry and Photophyics of Coordination Compounds I"*, 2007.
51. R. M. Williams, L. D. Cola, F. Hartl, J.-J. Lagref, J.-M. Planeix, A. D. Cian and M. W. Hosseini, *Coordination Chemistry Reviews*, 2002, **230**, 253-261.
52. N. Armaroli, G. Accorsi, F. Cardinali and A. Listorti, *Photochemistry and Photophysics of Coordination Compounds I.*

53. D. R. McMillin, M. T. Buckner and B. T. Ahn, *Inorganic Chemistry*, 1977, **16**, 943-945.
54. R. M. Everly and D. R. McMillin, *The Journal of Physical Chemistry*, 1991, **95**, 9071-9075.
55. A. J. Pallenberg, K. S. Koenig and D. M. Barnhart, *Inorganic Chemistry*, 1995, **34**, 2833-2840.
56. M. Ruthkosky, C. A. Kelly, F. N. Castellano and G. J. Meyer, *Coordination Chemistry Reviews*, 1998, **171**, 309-322.
57. M. T. Miller, P. K. Gantzel and T. B. Karpishin, *Inorganic Chemistry*, 1998, **37**, 2285-2290.
58. M. T. Miller, P. K. Gantzel and T. B. Karpishin, *Inorganic Chemistry*, 1999, **38**, 3414-3422.
59. Z. A. Siddique, Y. Yamamoto, T. Ohno and K. Nozaki, *Inorganic Chemistry*, 2003, **42**, 6366-6378.
60. M. Iwamura, S. Takeuchi and T. Tahara, *Journal of the American Chemical Society*, 2007, **129**, 5248-5256.
61. Y. Leydet, D. M. Bassani, G. Jonusauskas and N. D. McClenaghan, *Journal of the American Chemical Society*, 2007, **129**, 8688-8689.
62. O. Green, B. A. Gandhi and J. N. Burstyn, *Inorganic Chemistry*, 2009, **48**, 5704-5714.
63. C. T. Cunningham, K. L. H. Cunningham, J. F. Michalec and D. R. McMillin, *Inorganic Chemistry*, 1999, **38**, 4388-4392.
64. E. A. M. Geary, in *School of Chemistry*, The University of Edinburgh, Edinburgh, 2005.
65. E. A. M. Geary, N. Hirata, J. Clifford, J. R. Durrant, S. Parsons, A. Dawson, L. J. Yellowlees and N. Robertson, *Dalton Transactions*, 2003, 3757-3762.
66. W. Paw, S. D. Cummings, M. A. Mansour, W. B. Connick, D. K. Geiger and R. Eisenberg, *Coordination Chemistry Reviews*, 1998, **171**, 125.
67. E. J. L. McInnes, R. D. Farley, S. A. Macgregor, K. J. Taylor, L. J. Yellowlees and C. C. Rowlands, *Journal of the Chemical Society, Faraday Transactions*, 1998, **94**, 2985-2991.
68. N. Armaroli, G. Accorsi, M. Holler, O. Moudam, J. F. Nierengarten, Z. Zhou, R. T. Wegh and R. Welter, *Advanced Materials*, 2006, **18**, 1313.

# 2. Chapter Two

# Experimental Techniques

## 2.1 Electrochemistry

The electrochemical technique of Cyclic Voltammetry (CV) has been used in this work to gain an understanding about the electron transfer kinetics and investigate the chemical reactivity of our species. This section will explain how this information is extracted from a CV and used to explain the behaviour of our complexes. The following definitions and explanations are applied throughout this thesis to describe the behaviour of our complexes. The details of the three electrode system and general experimental set up are given in the relevant experimental sections of subsequent chapters.

A CV experiment involves sweeping the applied potential at a fixed rate between two values in both positive and negative directions. The resulting cyclic voltammogram is a plot of current response as a function of voltage, known as a voltammogram, with the example for an ideal electrochemically-reversible, single-electron transfer shown in Figure 1.

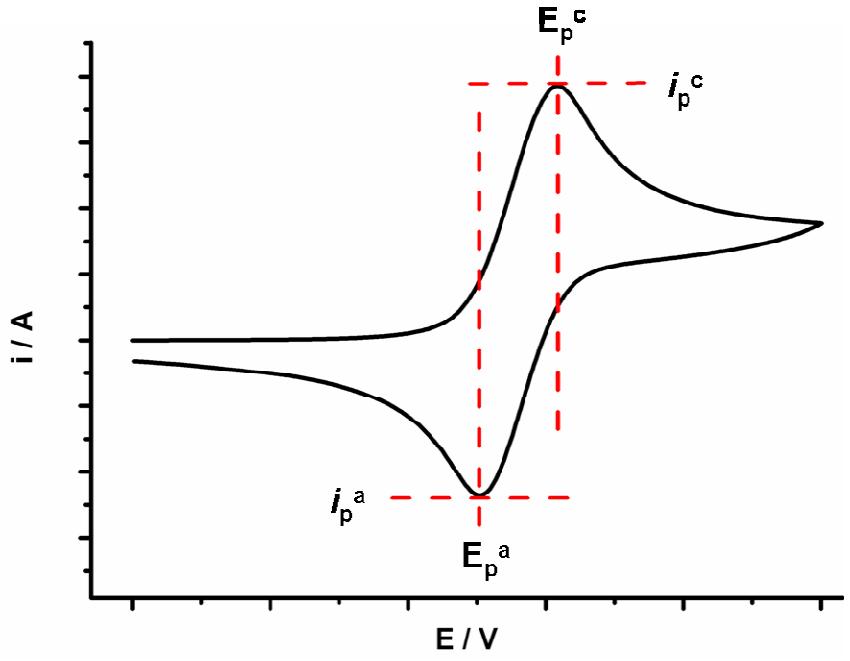


**Fig. 1** Cyclic Voltammogram for an ideal electrochemically-reversible reaction. Where; $E_p^c$ = voltage of peak current (cathodic); $i_p^c$ = peak current (cathodic); $E_p^a$ = voltage of peak current (anodic); $i_p^a$ = peak current (anodic).

The shape of the voltammogram can be explained by considering how the equilibrium of electrochemical species at the electrode is influenced by voltage. For the above example of an electrochemically-reversible reaction, the rate of electron transfer is fast compared to the voltage sweep rate. This demonstrates that an equilibrium has been established at the electrode surface, which can be described by the Nernst equation;

$$E = E^{\theta} + \frac{RT}{nF} \ln \frac{[\text{oxidised}]}{[\text{reduced}]}$$

where E = applied potential difference; $E^{\theta}$ = standard electrode potential; R = universal gas constant; T = absolute temperature; n = number of moles of electrons transferred in the cell reaction; F = Faraday constant.

The equilibrium at the surface of the electrode alters as the voltage is scanned due to the conversion of reactant to product (the above equation describes the conversion of oxidised to reduced species). The result is the flow of current, which increases as more reactant is converted to product (Figure 1). The peak in current can be explained by mass transport effects, for as the reactant is converted to product a diffusion layer forms above the surface of the electrode. Eventually this layer becomes sufficiently thick so as to cause the flux of reactant to the electrode surface to no longer satisfy the Nernst equation, and hence the current begins to drop.

The voltammogram shown in Figure 1 was recorded at a fixed scan rate. When voltammograms of the same solution are recorded at varying scan rates there are two main features of the CV that are affected. Firstly the increasing scan rate causes an increase in current response if the reaction is a reversible single electrode transfer. This arises as a slower scan (decreased scan rate) allows the diffusion layer to grow much further than it would during a faster scan. This therefore reduces the flux to the surface of the electrode, and as flux is proportional to the

magnitude of the current, a smaller current response is seen for slower scan rates. The second feature to be discussed is that the current maximum occurs at the same voltage regardless of scan rate. This is a characteristic property of a reversible electron transfer due to the rapid electron transfer kinetics involved. It is easier to explain this phenomenon by taking a system where the voltage of maximum current does vary with scan rate. In this case the electron transfer kinetics are slower relative to the voltage scan rate, and therefore do not follow the Nernst equation as the equilibrium at the electrode surface cannot be established in the available time scale. The maximum current occurs at varying potentials depending on the scan rate as a result of it taking longer for the current to respond to the applied voltage.

Based upon the above behaviour it is possible to describe the electrochemical reaction occurring for a given system. For a reaction to be described as an electrochemically-reversible reaction the following characteristics must be exhibited; (i) The two peak current (Figure 1; $i_p^c$ and $i_p^a$) must have a peak separation of:

$$E = E_P^{\mathrm{a}} - E_P^{\mathrm{c}} = \frac{59}{n} mV$$

(ii) the voltage of maximum current does not alter as a function of scan rate; (iii) the ratio of peak currents is equal to one: $\frac{i_P^{\mathrm{a}}}{i_P^{\mathrm{c}}} = 1$; and (iv) the peak currents are proportional to the square root of the scan rate: $i_P^{\mathrm{a}}$ and $i_P^{\mathrm{c}} \propto \sqrt{v}$. If these criteria are not met the reaction is electrochemically irreversible.

## 2.2 Spectroscopy

### 2.2.1 Absorption Spectroscopy

For the work described in this thesis absorption can be defined as the electrons of an atom taking up the energy of a photon. This can occur when the energy of the radiation matches the energy between two energy levels and certain selection rules are adhered to (Figure 2). Spin multiplicity will be discussed further in section 2.2.2. Analytical methods quantify the extent of absorption by measuring the absorbance (A) of a chemical species. Through the Beer-Lambert Law (given below) it is possible to determine how strongly a species absorbs at a given wavelength by the calculation of the molar extinction coefficient (ε);

$$A = c \varepsilon l$$

where; c = the concentration of the absorbing species and l = the path length. The Beer-Lambert law shows that the absorbance of a chemical species is proportional to the thickness of the sample and the concentration of the sample. These experimental measurements are used throughout this thesis to explain the behaviour of the complexes investigated.

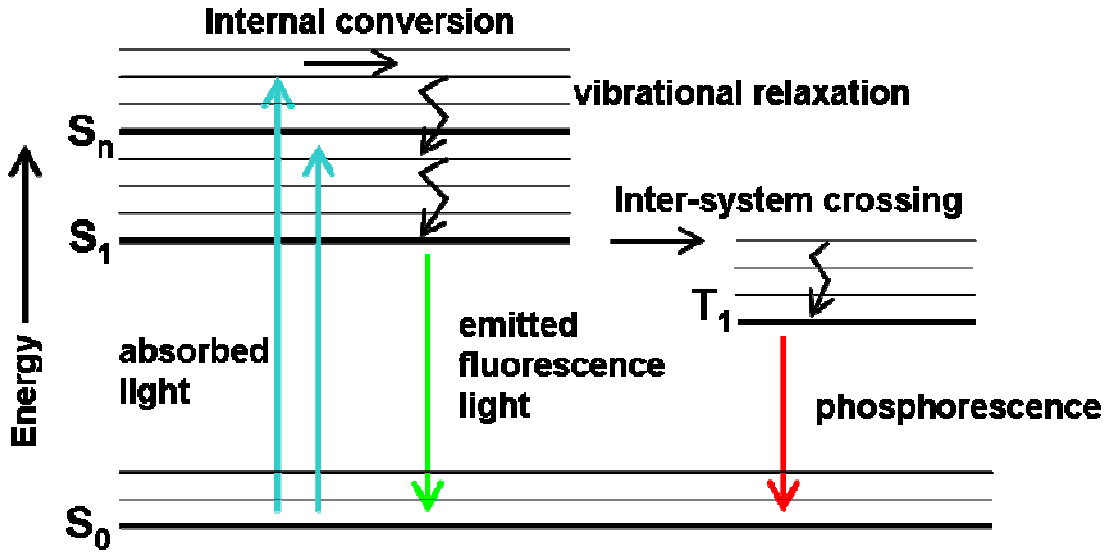


**Fig. 2** Jablonski Diagram

## 2.2.2 Emission Spectroscopy

Once a photon has been absorbed by a chemical species the energy is subsequently released again in some manner; what goes up must come down. This can be achieved by the species emitting light or by non-radiative decay process. These processes and the information they can provide about the chemical species being explored will be discussed in the following sections with the use of a Jablonski diagram (Figure 2). The experimental details used for our emission spectroscopy measurements are given in the experimental sections of the relevant subsequent chapters.

Before the processes are defined in detail it should be stated that the example used during this chapter has a singlet ground state ($S_0$). The electronic states of molecules are defined in terms of the spin multiplicity of the state, which is given by 2s+1, where s is the total spin. For a singlet (S), there are no unpaired electrons, s=0, and the spin multiplicity is one. For a triplet (T) state, there are two unpaired electrons, s=1, and the spin multiplicity is three.

### 2.2.2.1 Fluorescence

At room temperature the majority of molecules occupy the lowest vibrational level of their ground state ($S_0$), and upon the absorption of light are taken into any of the vibrational levels associated with their singlet excited states, from $S_1$ up to $S_n$ (Figure 2). If the molecule is excited into an excited state of higher energy than $S_1$ (i.e. $S_n$) then through a process known as internal conversion it will return to $S_1$ (Figure 2). The molecule falls to the lowest vibrational level of the excited state ($S_1$) via vibrational relaxation, (Figure 2), due to excess vibrational energy being quickly lost through collisions. Fluorescence emission is then observed when the molecule returns to any of the vibrational levels of the singlet ground state, with the emission of a photon of an energy that matches the energy difference between the two electronic states. Fluorescence is formally defined as a radiative transition between electronic states with the same multiplicity.

### 2.2.2.2 Phosphorescence

The excitation of a molecule takes place in the same way whether the molecule goes on to exhibit fluorescence and phosphorescence, the differences in the two processes takes place after this initial event. Once an electron is promoted into a higher orbital a singlet or triplet state can be adopted. If the electron spins are anti-parallel the state is known as a spin singlet. However, an alternative arrangement would be to have the spins aligned parallel, creating a triplet electronic state. Inter-system crossing is the indirect process of going from an excited singlet state to a triplet state ($T_1$) (Figure 2), and the emission from this triplet state is known as phosphorescence. Phosphorescence is formally defined as emission occurring between states of different spin multiplicities.

It should be noted that transitions from the ground (singlet) state to the triplet state, and the reverse transition, from the triplet state to the ground state and intersystem crossing are formally forbidden. This is highlighted when the time taken for phosphorescence to occur is compared with that for fluorescence: $10^{-4}$ to $10^{2}$ seconds and $10^{-9}$ to $10^{-6}$ seconds respectively. This significant difference in emission time can be used to aid in the assignment of a process as being either the result of fluorescence or phosphorescence. Another crucial difference between phosphorescence and fluorescence that can be used to assign the type of emission taking place is the spectral shift between excitation and emission peaks. A Stokes shift can be described as the difference in band maxima between the absorption and emission peaks that arise from the same electronic transition. A more significant spectral shift, often referred to as a pseudo-Stokes shift, is observed when the emission originates from a triplet state, as the triplet state is at lower energy than the corresponding singlet state, meaning emission at longer wavelength (Figure 2).

Emission spectroscopy can be used to allow the determination of several properties. These include the absorption and emission energies (previously discussed), quantum yields (Φ) and lifetime of emission (τ). A quantum yield is a measure of the efficiency of light emission by a molecule, as shown in the equation below;

$$\Phi = \frac{\text{number of photons emitted}}{\text{number of photons absorbed}}$$

The lifetime of emission provides information about the excited state lifetime of a molecule. It usually follows exponential first order kinetics and is define in the following equation, where $k_{obs}$ is the rate constant of decay of the excited state;

$$\tau = \frac{1}{k_{obs}}$$

The rate constant of decay can then be divided into radiative decay ($k_{rad}$) and non-radiative deactivation pathways ($\Sigma k_{nr}$):

$$\tau = \frac{1}{k_{rad} + \Sigma k_{nr}}$$

It is these non-radiative deactivation pathways that act to reduce the quantum yield of an emission process from unity. Non-radiative deactivation describes any process by which a molecule returns to its ground state without the emission of light. Common methods for non-radiative deactivation, especially for molecules in the longer lived triplet states, are by collisions with solvent molecules (collisional quenching) and vibrational deactivation. This is demonstrated by the increased emission exhibited by most molecules upon the freezing of the solvent or dispersing of the emissive materials in a rigid matrix, when these collisions and vibrations are minimised.

## 2.3 Computational

Density functional calculations have been used in this work to complement our experimental measurements and aid our understanding of the behaviour of the complexes under investigations. The details of the computational methodology are given in the experimental sections of the relevant subsequent chapters. The computational methods employed in this thesis only utilise a small proportion of the computational techniques available, and it will only be these methods which will be explained in detail here. Initially, however, the explanation for using these methods over alternatives will be outlined.

Computational chemistry can be split into two main methodologies, the first of these following classical physics; molecular mechanics, and the second, *ab initio* molecular orbital theory, which follows the laws of quantum mechanics. When calculations are carried out using molecular mechanic the atoms are treated as classical objects and any explicit details of the behaviour of the electrons is ignored. Therefore despite the ease and speed at which these calculations can be run they are not useful for our purposes as they ignore the electrons preventing the simulation of bond energies, molecular orbitals, electron densities and excited state properties, all of which are of great interest to this work.

### 2.3.1 *Ab Initio* Molecular Orbital Theory

Computational calculations run following this methodology aim to obtain information about the structure and properties of the molecule of interest by approximating solutions to the Schrödinger equation;

$$\hat{H}\Psi = E\,\Psi$$

where $\hat{H}$ is the Hamiltonian operator, which acts on the wavefunction, $\Psi$, to give, E, the energy of the molecule. These parameters will be discussed in more detail below. In essence these quantum mechanical methods model the electrons explicitly, and it is for this reason we chose to utilise quantum mechanics. Obtaining calculations where the electrons have been modelled allows the simulation of almost any molecular property. Another benefit of *ab initio* calculations is that input files only describe the atomic coordinates and spin state meaning that the molecular orbitals are calculated on a case by case basis making this technique applicable to any type of molecule.

The Hamiltonian operator is the total energy operator, and contains terms describing the nuclear-nuclear potential energy, the nuclear-electron potential energy, the electron-electron potential energy, and the nuclear and electron kinetic energy. This therefore makes the Schrödinger equation complicated to solve for multi-electron systems as the motion of both the electrons and the nuclei need to be correlated. To overcome this problem approximations of these parameters are made, with the most significant of these being the Born-Oppenheimer approximation.

The electrons in an atom are moving far faster than the nucleus, so fast in fact that it is almost as if the electrons only ever really see a fixed set of nuclear co-ordinates. The Born-Oppenheimer approximation separates the nuclear and electron degrees of freedom and allows us to deal with the electrons in the presence of a fixed nucleus. In doing this the nuclear kinetic energy term is removed and thus the nuclear-nuclear potential is easier to simulate as it is just the potential from a fixed set of positive charges. The approximation also means that the nuclear-electron potential can be calculated with relative ease as the electrons just see a fixed set of positive charges.

The only parts of the Hamiltonian left to solve after the Born-Oppenheimer approximation has been applied are the electron kinetic energy and the electron-electron potential, and it is this last term that causes difficulties as electrons are charged and have spin. These characteristics cause the motions of the electrons to perturb the behaviour of all the other electrons electrostatically and via exchange. A method to solve this would be to break up this big many body problem into a summation of one particle equations, however in doing this the correlation of the motion of the electrons would be ignored.

To overcome this limitation Hartree theory attempts to simplify electron-electron correlation by ignoring instantaneous electron motion and assuming each electron moves in the average potential of all the others. In doing this the complicated multi-electron wavefunction is separated into spin-orbitals, or one-electron wavefunctions, that describing each electron. The calculation is solved self-consistently and each one-electron wavefunction combined to get the total molecular wavefunction. However, Hartree theory is in violation of the Pauli Exclusion Principle and is therefore often combined with another known as Fock theory to become Hartree-Fock (HF) theory. Fock theory acts to model the pairing of opposite spins in the molecule by using an anti-symmetric wavefunction.

The combination of these two theories means that it is possible to calculate ~99 % of the total energy of a molecule, with the missing energy being the correlation energy (removed by Hartree theory). The practical result of this is that bond distances are typically calculated as being too short. There have been methods developed in an attempt to overcome this problem but they require too high a level of computational performance for this work. All *ab initio* methods require four variables to model each electron; three positional (x, y, z) and one spin. This led us to our choice of computational methodology of Density Functional Theory (DFT).

### 2.3.2 Density Functional Theory

DFT looks to reduce the number of variables involved in a calculation by modelling both the electron correlation and electron exchange, requiring only the three positional variables (x, y, z). In doing this the total energy of a system of electrons is modelled, which is a functional of the electron density of the system. The technique requires equations to be solved for each electron using what are known as the Kohn-Sham equations. These equations can be used to solve for the electron density and can be viewed as being similar to the spin-orbitals used in HF theory. However the electron interactions are still very difficult to solve, which results in the exchange/correlation functional, $E_{XC}$, not being known. This functional is trying to simulate the interactions between the electrons and is constantly trying to be improved upon.

There are several approximations that are used that give different functionals: Local Density Approximation (LDA), Generalised Gradients Approximation (GGA) and Hybrid Density Functional Theory. LDA takes into account the electron density at a given point in space without regard to the surroundings, and therefore is not suitable for this work as it struggles with systems with varying electron density. GGA calculations take into account an electron density gradient which improves the simulation of varying electron density. The calculations carried out for this work used a hybrid density functional theory approximation, B3LYP.[1] This functional combines Hartree-Fock (HF) theory with DFT (GGA), which allows the simulation of electron-electron exchange to be exact thanks to the HF theory, and the electron-electron correlation to be approximated via DFT. This results in higher accuracy calculations that are achievable with less demanding methods.

The Schrödinger equation describes how the Hamiltonian operator acts upon the wavefunction to obtain the permitted energy levels of the molecule. Now we move to correctly model the wavefunction mathematically.

We have seen how both HF and DFT break the multi-electron wavefunction down into component one-electron functions, spin-orbitals and Kohn-Sham orbitals, respectively. The form of these one-electron functions is unknown; however they can be modelled by an expansion of a complete set of known functions. This can be achieved by applying the concept of basis functions and involves the calculation of expansion co-efficients using the Variational Principle in a self-consistent manner. In this work the contribution weighting of each Gaussian type basis function is calculated within each basis set.

The basis set used through this work is LANL2DZ[2-4] that includes an effective core potential for the Cu atom, sometimes known as a pseudopotential. This replaces the core electrons with an effective potential, removing the need for core basis functions that involve large sets of Gaussians. The pseudopotential also accounts for the relativistic effects of the Cu atom. A valence double zeta part is also included in the LANL2DZ basis set that places two basis functions to describe each valence atomic orbital, allowing the calculations to more accurately simulate the bonding in the molecule. It is a compromise between size of basis set to give improved accuracy, and computational cost.

#### 2.3.2.1 Solvent Effects

In order to make the calculations more applicable to our experimental results the inclusion of solvent had to be investigated. This was achieved by applying a self-consistent reaction field (SCRF) method to the calculations using a polarisable continuum model (PCM).[5] This method

can be thought of as placing our molecule in a cavity inside a polarisable medium with a given dielectric constant. The magnitude of this dielectric constant corresponded to the nature of the solvent being represented.

### 2.3.3 Geometry Optimisation

Geometry optimisation attempts to find the minimum energy structure of a molecule, which is a type of stationary point. There are three types of stationary point, the first is known as a minimum and is defined as when the curvature remains positive through the stationary point (k all real). The second is a maximum and can be identified when the curvature remains negative through the stationary point. The third type of stationary point is a point of inflection and can be identified as a transition state, and is when the curvature changes sign when passing through the stationary point. It is the minimum stationary points which are of interest in this work as they represent a low energy structure. However, a potential energy surface (PES), can contain more than one minimum as molecules can adopt more than one stable structure, known as conformers. The lowest energy minimum is known as the global minima, and the other, higher energy minima, are known as local minima. The molecule may exist in the global minimum structure only, or it may be able to go between several minima, and this depends on the thermodynamics and kinetics of the molecule and the size of the barriers between the minima. It should be noted that identifying all minima on the PES of a complicated multi-atomic system can be computationally expensive and therefore is not regularly carried out for work of the nature presented in this thesis.

It is known that calculating the first derivative of a function yields the gradient, and when this is at a minimum and the gradient is zero, it is known as a stationary point. Now, when the first

derivative of the potential energy is calculated with respect to the nuclear positions, the force (F) is the product:

$$\frac{dV}{dx} = \mathrm{F}$$

Therefore a stationary point is achieved here when the forces of the atoms are zero.

The basic processes taking place during a geometry optimisation calculation are looking for these stationary points, and can be described as a loop within a loop. In the manner described above (section 2.3.1), the wavefunction is calculated for the initial (input) atomic configuration with the atoms fixed in the configuration. The first derivative of the potential energy is then taken as a function of all nuclear positions, giving the gradient (force). The calculation stops when the gradient (force) is below convergence criteria set for the calculation as it deems a minimum has been found and that the force on each atom is zero. If the gradient (force) is not below the convergence criteria the atoms are moved in such a way so as to minimise the force on each. This can sometimes be achieved using an estimation of the second derivative of the energy which gives the curvature of the PES and an estimate of the force constants. These steps are repeated until the calculated gradient (forces) is below the set convergence criteria and a stationary point is identified.

A frequency calculation is then carried out to identify the nature of the stationary point, and this is done in Gaussian by modelling bonds as simple balls and springs with harmonic potentials. The potential energy of a harmonic oscillator system can be described as shown in the following equation:

$$V = \tfrac{1}{2} kx^2$$

Where, V = potential energy, k = the force constant of the bond, and x = the displacement from the equilibrium position. This is achieved by calculating (not estimating) the curvature by taking the second derivative of the energy. This is also equal to the force constants for the vibration, as shown in the following equation;

$$\frac{d^2V}{dx^2} = \frac{dF}{dx} = k$$

This allows us the ensure the calculated frequencies are not imaginary as the force constant can be related to the vibrational frequency (v) of the bond;

$$v = \frac{1}{2\pi}\left(\frac{k}{m}\right)^{1/2}$$

Where, m = reduced mass. The above equation states that if k is negative, and therefore the curvature is negative the vibrational frequency will become imaginary as you are taking the square root of a negative number.

Geometry optimisations can be difficult for transition metal complexes due to the similar energies of the d-orbitals. The difficulties arise in the calculation of the wavefunctions and therefore hybrid DFT is the most common method, and has been used for this work.

#### 2.3.3.1 Calculating Molecular Orbitals

One of the main interests of our work is investigating the electronic transitions taking place within our systems, therefore having the ability to visualise the molecular orbitals present, when coupled with our experimental results aids in our understanding of the chemistry taking place.

This is achieved for DFT by the visualisation of the spatial location of the electrons calculated by the Kohn-Sham orbitals.

### 2.3.4 Time-Dependent DFT

As stated above, our work seeks to explore the electronic transitions taking place in our systems and another way to do this is to simulate UV-Vis spectra via a method known as time-dependent DFT (TDDFT). The graphical interface Gabedit[6] has been used to visualise the UV-Vis simulated spectra. This method allows the simulation of information based on the molecule being in the presence of time-dependent potentials of an electric field. The potential experienced by the system is varied to simulate the absorption of a photon and as the wavefunctions are dependent upon this term, the effect this change has on the electron density of the system can be determined.

The resulting simulated spectra tend to have the correct number of absorption peaks with the correct relative intensities, but the wavelength at which these transitions take place are often overestimated. Alongside this information is also given the assignment of these transitions; the nature of the transition that gave rise to the calculated absorptions. This is of real benefit because this information is not readily available experimentally and can therefore further our understanding of our systems.

## 2.4 Solar Cell Manufacture

There are many methods used to manufacture a DSSC in a laboratory environment that have been developed to investigate and improve the overall efficiencies produced by the device. The work presented in this thesis looks to screen Cu(I) sensitisers molecules and hence overall optimisation of the solar cell is not required. For this reason we have used a typical method of DSSC manufacture which is outlined below.

The fabrication of the DSSCs used in this work involved the preparation of a working electrode and a counter electrode for each complete DSSC. Fluorine doped tin oxide conductive glass was cut for the counter electrodes and two holes drilled through them so as to allow the introduction of electrolyte once the final cell was constructed (Figure 3 (i)). The conductive sides of the counter electrodes were then coated with a layer of platinum (via a Platisol solution) following the previously reported procedure (Figure 3 (ii)).[7]

The working electrodes were prepared by doctor-blading titanium dioxide paste (Figure 3 (iii)) (Dyesol, DSL-18NR-T), onto cleaned fluorine doped tin oxide conductive glass (TEC 8, Pilkington, UK). Doctor-blading is the process of applying an even thin film of specified width and thickness onto the surface of the glass. This was achieved by using two thicknesses of Kapton tape spaced 1 cm apart. The films were then dried at 100 °C for 15 min and sintered at 450 °C for 30 min to remove any unwanted organics and to form a mesoporous film structure. The thickness of the film has previously been estimated at about 18 μm. The $TiO_2$ films on the working electrode were sensitised with our sensitiser molecules by soaking in dye baths (Figure 3 (iv)) of specified concentrations and solvents and for a given period of time (see relevant Chapters).

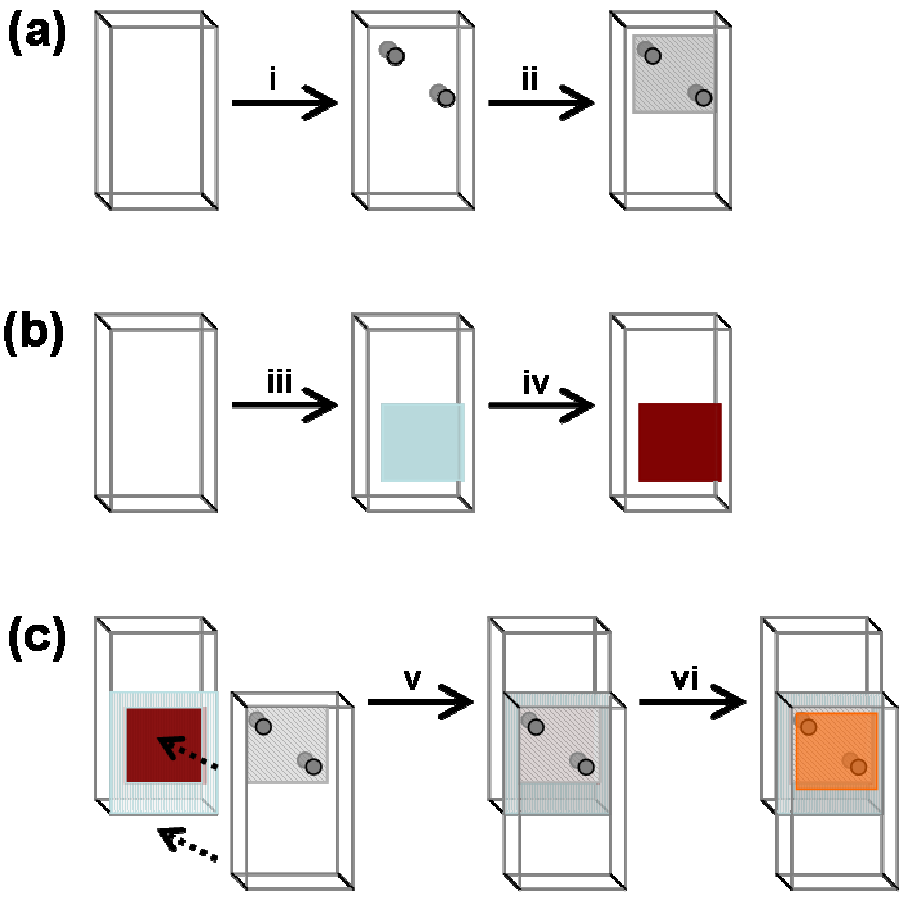


**Fig. 3** DSSC Manufacture of the; (a) Counter electrode; (b) Working electrode; (c) complete DSSC

Manufacture of the cells was completed by sealing the working and counter electrodes together using a thermal plastics spacer (Surlyn 1702, 25 μm, Solaronix) at 120 ˚C (Figure 3 (v)). The electrolyte was introduced into the cell, which was subsequently sealed using Kapton tape (Figure 3 (vi)). The default electrolyte used throughout this work was 0.6 M LiI, 0.03 M $I_2$, 0.1 M Guanidinium thiocyanate, 0.5 M 4-tert-butylpyridine, 15:85 Valeronitrile:Acetonitrile. The active area of the cell was 1 $cm^2$.

## 2.4.1 Additional Working Electrode Treatments

During our work we carried out the manufacture of cells that included two additional treatments reported in the literature to enhance overall cell performance (Chapter Three).[8-14] The first of these treatments was the inclusion of Chenodeoxycholic acid (Cheno) as an additive in the dye baths. The Cheno was added at the same time as the sensitiser. The concentrations used are given in Chapter Three.

A $TiCl_4$ post-treatment of the $TiO_2$ films was carried out prior to sensitiser adsorption. The $TiO_2$ coated FTO cells were coated with a 40 mM aqueous $TiCl_4$ solution and placed into a steam bath at 70 $^{\circ}$C for 30 min. The cells were removed, washed with deionised water, dried at 100 $^{\circ}$C for 15 min and then sintered at 500 $^{\circ}$C for 30 min. Dye adsorption was then carried out as described above.

## 2.5 Solar Cell Efficiency Measurements

One of the most important properties of a solar cell is the overall efficiency, $\eta_{glaboal}$, which is defined as the ratio of output ($P_{out}$) to input ($P_{in}$) power;

$$\eta_{global} = \frac{P_{out}}{P_{in}} = \frac{I_{SC} V_{OC} ff}{P_{in}}$$

where $I_{SC}$ is the short circuit current, $V_{OC}$ is the open circuit voltage and *ff* is the fill factor. Each of these parameters will be explained below. The current-voltage characteristics of the cells were measured under simulated AM 1.5 illumination (100 $mWcm^{-2}$) provided by a solar simulator (1 kW Xe with AM 1.5 filter, Müller) calibrated using a Digital Solar Power Meter.

The open circuit voltage can be described as the voltage across a cell when no current is being drawn, and the short circuit current is when the current drawn out of the cell results in it short circuiting. Both of these parameters can be seen in Figure 4 which depicts a typical *I-V* curve obtained from a DSSC. The third parameter required to calculate the overall efficiency is the fill factor, which looks at how the behaviour observed compares to that of an ideal DSSC (Figure 4);

$$ff = \frac{P_{max}}{I_{SC} V_{OC}}$$

where $P_{max}$ is the maximum power produced by the DSSC being tested (Figure 4).

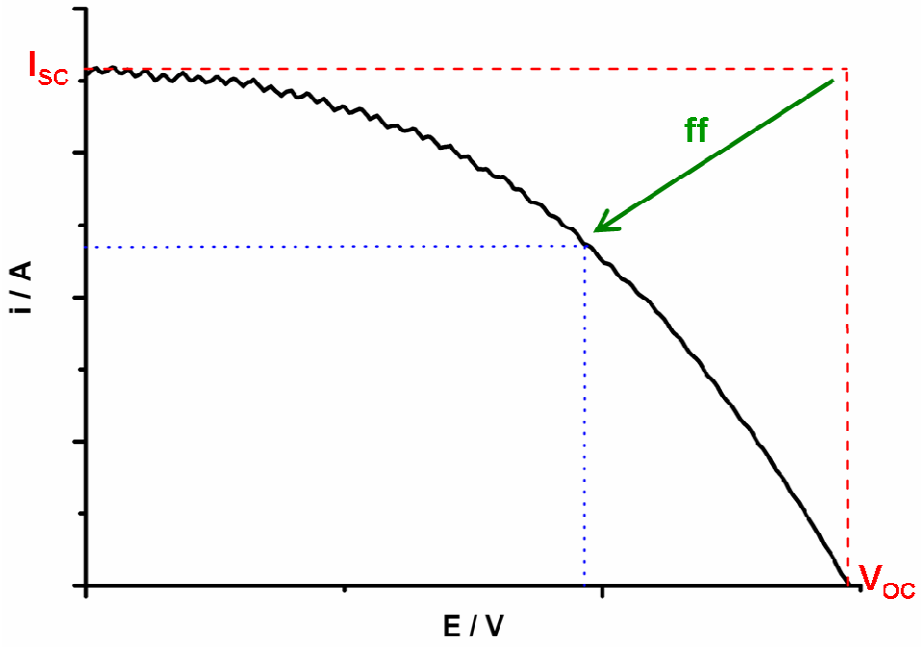


**Fig. 4** I-V Curve for a typical DSSC with the key parameters labelled. Red dashed line = ideal DSSC function; black solid line = experimentally recorded curve; blue dotted line highlights power produced by system.

## 2.6 References


1. A. D. Becke, *The Journal of Chemical Physics*, 1993, **98**, 5648-5652.
2. P. J. Hay and W. R. Wadt, *The Journal of Chemical Physics*, 1985, **82**, 270-283.
3. P. J. Hay and W. R. Wadt, *The Journal of Chemical Physics*, 1985, **82**, 299-310.
4. W. R. Wadt and P. J. Hay, *The Journal of Chemical Physics*, 1985, **82**, 284-298.
5. A. Vleck Jr and S. Zális, *Coordination Chemistry Reviews*, 2007, **251**, 258-287.
6. A. R. Allouche, *Journal of Computational Chemistry*, 2010, **31**, 174-182.
7. N. Papageorgiou, W. F. Maier and M. Gratzel, *Journal of The Electrochemical Society*, 1997, **144**, 876-884.
8. K. Sayama, S. Tsukagoshi, T. Mori, K. Hara, Y. Ohga, A. Shinpou, Y. Abe, S. Suga and H. Arakawa, *Solar Energy Materials and Solar Cells*, 2003, **80**, 47-71.
9. R. Chen, X. Yang, H. Tian, X. Wang, A. Hagfeldt and L. Sun, *Chemistry of Materials*, 2007, **19**, 4007-4015.
10. H. Choi, J. K. Lee, K. H. Song, K. Song, S. O. Kang and J. Ko, *Tetrahedron*, 2007, **63**, 1553-1559.
11. S. Ito, H. Miura, S. Uchida, M. Takata, K. Sumioka, P. Liska, P. Comte, P. Pechy and M. Gratzel, *Chemical Communications*, 2008, 5194-5196.
12. J. H. Yum, S. Moon, R. Humphry-Baker, P. Walter, T. Geiger, F. Nuesch, M. Gratzel and M. K. Nazeeruddin, *Nanotechnology*, 2008, **19**, 424005.
13. M. K. Nazeeruddin, A. Kay, I. Rodicio, R. Humphry-Baker, E. Mueller, P. Liska, N. Vlachopoulos and M. Graetzel, *Journal of the American Chemical Society*, 1993, **115**, 6382-6390.
14. P. M. Sommeling, B. C. O'Regan, R. R. Haswell, H. J. P. Smit, N. J. Bakker, J. J. T. Smits, J. M. Kroon and J. A. M. van Roosmalen, *The Journal of Physical Chemistry B*, 2006, **110**, 19191-19197.

# 3. Chapter Three:

# [Cu(I)(POP)(bipyridyl)]

# and Related Complexes

## 3.1 Introduction

Recent research into the electrochemical and photophysical properties of phenanthroline- and bipyridine-based Cu(I) complexes[1-4] has shed new light on the potential Cu(I) complexes could hold for application in dye-sensitised solar cells (DSSCs).[2, 3, 5-7] As discussed in detail previously in Chapter One, research into first row transition metal DSSC sensitisers has to date been limited due to their often extremely short-lived excited states compared to 2nd and 3rd row transition metal complexes. These short-lived excited states arise from the low lying metal d-d excited states which allow non-radiative decay of the MLCT excited state. This is a limiting factor in terms of DSSC functionality as charge injection from the dye is not efficiently achieved.[8, 9] Chapter One outlines the design strategies that have been employed to overcome this restriction and exploit first row transition metal complexes in DSSC application. As a result the focus of this introduction will be on the method utilised for the work reported in this chapter.

Cu(I) complexes can display longer excited-state lifetimes due to their $d^{10}$ configuration meaning non-radiative decay into low lying metal d-d metal- orbitals is not possible as they are full. This fact has meant that Cu(I) DSSC devices manufactured in labs have had success producing power-conversion efficiency of 2.6%[10] (discussed in Chapter One). To date however, Cu(I) DSSC research has been limited to homoleptic sensitisers,[2, 3, 5, 7] and in this work we extend this to an initial investigation of heteroleptic Cu(I) complexes.

Chapter One outlines the benefits of using heteroleptic transition metal sensitisers in DSSCs in order to control directionality of the MLCT transition across the complex to minimise recombination losses, and also allow tuning of the properties required of a dye (see next paragraph).[11] An additional benefit of the use of heteroleptic ligands in Cu(I) complexes is that

they may be used as "blocking groups" to sterically constrain the molecule[1, 9, 12] and prevent the Cu(I)/Cu(II)[12, 13] redox process induced conformational geometry change from distorted tetrahedral to tetragonally-flattened, respectively.[9] Research investigating Cu(I) bis-phenanthroline complexes[1, 9, 12, 14, 15] has revealed that substituents in the 2- and 9-positions of the phenanthroline ligand can achieve this constraint, and a similar approach has been utilised for DSSC Cu(I) sensitisers by including substituents groups in the 6,6′-positions of the bipyridine.[2, 3, 5, 7] However the need for 6,6′-substituents leads to increased synthetic complexity of the bipyridine ligands. It should be noted that the bipyridine ligands also require 4,4′-acid substitutents to bind to $TiO_2$.[2, 3, 5-7]

Here we build on the existing Cu(I) sensitiser work and investigate heteroleptic Cu(I) complexes. The complexes synthesised are based on Cu(bipyridyl) complexes with the inclusion of a second ligand which, through suitable ligand selection, could tune the properties of the complex to be more DSSC suitable. For example, this second ligand could be a chromophore, allowing absorption of increased quantities of light; it could be selected so that a neutral complex is formed consistent with the large majority of high-efficiency sensitisers; it could create MLCT charge directionality across the molecule to minimise recombination losses; it could be used to maintain a pseudo-tetrahedral geometry upon excitation of the complex in order to limit non-radiative decay of the excited state of the complex. This work is focused on the latter two of these properties, firstly by placing the LUMO on the bipyridyl ligand and the HOMO on the Cu(I), charge directionality is hoped to be created in the desired direction. Secondly, a bulky ligand may enable the simpler 4,4′-($CO_2H$)-bipyridine to be used as the $TiO_2$-binding ligand without requiring 6,6′-substitution, and therefore simplify the intensive bipyridine synthesis required for previous Cu(I)-based sensitisers.

The second or "blocking" ligand investigated in this chapter is the geometrically inflexible co-ligand bis[2-(diphenylphosphanyl)phenyl] ether; POP (Figure 1), which has been used

effectively in OLED studies due to the rigid and inflexible geometry it can impose on the complex.[8, 16, 17] Shown in Figure 1 are several literature examples of Cu(I)(POP) complexes where in most cases the diimine ligand is phenanthroline-based. The photophysics of these complexes will be discussed in more detail in Chapter Four alongside the properties of our novel complexes.

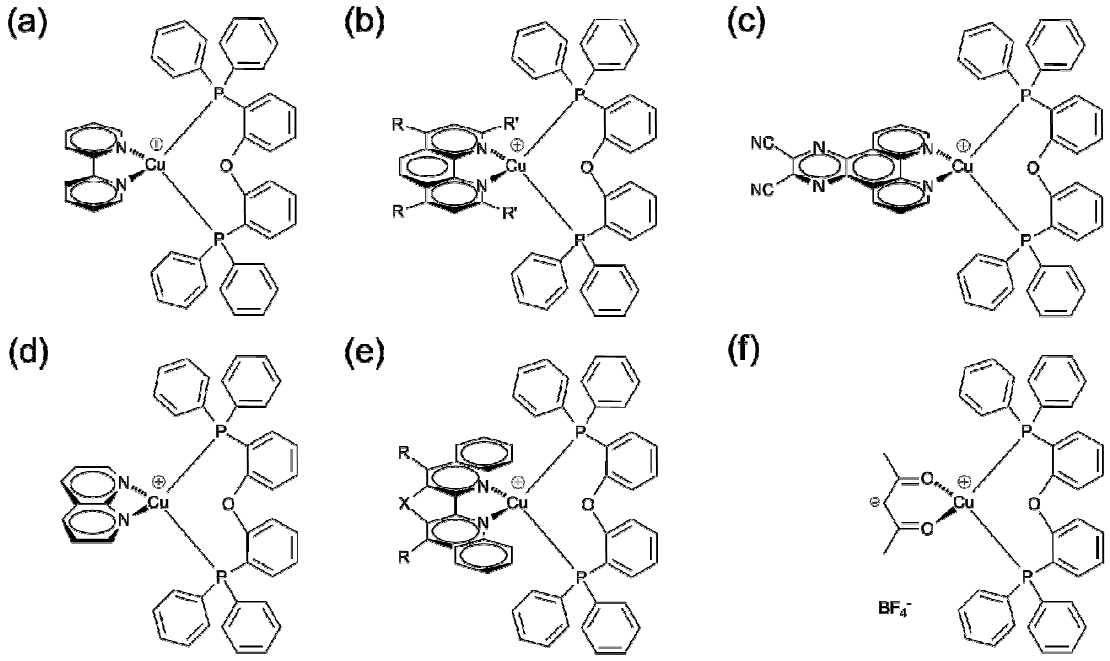


**Fig. 1** Selected Cu(I)(POP) complexes from the literature; (a),[18] (b),[9, 14, 18, 19] (c),[20] (d),[21] (e)[22] and (f)[23]

There are limited examples of Cu(POP)(bipyridyl) complexes[18, 24] used in this role as their emissive properties are less attractive compared to their phenanthroline counterparts.[18] Research carried out by Yang *et al.*[18] includes crystal structures of $[Cu(I)(POP)(bpy)]^+$ and $[Cu(POP)(dmphen)]^+$ (dmphen = 2,9-dimethyl-phenanthroline) presented with Density Functional Theory (DFT) and Time-dependant (TD) DFT calculations which will be discussed alongside results presented in this chapter. It should be noted here that these computational calculations were carried out without solvent and with a simplified POP structure (see Section 3.2).

Under investigation in our work is whether the required complex inflexibility can be imposed solely through the POP ligand without requiring 6,6′-substitution on the bipyridine ligand, and to this end a family of Cu(I)(bipyridine)$_2$ and Cu(I)(POP)(bipyridine) complexes with varying 4,4′- and 6,6′-substitutents have been synthesised, and subsequently electrochemically and photophysically characterised. All complexes discussed in this chapter are given in Figures 2 and 3.

The electrochemical and photophysical properties of the complexes were investigated using UV/Vis spectroscopy, electrochemistry and fluorescence spectroscopic studies. The series of homoleptic complexes (**1 - 4**) were synthesised initially to allow comparison with existing DSSC Cu(I) sensitisers, and to facilitate assignment of the electrochemical and spectroscopic properties of the heteroleptic series outlined here. Solar cell function of **6** was investigated using I-V characterisation. Density Functional Theory (DFT) and Time-Dependent DFT (TD-DFT) calculations were used to support and further investigate the electronic properties of complexes **5**, **6**, **8** and **10**.

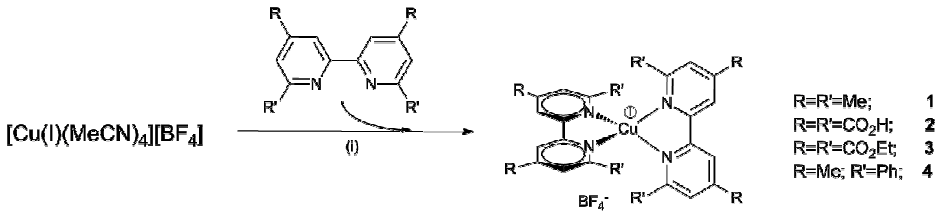


**Fig. 2** Synthetic Reaction Scheme for homoleptic complexes reported in this work. All procedures carried out under a nitrogen atmosphere. (i) **1** degassed chloroform; **2** dry, degassed MeOH; **3** dry, degassed DCM; **4** see section 3.2.2

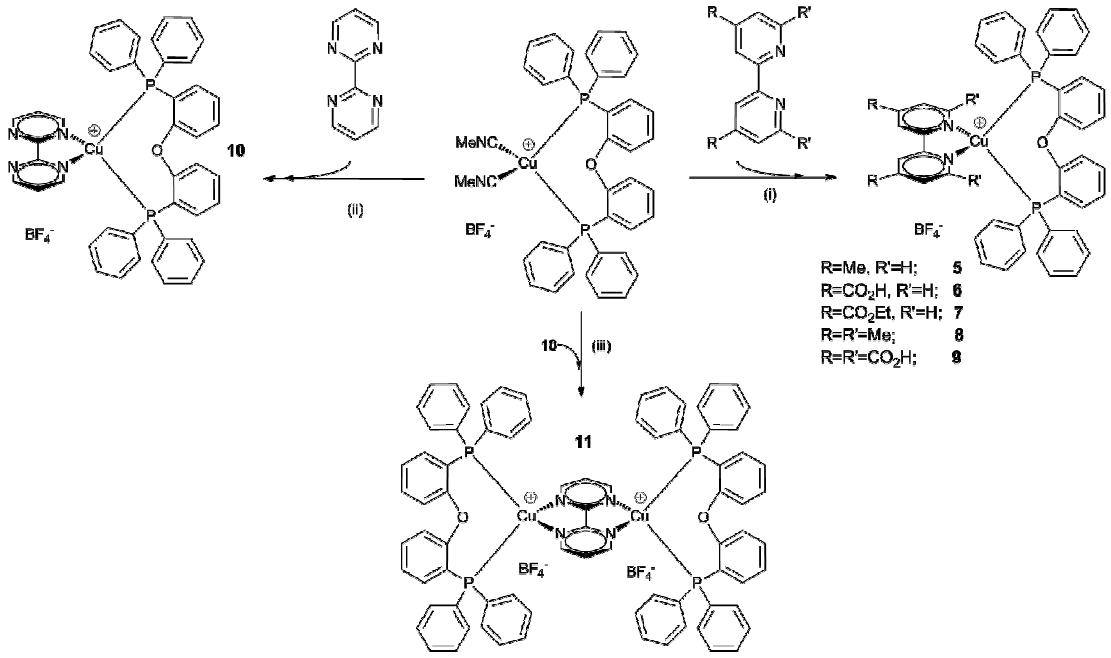


**Fig. 3** Synthetic Reaction Scheme for heteroleptic complexes reported in this work. (i) **5, 6**, **7**, **9** acetone; **8** anhydrous acetonitrile (ii) DCM (iii) acetone.

## 3.2 Results and Discussion

### 3.2.1 Syntheses

The ligands 4,4′-dicarboxy-2,2′-bipyridine (dcbpy), 4,4′-di($CO_2$Et)-2,2′-bipyridine (decbpy), 4,4′,6,6′-tetramethyl-2,2′-bipyridine (tmbpy) and 4,4′-dimethyl-6,6′-diphenyl-2,2′-bipyridine (dpdmbpy), and the starting complex [Cu(MeCN)$_4$][$BF_4$] were synthesised using modified literature methods as described in the Experimental section. 4,4′,6,6′-Tetracarboxy-2,2′-bipyridine (tcbpy) and 4,4′,6,6′-tetra($CO_2$Et)-2,2′-bipyridine (tecbpy) are novel ligands that were synthesised via oxidation of the tmbpy ligand as described in the Experimental section. The ligand bis[2-(diphenylphosphanyl)phenyl] ether (POP) and the starting complex [Cu(POP)(MeCN)$_2$][$BF_4$] were synthesised by Dr Omar Moudam and samples taken and used in this work. The reaction schemes shown in Figures 2 and 3 demonstrate how the Cu(I) complexes were synthesised by simple addition, with stirring, of the relevant starting materials in stoichiometric amounts, to the appropriate solvent at room temperature. It should be noted that [Cu(tcbpy)$_2$][$BF_4$] (**2**), and [Cu(POP)(tcbpy)][$BF_4$] (**9**) were synthesised and characterised by $^1$H NMR under nitrogen, but were not air stable and so were not further investigated. The methyl and ester analogues have been synthesised alongside the acids, despite not being directly applicable for use in a DSSC, as they can give insight into the properties of the acid complexes while being more convenient for detailed characterisation due to better solubility. In addition there were also attempts to synthesise [Cu(POP)(dpdmbpy)][$BF_4$] and the acid analogue however we believe, due to excessive steric constraints, this is not possible. This hypothesis is further supported by the lack of a 6,6′-phenyl-substituted phenanthroline Cu(I)(POP) complex in the literature This complex although not successful here was not abandoned, and will be discussed again in Chapter Seven.

The Cu(I) complexes **1**, **3**, **5** - **8** and **10** were characterised by $^{1}$H NMR, ESI-MS, +FAB-MS and elemental analysis, verifying molecular structures.

## 3.2.2 Structure Analysis

The single crystal structures of $[Cu(II)(dmbpy)_2Cl][BF_4]$ and compounds **1**, **4**, **5**, **7**, **8**, **10** and **11** have been determined allowing insight into the structural features of these complexes, in particular the blocking group effects. Images of the structures are shown in Figures 4 and 5 and structural parameters are given in Tables 1, 2 and 3. All crystals were grown from solutions open to air. Refinement of the crystal structure of **5** was not possible to a publishable level (R<10%) and therefore only a connectivity image and not detailed structural information will be quoted in this work. Despite obtaining crystal structures for **4** and **11**, we were unable to isolate the complexes in their pure form and therefore further characterisation was not carried out. In attempting to crystallise the 4,4′-dimethyl-2,2′-bipyridine analogue of **1**, the complex oxidised in air along with coordination of chlorine to give $[Cu(II)(dmbpy)_2Cl][BF_4]$ (Figure 4). In contrast, the structures of **1** and **4** illustrate the stabilisation of the Cu(I) oxidation state by addition of methyl or phenyl group in the 6,6′-positions of the bipyridine (Figure 4). The angle between the planes of the two bipyridyls for **1** is 72.18º and for **4** is 56.29º, giving pseudo-tetrahedral geometries and suggesting considerable flexibility of this geometric parameter.

**Table 1** Selected bond lengths (Å) and bond angles (deg) of complexes $[Cu(dmbpy)_2Cl][BF_4]$, **1** and **4**

| | $[Cu(dmbpy)_2Cl][BF_4]$ | **1** | **4** |
|---|---|---|---|
| Cu-N(1A) | 2.154(2) | 2.055(2) | 1.9825(15) |
| Cu-N(1B) | 2.082(2) | 2.056(2) | 1.9815(15) |
| Cu-N(2A) | 2.001(2) | 2.055(2) | 2.0133(15) |
| Cu-N(2B) | 1.981(2) | 2.056(2) | 2.0204(14) |
| N(1A)-Cu-N(1B) | 100.97(8) | 117.63(9) | 149.05(5) |
| N(2A)-Cu-N(2B) | 169.34(8) | 117.63(9) | 136.00(5) |
| N(1A)-Cu-N(2B) | 91.78(8) | 134.37(9) | 108.85(6) |
| N(2A)-Cu-N(1B) | 96.60(8) | 134.37(9) | 108.16(6) |
| N(1A)-Cu-N(2A) | 79.07(8) | 80.60(13) | 83.57(6) |
| N(1B)-Cu-N(2B) | 79.64(8) | 80.63(13) | 82.93(6) |

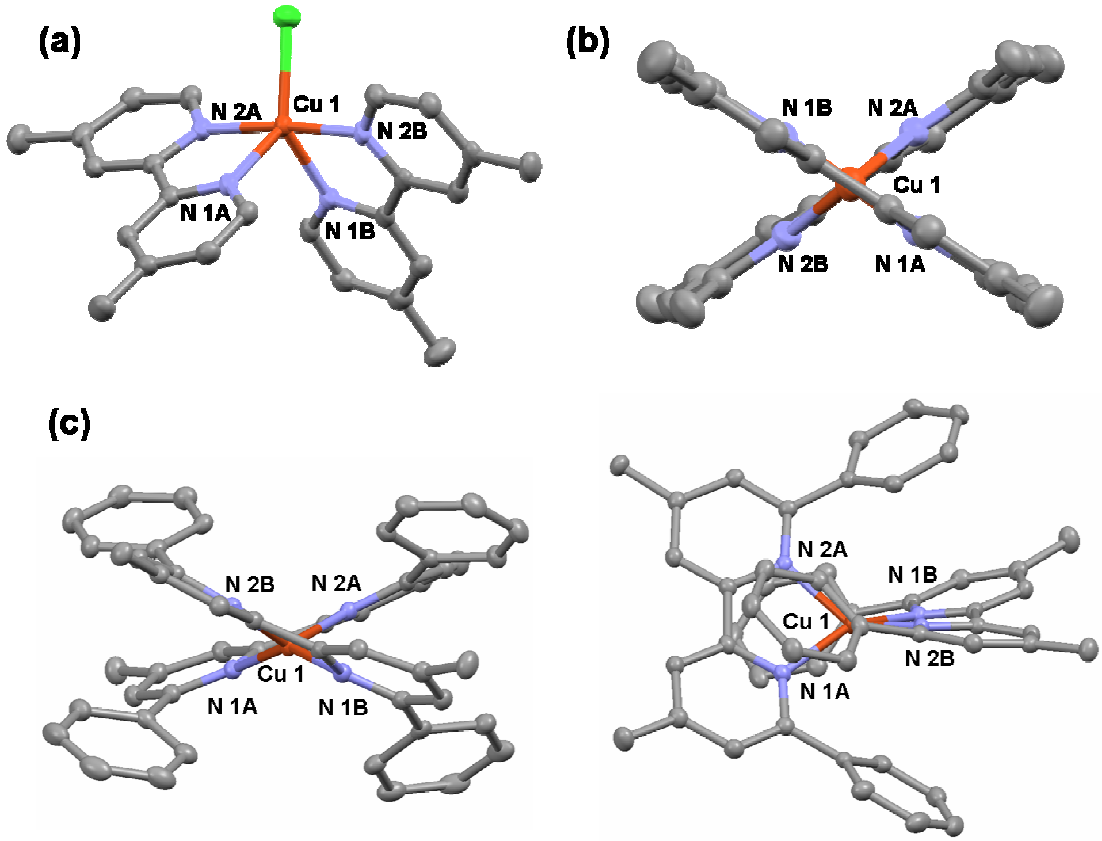


**Fig. 4** Mercury plots of (a) $[Cu(dmbpy)_2Cl][BF_4]$; (b) **1**; (c) **4**. Thermal ellipsoids are drawn at the 50% probability level. $[BF_4]$ counter ion omitted for clarity. Selected bond lengths and bond angles for $[Cu(dmbpy)_2Cl][BF_4]$ involving the chloride atom: Cu-Cl: 2.2770(7) Å; Cl-Cu-N(1A) 123.54(6) º; Cl-Cu-N(2A) 93.08(6) º; Cl-Cu-N(1B) 135.48(6)º; Cl-Cu-N-(2B) 96.57 (6)º.

The crystal structures of the heterolpetic complexes (**5**, **7**, **8**, **10** and **11**) shown in Figure 5 illustrate the role of POP in the stabilisation of a Cu(I) oxidation state over Cu(II) in air, as the complexes are forced to adopt distorted tetrahedral conformations with reduced structural flexibility. The angles between the bipyridyl plane and the P-Cu-P plane for these complexes range from 81.95º to 88.61º indicating a geometry closer to tetrahedral than that of **1** and **4** (Table 1, 2 and 3). Additionally, the bite angle of POP in each case remains comparatively close to that expected for an ideal tetrahedron (Tables 2 and 3).

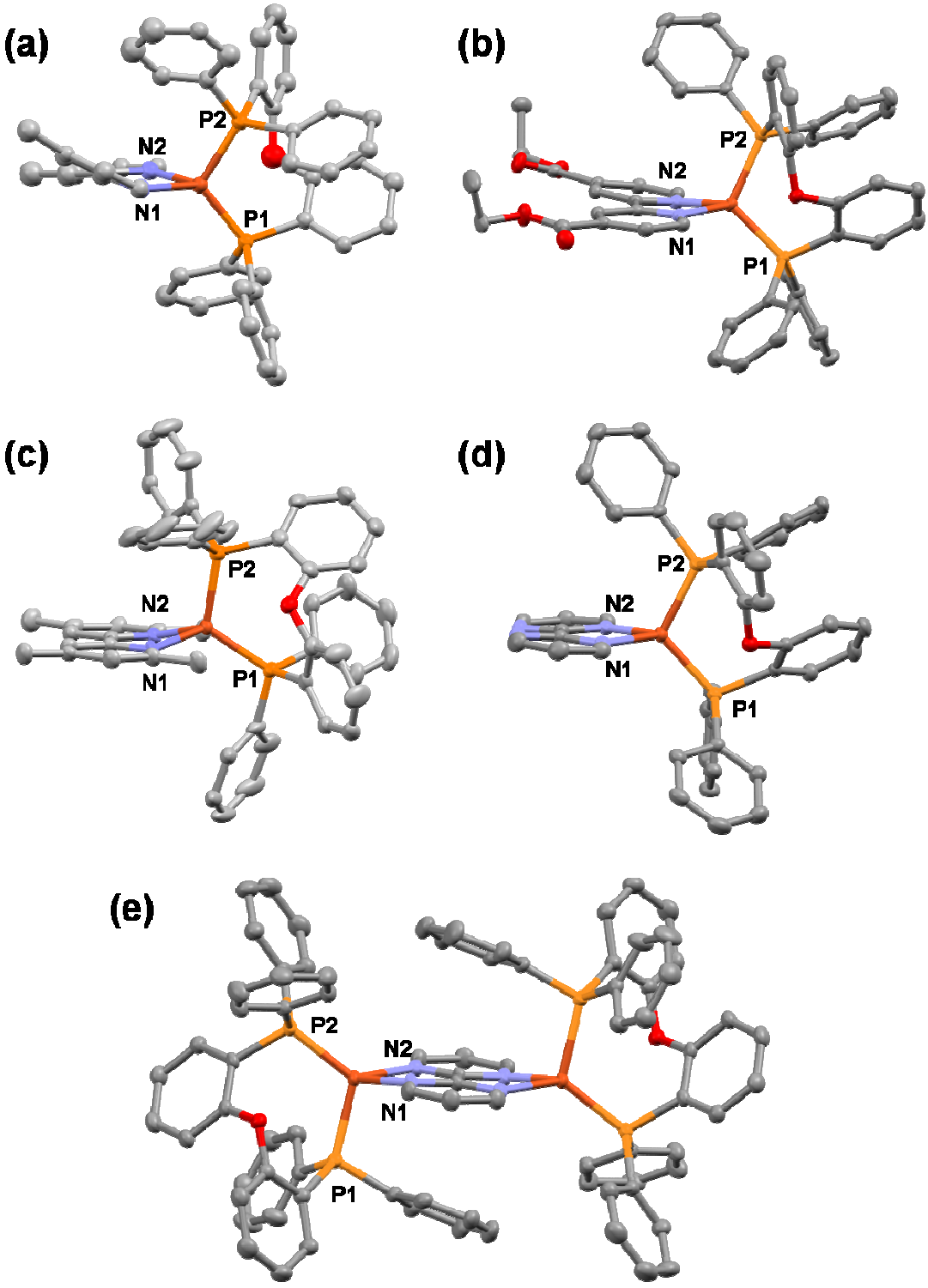


**Fig. 5** Mercury plots of (a) **5**, (b) **7**, (c) **8**, (d) **10** and (e) **11.** Thermal ellipsoids are drawn at the 50% probability level. **11** lies on an inversion centre. The [$BF_4$] counter ions are omitted for clarity

**Table 2** Selected bond lengths (Å) and bond angles (deg) from single crystal X-ray crystallography and from solvated DFT calculations for **8**.

| | **7** [a] | **8** [a] | **8** [b] |
|---|---|---|---|
| Cu-N(1) | 2.037(2) | 2.089(3) | 2.136 |
| Cu-N(2) | 2.0621(19) | 2.097(3) | 2.116 |
| Cu-P(1) | 2.2213(6) | 2.2518(11) | 2.478 |
| Cu-P(2) | 2.2466 (6) | 2.2901(11) | 2.493 |
| N(1)-Cu-N(2) | 80.31(8) | 79.64(13) | 79.86 |
| N(1)-Cu-P(1) | 128.86(6) | 121.85(9) | 117.27 |
| N(2)-Cu-P(1) | 111.46(5) | 117.03(10) | 114.76 |
| N(1)-Cu-P(2) | 109.74(6) | 103.50(10) | 113.66 |
| N(2)-Cu-P(2) | 112.26(5) | 114.35(9) | 117.90 |
| P(1)-Cu-P(2) | 110.40(2) | 115.25(4) | 110.58 |
| bpy plane-PCuP plane | 84.05 | 81.95 | N/A |
| Cu-P(2)-C$^{\dagger}$ | 114.37(8) | 113.30(15) | 114.16 |

[a] Crystal structure; [b] DFT geometry optimisation with acetonitrile polarizable continuum; $^{\dagger}$ for **7** C=C17; for **8** C=C35

**Table 3** Selected bond lengths (Å) and bond angles (deg) from single crystal X-ray crystallography for **10**, **11** and [Cu(POP)(bpy)]$^{+}$ and [Cu(POP)(dmphen)]$^{+}$;[18] and from solvated DFT calculations for **10**.

| | **10** [a] | **10** [b] | **11**[a] | [Cu(POP)(bpy)]$^{+}$ [a] | [Cu(POP)(dmphen)]$^{+}$ [a] |
|---|---|---|---|---|---|
| Cu-N(1) | 2.068(2) | 2.105 | 2.103(2) | 2.085 | 2.098 |
| Cu-N(2) | 2.093(2) | 2.107 | 2.070(2) | 2.034 | 2.075 |
| Cu-P(1) | 2.2482(7) | 2.400 | 2.2158(7) | 2.245 | 2.285 |
| Cu-P(2) | 2.2756(7) | 2.411 | 2.2851(7) | 2.232 | 2.228 |
| N(1)-Cu-N(2) | 79.74(8) | 79.64 | 80.16(8) | 80.13 | 81.39 |
| N(1)-Cu-P(1) | 121.08(6) | 121.96 | 128.91(6) | 123.58 | 108.88 |
| N(2)-Cu-P(1) | 118.49(6) | 115.30 | 119.24(6) | 114.73 | 118.84 |
| N(1)-Cu-P(2) | 108.47(6) | 106.85 | 102.14(6) | 114.72 | 119.55 |
| N(2)-Cu-P(2) | 113.65(6) | 112.25 | 102.75(6) | 109.40 | 105.40 |
| P(1)-Cu-P(2) | 111.77(2) | 114.50 | 116.30(3) | 111.97 | 117.04 |
| bpy plane-PCuP plane | 85.77 | N/A | 88.61 | N/A | N/A |
| Cu-P(2)-C$^{\dagger}$ | 115.58(8) | 115.89 | 107.54(9) | N/A | N/A |

[a] Crystal structure; [b] DFT geometry optimisation with acetonitrile polarizable continuum; $^{\dagger}$ for **10** C=C9; for **11** C=C35

The blocking functionality of POP arises as one of the phenyl rings attached to the phosphorus atoms is constrained to be over the bipyridyl ligand resulting in H-phenyl-to-bipyridyl plane distances of 2.891 Å, 2.477 Å, 2.941 Å, 2.790 Å for **7**, **8**, **10** and **11** respectively that prevent structural distortion. This geometrical arrangement is caused by the rigid nature of the chelating ring (Cu-P-C-C-O-C-C-P) which is shown in Figure 6. As can be seen from Table 4, among the four structures presented here there is little variation between the angles within the chelate ring providing strong support for the lack of flexibility in the POP coordination geometry and hence the rigidty of the whole molecule. In general, the structures show little geometric deviation

compared with eleven POP containing Cu(I)-structures described in the literature;[9, 17, 18, 21-23] comparative values for $[Cu(POP)(bpy)]^+$ and $[Cu(POP)(dmphen)]^+$ are given in Table 3.[18] Furthermore, the structures of **5**, **7** and **10** clearly demonstrate that in a heteroleptic complex with an appropriate co-ligand, 6,6′-substituted bipyridine ligands are not required to maintain an air-stable Cu(I)-complex. This enables the use in Cu(I) DSSC sensitisers of the straightforward dcbpy ligand widely exploited in Ru sensitisers and bypassing the need for more complex multiply substitued bipyridyl ligands.

**Table 4** Crystallographic data for complexes **7**, **8**, **10** and **11**. Angles a - g defined in Figure 6.

| | **7** | **8** | **10** | **11** |
|---|---|---|---|---|
| bpy plane-H[†] | 2.790 | 2.477 | 2.891 | 2.939 |
| a | 114.35(8) | 111.23(13) | 114.11(8) | 120.35(9) |
| b | 120.27(17) | 118.2(3) | 120.41(19) | 119.49(19) |
| c | 119.4(2) | 115.0(4) | 120.5(2) | 118.9(2) |
| d | 114.82(17) | 120.5(3) | 117.31(19) | 116.42(19) |
| e | 116.5(2) | 119.4(4) | 116.4(2) | 115.8(2) |
| f | 118.90(17) | 118.7(3) | 117.09(18) | 118.15(19) |
| g | 111.56(8) | 117.69(13) | 109.38(8) | 108.78(8) |

[†]for **7** H=H18; for **8** H=H314; for **10** H=H341; for **11** H=H271.

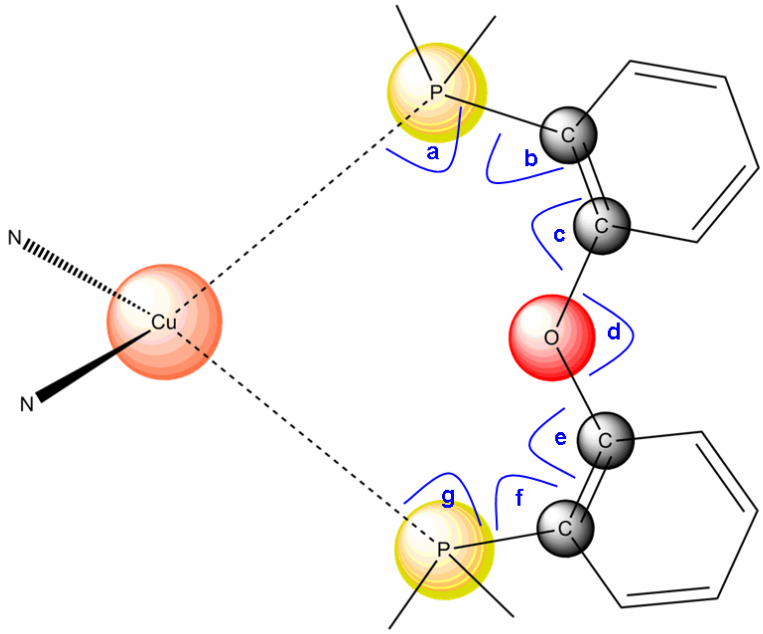


**Fig. 6** Schematic of the POP chelate ring illustrating the angle labelling (a - g) for (Cu-P-C-C-O-C-C-P) in complexes **7**, **8**, **10** and **11**.

### 3.3.3 DFT and TDDFT calculations

Calculations were carried out for **5**, **6**, **8** and **10** using Gaussian 03[25] with the B3LYP/LANL2DZ[26-29] functional and basis set with induced solvent effects. This level of theory has been used successfully in the literature to calculate the structural and electronic properties of a number of coordination complexes.[18] Calculation details are outlined in full in the Experimental section. The optimised geometries for **5**, **8** and **10** are in very good agreement with the structures obtained crystallographically (Tables 2 and 3), but as expected the DFT calculated solvated bond lengths are longer than those in the crystal structure. There is a small variation between the DFT optimised geometries and the crystal structures in the orientation of the non-blocking phenyl groups on the POP ligands. We believe this to have little effect on the energy and behaviour of these complexes and will discuss this further in Chapter Four. Packing forces present in the calculated liquid-phase are weaker than those in the solid-phase. The DFT calculated gas-phase and solution-phase structures for **5**, **6**, **8** and **10** produce identical overall structure energies and comparable bond distances and angles.

Time dependent density functional theory (TDDFT), also at the B3LYP/LANL2DZ level of theory, was used to probe the electronic transitions that give rise to the visible and near-UV absorption of each complex. Although current TDDFT implementations have a tendency to underestimate the energy of charge-transfer interactions, the method has been shown to provide useful qualitative information on the electronic structure and photophysical behaviour of similar coordination complexes.[18] Seventy singlet-singlet transitions were calculated with solvent, for each complex. Analysis of the components of the TDDFT expansion shows that the majority of predicted transitions are not well described by a single electron-promotion, but involve transitions between several different orbital pairs.

The nature of each electronic transition was determined by inspection (Argus Lab[30]) of each contributing molecular orbital as an isosurface map. Many of the calculated occupied and virtual orbitals were seen to be of mixed character, with electron density simultaneously present on both the ligand and metal. However, the electronic transitions could broadly be classified into three distinct types; metal-to-ligand-charge-transfer (MLCT), where the occupied orbital is predominantly metal based and the virtual orbital ligand based, either on the POP or bpy; ligand-ligand (LL), where the transition involves occupied and virtual orbitals on the same ligand; and ligand-to-ligand-charge-transfer (LLCT), where the transition involves occupied and virtual orbitals on different ligands. These are discussed further in the context of the experimental results below.

### 3.3.4 UV-Vis Absorption Spectroscopy

The experimental and calculated UV-Vis absorption spectra are shown in Figure 7, with the main absorption bands and related extinction coefficients given in Table 5. For each complex the experimental spectra show two distinct groupings; very strong absorption in the near uv and weaker absorption bands in the visible that are sensitive to the nature of the biypridine substituents. From previous work,[1] it is known that the absorption peak of the $\pi \rightarrow \pi^*$ intra-bipyridine transition occurs between 300-320nm. Each complex in the homoleptic series exhibits an absorption peak in this range (Table 5), however this absorption peak cannot be resolved for the heteroleptic series as it is believed to be masked by the stronger POP ligand UV absorption band. In the absorbance spectra collected for **5** and **8** the shoulder present at 320 nm may possibly be attributed to the bipyridyl absorption.

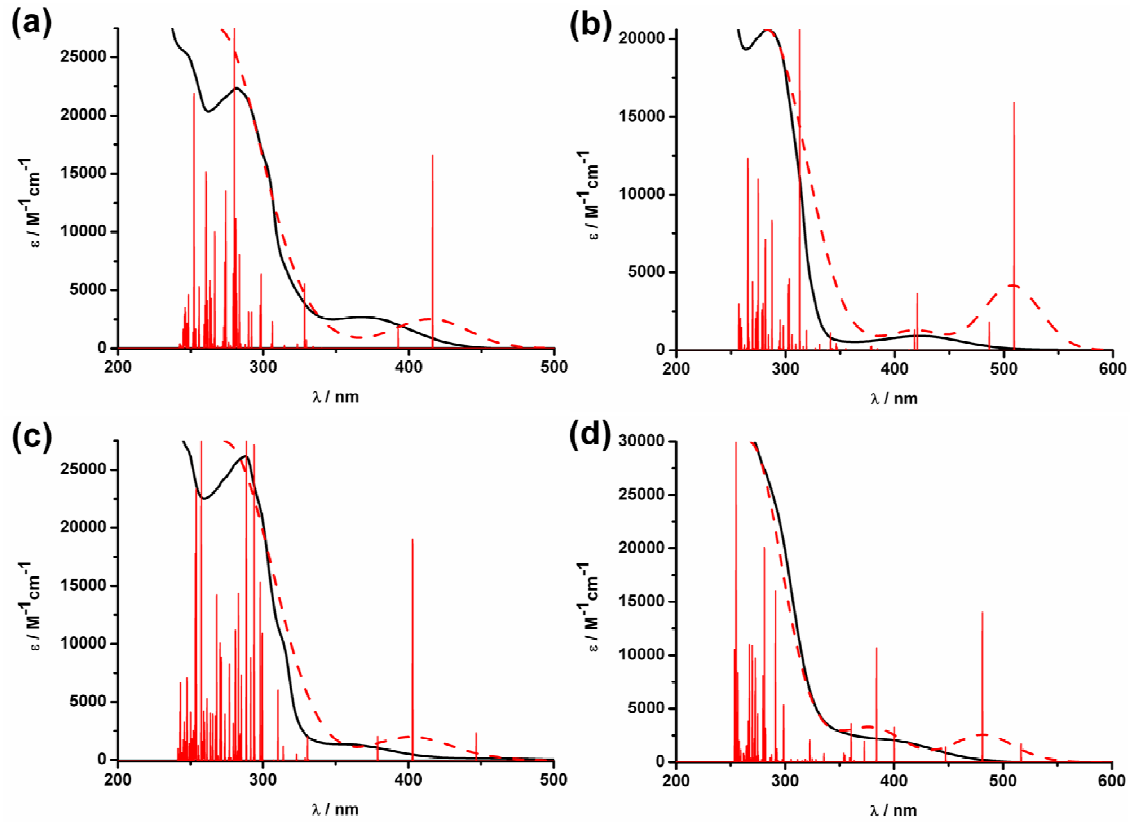


**Fig. 7** Theoretical UV/Vis Absorption Spectra against Experimental Absorption Spectra for (a) **5**; (b) **6**; (c) **8**; (d) **10**. Where lines are Gaussian and red solid columns = calculated electronic transisiton; red dotted line = calculated spectra; black solid line = solution spectrum of (a) **5,** (b) **7**, (c) **8** and (d) **10** in MeCN.

The TDDFT calculations reproduce the experimental spectra reasonably well in the UV region, predicting a large number of transitions with significant oscillator strength (Figure 7). Examination of the molecular orbitals involved in each transition shows that the UV absorption bands are dominated by $\pi \rightarrow \pi^*$ transitions on both the bipyridine and the POP ligands (see Appendix A).

**Table 5** Absorbance Measurements for all Complexes. **1** and **5** - **10** carried out in MeCN; **3** carried out in DCM

| **Complex** | **Absorption / $\lambda_{max}$ (nm) ($\varepsilon_{max}$(x10$^3$M$^{-1}$cm$^{-1}$))** | | | | |
|---|---|---|---|---|---|
| | **Intraligand Transitions** | | | **MLCT** | |
| dpdmbpy | 265 (27.5) | 305 (16.3) | 349 (0.3) | | |
| **1** | | 300 (25.8) | | 358 (1.4) | 449 (3.5) |
| **3** | | 315 (32.0) | | 477 (4.9) | 594 (7.4) |
| $[CuPOP(MeCN)_2]^+$ | | 272 (14.2) | | | |
| **5** | 248 (25.1) | 282 (22.6) | | 369 (3.2) | |
| **6** | | 276 | | 416 | |
| **7** | 246 (26.6) | 290 (19.7) | | 424 (2.4) | |
| **8** | 250 (26.3) | 288 (25.5) | | 358 (2.2) | 460 (0.2) |
| **10** | 247 (35.5) | 294 (16.1) | | 403 (2.0) | |

The longer wavelength bands have been assigned as Cu(I) to bipyridyl MLCT transfer bands based upon comparison with literature. This assignment is supported by the calculated energies and deduced characters of the frontier orbitals (Table 6 and also see Appendix A) and the percentage contribution to the lowest energy MLCT bands, of each orbital pair (Table 7) in the TDDFT expansion. It must be noted that TDDFT has a tendency to over stabilise, and indeed the calculated MLCT absorptions are consistently predicted at lower energy than those seen experimentally.[18, 31]

**Table 6** TD-DFT calculated visible absorption wavelengths for **5**, **6**, **8** and **10**, indicating the molecular orbitals involved and their relative contribution to the absorption.

| **Complex** | **Main Visible Absorbance / nm** | **Oscillator Strength (f)** | **Main Charge Transitions** | | **Relative contribution** |
|---|---|---|---|---|---|
| | | | **MO from** | **MO to** | |
| **5** | 416 | 0.0894 | HOMO-1 | LUMO | 16 % |
| | | | HOMO | LUMO | 84 % |
| **6** | 509 | 0.1192 | HOMO | LUMO | 100 % |
| | 420 | 0.0275 | HOMO-3 | LUMO | 29 % |
| | | | HOMO-2 | LUMO | 10 % |
| | | | HOMO | LUMO+1 | 61 % |
| **8** | 402 | 0.0661 | HOMO-1 | LUMO | 59 % |
| | | | HOMO-2 | LUMO | 41 % |
| **10** | 481 | 0.0500 | HOMO-1 | LUMO | 37 % |
| | | | HOMO | LUMO | 63 % |
| | 383 | 0.0382 | HOMO-1 | LUMO+1 | 46 % |
| | | | HOMO | LUMO+1 | 54 % |

**Table 7** Percentage contributions from component parts of **5**, **6**, **8** and **10** to selected molecular orbitals. Also quoted are the calculated energies for these molecular orbitals.

| Complex | MO | MO Character | MO energy / eV | % Contribution from | | |
|---|---|---|---|---|---|---|
| | | | | Cu-based orbitals | POP-based orbitals | Bpy-based orbitals |
| **5** | HOMO-1 | $d_{xz}$ or $d_{yz}$ | -5.99 | 63.78 | 8.80 | 27.42 |
| | HOMO | $d_{xz}$ or $d_{yz}$ | -5.87 | 44.34 | 50.38 | 5.28 |
| | LUMO | π*-bpy | -2.27 | 1.48 | 5.68 | 92.84 |
| **6** | HOMO-3 | | -6.60 | 14.09 | 83.47 | 2.44 |
| | HOMO-2 | | -6.42 | 38.48 | 54.01 | 7.51 |
| | HOMO | | -6.08 | 36.98 | 58.41 | 4.61 |
| | LUMO | π*-bpy | -3.16 | 2.57 | 4.25 | 93.18 |
| | LUMO+1 | π*-bpy | -2.60 | 0.40 | 0.53 | 99.07 |
| **8** | HOMO-2 | $d_{xy}$ | -6.27 | 51.93 | 38.80 | 9.27 |
| | HOMO-1 | $d_{xz}$,or $d_{yz}$ | -6.03 | 61.10 | 18.98 | 19.92 |
| | LUMO | π*-bpy | -2.12 | 1.44 | 4.24 | 94.32 |
| **10** | HOMO-1 | | -6.33 | 59.87 | 12.00 | 28.13 |
| | HOMO | | -6.07 | 38.12 | 56.37 | 5.51 |
| | LUMO | π*-bpy | -2.92 | 1.47 | 3.80 | 94.73 |
| | LUMO+1 | π*-bpy | -2.27 | 1.97 | 3.41 | 94.62 |

For the 4,4′-disubstituted complexes (**5** and **6**) the TDDFT calculations agree with experimental data in placing the MLCT absorption for **6** at lower energy than that of **5**. The proposed explanation for this, based upon the previous experimental data, is that **6** has a lower lying LUMO as a result of the electron-withdrawing acid substituents. This proposal can be further confirmed upon inspection of the DFT results, with Figure 8 which shows molecular orbital images for the LUMO of **5** and **6**. As shown in Figure (b), **6** displays increased delocalisation of the LUMO onto the acid groups, which acts to lower the energy of the LUMO (Table 7), which subsequently reduces the required MLCT energy, causing the absorption to take place at longer wavelength.

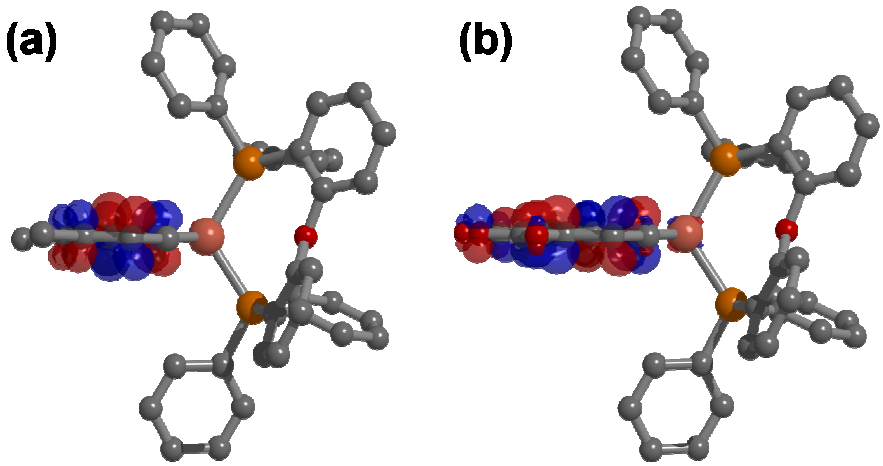


**Fig. 8** Isosurface images generated from DFT calculations of (a) LUMO for **5**; (b) LUMO for **6**

The MO diagram for **5** looks almost as expected for a pseudo-tetrahedral complex (Figure 9). Three MOs are close in energy (HOMO, HOMO-1 and HOMO-2) and approximate as $t_2$ ($d_{xy}$, $d_{xz}$ and $d_{yz}$), and another two MOs at lower energy (HOMO-4 and HOMO-5) which approximate as e ($d_{x2-y2}$ and $d_{z2}$). The MLCT transition can therefore be said to be $t_2$ to $\pi^*$ (bipyridine) in nature. Despite the lowest energy MLCT transition taking place in **6**, **8** and **10** being of the same character, their MO diagrams vary more from the ideal pseudo-tetrahedral model due to increased interactions with the ligand-based orbitals (see Appendix A).

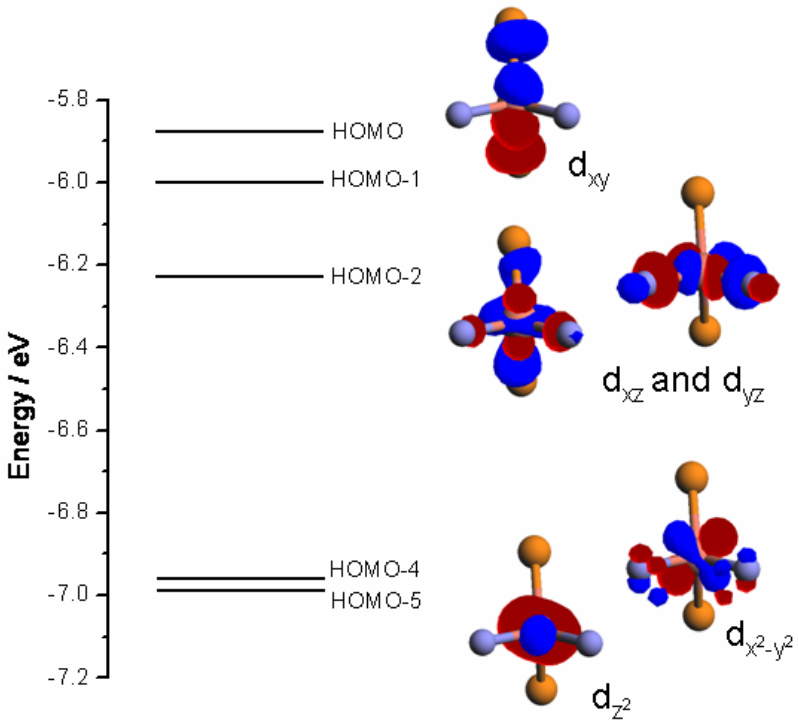


**Fig. 9** Molecular Orbital Diagram for **5** showing assignment of d-orbitals.

Inspection of Table 7 demonstrates that the LUMO and LUMO+1 orbitals for all four of the complexes are bpy-based, and that the HOMO to HOMO-3 orbitals are Cu(I)- and POP-based, as predicted. This is of importance as the main charge-transfer transitions occur between these orbitals (see Table 6), indicating MLCT across the molecule in the desired direction for DSSC function: towards the acid groups bound to the $TiO_2$.

### 3.3.5 Emission Spectroscopy

Excitation and emission spectra were investigated for **5**, **8** and **10** in ethanol at room temperature and in a frozen glass at 77 K. For comparison, data was also collected for the uncomplexed dmbpy, tmbpy and dpdmbpy ligands, and the precursor complex $[CuPOP(MeCN)_2][BF_4]$. Maxima values are given in Table 8 with absorption and emission spectra for **5** and **8** (the two most emissive complexes) given in Figure 10, and all spectra collected given in Figure 11.

Complex **10** was found to be emissive only at 77 K and not at room temperature. Complexes **5** and **8** both showed room-temperature emission with a significant increase in intensity upon freezing accompanied by some shifting of the absorption and emission maxima (Table 8). This behaviour is consistent with emission from a triplet MLCT state in keeping with characteristic behaviour of related Cu(I) polypyridyl complexes.[14]

**Table 8** Excitation and Emission Measurements for dmby, tmbpy, dpdmbpy $[CuPOP(MeCN)_2][BF_4]$, **4**, **5**, **8**, and **10**.

| Compound | Room-temperature EtOH | | 77 K rigid matrix (EtOH) | |
|---|---|---|---|---|
| | Excitation Maxima $\lambda_{max}$ / nm | Emission Maxima $\lambda_{max}$ / nm | Excitation Maxima $\lambda_{max}$ / nm | Emission Maxima $\lambda_{max}$ / nm |
| Dmbpy | 300, 330 | 410 | Not recorded | Not recorded |
| Tmbpy | 264, 304 | 373 | Not recorded | Not recorded |
| $[CuPOP(MeCN)_2]^+$ | 324 | 457 | Not recorded | Not recorded |
| **5** | 408 | 618 | 340 | 592 |
| **8** | 369 | 554 | 369 | 527 |
| **10** | Not observed | Not observed | 328, 356 | 515 |

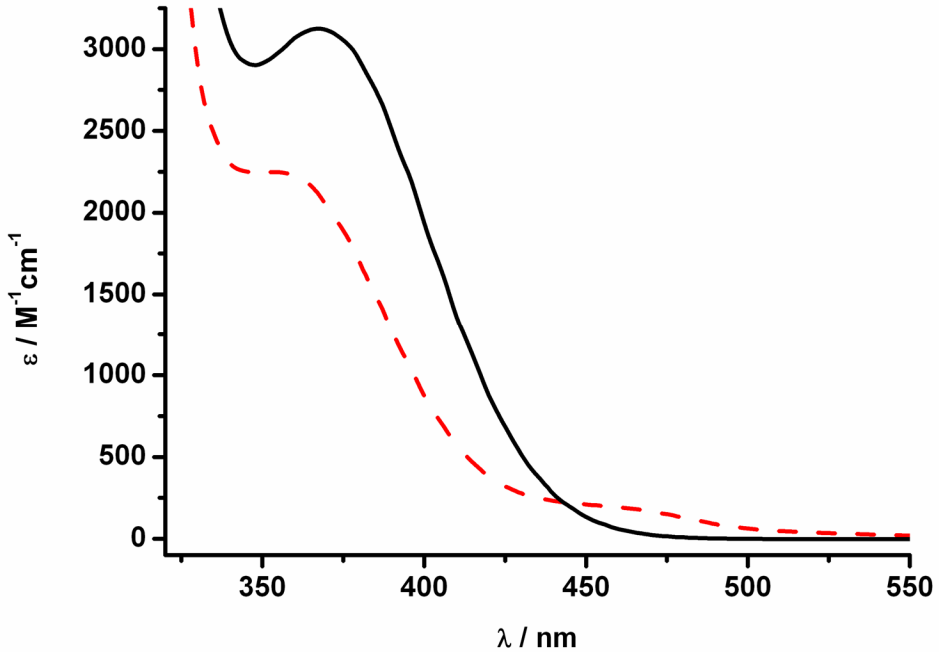


**Fig.10** Absorbance and Emission Spectra for **5** (solid black line) and **8** (red dashed line). Absorbance spectrum carried out in MeCN; Emission spectrum recorded in a rigid matrix of EtOH (77 K).

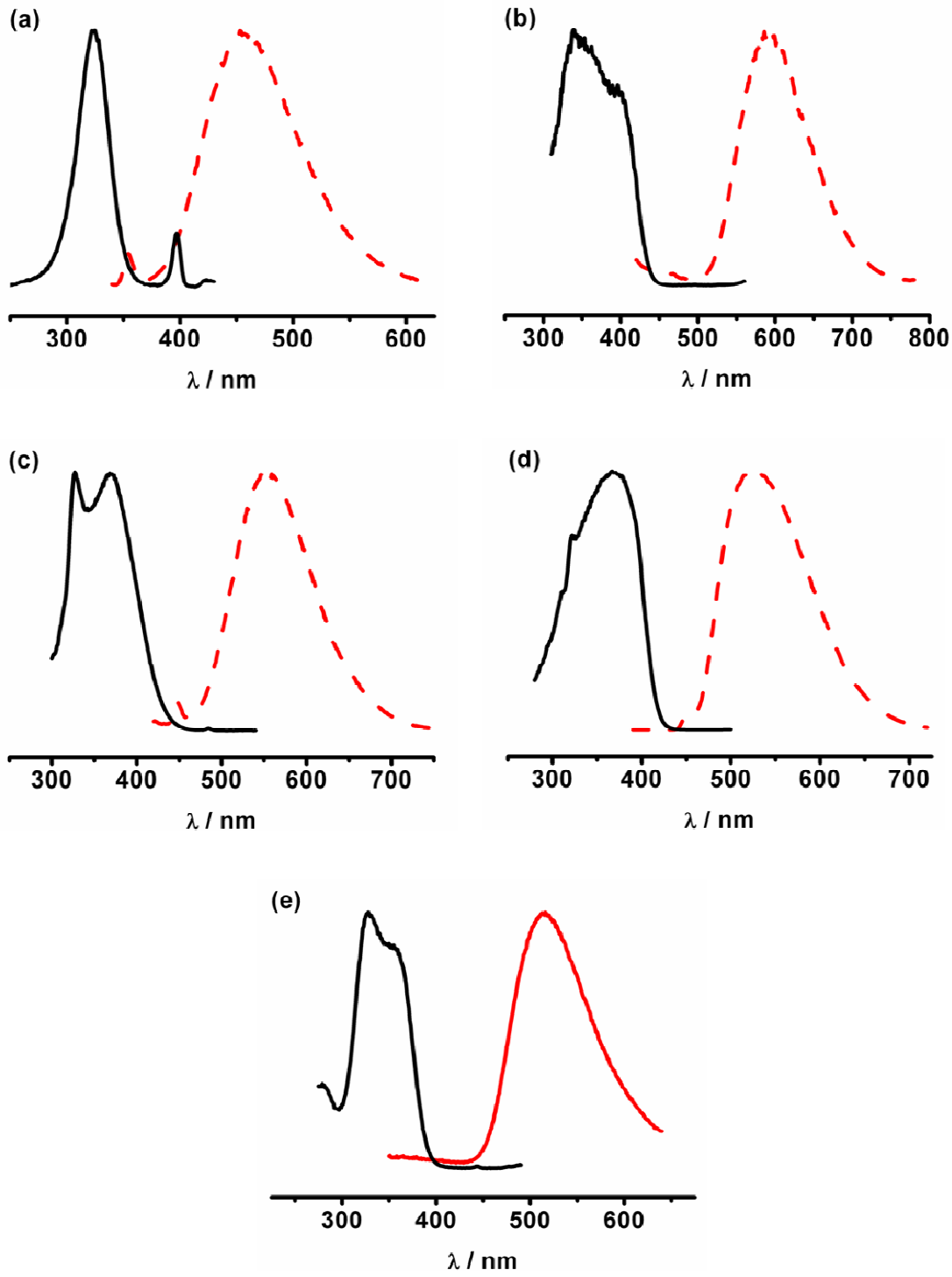


**Fig. 11** Excitation (black line) and Emission (red line) Spectra for, (a) $[CuPOP(MeCN)_2][BF_4]$ at 300 K; (b) **5** at 77 K; (c) **8** at 300 K; (d) **8** at 77 K; (e) **10** at 77 K. All in EtOH.

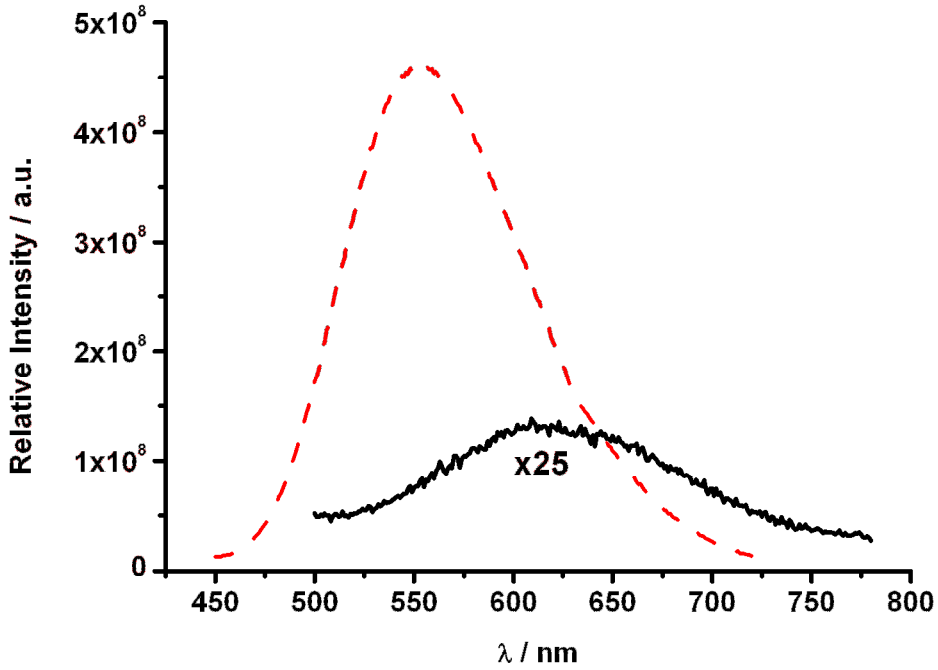


**Fig. 12** Emission Spectra for **5** (black solid line) and **8** (red dashed line) recorded in EtOH at 300 K. The spectra have been normalised against concentration of solution used.

Figure 12 shows a comparison of the emission intensity for **5** and **8**, where the excitation wavelengths used for both complexes have comparable molar absorption coefficients. The role of the 6,6′-methyl groups on the bipyridine ligand is apparent in providing additional steric constraint to the complex leading to the significantly greater emission intensity of **8**. Nevertheless, the observation of emission from **5** and **10**, all of which lack 6,6′-substituents on the bipyridyl, demonstrates the role of the ancilliary POP ligand in providing structural rigidity to the complex. To function as a sensitiser in a DSSC, a complex must possess a sufficiently long excited-state lifetime to enable charge injection into the semiconductor condution band and the observation of photoluminescence is generally taken as an indication that the excited-state lifetime will be sufficiently long. Alongside the structural studies, the observed emission from **5** and **10** demonstrates the suitability of using the dcbpy ligand in conjunction with a sterically-blocking co-ligand to design Cu(I) DSSC sensitisers. Due to the qualitatively large photoluminescence observed for **8**, the photophysical properties of complexes **5** and **8** were investigated in a variety of media and a range of temperatures along with computational studies

of structural rigidity in the excited state. This work will be reported and discussed in Chapter Four.

### 3.3.6 Electrochemistry

The redox potentials for all complexes are shown in Table 9 and Figure 13 shows the cyclic voltammogram of 5 to illustrate the *general curve* observed for the heteroleptic complexes. The first oxidation potential for the homoleptic complexes occurs within the range +0.75 to +0.91 V and can be assigned as an irreversible Cu(I)/Cu(II) redox process. The corresponding Cu(I)/Cu(II) oxidation for the heteroleptic complexes (**5** – **8**) occurs at more positive potentials, around +1.4 V (Table 9). This increase in Cu(I) oxidation potential is due to the orbital interaction with the electron withdrawing POP ligand.[14] The oxidation potentials vary little across **5** – **8**, suggesting the HOMO is largely Cu(I)/POP in character as this feature is invariant across the series. This is also consistent with the TDDFT results shown in Tables 6 and 7 and suggest that **6** is appropriate for use as a DSSC sensitiser since positive charge density on the oxidised sensitiser will be located away from the semiconductor. For long-term DSSC operation, it would clearly be preferable to develop sensitisers that exhibit chemically reversible oxidations, however the acid analogue, **6**, is still viable for study as a model sensitiser since cyclic voltammetry experiments occur on a far longer timescale relative to those taking place in a DSSC device.

**Table 9** Oxidation and Reduction Potentials for all Complexes; **1**, **4-8** and **10** = 0.3M $TBABF_4$/MeCN; **3** = 0.3M $TBABF_4$/DCM.

| Complex | $E_{½}$ (V vs. Ag/AgCl) | | | | | | | |
|---|---|---|---|---|---|---|---|---|
| | $E_{Red.4}$ | $E_{Red.3}$ | $E_{Red.2}$ | $E_{Red.1}$ | $E_{Ox.1}$ | $E_{Ox.2}$ | $E_{Ox.3}$ | $E_{Ox.4}$ |
| **1** | | | -1.68 | -1.34 | +0.77 | | | |
| **3** | | | -1.27 | -0.87 | +0.91* | | | |
| **5** | | | | -1.60 | +1.44 | +1.73 | | |
| **6** | | | -1.61 | -1.40 | +1.41 | +1.64 | | |
| **7** | | | -1.52 | -0.91 | +1.42 | +1.68 | | |
| **8** | | | | -1.66 | +1.41 | +1.65 | | |
| **10** | -1.63 | -1.44 | -1.08 | -0.78* | +0.55* | +1.24 | +1.44 | +1.75 |

Upon comparison with literature,[1] the reductions exhibited by all the complexes can be assigned as bipyridyl-ligand based, which is consistent with the predictions from TDDFT. The variation in reduction potential seen for the complexes is consistent with their calculated LUMO energies, with the acid and ester analogues requiring a less negative reduction potential due to the extended conjugation. These electrochemical results support the expectation that the charge transfer transition will have directionality in the desired direction; towards the carboxylate groups (on the bipyridyl ligand) that bind to $TiO_2$.

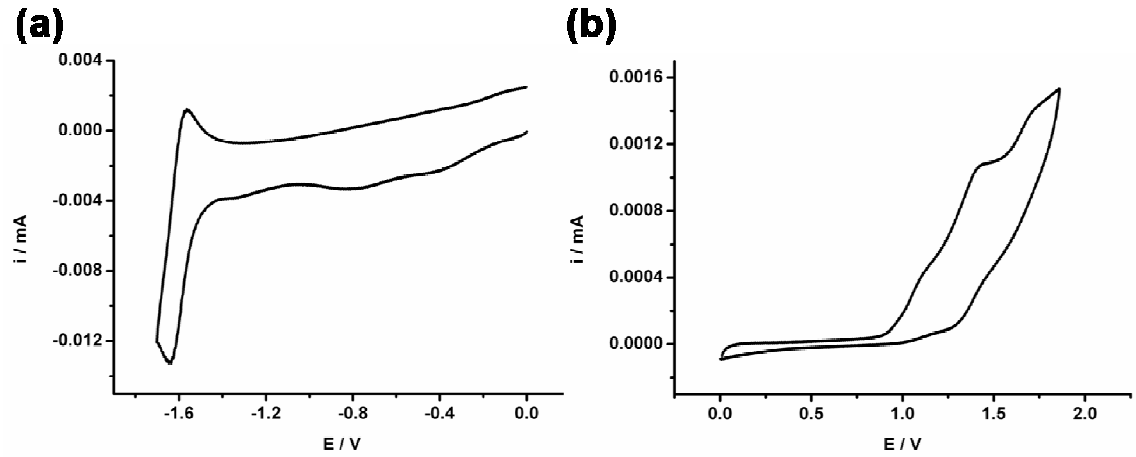


**Fig. 13** Cyclic Voltammograms of **5** showing (a) reduction peaks and (b) oxidation peaks in 0.3M $TBABF_4$/MeCN at 298 K

### 3.3.7 Solar Cell Measurements

*I-V* characterisation was carried out on solar cells made using **6** adsorbed onto $TiO_2$ films. Cell construction and treatments are outlined in the Experimental section and power-conversion efficiency was determined while irradiating under AM 1.5 light (100 $mWcm^{-2}$). Cell efficiencies (η) were calculated using the resulting values of $I_{SC}$ = short circuit current (mA), $V_{OC}$ = open circuit voltage (mV) and ff = fill factor as described in the Experimental section.

Adsorption studies revealed the dye bath conditions yielding the optimum $TiO_2$ surface coverage of **6** to be a sensitiser concentration of 2 mM in diethyl ether. The results for 1 mM diethyl ether dye baths have also been quoted for completeness. Approximate relative $TiO_2$ surface coverage was determined using UV/Vis spectroscopy. This method also allowed confirmation that the dye bound without degradation by comparison with the absorption spectra of **6** in solution (Figure 13). Photocurrent and photovoltage results for a selected range of these cells are shown in Table 10 and in Figure 14, and for comparative reasons; N719 DSSCs were constructed and tested following the same procedures.

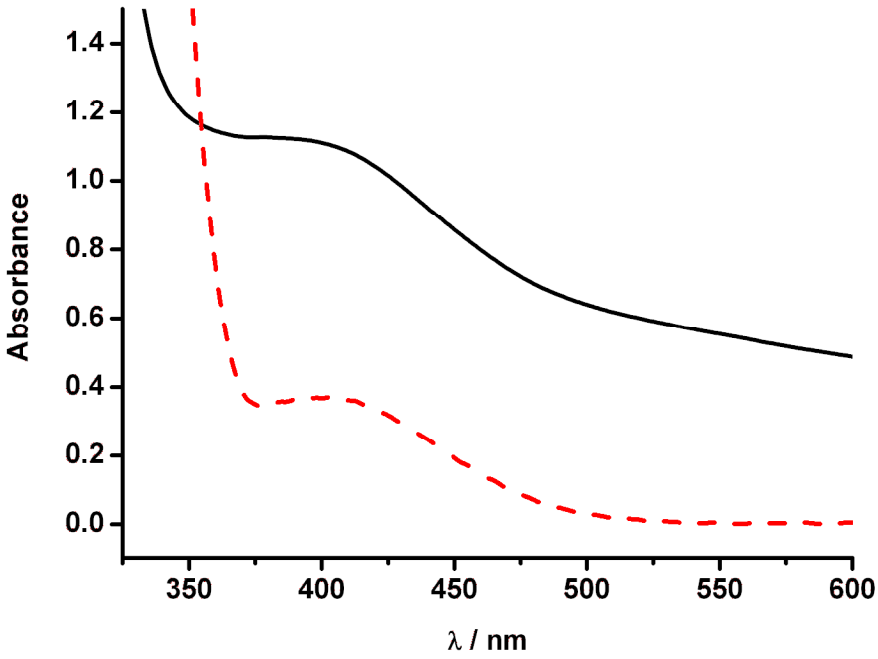


**Fig. 14** UV/Vis Absorption Spectrum for **6** in MeCN (black solid line) and **6** adsorbed onto $TiO_2$ (red dashed line)

The observed photovoltages for cells using **6** were consistently around 350 mV lower than that observed for N719 (Di-tetrabutylammonium cis-bis(isothiocyanato) bis(2,2'-bipyridyl-4,4'-dicarboxylato) ruthenium(II)) (753 mV), and lower than the best homoleptic Cu(I) sensitisers quoted in the literature (around 550 mV).[2, 3, 5-7] The photocurrents were also significantly lower than those recorded for our N719 cells and for existing homoleptic Cu(I) sensitisers (up to 0.3 mA compared to 8.0 and 5.0 mA respectively). This, however, is as expected due to the blue shift of the MLCT absorption caused by the electron-accepting POP ligand such that the complex only just absorbs in the visible region ($\lambda_{max}$ = 394 nm). The low photocurrents may also play a role in the reduced photovoltages displayed using this sensitiser

**Table 10** *IV* Characterisation Data for **6**. Dye Bath diethyl ether. Adsorption time 24 h. $V_{OC}$ = open circuit potential, $I_{SC}$ = short circuit current, ff = fill factor, η = power conversion efficiency. N719 measure $I_{SC}$ = 7.96 mA; $V_{OC}$ = 753 mV; ff = 0.51 and η = 3.05 %.

| Dye Concentration / mM | Cheno Concentration / mM | post-treated with $TiCl_4$ | $I_{SC}$ / mA | $V_{OC}$ / mV | ff | η / % |
|---|---|---|---|---|---|---|
| 1 | N/A | N | 0.176 | 361 | 0.51 | 0.032 |
| 2 | N/A | N | 0.233 | 347 | 0.65 | 0.053 |
| 1 | 1 | N | 0.198 | 333 | 0.48 | 0.030 |
| 2 | 2 | N | 0.300 | 373 | 0.45 | 0.050 |
| 1 | N/A | Y | 0.210 | 388 | 0.47 | 0.038 |
| 2 | N/A | Y | 0.230 | 345 | 0.58 | 0.046 |

The studies reported in Table 10 include two additional DSSC fabrication procedures which are outlined in the literature. The adapted procedures used in this work were given previously in the Experimental section. Firstly, the inclusion of Chenodeoxycholic acid (Cheno) in the dye baths was carried out as it has been shown to dramatically improve the short circuit currents produced in some systems[32-36] by acting as a spacer group on the $TiO_2$ surface, limiting the extent of dye aggregation. A range of dye:Cheno concentration ratios were tried for **6** with representative examples in Table 10 and Figure 15. Improved photocurrents for the dye:Cheno cells over the non-Cheno cells was observed in every case, with an optimum ratio of 1:1, although no improvement to the photovoltage was seen.

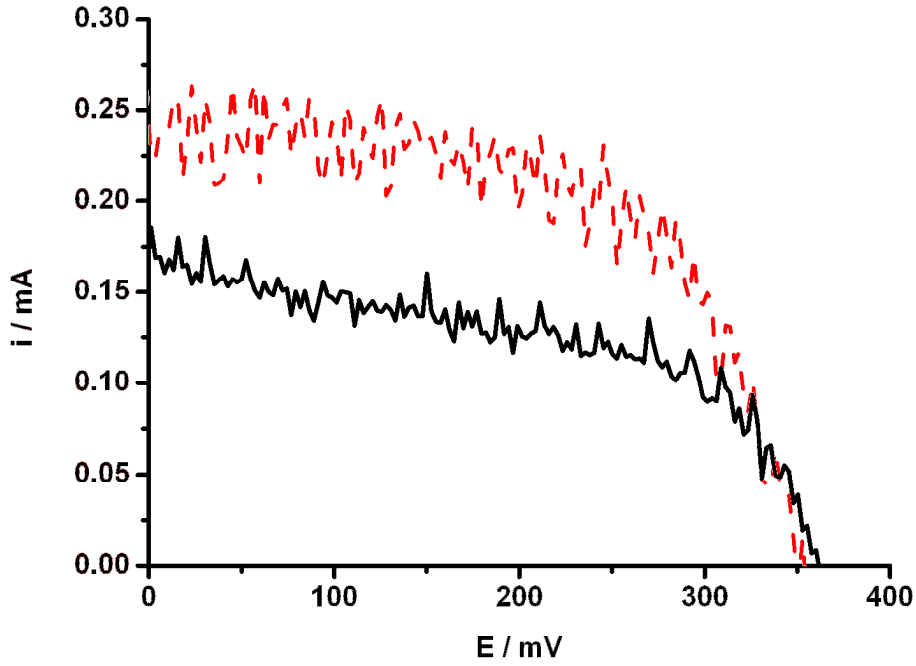


**Fig. 15** *I-V* Curve for **6.** Black solid line = Dye Bath concentration 1 mM; Red dashed line = dye bath concentration 2 mM.

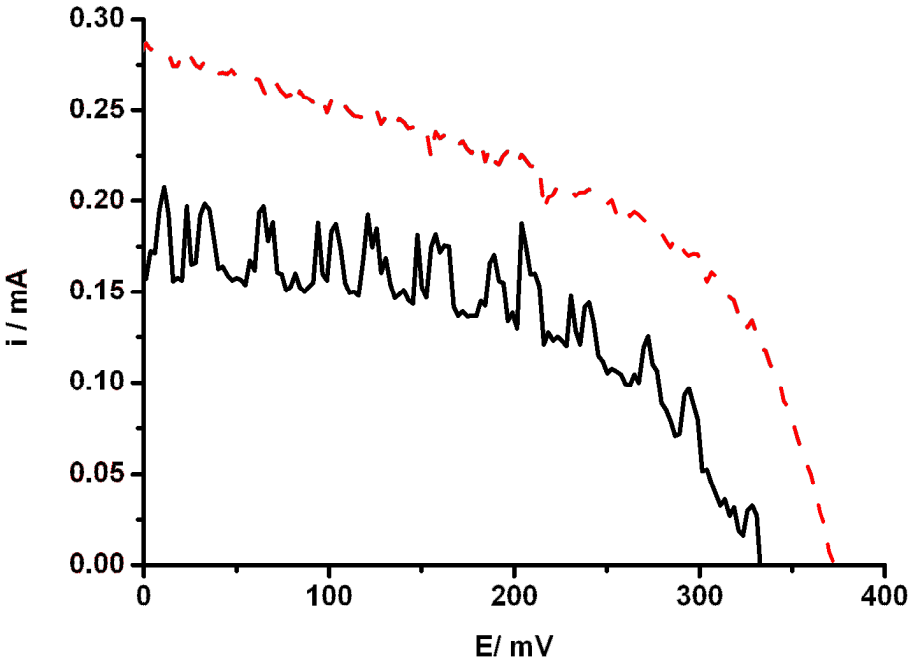


**Fig. 16** *I-V* Curve for **6**. Black solid line = Dye Bath and Cheno concentration is 1 mM; red dashed line = Dye Bath and Cheno concentration is 2 mM.

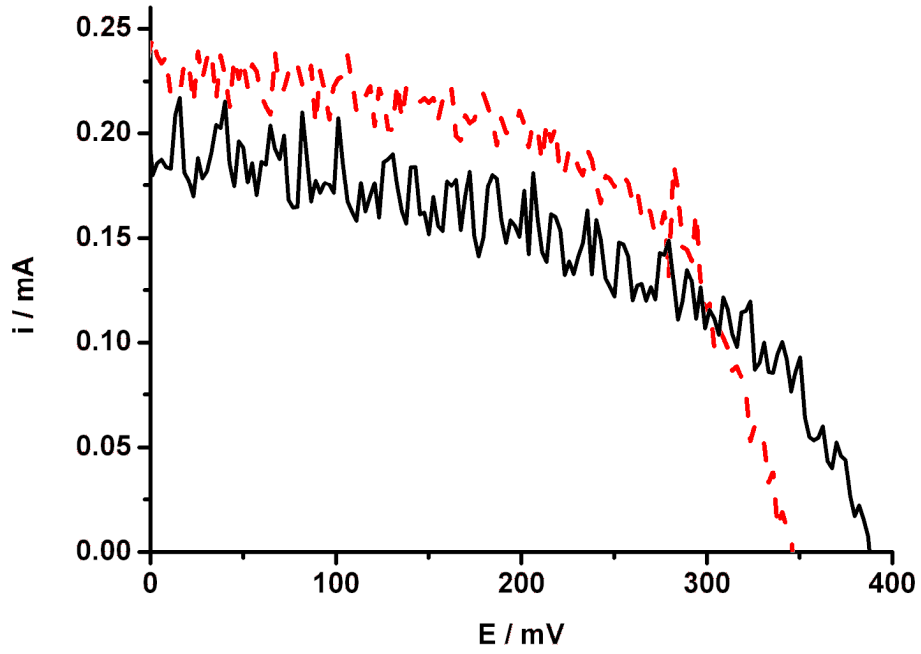


**Fig. 17** *I-V* Curve for **6**. Black solid line = $TiCl_4$ post-treatment used with Dye Bath concentration of 1 mM; red dashed line = $TiCl_4$ post-treatment used with Dye Bath concentration 2 mM.

Secondly, a $TiCl_4$ post-treatment of the $TiO_2$ film prior to adsorption of the sensitiser was applied as a potential method for improving photocurrents.[36-38] No improvement to photocurrent was recorded upon the introduction of the $TiCl_4$ post-treatment, and photovoltages remained within the same range seen throughout this work (Table 10 and Figure 16).

Despite the low power-conversion efficiency of cells sensitised with **6**, the key feature of the work is the demonstration of sensitiser function for a dye of this design. The POP ligand was chosen for its known steric rigidity and successfully demonstrates that simple dcbpy ligands can be used in heteroleptic Cu(I) DSSC sensitisers due to the chemical stability and sufficiently-long excited-state lifetime imposed by the POP. The low power-conversion efficiency is largely the result of poor harvesting of the solar spectrum by the dye leading to low $I_{SC}$. Our future work is now focused on the development of sterically-constraining co-ligands that also impart more optimised spectroscopic characteristics on heteroleptic Cu(I) DSSC sensitisers.

## 3.4 Conclusions

Shown here is the synthesis of a series of homoleptic complexes of general formula [Cu(I)(diimine)$_2$][$BF_4$] (**1** – **4**), and a series of heteroleptic complexes of the general formula [Cu(I)(POP)(diimine)][$BF_4$] (**5** – **10**). Electrochemical, spectroscopic and computational methods were used to understand the electronic characteristics of these complexes. In particular, this work demonstrates the first example of a heteroleptic Cu(I) complex, [Cu(I)(POP)(dcbpy)][$BF_4$] (**6**), that functions as a sensitiser in a dye-sensitised solar cell. The photocurrents and photovoltages achievable by **6** are lower than existing Cu(I)-sensitisers[7] but this is a result of the dye absorbing weakly in the visible region ($\lambda_{max}$ = 394 nm and $\varepsilon_{max}$ = $3.3x10^3\ M^{-1}cm^{-1}$).

A key point of this work is that stable heteroleptic Cu(I)-sensitisers can be achieved with simple 4,4′($CO_2H$)-bipyridine, synthetically less intensive to produce than the 4,4′,6,6′-substituted analogues. To advance upon this work Chapters 5 and 7 look at replacing the POP ligand with a more suitable second ligand that can have a beneficial impact on the absorption properties of the sensitiser as well as providing the required steric constraint.

## 3.5 Experimental

### 3.5.1 General Procedures

The synthesis of bis[2-(diphenylphosphanyl)phenyl] ether (POP) was carried out my Dr Omar Moudam following a literature procedure.[14] The synthesis of 4,4′-dicarboxy-2,2′-bipyridine (dcbpy),[39] 4,4′-di($CO_2$Et)-2,2′-bipyridine (decbpy),[40] 4,4′,6,6′-tetramethyl-2,2′-bipyridine (tmbpy),[41] 4,4′-dimethyl-6,6′-diphenyl-bipyridine (dpdmbpy),[13] [Cu(MeCN)$_4$][$BF_4$][42] and [Cu(POP)(MeCN)$_2$][$BF_4$][14] were carried out according to literature procedures. 4,4′,6,6′-tetracarboxy-2,2′-bipyridine (tcbpy) and 4,4′,6,6′-tetra($CO_2$Et)-2,2′-bipyridine (tecbpy) are novel ligands and have been synthesied using adapted literature methods.[40] 4,4′-dimethyl-2,2′-bipyridine (dmbpy), bipyrimidine (bpym) and all other chemicals were purchased from Aldrich and used as received.

Electrochemistry was carried out using a Pt working electrode, Pt rod counter electrode and Ag/AgCl reference electrode. All electrochemical experiments were carried out in either acetonitrile or DCM and the supporting electrolyte used was $TBABF_4$ (0.3M). After each experiment the reference electrode was calibrated against the ferrocene/ferrocenium couple which was found to be at 0.55 V. The absorption spectra were recorded using a PerkinElmer Lambda 9 spectrophotometer controlled using the UV/Winlab software. Emission spectra were recorded at room temperature and using frozen samples, with ethanolic solutions of **5**, **8**, **10**, [CuPOP(MeCN)$_2$][$BF_4$], dmbpy and tmbpy (0.1 – 0.6 mM), using a Fluoromax2 fluorimeter controlled by the ISAMain software.

Density functional theory calculations were performed using the Gaussian 03 program[25] with the starting structures for **5**, **6** and **8** inputted using the builder program Arguslab and the crystal

structure coordinates used as the starting point for **10**. All calculations were carried out using the Becke's three parameter exchange functional with the Lee-Yang-Parr for the correlation functional (B3LYP),[29] using the Los Alamos National Laboratory basis sets, known as LANL2DZ (developed by Hay and Wadt),[26-28] which comprises ECP + double zeta for copper, and the all-electron valence double zeta basis sets developed by Dunning (D95V) for light atoms.[43] Frequency calculations were carried out to ensure that optimised geometries were minima on the potential energy surface. Solvent effects were included via the self-consistent reaction field (SCRF) method using the polarised continuum model (PCM),[44] with slight modifications to the default cavity parameters to aid convergence. Time-dependent density functional theory (TDDFT) was performed in an acetonitrile polarisable continuum model, with the first 70 singlet transitions calculated. ArgusLab[30] was used to generate the orbital isosurface maps.

#### 3.5.1.1 4,4′-dicarboxy-2,2′-bipyridyl (dcbpy)

An adapted literature method was used for preparation of dcbpy.[39] dmbpy (500 mg, 2.7 mmol) added to sulphuric acid (12.5 ml, 220 mmol) and heated to 80 °C. Potassium dichromate (2395 mg, 8.1 mmol) was added slowly, maintaining a temperature between 75-80 °C. the soluation was poured over ice water (80 ml) resulting in a formation of a yellow precipitate, after stirring for 30 minutes. The precipitate was filtered and washed with water. The solid was added to 50 % nitric acid (15 ml) and refluxed for 4 h at 125 °C. The solution was added to ice water (80 ml) and stirred for 30 minutes and the put into the fridge overnight to induce crystallisation. The resulting white powder was filtered and washed with water. Yield = 86.5 %, 572 mg. $\delta_H$ (DMSO, 400MHz)/ppm = 13.84 (s, 1H, CO2H), 8.93 (d, 2H, H-bpy), 8.86 (s, 2H, H-bpy), 7.93 (d, 2H, H-bpy). MS (negative ESI); *m/z*: 242.93 (M+). Elemental analysis: Calculated for $C_{12}H_8N_2O_4$: C 59.02, H 3.30, N 11.47. Found: C 58.67, H 2.89, N 11.47.

#### 3.5.1.2 4,4′-tetraethyl ester-2,2′-bipyridyl (decbpy)

An adapted literature method was used for the preparation of decbpy.[40] dcbpy (400 mg, 1.6 mmol) was dissolved in concentrated sulfuric acid (9 ml) with ethanol (96 ml), and refluxed for 24 h at 85 °C under a nitrogen atmosphere. The solution was poured over ice water (150 ml) and the precipitate washed with water. The product was recrystallised from ethanol, yielding a white powder. Yield = 57.4 %, 282 mg. $\delta_H$ (DMSO, 400MHz)/ppm = 8.97 (d, 2H, H-bpy), 8.86 (s, 2H, H-bpy), 7.97 (d, 2H, H-bpy), 4.43 (q, 4H, O-$CH_2$), 1.39 (t, 6H, $CH_3$). MS (positive ESI); *m/z*: 301.2 (M+). Elemental analysis: Calculated for $C_{16}H_{16}N_2O_4$: C 63.99, H 5.37, N 9.33. Found: C 62.27, H 3.80, N 8.99.

#### 3.5.1.3 4,4′-6,6′-tetramethyl-2,2′-bipyridyl (tmbpy)

Adapted literature method used for the synthesis of tmbpy.[41] 10% Pd/C (2.725 g) was added to freshly distilled 2,4-lutidine (90 ml) and refluxed at 120 °C, under nitrogen for 72 h. The solution was allowed to cool slightly, benzene (40 ml) added and the solution refluxed at 120 °C for 40 minutes. The mixture was filtered hot to remove the catalyst and the solution concentrated by vacuum distillation. Recrystallisation of the residue from ethyl acetate produced a white crystalline solid that was collected by filtration. Yield = 4 %, 711 mg. $\delta_H$ (250MHz, $CDCl_3$) = 7.92 (s, 2H, H-bpy), 6.99 (s, 2H, H-bpy), 2.52 (s, 6H, $CH_3$), 2.31 (s, 6H, $CH_3$). MS (positive ESI); *m/z*: 213 $(M+H)^+$. Elemental analysis: Calculated for $C_{14}H_{16}N_2$: C 79.21, H 7.60, N 13.20. Found: C 79.21, H 7.73, N 13.20.

#### 3.5.1.4 4,4′-6,6′-tetracarboxy-2,2′-bipyridyl (tcbpy)

An adapted literature method was used for the synthesis of tcbpy.[40] tmbpy (174 mg, 0.8 mmol) was added to a solution of potassium permanganate (1.32 g, 8.4 mmol) in deionised water (150

ml) and refluxed for 18 h; until a black solid in a colourless solution is observed. The black precipitate was removed by filtration and conc. HCl (6 ml) added dropwise with stirring, until no more precipitate formed. The precipitate was collected by filtration. Yield = 22 %, 60 mg. $\delta_H$ (250MHz, $D_20$/NaOD) = 8.61 (s, 2H, H-bpy), 8.32 (s, 2H, H-bpy). Elemental analysis: Calculated for $C_{14}H_8N_2O_8$: C 50.61, H 2.43, N 8.43. Found: C 43.11, H 1.36, N 6.55.

### 3.5.1.5 4,4′-6,6′-tetraethyl ester-2,2′-bipyridyl (tecbpy)

Adapted literature method used for the synthesis of tecbpy.[40] tcbpy (0.4 g, 1.2 mol) was refluxed in conc. $H_2SO_4$ (8 ml) in absolute ethanol (75 ml) at 85 °C, under nitrogen for 24 h. The product was recrystallised from ethanol and collected by filtration. $\delta_H$ (250MHz, $CDCl_3$) = 9.17 (s, 2H, H-bpy), 8.62 (s, 2H, H-bpy), 4.52 (m, 4H, - C**H$_2$**-$CH_3$), 1.43 (m, 6H, -$CH_2$-C**H$_3$**). MS (negative ESI)l; *m/z*: 445 $(M+H)^+$, 467 $(M+Na)^+$, 910 $(2M+Na)^+$. Elemental analysis: Calculated for $C_{22}H_{24}N_2O_8$: C 59.45, H 5.41, N 6.31. Found: C 59.20, H 5.22, N 6.14.

### 3.5.1.6 6,6′-diphenyl-4,4′-dimtheyl-2,2′-bipyridyl (dpdmbpy)

Adapted literature method used for the synthesis of dpdmbpy[13]. Under a dry, nitrogen atmosphere dcbpy (2.0 g , 10.8 mmol) was dissolved in dry toluene (70 ml). The solution cooled to 0 °C and PhLi (30 ml, 60 mmol) was added such that the temperature was maintained between 0 °C and 10°C, and the solution then stirred for 72 h. The solution was cooled to 0 °C and ice (100 ml) added, again ensuring the temperature remained below 0 °C. The organic layer was collected (extraction with DCM), MnO2 (20.5 g) added and the reaction stirred for 24 h before drying with $MgSO_4$ (2.0 g). Ethanol (100 ml) was then added at 0 °C and stirred for 1 h before concentrating the solution to obtain the product as a precipitate. Yield = 5.4 %, 193 mg. $\delta_H$ ($CDCl_3$, 250MHz)/ppm = 8.15 (s, 2H, H-phenyl), 7.60 (d, 4H, H-phenyl), 7.51 (s, 2H, H-

phenyl), 7.43 (m, 6H, H-phenyl), 2.42 (s, 6H, H-methly). Elemental analysis: calculated for $C_{24}H_{20}N_2$: C 85.68, H 5.99, N 8.33. Found: C 85.44, H 4.45, N 8.12.

#### 3.5.1.7 $[Cu(MeCN)_4][BF_4]$

Copper (0) powder (5.00 g, 0.08 mol) and Cu(II) tetrafluoroborate hydrate (18.50 g, 0.08 mol) were stirred in degassed acetonitrile (300 ml) for 7 h. The blue solid was then removed by filtration and the solvent was removed under reduced pressure and the solid stored under nitrogen.

#### 3.5.1.8 $[Cu(tmbpy)_2][BF_4]$ (1)

$[Cu(MeCN)_4][BF_4]$ (140 mg, 0.45 mmol) and tmbpy (200 mg, 0.89 mmol) were stirred in 20 mL degassed chloroform under nitrogen for 30 min. The solvent was removed under reduced pressure and the solid obtained triturated in hexane. The product was obtained by filtration. Yield = 75 %, 193 mg. $\delta_H$ (DMSO, 250MHz)/ppm = 8.36 (s, 4H, H-bpy), 7.42 (s, 4H, H-bpy), 2.45 (s, 12H, $CH_3$), 2.11 (s, 12H, $CH_3$). MS (positive ESI); *m/z*: 487.10 $(M\text{-}BF_4^-)^+$. Elemental analysis: calculated for $C_{28}H_{32}BCuF_4N_4$: C 58.49, H 5.61, N 9.74. Found: C 57.78, H 5.46, N 9.57.

#### 3.5.1.9 $[Cu(tcbpy)_2][BF_4]$ (2)

$[Cu(MeCN)_4][BF_4]$ (20.5 mg, 0.07 mmol) and tcbpy (42.3 mg, 0.13 mmol) were stirred in 5 mL degassed, dry MeOH under nitrogen for 2 h. A white solid (uncomplexed tcbpy) was removed by filtration. The pure product was then obtained by precipitation with isopropyl alcohol overnight. Yield = 32 %, 17 mg. $\delta_H$(DMSO, 250 MHz)/ppm: 8.84 (s, 4H, H-bpy), 8.22 (s, 4H,

H-bpy). MS (positive ESI): *m/z* = 725.31 $(M\text{-}BF_4^-)^+$. Elemental analysis: calculated for $C_{28}H_{16}BCuF_4N_4O_{16}$: C 41.27, H 1.98, N 6.88. Found: C 41.44, H 2.24, N 7.96.

### 3.5.1.10 $[Cu(tecbpy)_2][BF_4]$ (3)

$[Cu(MeCN)_4][BF_4]$ (14.2 mg, 0.05 mmol) and tecbpy (40 mg, 0.09 mmol) were stirred in 50 mL degassed, dry DCM under nitrogen for 30 min. The pure product was obtained by precipitation with isopropyl alcohol. Yield = 53 %, 28 mg. $\delta_H$ ($CDCl_3$, 250MHz)/ppm = 9.15 (s, 4H, H-bpy), 8.69 (s, 4H, H-bpy), 4.54 (q, J = 7.10 Hz, 8H, $-CH_2-CH_3$), 3.88 (q, J = 7.14 Hz, 8H, $-CH_2-CH_3$), 1.47 (t, J = 7.18 Hz, 12H, $-CH_2-CH_3$), 1.03 (t, J = 7.11 Hz, 12H, $CH_2-CH_3$). MS (positive ESI); *m/z*: 950 $(M\text{-}BF_4^-)^+$. Elemental analysis: calculated for $C_{44}H_{48}N_4O_{16}CuBF_4.CH_2Cl_2$: C 48.08, H 4.48, N, 4.98. Found: C 47.60, H 4.33, N 4.79.

### 3.5.1.11 $[Cu(POP)(dmbpy)][BF_4]$ (5)

$[Cu(POP)(MeCN)_2][BF_4]$ (201 mg, 0.26 mmol) and dmbpy (51 mg, 0.06 mmol) were stirred in 5 mL acetone for 3 h resulting in an orange solution. The solvent was removed under reduced pressure. The pure product was then obtained by reprecipitation from acetonitrile upon addition of isopropyl alcohol and leaving overnight. Yield = 67 %, 153 mg. $\delta_H$(DMSO, 250 MHz)/ppm:. 8.51 (s, 2H, H-bpy), 8.37 (d, 2H, H-bpy), 7.47-7.15 (m, 18H, H-POP), 7.09 (t, 2H, H-bpy), 6.98 (m, 8H, H-POP), 6.61 (m, 2H, H-POP), 2.47 (s, 6H, $CH_3$-bpy). MS (positive FAB): *m/z* = 784.7 $(M\text{-}BF_4^-)^+$. Elemental analysis: calculated for $C_{48}H_{40}BCuF_4N_2OP_2$: C 66.03, H 4.62, N 3.21. Found: C 65.58, H 4.42, N 3.90.

### 3.5.1.12 [Cu(POP)(dcbpy)][$BF_4$] (6)

[Cu(POP)($MeCN)_2$][$BF_4$] (100 mg, 0.13 mmol) and dcbpy (28 mg, 0.03 mmol) were stirred in 5 mL acetone for 3 h resulting in a yellow solution. The pure product was then obtained by reprecipitation upon addition of isopropyl alcohol and leaving overnight. Yield = 26 %, 96 mg. $\delta_H$(DMSO, 250 MHz)/ppm: 9.17 (s, 2H, H-bpy), 8.91 (d, 2H, H-bpy), 8.07 (d, 2H, H-bpy), 7.4 (m, 28H, H-POP). MS (positive ESI): *m/z* = 844.80 $(M\text{-}BF^-)^+$. Elemental analysis: calculated for $C_{50}H_{41}CuN_2O_5P_2.BF_4$: C 62.41, H 4.30, N 2.91. Found C 62.06, H 4.40, N 2.77.

### 3.5.1.13 [Cu(POP)(decbpy)][$BF_4$] (7)

[Cu(POP)($MeCN)_2$][$BF_4$] (201 mg, 0.26 mmol) and decbpy (51 mg, 0.05 mmol) were stirred in 5 mL acetone for 3 h resulting in an orange solution. The solvent was removed under reduced pressure. The pure product was then obtained by reprecipitation upon addition of isopropyl alcohol and leaving overnight. Yield = 87%. 231 mg, $\delta_H$(DMSO, 250 MHz)/ppm: 8.79 (s, 2H, H-bpy), 8.75 (d, J = 4.74 Hz, 2H, H,-bpy), 7.98 (dd, J = 1.32 Hz, J = 5.42 Hz, 2H, H-bpy), 7.10 (m, 28H, H-POP), 4.53 (dd, J = 7.07 Hz, 4H, $CH_2CH_3$), 1.49 (t, J = 7.13 Hz, 6H, $CH_2CH_3$). MS (positive ESI): *m/z* = 784.87 $(M\text{-}BF^-)^+$. Elemental analysis: calculated for $C_{54}H_{49}CuN_2O_5P_2.BF_4$: C 63.14, H 4.48, N 2.83. Found C 62.71, H 4.36, N 2.11.

### 3.5.1.14 [Cu(POP)(tmbpy)][$BF_4$] (8)

[Cu(POP)($MeCN)_2$][$BF_4$] (101 mg, 0.13 mmol) and tmbpy (25 mg, 0.03 mmol) were stirred in 10 mL anhydrous acetonitrile under $N_2$ for 3 h resulting in an orange solution. The volume of reaction mixture was reduced by half under reduced pressure. The pure product was then obtained upon addition of isopropyl alcohol and leaving overnight. The desired product remains in the filtrate and is obtained by solvent removal under reduced pressure. Yield = 75 %,

90 mg. $\delta_H$(DMSO, 250 MHz)/ppm: 8.09 (s, 2H, H-bpy), 6.85-7.34 (m, 30H, H-bpy and POP), 2.37 (s, 6H, $CH_3$), 2.31 (s, 6H, $CH_3$). MS (positive FAB): *m/z* (%) = 812.6 $(M\text{-}BF^-)^+$. Elemental analysis: calculated for $C_{52}H_{49}BCuF_4N_2OP_2$: C 66.64, H 4.92, N 3.11. Found C 66.40, H 4.76, N 3.00.

#### 3.5.1.15 [Cu(POP)(tcbpy)][$BF_4$] (9)

[Cu(POP)$(MeCN)_2$][$BF_4$] (100 mg, 0.13 mmol) and tcbpy (45 mg, 0.04 mmol) were stirred in 5 mL acetone for 3 h resulting in a dark purple solution and white solid. The white solid was removed by filtration. The pure product was then obtained by reprecipitation upon addition of isopropyl alcohol and leaving overnight. The desired product remains in the filtrate and was obtained by solvent removal under reduced pressure. Yield =53 %, 72 mg. $\delta_H$(DMSO, 250 MHz)/ppm: 9.32 (s, 2H, H-bpy), 8.72 (s, 2H, H-bpy), 6.87-7.67 (m, 28H, POP). MS (positive FAB): *m/z* (%) = 617.3 (CuPOP). Elemental analysis: calculated for $C_{50}H_{36}BCuF_4N_2O_9P_2$: C 58.81, H 3.55, N 2.74. Found C 59.10, H 3.88, N 2.86.

#### 3.5.1.16 [Cu(POP)(bpym)][$BF_4$] (10)

[Cu(POP)$(MeCN)_2$][BF4] (486 mg, 0.63 mmol) and bpym (100 mg, 0.63 mmol) were stirred in 20 mL DCM. The product was obtained by concentration of the reaction mixture then precipitation by the addition of ether. Yield = 64 %. $\delta_H$($CD_3OD$, 250 MHz)/ppm: 8.90 (s, 4H, H-bpym), 7.59-6.77 (m, 30H, H-bpym and H-POP). Elemental analysis: calculated for $C_{44}H_{34}BCuF_4N_4OP_2$: C 62.39, H 4.05, N 6.61. Found C 61.56, H 3.43, N 6.34

#### 3.5.1.17 $[Cu_2(POP)_2(\mu\text{-bpym})][(BF_4)_2]$ (11)

$[Cu(POP)(MeCN)_2][BF4]$ (33 mg, 0.04 mmol) and 11 (34 mg, 0.04 mmol) were stirred in 5 mL acetone for 30 h. The product was obtained by concentration of the reaction mixture then precipitation by the addition of ether. Despite obtaining a crystal structure we were unable to obtain a pure product with satisfactory elemental analysis. Yield = 48 %, 32 mg. $\delta_H$(DMSO, 250 MHz)/ppm: 9.01 (s, 4H, H-bpym), 7.85-6.58 (m, 58H, H-bpym and H-POP). Elemental analysis: calculated for $C_{82}H_{66}B_2Cu_2F_8N_4O_2P_4$: C 62.56, H 4.07, N 3.65. Found C 59.06, H 3.96, N 3.01.

## 3.5.2 X-ray Crystallography

Crystals of $[Cu(dmbpy)_2Cl][BF_4]$ were grown by slow diffusion of diethyl ether into a saturated DCM solution of **5**. Crystals of **1** and **10** were grown by slow diffusion of diethyl ether into a saturated DCM solution of **1** or **10** respectively. Crystals of **4** were grown in a deuterated DMSO solution of an attempted synthesis of $[CuPOP(dpdmbpy)][BF_4]$. Crystals of **7** were grown by slow diffusion of diethyl ether into a saturated solution of **7** in acetonitrile. Crystals of **11** was grown by slow diffusion of hexane into a saturated solution of **11** in acetone. Single crystal X-ray diffraction data are given in Tables 11 and 12 and were collected using Mo-Kα radiation (λ = 0.71073 Å) on a Smart APEX CCD diffractometer equipped with an Oxford Cryosystems low-temperature device operating at 150 K. An absorption correction was applied using the multi-scan procedure SADABS.[45] The structures were solved by direct methods (Shelx[46] for $[Cu(dmbpy)_2][BF_4]$, **1**, **4**, **8** and **7**; and SIR92[47] for **10** and **11** and refined by full-matrix least squares against $|F|^2$ using all data (Shelx[46] for $[Cu(dmbpy)_2][BF_4]$, **1**, **4**, **8** and **7**; and CRYSTALS[48] for **10** and **11**. Figures were prepared using the programme Mercury.[49] All non-H atoms were refined with anisotropic displacement parameters.

**Table 11** X-Ray crystallography data for the Homoleptic Complexes $[Cu(dmbpy)_2Cl][BF_4]$, **1** and **4**

| | $[Cu(dmbpy)_2Cl][BF_4]$ | **1** | **4** |
|---|---|---|---|
| CCDC deposition number | 771442 | 771443 | N/A |
| Empirical Formula | $(C_{24}H_{24}N_4CuCl)_2.(BF_4)_2.(CH_2Cl_2)$ | $C_{28}H_{32}N_4Cu.\ BF_4$ | $C_{48}H_{40}N_4Cu.\ 2(BF_4).2(CHCl_3)$ |
| Formula weight | 1193.47 | 574.93 | 1148.74 |
| T / K | 150(2) | 150(2) | 100(2) |
| Crystal colour | Cyan | Orange | Dark Green |
| Crystal dimensions | 0.50x0.40x0.30 | 0.90x0.59x0.43 | 0.1721x0.1682x0.0708 |
| Crystal system | triclinic | monoclinic | orthorhombic |
| Space group | *P*-1 | *C*2/*c* | *Pna21* |
| *a* / Å | 10.8528(3) | 13.8531(14) | 26.0652(4) |
| *b* / Å | 14.4072(4) | 16.4771(14) | 7.82870(10) |
| *c* / Å | 17.6085(5) | 13.5039(19) | 24.2125(3) |
| α / ° | 83.9868(16) | 90 | 90 |
| β / ° | 74.9744(14) | 119.730(7) | 90 |
| γ / ° | 73.3850(14) | 90 | 90 |
| *V* / $Å^3$ | 2546.69(12) | 2676.7(5) | 4940.72(12) |
| *Z* | 4 | 4 | 4 |
| $D_{calcd}$ / $Mgm^{-3}$ | 1.556 | 1.427 | 1.544 |
| Independent reflections | 8998 $[R_{int}=0.0411]$ | 2747 $[R_{int}=0.0492]$ | 8613 $[R_{int}=0.0336]$ |
| Data/restraints/ Parameters | 8998/0/666 | 2747/184/190 | 8613/1/645 |
| Absorption correction / $mm^{-1}$ | 1.119 | 0.869 | 4.225 |
| $R_1/wR_2$ (observed data: $F^2>2\sigma(F^2)$) | 0.0366/0.0933 | 0.0526/0.1470 | 0.0233/0.0633 |

**Table 12** X-Ray crystallography data for the Heteroleptic complexes **7**, **8**, **10** and **11**

| | **7** | **8** | **10** | **11** |
|---|---|---|---|---|
| CCDC deposition number | 771439 | N/A | 771440 | 771441 |
| Empirical Formula | $C_{52}H_{44}N_2CuO_5P_2.BF_4.C_2H_3N$ | $C_{50}H_{44}CuN_2OP_2.BF_4.C_6H_{14}$ | $C_{44}H_{34}N_4OP_2Cu.BF_4$ | $C_{80}H_{62}N_4O_2P_4Cu_2.2[BF_4].2[C_3H_6O]$ |
| Formula weight | 1030.24 | 987.39 | 847.08 | 1652.15 |
| T / K | 100(2) | 100(2) | 150(2) | 150(2) |
| Crystal colour | Orange | Yellow | Orange | Orange-Yellow |
| Crystal dimensions | 0.15x0.15x0.08 | 0.12x0.14x0.23 | 0.22x0.33x0.36 | 0.15x0.21x0.25 |
| Crystal system | Triclinic | Triclinic | Monoclinic | Triclinic |
| Space group | *P*-1 | *P*-1 | $P2_1/c$ | *P*-1 |
| *a* / Å | 12.3345(3) | 11.35159(16) | 9.5405(2) | 11.3321(3) |
| *b* / Å | 12.6111(3) | 12.3287(2) | 19.8580(4) | 13.2821(3) |
| *c* / Å | 18.0200(4) | 17.7320(3) | 20.4442(4) | 14.2188(3) |
| α / ° | 98.4411(13) | 70.8270(17) | 90 | 108.665(1) |
| β / ° | 100.4738(12) | 80.0951(13) | 95.4810(10) | 105.605(1) |
| γ / ° | 113.2549(12) | 77.4948(14) | 90 | 97.186(1) |
| *V* / Å$^3$ | 2457.18(10) | 2274.59(7) | 3855.55(14) | 1899.81(7) |
| *Z* | 2 | 2 | 4 | 1 |
| $D_{calcd}$ / Mgm$^{-3}$ | 1.392 | 1.44 | 1.459 | 1.440 |
| Independent reflections | 10570 [$R_{int}$=0.0606] | 8960 [$R_{int}$=0.049] | 10239 [$R_{int}$=0.038] | 10287 [$R_{int}$=0.037] |
| Data/restraints/ Parameters | 10570/63/680 | 8960/0/505 | 10239/0/514 | 10287/0/496 |
| Absorption correction / mm$^{-1}$ | 0.577 | 1.845 | 0.711 | 0.719 |
| $R_1$/$wR_2$ (observed data: $F^2>2\sigma(F^2)$) | 0.0422/0.0933 | 0.0937/0.0810 | 0.0485/0.1071 | 0.0537/0.1160 |

## 3.6 References


1. N. Armaroli, *Chemical Society Reviews*, 2001, **30**, 113-124.
2. N. Alonso-Vante, J.-F. Nierengarten and J.-P. Sauvage, *Dalton Trans.*, 1994, 1649-1654.
3. S. Sakaki, T. Kuroki and T. Hamada, *Journal of the Chemical Society, Dalton Transactions*, 2002, 840-842.
4. A. Barbieri, G. Accorsi and N. Armaroli, *Chemical Communications*, 2008, 2185-2193.
5. T. Bessho, E. C. Constable, M. Graetzel, A. H. Redondo, C. E. Housecroft, W. Kylberg, M. K. Nazeeruddin, M. Neuburger and S. Schaffner, *Chemical Communications*, 2008, 3717-3719.
6. A. H. Rendondo, E. C. Constable and C. E. Housecroft, *CHIMIA International Journal for Chemistry*, 2009, **63**, 205-207.
7. E. C. Constable, A. H. Redondo, C. E. Housecroft, M. Neuburger and S. Schaffner, *Dalton Transactions*, 2009, 6634-6644.
8. S. Ferrere and B. A. Gregg, *Journal of the American Chemical Society*, 1998, **120**, 843-844.
9. S.-M. Kuang, D. G. Cuttell, D. R. McMillin, P. E. Fanwick and R. A. Walton, *Inorganic Chemistry*, 2002, **41**, 3313-3322.
10. N. Robertson, *ChemSusChem*, 2008, **1**, 977-979.
11. L. Spiccia, G. B. Deacon and C. M. Kepert, *Coordination Chemistry Reviews*, 2004, **248**, 1329-1341.
12. N. Armaroli, G. Accorsi, F. Cardinali and A. Listorti, *Photochemistry and Photophysics of Coordination Compounds I*.
13. R. M. Williams, L. D. Cola, F. Hartl, J.-J. Lagref, J.-M. Planeix, A. D. Cian and M. W. Hosseini, *Coordination Chemistry Reviews*, 2002, **230**, 253-261.
14. N. Armaroli, G. Accorsi, M. Holler, O. Moudam, J. F. Nierengarten, Z. Zhou, R. T. Wegh and R. Welter, *Advanced Materials*, 2006, **18**, 1313.
15. M. Ruthkosky, C. A. Kelly, F. N. Castellano and G. J. Meyer, *Coordination Chemistry Reviews*, 1998, **171**, 309-322.
16. O. Moudam, A. Kaeser, B. Delavaux-Nicot, C. Duhayon, M. Holler, G. Accorsi, N. Armaroli, I. Seguy, J. Navarro, P. Destruel and J.-F. Nierengarten, *Chemical Communications*, 2007, 3077-3079.
17. T. McCormick, W.-L. Jia and S. Wang, *Inorganic Chemistry*, 2005, **45**, 147-155.
18. L. Yang, J.-K. Feng, A.-M. Ren, M. Zhang, Y.-G. Ma and X.-D. Liu, *European Journal of Inorganic Chemistry*, 2005, **2005**, 1867-1879.
19. A. Listorti, G. Accorsi, Y. Rio, N. Armaroli, O. Moudam, A. Gel gout, B. a. Delavaux-Nicot, M. Holler and J.-F. o. Nierengarten, *Inorganic Chemistry*, 2008, **47**, 6254-6261.
20. S. Zisheng and et al., *Journal of Physics D: Applied Physics*, 2008, **41**, 085103.
21. U. Monkowius, Y. N. Svartsov, T. Fischer, M. Zabel and H. Yersin, *Inorganic Chemistry Communications*, 2007, **10**, 1473-1477.
22. Q. Zhang, J. Ding, Y. Cheng, L. Wang, Z. Xie, X. Jing and F. Wang, *Advanced Functional Materials*, 2007, **17**, 2983.
23. Y.-M. Xie and J.-H. Wu, *Inorganic Chemistry Communications*, 2007, **10**, 1561-1564.
24. L. Zhang, B. Li and Z. Su, *Langmuir*, 2009, **25**, 2068-2074.
25. M. J. Frisch, G. W. Trucks, H. B. Schlegel, G. E. Scuseria, M. A. Robb, J. R. Cheeseman, J. A. M. Jr., T. Vreven, K. N. Kudin, J. C. Burant, J. M. Millam, S.S.Iyengar, T. J., V. Barone, B. Mennucci, M. Cossi, G. Scalmani, N. Rega, G. A. Petersson, H. Nakatsuji, M. Hada, M. Ehara, K. Toyota, R. Fukuda, J. Hasegawa, M. Ishida, T. Nakajima, Y. Honda, O. Kitao, H. Nakai, M. Klene, X. Li, J. E. Knox, H. P. Hratchian, J. B. Cross, V. Bakken, A. C., J. Jaramillo, R. Gomperts, R. E. Stratmann, O.

Yazyev, A. J. Austin, R. Cammi, C. Pomelli, J. W. Ochterski, P. Y. Ayala, K. Morokuma, G. A. Voth, P. Salvador, J. J. Dannenberg, V. G. Zakrzewski, S. Dapprich, A. D. Daniels, M. C. Strain, O. Farkas, D. K. Malick, A. D. Rabuck, K. Raghavachari, J. B. Foresman, J. V. Ortiz, Q. Cui, A. G. Baboul, S. Clifford, C. J., B. B. Stefanov, G. Liu, A. Liashenko, P. Piskorz, I. Komaromi, R. L. Martin, D. J. Fox, T. Keith, M. A. Al-Laham, C. Y. Peng, A. Nanayakkara, M. Challacombe, P. M. W. Gill, B. Johnson, W. Chen, M. W. Wong, C. Gonzalez and J. A. Pople, *Gaussian 03, Revised C.02, Gaussian, Inc., Wallingford, CT*, 2004.

26. W. R. Wadt and P. J. Hay, *The Journal of Chemical Physics*, 1985, **82**, 284-298.
27. P. J. Hay and W. R. Wadt, *The Journal of Chemical Physics*, 1985, **82**, 270-283.
28. P. J. Hay and W. R. Wadt, *The Journal of Chemical Physics*, 1985, **82**, 299-310.
29. A. D. Becke, *The Journal of Chemical Physics*, 1993, **98**, 5648-5652.
30. M. A. Thompson, http://www.arguslab.com.
31. K. L. McCall, J. R. Jennings, H. Wang, A. Morandeira, L. M. Peter, J. R. Durrant, L. J. Yellowlees, J. D. Woollins and N. Robertson, *Journal of Photochemistry and Photobiology A: Chemistry*, 2009, **202**, 196-204.
32. S. Ito, H. Miura, S. Uchida, M. Takata, K. Sumioka, P. Liska, P. Comte, P. Pechy and M. Gratzel, *Chemical Communications*, 2008, 5194-5196.
33. R. Chen, X. Yang, H. Tian, X. Wang, A. Hagfeldt and L. Sun, *Chemistry of Materials*, 2007, **19**, 4007-4015.
34. H. Choi, J. K. Lee, K. H. Song, K. Song, S. O. Kang and J. Ko, *Tetrahedron*, 2007, **63**, 1553-1559.
35. K. Sayama, S. Tsukagoshi, T. Mori, K. Hara, Y. Ohga, A. Shinpou, Y. Abe, S. Suga and H. Arakawa, *Solar Energy Materials and Solar Cells*, 2003, **80**, 47-71.
36. J. H. Yum, S. Moon, R. Humphry-Baker, P. Walter, T. Geiger, F. Nuesch, M. Gratzel and M. K. Nazeeruddin, *Nanotechnology*, 2008, **19**, 424005.
37. M. K. Nazeeruddin, A. Kay, I. Rodicio, R. Humphry-Baker, E. Mueller, P. Liska, N. Vlachopoulos and M. Graetzel, *Journal of the American Chemical Society*, 1993, **115**, 6382-6390.
38. P. M. Sommeling, B. C. O'Regan, R. R. Haswell, H. J. P. Smit, N. J. Bakker, J. J. T. Smits, J. M. Kroon and J. A. M. van Roosmalen, *The Journal of Physical Chemistry B*, 2006, **110**, 19191-19197.
39. P. G. Hoertz, A. Staniszewski, A. Marton, G. T. Higgins, C. D. Incarvito, A. L. Rheingold and G. J. Meyer, *Journal of the American Chemical Society*, 2006, **128**, 8234-8245.
40. F. H. Case, *Journal of the American Chemical Society*, 1946, **68**, 2574-2577.
41. P. Ghosh and T. G. Spiro, *Journal of the American Chemical Society*, 1980, **102**, 5543-5549.
42. O. Moudam, in *LCC-Toulouse*, LCC-Toulouse, Toulouse, 2007.
43. T. H. Dunning, H. F. Schaefer and P. J. Hay, *in Modern Theoretical Chemisrty, Ed III*, Plenum, New York, 1976.
44. A. Vleck Jr and S. Zális, *Coordination Chemistry Reviews*, 2007, **251**, 258-287.
45. G. M. Sheldrick, University of Gottingen, Germany.
46. G. Sheldrick, *Acta Crystallographica Section A*, 2008, **64**, 112-122.
47. A. Altomane, G. Cascarano, C. Giacovazzo, A. Guagliardi, M. C. Burla, G. Polidori and M. Carnalli, *Journal of Applied Crystallography*, 1994, **27**, 435.
48. P. W. Betteridge, J. R. Carruthers, R. I. Cooper, K. Prout and D. J. Watkin, *Journal of Applied Crystallography*, 2003, **36**, 1487.
49. C. F. Macrae, P. R. Edgington, P. McCabe, E. Pidcock, G. P. Shields, R. Taylor, M. Towler and J. van de Streek, *Journal of Applied Crystallography*, 2006, **39**, 453-457.

# 4. Chapter Four

# Emission Spectroscopy and Computational Study of 5 and 8

## 4.1 Introduction

The work described in this chapter furthers the photophysical investigation of **5** and **8** that was presented in the Emission Spectroscopy section of Chapter Three. The initial studies reported in Chapter Three suggested **8** to be significantly more emissive than **5**. Here we look both experimentally and computationally to expand the explanation for this difference in emission behaviour.

Electroluminescent transition metal complexes are of great interest for devices such as organic light-emitting diodes (OLEDs),[1, 2] light-emitting electrochemical cells (LECs)[3-5] and are related to complexes used in dye-sensitised solar cells (DSSCs).[6-8] Heavy metal complexes based on Ru(II),[9-12] Ir(III)[13, 14] and Pt(II)[15-17] have been the main contenders in these roles due to their high quantum yields, reversible redox processes and tuneable emission wavelengths through intelligent ligand design. Related research into first row transition metal complexes has been gaining momentum in the last 30 years, thanks to the early work of McMillin,[18] due to their reduced cost, higher abundance and lower toxicity compared to heavy metals. The limiting factor for first row transition metals is that they generally exhibit shorter lived excited states due to non-radiative decay (discussed in Chapter One) that result in low quantum yields.

As discussed previously the full d-subshells of Cu(I) complexes limits the extent of excited state non-radiative decay, with some Cu(I) complexes exhibiting lifetimes up to 200 μs and increased quantum yields. Cu(I) complexes are also redox active, a requirement of the active material present in OLEDs, LECs and DSSCs. These factors make them attractive alternative replacements for Ru(II) electroluminescent complexes.[8, 19]

However the conformational geometry change that occurs during the Cu(I)/Cu(II) redox process or during MLCT,[20, 21] (Chapter One) can lead to solvent attack of the excited molecule, known

as exciplex quenching, and can also lead to complex degradation and decomposition. Coupled with the slow electron transfer kinetics also induced by the conformational change, these properties have made Cu(I) complexes less appealing for use in devices. The extent and effect this conformational change has on the electroluminescent properties has been extensively investigated in the hope of improving their applicability. This has been attempted by designing ligands that coordinate to sterically constrain the molecule to the pseudo-tetrahedral geometry, therefore limiting the extent of the geometrical flattening.[19-21 18, 22-30 31]

Investigation into heteroleptic Cu(I) complexes for electroluminescent device application has been an active field for over ten years, with [Cu(I)(NN)(PP)] complexes yielding quantum yields approaching those observed for the best Ru(II) complexes.[31-37] One particularly successful family contains the ligand bis[2-(diphenylphosphino) phenyl]ether (POP), with the most research carried out into [Cu(POP)(1,10-phenanthroline)]$^+$ complexes,[38-43] where $\Phi_{PL}$ of around 70% were achieved.[41, 44] Little work has been done to investigate the emission behaviour of the analogous [Cu(POP)(2,2′-bipyridine)]$^+$ complexes, presumably due to the typically lower quantum yields observed for Cu(I)(bipyridine) complexes in comparison with the analogous phenanthrolines.[45, 46]

In this work we have continued our studies into the emissive properties of [Cu(POP)(dmbpy)][$BF_4$]: **5** and [Cu(POP)(tmbpy)][$BF_4$]: **8**. The complexes were investigated in aerated and de-aerated EtOH solutions at 300 K, in EtOH at 77 K, and dispersed in a PMMA film at 300 K. The emission spectra, lifetimes and quantum yields were recorded where appropriate. Alongside these photophysical results we present a computational (DFT) investigation to explore the link between the structural rigidity of a complex and its photophysical properties.

## 4.2 Results and Discussion

### 4.2.1 Syntheses

The ligand tmbpy and starting material $[Cu(POP)(MeCN)_2][BF_4]$ were synthesised using modified literature methods.[47, 48] As stated in Chapter Three, $[Cu(POP)(MeCN)_2][BF_4]$ was synthesised by Dr Omar Moudam and a sample used throughout this work. The ligand dmbpy and all other chemicals were purchased from Aldrich and used as received. The synthesis procedures for **5** and **8** have been described in Chapter Three.[49] Both complexes were characterised by $^1$H NMR, +FAB-MS and elemental analysis, verifying molecular structures. Additional structure verification for **8** was achieved by single crystal X-ray crystallography (Chapter Three). Refinement of the crystal structure of **5** was not possible to publishable level (R<10%) and therefore only a connectivity image and not detailed structural information will be quoted in this work. The UV/Vis absorption spectroscopy and electrochemical behaviour of **5** and **8** in acetonitrile were reported in Chapter Three.[50] For this work the absorption spectroscopy of **5** and **8** were carried out in ethanol to allow direct comparison with the fluorescence spectroscopy.

### 4.2.2 DFT and TDDFT Calculations

Calculations were carried out for the singlet and triplet states of **5** and **8** using Gaussian 03[51] with the B3LYP/LANL2DZ[52-55] functional and basis set in order to explore their ground and excited states respectively. The singlet calculations were run with induced solvent effects to explore the ground state of the complex and the MLCT transitions taking place within the two complexes. The singlet calculations could also be compared to the experimentally collected data to give an indication of the accuracy of our computational system. The triplet calculations

have been used to investigate the excited state properties of these two complexes, both geometrically and electronically, which was hoped to give insight into the connection between these properties within these systems. However, due to computational difficulties it was not possible to calculate an optimised geometry for the triplet states of either complex, and by this it means a minimum energy structure was not obtained (see Chapter Two, section 2.3.3), and so a single point solvent calculation was carried out instead. A single point solvent calculation involves taking a computationally optimised structure carried out without the presence of solvent, and then applying a polarisable continuum model (Chapter Two, section 2.3.2.1) and re-calculating the energy of the structure without optimising the geometry. It was felt this method could be applied to these structures as little variation in geometry was observed in the structures as solvents were introduced. The results obtained are less accurate but they give an adequate indication of the predicted complex behaviour. Input starting structures for the singlet and triplet states of **5** and **8** were built using the builder program ArgusLab. The triplet state form of **8** was also calculated starting from the crystal structure coordinates. The reasons behind these choices are explained throughout the rest of this chapter. This level of theory has been used successfully both in our previous work (Chapter Three) and in the literature to calculate the structural and electronic properties of a number of coordination complexes.[56] Calculation details are outlined in full in the Experimental section. The DFT calculated gas-phase and solution-phase structures for **5** and **8** produce identical overall structure energies and comparable bond distances and angles. The central bond lengths and angles for the optimised geometry are in good agreement with the structure obtained from the crystal structure (Table 1), but as mentioned in Chapter Three, the variation in the geometry of the POP ligand has minimal effect on the overall energy of the complex (see later in this chapter). This therefore suggests that for the system under investigation here, the crystal structure obtained is probably only one of the many possibilities achievable conformations this complex adopts when in solution.

Time dependent density functional theory (TDDFT), also at the B3LYP/LANL2DZ level of theory, was used to probe the electronic transitions that give rise to the visible and near-UV absorption of each complex in the singlet ground state. Although current TDDFT implementations have a tendency to underestimate the energy of charge-transfer interactions, the method has been shown to provide useful qualitative information on the electronic structure and photophysical behaviour of similar coordination complexes (Chapter Three).[56]

**Table 1** Selected bond lengths (Å) and bond angles (deg) from single crystal X-ray crystallography for **8** and from solvated DFT calculations for **5** and **8** in their singlet ground states.

| | **5**[b] | **8** [a] | **8** [b] |
|---|---|---|---|
| Cu-N(1) | 2.103 | 2.089(3) | 2.134 |
| Cu-N(2) | 2.090 | 2.097(3) | 2.118 |
| Cu-P(1) | 2.426 | 2.2518(11) | 2.477 |
| Cu-P(2) | 2.428 | 2.2901(11) | 2.492 |
| N(1)-Cu-N(2) | 80.01 | 79.64(13) | 79.99 |
| N(1)-Cu-P(1) | 110.94 | 121.85(9) | 116.97 |
| N(2)-Cu-P(1) | 118.69 | 117.03(10) | 114.27 |
| N(1)-Cu-P(2) | 115.58 | 103.50(10) | 113.93 |
| N(2)-Cu-P(2) | 114.82 | 114.35(9) | 117.98 |
| P(1)-Cu-P(2) | 112.84 | 115.25(4) | 110.83 |
| bpy plane-PCuP plane | N/A | 81.95 | N/A |
| Cu-P(2)-C$^{\dagger}$ | 114.49 | 113.30(15) | 114.52 |

[a] Crystal structure; [b] DFT geometry optimisation with ethanol polarizable continuum; $^{\dagger}$ for **8** [a] C=C35

To produce a calculated UV-Vis spectrum seventy singlet-singlet transitions were calculated with solvent, for each complex in the singlet ground state. Analysis of the components of the TDDFT expansion shows that the majority of the predicted transitions are not well described by a single electron-promotion, but involve transitions between several different orbital pairs (Appendix B). The nature of each electronic transition was determined by visual inspection (Argus Lab[57]) of each contributing molecular orbital as an isosurface map. As for the calculations discussed in Chapter Three, many of the calculated occupied and virtual orbitals were seen to be of mixed character, with the electronic transitions being broadly classified into three distinct types; MLCT, LL and LLCT (see Chapter Three, section 3.3.3).

## 4.2.3 UV-Vis Absorption Spectroscopy

The experimental and calculated UV-Vis absorption spectra for **5** and **8** in ethanol are shown in Figure 1, with the experimental main absorption bands and related extinction coefficients given in Table 2. Both complexes exhibit almost identical absorption behaviour in ethanol to those produced in acetonitrile (Chapter Three; section 3.3.4): strong absorption in the near UV and weaker absorption bands in the visible that are sensitive to the nature of the biypridine substituents.

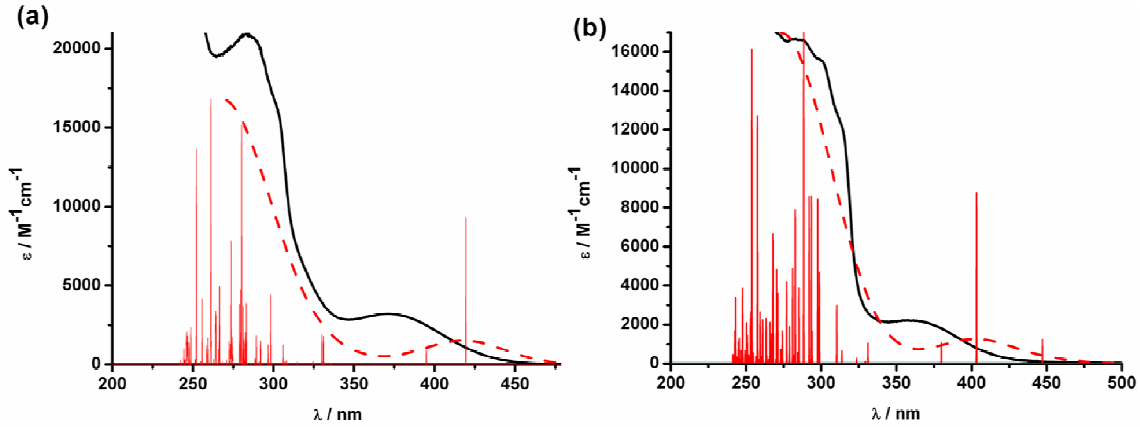


**Fig. 1** Theoretical UV/Vis Absorption Spectra against Experimental Absorption Spectra for (a) **5** and (b) **8**. Where red solid columns = calculated electronic transisiton; red dotted line = calculated spectra; black solid line = solution spectrum of (a) **5** and (b) **8** in EtOH.

**Table 2** Absorbance Measurements for **5** and **8** carried out in EtOH

| | $\lambda_{max}$ / nm ($\varepsilon_{max}$ (x$10^3$ $M^{-1}cm^{-1}$)) | | | |
|---|---|---|---|---|
| | Intraligand transitions | | MLCT | |
| **5** | 250 (32.6) | 280 (27.6) | 375 (3.7) | |
| **8** | 250 (22.3) | 288 (19.0) | 365 (1.9) | 463 (0.1) |

The TDDFT calculations carried out on the optimised singlet ground state structure reproduce the experimental spectra reasonably well in the UV region, predicting a large number of transitions with significant oscillator strength (Figure 1 and Table 3). Again, as seen for the calculations using acetonitrile, examination of the molecular orbitals involved in each transition shows that the UV absorption bands are dominated by $\pi \rightarrow \pi^*$ transitions on both the bipyridine and the POP ligands (Appendix B). Based upon these data the longer wavelength bands have been assigned as Cu(I) to bipyridyl MLCT transfer bands (Table 3 and 4, and Figures 2 and 3). It must be noted that TDDFT has a tendency to over stabilise, and indeed the calculated MLCT absorptions are consistently predicted at lower energy than those seen experimentally.[56, 58]

**Table 3** TD-DFT calculated visible absorption wavelengths for **5** and **8**, indicating the molecular orbitals involved and their relative contribution to the absorption.

| Complex | Main Visible Absorbance / nm | Main Charge Transitions | | Relative contribution |
|---|---|---|---|---|
| | | MO from | MO to | |
| **5** | 454 | HOMO-1 | LUMO | 100% |
| | 419 | HOMO | LUMO | 100 % |
| **8** | 447 | HOMO-1 | LUMO | 41 % |
| | | HOMO | LUMO | 59 % |
| | 403 | HOMO-1 | LUMO | 59 % |
| | | HOMO | LUMO | 41 % |

**Table 4** Percentage contributions from component parts of **5** and **8** to selected molecular orbitals. Also quoted are the calculated energies for these molecular orbitals.

| Complex | MO | MO energy / eV | % Contribution from | | |
|---|---|---|---|---|---|
| | | | Cu-based orbitals | POP-based orbitals | Bpy-based orbitals |
| **5** | HOMO-1 | -6.03 | 64.32 | 8.16 | 27.52 |
| | HOMO | -5.91 | 43.50 | 51.62 | 4.88 |
| | LUMO | -2.33 | 1.47 | 4.89 | 93.64 |
| **8** | HOMO-1 | -6.10 | 61.15 | 19.32 | 19.53 |
| | HOMO | -5.86 | 50.89 | 36.87 | 12.24 |
| | LUMO | -2.26 | 1.44 | 4.17 | 94.39 |

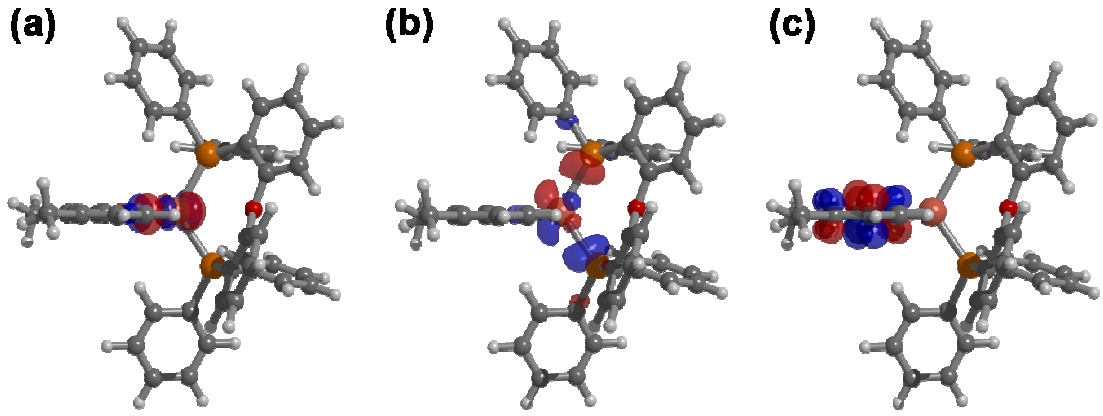


**Fig. 2** Molecular Orbital (a) HOMO-1, (b) HOMO and (c) LUMO for **5**

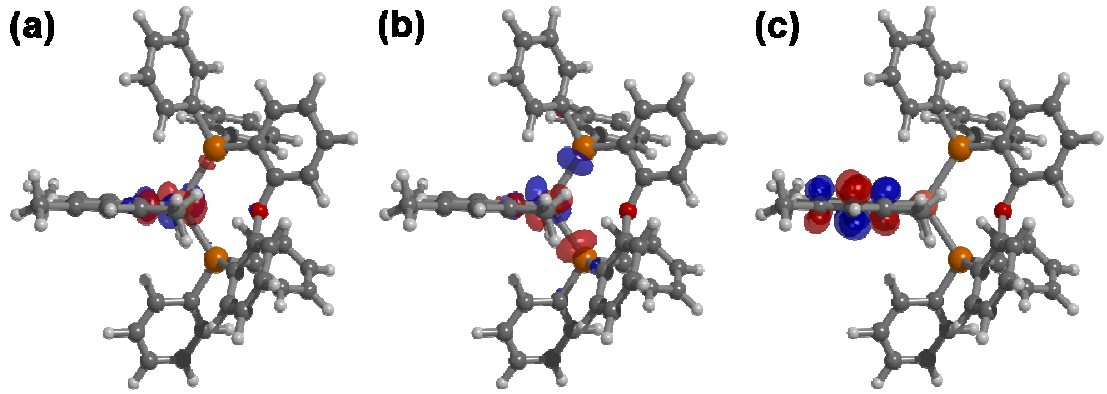


**Fig. 3** Molecular Orbital (a) HOMO-1, (b) HOMO and (c) LUMO for **8**

## 4.2.4 Emission Spectroscopy

Emission spectra were recorded in de-aerated ethanol at 300 K, ethanol at 77 K, and in PMMA at 300 K. Emission maximum, lifetime and quantum yield values are given in Table 5 with full emission spectra given in Figure 4. Excited state decay curves were recorded for **5** and **8** in de-aerated ethanol at 300 K and ethanol at 77 K, yielding mono-exponential decays, and in PMMA at 300 K, yielding decays which are 3-exponential. The shortest component for both complexes in the 3-exponential can be identified as scattered light (around 90 ns) and allows the first 500 ns of the decay to be omitted. The decay can then be fit with a bi-exponential function and the times are given in Table 5. It should be noted here that the decays times are consistent with the

quantum yield values in all cases. The decay time recorded for **5** at 300 K is lower than the threshold range of the instrument used for this study and cannot be taken to be accurate. All decay curves are given in Appendix B. An integrating sphere was used to measure the quantum yield of **8** in de-aerated ethanol at 300 K and for **5** and **8** in PMMA films at 300 K. Measurements were attempted for **5** in de-aerated ethanol at 300 K but the quantum yield was too small to be recorded accurately.

A quantum yield of 65 % was recorded for **8** in PMMA, which is amongst the highest seen in the literature for a Cu(I) complex.[41] This value is considerably larger than the quantum yield recorded in EtOH at 300 K ($\Phi_{PL}$ = 5 %). However these results can only be taken as preliminary results as the decay times are not consistent with the quantum yields; they do not show a significant enough difference between the two complexes (Table 5). Due to this, the experiments need to be repeated to identify the processes taking place when these complexes are put into PMMA. The following hypotheses stand if the quantum yields recorded are the true quantum yields for these complexes. The high quantum yield can be attributed to two principal factors. The PMMA is expected to form a rigid matrix around the complex limiting geometric movement, and this is evidenced by the lower quantum yield observed for **8** in fluid solution. Furthermore, the additional 6,6′-methyl groups present on the tmbpy ligand act to sterically constrain the molecule, limiting the extent of non-radiative decay of the MLCT excited state. This reasoning is supported by the much lower quantum yields observed for **5** under the same conditions (Table 5).

**Table 5** Emission data for **5** and **8** recorded in ethanol and PMMA

| | EtOH 300k de-aerated | | | EtOH 77 K | | | PMMA 300 K | | |
|---|---|---|---|---|---|---|---|---|---|
| | $\lambda_{max}$ / nm | $\tau$ / μs | $\Phi_{PL}$ / % | $\lambda_{max}$ / nm | $\tau$ / μs | $\Phi_{PL}$ / % | $\lambda_{max}$ / nm | $\tau$ / μs | $\Phi_{PL}$ / % |
| **5** | 670 | [a] | <<1 | 615 | 15.3 | [b] | 575 | 37.2[c] | 4 |
| **8** | 575 | 2.6 | 5 | 540 | 72.3 | [b] | 530 | 49.2[c] | 65 |

[a]almost no emission observed; [b] not measured; [c] average value for bi-exponential decay.

**5** emits at longer wavelength than **8** regardless of suspension media and temperature (Figure 4 and Table 5). One possible explanation for this red shifting is that the MLCT excited state of **5** is able to relax to a lower energy structure due to the easier distortion from pseudo-tetrahedral Cu(I) towards pseudo-square planar Cu(II). Another contributing factor could be that the LUMO of **8** is at higher energy due to the increased number of electron donating methyl groups on the tmbpy compared to the dmbpy (present in **5**). This is evidenced in the blue shifted absorption seen for **8** (section 4.2.3), and the more negative reduction potential of **8** compared to **5**; 1.66 V and 1.60 V respectively (Chapter Three, section 3.3.6). The behaviour is also seen when the relative calculated energy gap between the singlet ground state and the triplet excited state of **5** and **8** are compared (in EtOH); 566 nm and 537 nm respectively, perhaps suggesting that this is an intrinsic property of the two complexes.

Upon cooling the ethanolic solutions from 300 K to 77 K, **5** and **8** exhibit a shift in emission peak position, (1272 $cm^{-1}$ and 1127 $cm^{-1}$ respectively) (see Figure 4 (a) and (b)), with the emission at 300 K being the more red shifted. At 77 K there is a restriction on the extent of solvent relaxation, which therefore affects the extent the excited molecule can relax, causing emission to occur at higher energy. The same comparison and explanation can be drawn between the measurements at 300 K in ethanol and at 300 K in PMMA (Figure 4 and Table 5). As predicted by the energy gap law, a lower energy excited state increases the rate of non-radiative decay,[59] therefore reducing the length of the excited state lifetime observed.

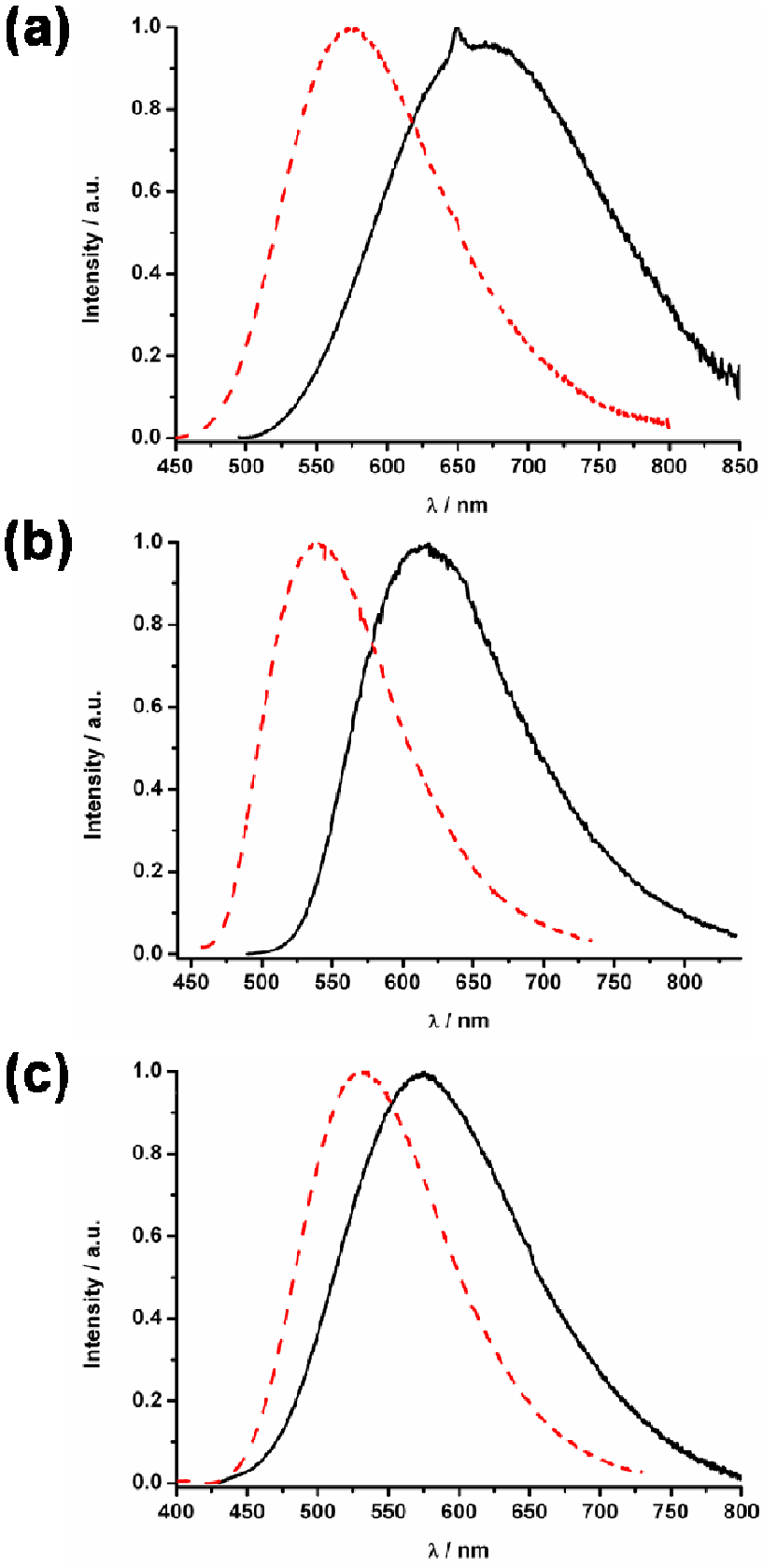


**Fig. 4** (a) 300 K**,** (b) 77 K and (c) PMMA 300 K
Black solid line = spectra for **5**; red dotted line = spectra for **8**

The excited state lifetimes recorded for **8** in ethanol at 77 K are 30 times longer than those recorded at 300 K (Table 5), and can be explained by the phenomenon described above. The excited state lifetimes of **8** are also considerably longer than **5** when compared in all media (Table 5). It is thought that this is due to the reduced freedom of movement the tmbpy ligand has in **8,** compared to the dmbpy ligand in **5**. This greater structural rigidity is caused by the additional methyls in the 6,6′-positions of the bipyridyl ligand in **8**.

### 4.2.5 Structural Analysis; Crystallographic and DFT

Triplet state computational studies were carried out using ArgusLab input structures of **8** and **5,** and starting from the crystal structure of **8**. The optimised geometries generated from the different starting structures revealed little difference between the energy of the structures but there was a difference in the POP orientation, as mentioned already in section 4.2.2. This variation in POP orientation observed in the optimised geometries appears to be dependent upon the orientation of the input structure. If the POP orientation is looked at in isolation, all of the optimised geometries yielded from the same input structure produce the same POP orientation, except in one observed case for **5**, which will be discussed shortly. The phenomenon, coupled with the presence of multiple structures with similar overall energies would suggest the presence of multiple local minima in the energy profiles of these two complexes (see Chapter Two, section 2.3.3). Identification of which of these (if any), is the global minima would require additional computational studies. It should also be noted that the orientation of the POP ligand observed in the DFT geometry optimisation structures (Figure 5) obtained from the crystal structure input structure vary from the orientation present in the crystal structure. This could be indicating that the crystal structure is not the global minima but a local minima that happened to yield crystals under the conditions utilised (see Chapter Three, section 3.5.2). These factors will be discussed in more detail through this section.

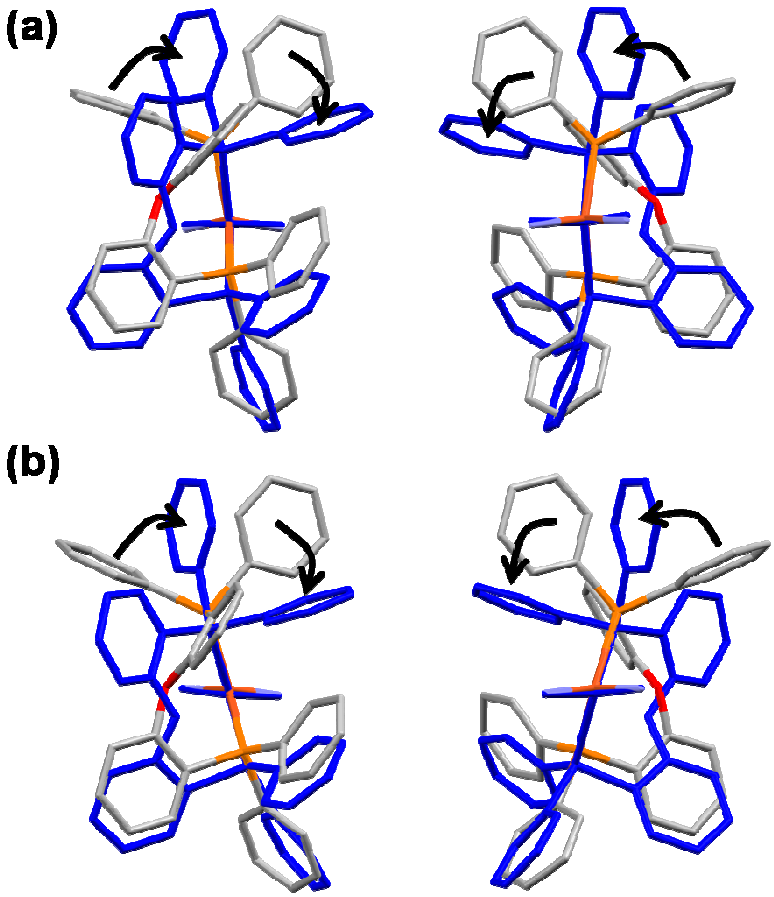


**Fig. 5** Structure Overlays for **8** of (a) the single crystal X-ray structure (multi-coloured structure) with the DFT singlet geometry optimisations for **8** starting from the input ArgusLab structure (blue structure); and (b) the DFT triplet geometry optimisations for **8** starting from the single crystal X-ray strucure (multi-coloured structure) with the DFT triplet geometry optimisations for **8** starting from the inputted ArgusLab structure (blue structure). Overlayed by matching the central metal atom and bipyridyl ligand. Bipyridyl ligand removed (apart from nitrogen atoms) for clarity.

The crystal structure of **8** and the connectivity image of **5** are shown in Figure 6 (a)(i) and (b)(i) respectively, and illustrate the role of POP in the stabilisation of a Cu(I) oxidation state over Cu(II) in air, by acting as a blocking ligand (Chapter Three, section 3.2.2). Here we explore this relationship using DFT methods to manipulate and fix the optimised geometries of **5** and **8** in their triplet states and then re-calculate the fixed manipulated geometries and the new overall complex energies. This manipulation was carried out by fixing the following torsion angles in the input structures which are highlighted in Figure 6 (a)(ii) and (b)(ii) and the atoms involved identified. For the ArgusLab input structures of **5** and **8**, both torsion angles were set to the same value, which are listed in Table 6 (a) and (b). However, due to a non-symmetrical

geometry, the crystal structure input structure of **8** had the two torsion angles set to different values, which are quoted in Table 6 (c). Figure 6 also identifies the bipyridyl plane present in both complexes that was tilted upon varying these torsion angles.

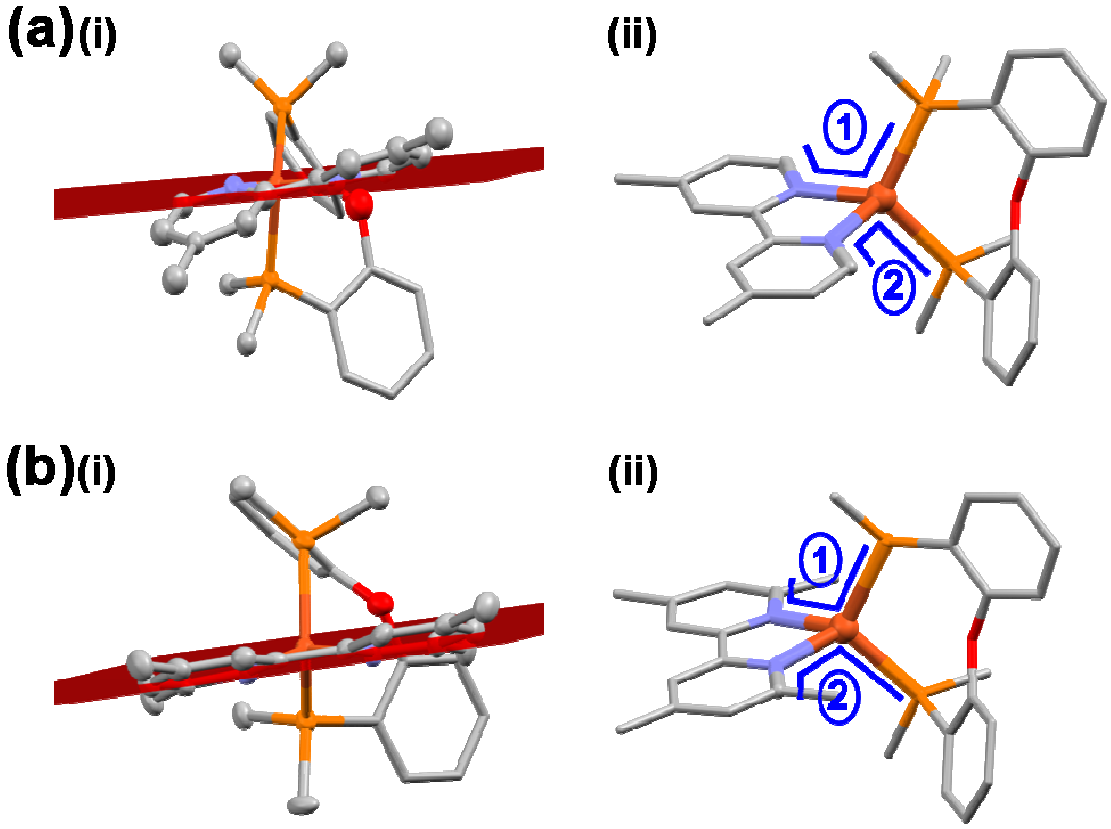


**Fig. 6** Mercury plots of the X-ray crystal structures of (a)(i) **5** and (b)(i) **8**, that highlight the bipyridyl plane; and DFT Geometry Optimised Singlet Ground State Structures of (a)(ii) **5** and (b)(ii) **8**: highlighting torsion bonds manipulated: where the atoms involved in the Argus lab iput structures of **5** and **8** are; in torsion angle 1 = C13-N3-Cu1-P16, and in torsion angle 2 = C6-N2-Cu1-P30; and in the crystal iput structure of **8** are; in torsion angle 1 = C45-N53-Cu1-P55, and in torsion angle 2 = C38-N52-Cu1-P54 . Note thermal ellipsoids are drawn at the 50% probability level. [$BF_4$] counter ion omitted for clarity.

**Table 6** Selected Torsion Angle and Relative Energies data from the DFT geometry optimisation of (a) $[Cu(POP)(dmbpy)]^+$, and (b) $[Cu(POP)(tmbpy)]^+$ starting from the ArgusLab inputted structures, and (c) [Cu(POP)(tmbpy)] starting from the crystal structure; All complexes are in their triplet states, without solvent.

**(a)**

| Torsion angle / º | Relative energy / kJmol$^{-1}$ |
|---|---|
| 60 | +7.21 |
| 65 | +3.77 |
| 70 | +1.31 |
| [a] | 0 |
| 80 | +0.43 |
| 85 | +2.98 |
| 90 | +7.19 |

[a] no manipulation; C13-N3-Cu1-P16 = 75.84º and C6-N2-Cu1-P30 = 75.43º

**(b)**

| Torsion angle / º | Relative energy / kJmol$^{-1}$ |
|---|---|
| 55 | +9.0x10$^6$ |
| 60 | +3.63 |
| 65 | +0.56 |
| [a] | 0 |
| 75 | +1.71 |
| 80 | +4.96 |
| 85 | +1.5x10$^7$ |

[a] no manipulation; C13-N3-Cu1-P16 = 69.91º and C6-N2-Cu1-P30 = 68.44º

**(c)**

| Torsion angle[b] / º | Relative energy / kJmol$^{-1}$ |
|---|---|
| 65 | +4.6x10$^6$ |
| 70 | +3.78 |
| 75 | +0.49 |
| [a] | 0 |
| 85 | +0.77 |
| 90 | +3.29 |
| 95 | +5.1x10$^6$ |

[a] no manipulation; C45-N53-Cu1-P55 = 80.63 º and C38-N52-Cu1-P54 =58.08 º; [b] C45-N53-Cu1-P55 quoted angle

The torsion angle was varied in both directions in 5 ° intervals starting from the unrestricted optimised geometry. Shown in Figure 7 are plots showing how the relative energy of the complexes (**5** and **8**) changes with torsion angle over a 30 ° range (Table 6 (a) and (b)), and identifies the lowest energy structure, and hence a local minima in each case. From this level of computational calculation it is not possible to state whether these are local or global minima. It was possible to calculate optimised geometries for the manipulated structure of **5** over this entire 30 ° range. An optimised structure was also obtained for **5** when the torsion angles were fixed at 55 °, where the complex displays a reduction in overall relative energy (-16.05 kJmol$^{-1}$ compared Table 6 (a)).

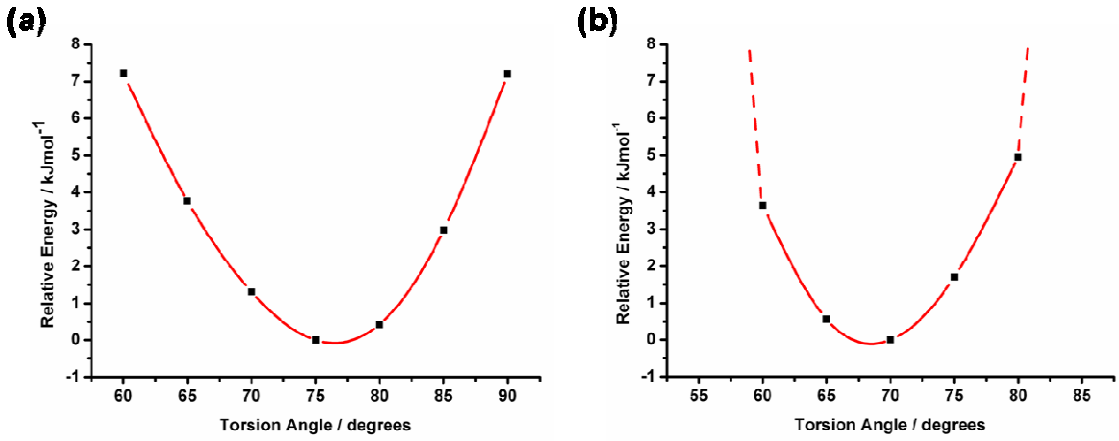


**Fig. 7** Plots of Torsional Angle against DFT calculated Relative Energies for (a) **5** and (b) **8**. Both DFT calculations starting from ArgusLab inputted structures. Note that y-axes are the same scale and x-axes are the same range and scale, and that the curve is there to act as a guide to the eye.

Forcing the dmbpy to adopt this extremely tilted conformation has resulted in a large structural movement of the POP ligand (Figure 8), which originates from an increased angle between the phenyl-O-phenyl backbone of the POP ligand. The explanation behind why this reduction in the energy of the complex occurs is not fully understood at this time. It is could be the result of the structural rearrangement alone but the same effect was not observed when a similar structural rearrangement was imposed upon **8** (Figure 9). Another possibility is that the electronic structure of the complex has changed significantly causing the central metal atom to be more Cu(II) in nature. To determine the cause would require additional computational calculations that were not possible during the timescale of this work.

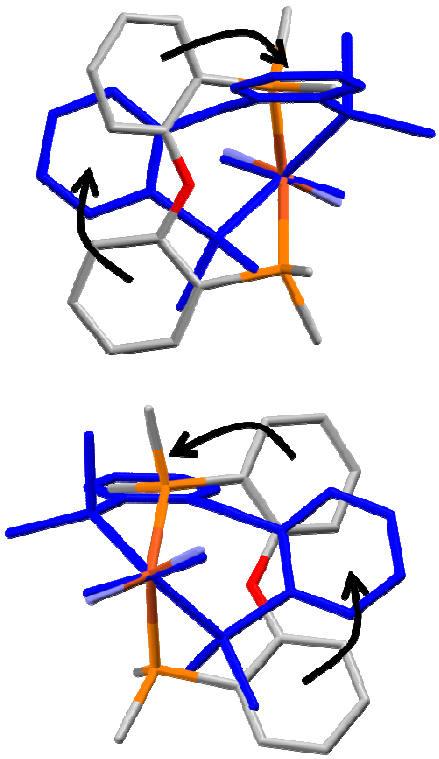

**Fig. 8** Structure Overlays of the DFT triplet geometry optimisations for **5** without restraints (multi-coloured structure) and with a 55 ° torsion angle imposed upon the dmbpy ligand (blue structure). Both started from an inputted ArgusLab structure. Overlayed by matching the central metal atom and bipyridyl ligand. Bipyridyl ligand removed (apart from nitrogen atoms) for clarity.

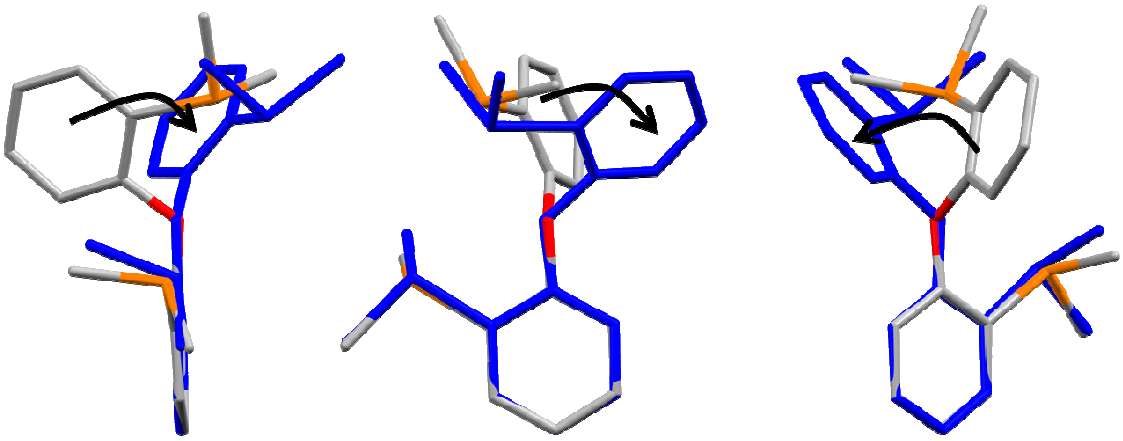

**Fig. 9** Structure Overlays for **8** of the DFT triplet geometry optimisations for **8** starting from the single crystal X-ray structure (multi-coloured structure) with the DFT triplet geometry optimisations for **8** starting from the inputted ArgusLab structure (blue structure). Overalyed by matching the lower phenyl ring in the POP ligand. Bipyridyl ligand, Cu(I) atom and phenyl rings (POPligand) removed for clarity.

Successful optimisation of **8** was not achievable once the torsion angle was increased by 15 ° in either direction as shown in Figure 7 (b); the dotted line indicating that a minimum energy structure was not achieved. Successful optimisation is thought to have not been possible as these manipulated structures place the 6,6′-methyl groups in too close a proximity to the phenyls of the POP ligand, therefore preventing a minimum energy structure being accessible. This demonstrates the increased rigidity enforced upon the structure of **8** compared to that present in **5** as a result of the steric demands of the 6,6′-methyl groups on the bipyridyl ligands. The curvature of the plots suggest a similarity in the flexibility of the two complexes within ± 10 ° of the optimised torsion angle over this limited range (Figure 7). This is being suggested as there is roughly the same energy increase with each 5 ° manipulation of the bpy ligand for both **5** and **8**.

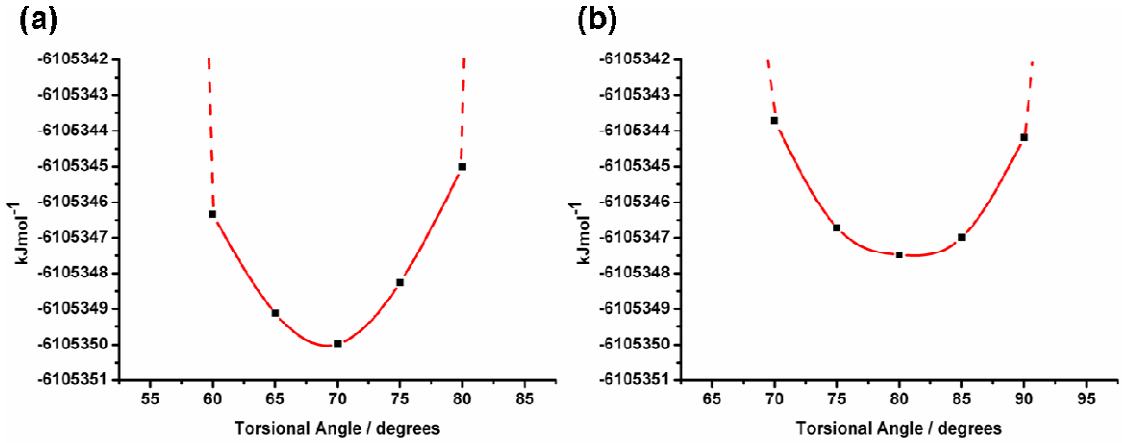


**Fig. 10** Plots of Torsional Angle against DFT calculated Relative Energies for (a) **8** staring from ArgusLab inputted structures and (b) **8** starting from crystal structure. Note that y-axes are the same range and scale and x-axes are the same scale, and that the curve is there to act as a guide to the eye.

Triplet geometry optimisation calculations starting from the crystal structure of **8** indicate that although these optimised geometries differ from those calculated from the ArgusLab input structure (Figure 5), they exhibit similar overall complex energies (Figure 10 and Tables 6 (b) and (c)). The structural difference arises from an increased angle between the phenyl-O-phenyl backbone of the POP ligand (Figure 9) present in the optimised geometry starting from the crystal structure. Their behaviour upon manipulation of the same torsion angles (described in Figure 6) is virtually the same (Figure 10 and Table 6 (c)). Optimised geometries cannot be calculated when the torsion angle is varied by 15 ° or more, and the variation in the energies of those structures calculated covers the same range of < 5 $kJmol^{-1}$.

## 4.3 Conclusions

Shown here is the photophysical characterisation of two Cu(I) complexes: [Cu(POP)(dmbpy)][$BF_4$] (**5**) and [Cu(POP)(tmbpy)][$BF_4$] (**8**). A computational investigation of the two complexes is presented alongside the experimental data in an attempt to gain a deeper understanding about the differences and similarities of their photophyical properties.

The quantum yield data and decay times recorded in PMMA are not consistent for either complex, and hence a firm conclusion cannot be drawn at this time. The experiments need to be repeated for both complexes in order to identify the processes taking place when these complexes are suspended in PMMA.

If the results recorded here are accurate then the observed quantum yield of 65 % (in PMMA), recorded for **8**, would be one of the highest quantum yield reported for a Cu(I)(bipyridyl) complex, and only a small number of Cu(I) complexes produce quantum yields of this magnitude or greater.[41, 44, 60, 61] This is of great interest to the fields of OLEDs and LECs as highly emissive Cu(I) complexes offer a cheaper alternative to those materials currently being exploited.

We have shown that the highly emissive nature of **8** in comparison to **5** (in EtOH), is due to the increased rigidity of the complex imposed by the blocking groups present on the bipyridyl ligands. This has been shown not only experimentally but has been supported by computational manipulation of the structures. Interestingly, **8** has similar flexibility to **5** within a ±10º range of the torsion angle between the ligands but, unlike **5**, is unable to flatten beyond this. This restraint enforced upon the magnitude of the conformational change achievable by **8** explains the order of magnitude increase in emission quantum yield compared with **5**. It may even suggest that even higher quantum yields could be attained with further structural rigidity.

In addition to this we have shown that there are multiple conformations available to the two complexes that involve rearrangement of the POP ligand, and have suggested that all of these conformations are achievable when the complexes are in solution. For **8**, we have identified, through computational studies, two structures of similar energy, and it may be that other conformations of similar energy could also be identified if sufficient time was given.

This work has uncovered what looks to be a complicated energy profile for **5** which is believed to be due to its relative structural flexibility. If this system was hoped to be understand fully it would require further computational investigation.

Our work has highlighted the importance of understanding the link between a complexes structural properties and its emissive behaviour, which is crucial knowledge if improvements are to be made to Cu(I) complexes.

## 4.4 Experimental

The absorption spectra were recorded using a Perkin Elmer Lambda 9 spectrophotometer controlled using the UV/Winlab software.

The experimental emission spectroscopy work was carried out as part of collaboration with Prof. Yersin at the University of Regensburg during a visit made to his laboratory. Dr Anita Jones at the University of Edinburgh provided determination of 3-exponential decay times. Spectroscopic measurements were carried out with **5** and **8** dissolved in ethanol at concentrations of about $10^{-5}$ moldm$^{-3}$. Doped PMMA (polymethylmethacrylate) films were prepared by dissolving the compounds (~1 wt %) and PMMA in $CH_2Cl_2$. Subsequently, the solutions were spin-coated on a quartz plate. Emission spectra at 300 K were measured with a steady-state fluorescence spectrometer (Jobin Yvon Fluorolog 3). Luminescence quantum yields were determined with an integrating sphere (Labsphere, 4P-GPS-033-SL), which exhibits a highly reflective Spectralon inside coating. The estimated relative error is about ±0.10, with $[Ru(bpy)_3]Cl_2$ (bpy=2,2'-bipyridine) in degassed acetonitrile as a standard reference solution ($\Phi_r$=0.062). Fluid solutions were degassed by at least three pump-freeze-thaw cycles with a final vapor pressure at 77 K of ~$10^{-5}$ mbar, while the PMMA films were measured under a nitrogen atmosphere. Experiments at low temperature were carried out in a He cryostat (Cryovac Konti Cryostat IT) in which He gas flow, He pressure, and heating were controlled. A pulsed Nd:YAG laser (IB Laser Inc., DiNY pQ 02) with a pulse width of about 7 ns was applied as excitation source for emission decay time measurements, using the third harmonic at 355 nm (28170 cm$^{-1}$).

Density functional theory calculations were performed using the Gaussian 03 program[51] with the starting structures for **5** and **8** inputted using the builder program Arguslab and the crystal structure coordinates where appropriate. All calculations were carried out using the Becke's

three parameter exchange functional with the Lee-Yang-Parr for the correlation functional (B3LYP),[55] using the Los Alamos National Laboratory basis sets, known as LANL2DZ (developed by Hay and Wadt),[52-54] which comprises ECP + double zeta for copper, and the all-electron valence double zeta basis sets developed by Dunning (D95V) for light atoms.[62] Frequency calculations were carried out to ensure that optimised geometries were minima on the potential energy surface. Solvent effects were included via the self-consistent reaction field (SCRF) method using the polarised continuum model (PCM),[63] with slight modifications to the default cavity parameters to aid convergence. Time-dependent density functional theory (TDDFT) was performed in an ethanol polarisable continuum model, with the first 70 singlet transitions calculated. ArgusLab[57] was used to generate the orbital isosurface maps.

## 4.5 References


1. F. G. Gao and A. J. Bard, *Journal of the American Chemical Society*, 2000, **122**, 7426-7427.
2. S. Y. Kim, J. M. Baik, H. K. Yu and J.-L. Lee, *Journal of Applied Physics*, 2005, **98**, 093707-093707.
3. Q. Pei, G. Yu, C. Zhang, Y. Yang and A. J. Heeger, *Science*, 1995, **269**, 1086-1088.
4. Q. Pei, Yang, G. Yu, C. Zhang and A. J. Heeger, *Journal of the American Chemical Society*, 1996, **118**, 3922-3929.
5. J. D. Slinker, J. A. DeFranco, M. J. Jaquith, W. R. Silveira, Y.-W. Zhong, J. M. Moran-Mirabal, H. G. Craighead, H. D. Abruna, J. A. Marohn and G. G. Malliaras, *Nature Materials*, 2007, **6**, 894-899.
6. B. O'Regan and M. Gratzel, *Nature*, 1991, **353**, 737-740.
7. M. K. Nazeeruddin, *Coordination Chemistry Reviews*, 2004, **248**, 1161-1164.
8. N. Robertson, *ChemSusChem*, 2008, **1**, 977-979.
9. J. G. Vos and J. M. Kelly, *Dalton Transactions*, 2006, 4869-4883.
10. M. K. Nazeeruddin, A. Kay, I. Rodicio, R. Humphry-Baker, E. Mueller, P. Liska, N. Vlachopoulos and M. Graetzel, *Journal of the American Chemical Society*, 1993, **115**, 6382-6390.
11. T. Meyer, *Pure and Applied Chemistry*, 1986, **58**, 1193-1206.
12. A. Juris, V. Balzani, F. Barigelletti, S. Campagna, P. Belser and A. von Zelewsky, *Coordination Chemistry Reviews*, 1988, **84**, 85-277.
13. S. L. Michael and B. Stefan, *Chemistry - A European Journal*, 2006, **12**, 7970-7977.
14. C. Pi-Tai and C. Yun, *Chemistry - A European Journal*, 2007, **13**, 380-395.
15. J. A. G. Williams, *Topics in Current Chemistry*, 2007, **281**, 205-268.
16. C.-M. Che, C.-C. Kwok, S.-W. Lai, A. F. Rausch, W. J. Finkenzeller, N. Zhu and H. Yersin, *Chemistry - A European Journal*, 2010, **16**, 233-247.
17. J. A. Gareth Williams, S. Develay, D. L. Rochester and L. Murphy, *Coordination Chemistry Reviews*, 2008, **252**, 2596-2611.
18. D. R. McMillin, M. T. Buckner and B. T. Ahn, *Inorganic Chemistry*, 1977, **16**, 943-945.
19. N. Armaroli, *Chemical Society Reviews*, 2001, **30**, 113-124.
20. R. M. Williams, L. D. Cola, F. Hartl, J.-J. Lagref, J.-M. Planeix, A. D. Cian and M. W. Hosseini, *Coordination Chemistry Reviews*, 2002, **230**, 253-261.
21. N. Armaroli, G. Accorsi, F. Cardinali and A. Listorti, *Top. Curr. Chem.*, 2007, **280**, 69-115.
22. R. M. Everly and D. R. McMillin, *The Journal of Physical Chemistry*, 1991, **95**, 9071-9075.
23. A. J. Pallenberg, K. S. Koenig and D. M. Barnhart, *Inorganic Chemistry*, 1995, **34**, 2833-2840.
24. M. Ruthkosky, C. A. Kelly, F. N. Castellano and G. J. Meyer, *Coordination Chemistry Reviews*, 1998, **171**, 309-322.
25. M. T. Miller, P. K. Gantzel and T. B. Karpishin, *Inorganic Chemistry*, 1998, **37**, 2285-2290.
26. M. T. Miller, P. K. Gantzel and T. B. Karpishin, *Inorganic Chemistry*, 1999, **38**, 3414-3422.
27. Z. A. Siddique, Y. Yamamoto, T. Ohno and K. Nozaki, *Inorganic Chemistry*, 2003, **42**, 6366-6378.
28. M. Iwamura, S. Takeuchi and T. Tahara, *Journal of the American Chemical Society*, 2007, **129**, 5248-5256.
29. Y. Leydet, D. M. Bassani, G. Jonusauskas and N. D. McClenaghan, *Journal of the American Chemical Society*, 2007, **129**, 8688-8689.

30. O. Green, B. A. Gandhi and J. N. Burstyn, *Inorganic Chemistry*, 2009, **48**, 5704-5714.
31. G. Che, Z. Su, W. Li, B. Chu, M. Li, Z. Hu and Z. Zhang, *Applied Physics Letters*, 2006, **89**, 103511-103513.
32. T. McCormick, W.-L. Jia and S. Wang, *Inorganic Chemistry*, 2005, **45**, 147-155.
33. U. Monkowius, Y. N. Svartsov, T. Fischer, M. Zabel and H. Yersin, *Inorganic Chemistry Communications*, 2007, **10**, 1473-1477.
34. Q. Zhang, J. Ding, Y. Cheng, L. Wang, Z. Xie, X. Jing and F. Wang, *Advanced Functional Materials*, 2007, **17**, 2983-2990.
35. Z. Su, W. Li, B. Chu, M. Xu, G. Che, D. Wang, L. Han, X. Li, D. Zhang, D. Bi and Y. Chen, *Journal of Physics D: Applied Physics*, 2008, **41**, 085103.
36. L. Zhang, B. Li and Z. Su, *The Journal of Physical Chemistry C*, 2009, **113**, 13968-13973.
37. G. Zhang, X. Li, X. Jiang and P. Sun, *Journal of Luminescence*, 2010, **130**, 976-980.
38. D. G. Cuttell, S.-M. Kuang, P. E. Fanwick, D. R. McMillin and R. A. Walton, *Journal of the American Chemical Society*, 2001, **124**, 6-7.
39. S.-M. Kuang, D. G. Cuttell, D. R. McMillin, P. E. Fanwick and R. A. Walton, *Inorganic Chemistry*, 2002, **41**, 3313-3322.
40. Q. Zhang, Q. Zhou, Y. Cheng, L. Wang, D. Ma, X. Jing and F. Wang, *Advanced Materials*, 2004, **16**, 432-436.
41. N. Armaroli, G. Accorsi, M. Holler, O. Moudam, J. F. Nierengarten, Z. Zhou, R. T. Wegh and R. Welter, *Advanced Materials*, 2006, **18**, 1313-1316.
42. N. Armaroli, G. Accorsi, G. Bergamini, P. Ceroni, M. Holler, O. Moudam, C. Duhayon, B. Delavaux-Nicot and J.-F. Nierengarten, *Inorganica Chimica Acta*, 2007, **360**, 1032-1042.
43. H. Xia, L. He, M. Zhang, M. Zeng, X. Wang, D. Lu and Y. Ma, *Optical Materials*, 2007, **29**, 667-671.
44. W. Sun, Q. Zhang, L. Qin, Y. Cheng, Z. Xie, C. Lu and L. Wang, *European Journal of Inorganic Chemistry*, **2010**, 4009-4017.
45. Y. Li, F. Ji-Kang, R. Ai-Min, Z. Ming, M. Yu-Guang and L. Xiao-Dong, *European Journal of Inorganic Chemistry*, 2005, **2005**, 1867-1879.
46. L. Zhang, B. Li and Z. Su, *Langmuir*, 2009, **25**, 2068-2074.
47. P. Ghosh and T. G. Spiro, *Journal of the American Chemical Society*, 1980, **102**, 5543-5549.
48. O. Moudam, LCC-Toulouse, France, 2007.
49. C. L. Linfoot, P. Richardson, T. E. Hewat, O. Moudam, M. M. Forde, A. Collins, F. White and N. Robertson, *Dalton Transactions*, 2010, **DOI: 10.1039.C0DT00190B**.
50. C. L. Linfoot, P. Richardson, T. E. Hewat, O. Moudam, M. M. Forde, A. Collins, F. White and N. Robertson, With Referees.
51. M. J. Frisch, G. W. Trucks, H. B. Schlegel, G. E. Scuseria, M. A. Robb, J. R. Cheeseman, J. A. M. Jr., T. Vreven, K. N. Kudin, J. C. Burant, J. M. Millam, S.S.Iyengar, T. J., V. Barone, B. Mennucci, M. Cossi, G. Scalmani, N. Rega, G. A. Petersson, H. Nakatsuji, M. Hada, M. Ehara, K. Toyota, R. Fukuda, J. Hasegawa, M. Ishida, T. Nakajima, Y. Honda, O. Kitao, H. Nakai, M. Klene, X. Li, J. E. Knox, H. P. Hratchian, J. B. Cross, V. Bakken, A. C., J. Jaramillo, R. Gomperts, R. E. Stratmann, O. Yazyev, A. J. Austin, R. Cammi, C. Pomelli, J. W. Ochterski, P. Y. Ayala, K. Morokuma, G. A. Voth, P. Salvador, J. J. Dannenberg, V. G. Zakrzewski, S. Dapprich, A. D. Daniels, M. C. Strain, O. Farkas, D. K. Malick, A. D. Rabuck, K. Raghavachari, J. B. Foresman, J. V. Ortiz, Q. Cui, A. G. Baboul, S. Clifford, C. J., B. B. Stefanov, G. Liu, A. Liashenko, P. Piskorz, I. Komaromi, R. L. Martin, D. J. Fox, T. Keith, M. A. Al-Laham, C. Y. Peng, A. Nanayakkara, M. Challacombe, P. M. W. Gill, B. Johnson, W. Chen, M. W. Wong, C. Gonzalez and J. A. Pople, *Gaussian 03, Revised C.02, Gaussian, Inc., Wallingford, CT*, 2004.
52. W. R. Wadt and P. J. Hay, *The Journal of Chemical Physics*, 1985, **82**, 284-298.

53. P. J. Hay and W. R. Wadt, *The Journal of Chemical Physics*, 1985, **82**, 270-283.
54. P. J. Hay and W. R. Wadt, *The Journal of Chemical Physics*, 1985, **82**, 299-310.
55. A. D. Becke, *The Journal of Chemical Physics*, 1993, **98**, 5648-5652.
56. L. Yang, J.-K. Feng, A.-M. Ren, M. Zhang, Y.-G. Ma and X.-D. Liu, *European Journal of Inorganic Chemistry*, 2005, **2005**, 1867-1879.
57. M. A. Thompson, http://www.arguslab.com.
58. K. L. McCall, J. R. Jennings, H. Wang, A. Morandeira, L. M. Peter, J. R. Durrant, L. J. Yellowlees, J. D. Woollins and N. Robertson, *Journal of Photochemistry and Photobiology A: Chemistry*, 2009, **202**, 196-204.
59. A. Lavie-Cambot, M. Cantuel, Y. Leydet, G. Jonusauskas, D. M. Bassani and N. D. McClenaghan, *Coordination Chemistry Reviews*, 2008, **252**, 2572-2584.
60. M. T. Miller, P. K. Gantzel and T. B. Karpishin, *Journal of the American Chemical Society*, 1999, **121**, 4292-4293.
61. F. Wei, L. Fang and Y. Huang, *Inorganica Chimica Acta*, **363**, 2600-2605.
62. T. H. Dunning, H. F. Schaefer and P. J. Hay, *in Modern Theoretical Chemisrty, Ed III*, Plenum, New York, 1976.
63. A. Vleck Jr and S. Zális, *Coordination Chemistry Reviews*, 2007, **251**, 258-287.

# 5. Chapter Five:

# Cu(pmppE)-based

# Complexes

## 5.1 Introduction

Chapters Three and Four of this work have thoroughly explored a series of Cu(I) complexes with the general formula [Cu(POP)(bpy)][$BF_4$]. The overall conclusion reached was that while the POP ligand forces the complex to maintain the required tetrahedral geometry through the steric constraints it exerts on the complex, POP is not the ideal choice of ligand for a DSSC sensitiser as the absorption wavelengths and oxidation potentials observed from the series are not suitable; MLCT $\lambda_{max}$ = ~400nm with $\varepsilon_{max}$ = ~2000 $M^{-1}cm^{-1}$, and oxidation potential = +1.4 V (Chapter Three). Chapter Four then goes on to explore the emissive properties of two of these complexes; [Cu(POP)(dmbpy)][$BF_4$] and [Cu(POP)(tmbpy)][$BF_4$]. The Cu(POP) complexes were a series of charged species, each complex having a $BF_4^-$ counter ion. However, inspection of the literature shows there to be a preference for DSSC sensitisers to be neutral complexes, and of further note, if these complexes were to be exploited for their emissive properties then the same is seen to be true; neutral complexes dominate the literature.

The main focus of this chapter is DSSC-driven and is therefore the replacement of the POP ligand with another co-ligand capable of providing adequate steric constraint to the complex, absorbing significant quantities of visible light, being synthetically simple to produce and yielding a neutral Cu(I) complex. A secondary focus of the work was to explore the possibility of synthesising new highly emissive Cu(I) complexes.

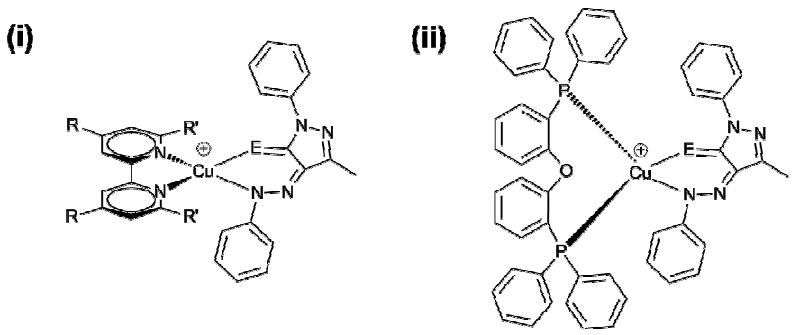


**Fig. 1** Structures of all complexes attempted for this Chapter; where R=Me or $CO_2H$; R'=H, Me or Ph; E = S and O.

The ligand system selected to replace POP is an hydrazono pyrazol-5-thiones(ones) of the general form (pmppE): 1-phenyl-3-methyl-4-phenylhydrazono-pyrazol-5-thione (pmppT) and 1-phenyl-3-methyl-4-phenylhydrazono-pyrazol-5-one (pmppO) (Figure 1). These hydrazono pyrazol-5-thiones(ones) have been used in the literature to promote a tetrahedral geometry for Zn(II) and to form neutral complexes,[1-3] and have been applied in the dye,[4-6] pharmaceutical,[7, 8] and metal extraction[9-13] industries.

Reported in this work is the first use of these ligands for application in a heteroleptic Cu(I) complex and the first time they have been connected with DSSC research. The synthesis of a family of [Cu(I)(pmppE)(bipyridine)] complexes (with varying 4,4′- and 6,6′-substitutents), and Cu(I)(pmppE)(POP) complexes was attempted (Figure 1). For the [Cu(I)(pmppE)(bipyridine)] complexes the 6,6′-substitutents were varied to investigate the blocking function of the pmppE complexes (Figure 1. R'=H, Me or Ph). The 4,4′-methyl analogues were attempted alongside the 4,4′-acids, despite not being directly applicable for use in a DSSC, as they can give insight into the properties of the acid complexes while being more convenient for detailed characterisation due to better solubility. However, successful synthesis was only achieved for those complexes given in the reaction schemes in Figure 2, and these will be discussed in more detail in the Results and Discussion section.

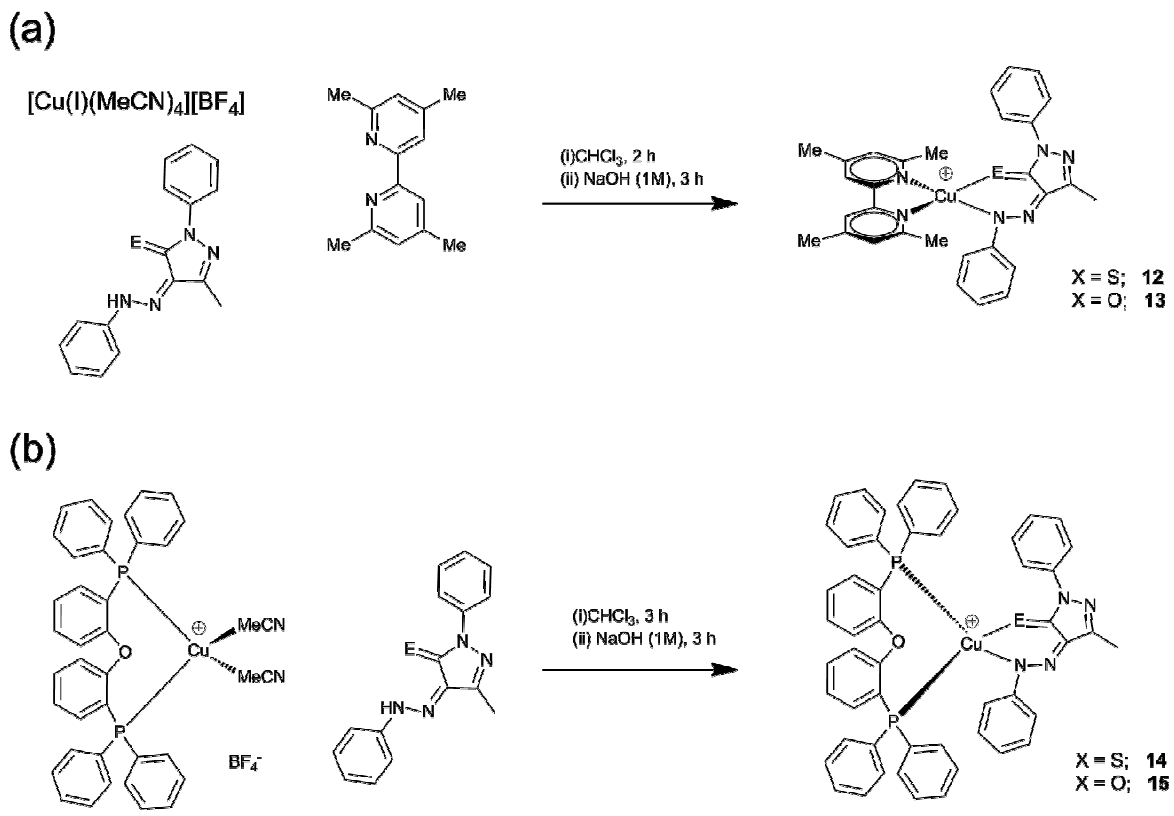


**Fig. 2** Synthetic Reaction Scheme for Complexes reported in this Chapter.
All procedures carried out under a nitrogen atmosphere

The electrochemical and photophysical properties of the complexes were investigated using UV/Vis spectroscopy, electrochemistry and fluorescence spectroscopic studies. The ligands pmppT and pmppO were synthesised by Dr Andrew Smith (working with Prof. Tasker at the University of Edinburgh)[2] and characterised during this research to facilitate assignment of the electrochemical and spectroscopic properties of the Cu(I) series outlined here.

## 5.2 Results and Discussion

### 5.2.1 Syntheses

The ligands 4,4′,6,6′-tetramethyl-2,2′-bipyridine (tmbpy), and 4,4′-dimethyl-6,6′-diphenyl-2,2′-bipyridine (dpdmbpy), and the starting complex $[Cu(MeCN)_4][BF_4]$ and were synthesised using modified literature methods as described in the Experimental section. The ligand bis[2-(diphenylphosphanyl)phenyl] ether (POP) and the starting complex $[Cu(POP)(MeCN)_2][BF_4]$ were synthesised by Dr Omar Moudam. Ligands pmppT and pmppO were synthesised by Dr Andrew Smith. The reaction schemes shown in Figure 2 demonstrate how the Cu(I) complexes were synthesised by simple addition, with stirring, of the relevant starting materials in stoichiometric amounts, to the appropriate solvent at room temperature. The methyl-substituted bipyridyl analogues have been synthesised despite not being directly applicable for use in a DSSC, as they can give insight into the properties of the acid complexes while being more convenient for detailed characterisation due to better solubility. The Cu(I) complexes **12 - 15** were characterised by $^1H$ NMR, ESI-MS, +FAB-MS and elemental analysis, verifying molecular structures.

In addition there were also attempts to synthesise [Cu(pmppE)(dmbpy)] and [Cu(pmppE)(dpdmbpy)] (Figure 1 (i) and (ii)). In the case of the [Cu(pmppE)(dmbpy)] pair of complexes we believe neither pmppE ligand is able to supply the required steric constraint to maintain a Cu(I) tetrahedral geometry. For the [Cu(pmppE)(dpdmbpy)] analogue however we believe the argument is the opposite; due to excessive steric constraints, the synthesis is not possible. These complexes, although not successfully isolated here, were not abandoned, and will be discussed again in Chapter Seven.

## 5.2.2 Structure Analysis

The single crystal structure of **15** was determined during this work allowing insight into the structural features of these complexes and of the pmppE ligands, in particular the blocking group effects. The structure of **15** is shown in Figure 3 with selected structural parameters given in Tables 1 and 2. The structure illustrates the stabilisation of the Cu(I) oxidation state with the angle between the O-C-C-N-N (pmppO) plane and the P-Cu-P (POP) plane being 86.60º, giving a pseudo-tetrahedral geometry (Table 1 (i)). Additionally, the bite angle of POP in each case remains comparatively close to that expected for an ideal tetrahedron (Table 1 (i)). As described in Chapter Three, the blocking functionality of POP arises as one of the phenyl rings attached to the phosphorus atoms is constrained to be over the pmppO ligand preventing structural distortion demonstrated by the distance between O-C-C-N-N plane - $H_{2A}$ (Figure 3 and Table 1(ii)). This geometrical arrangement of the chelating ring (Cu-P-C-C-O-C-C-P) described here (Table 1 (ii)), is consistent with those listed in Chapter Three section 3.2.2.

Inspection of this structure may also give us insight into why synthesis of the dmbpy analogues was not possible. It was hoped that the blocking functionality of the pmppE ligands provided by the phenyl group attached to the hydrazono nitrogen atom would be adequate to sterically constraint the complex and maintain tetrahedral geometry. However inspection of the crystal structure of **15** reveals that the Cu-N(15B)-C(16B) bond angle is 120.59(11) placing the phenyl group in such a conformation that a pseudo-square planar Cu(II) complex would be accessible and hence the predicted product.

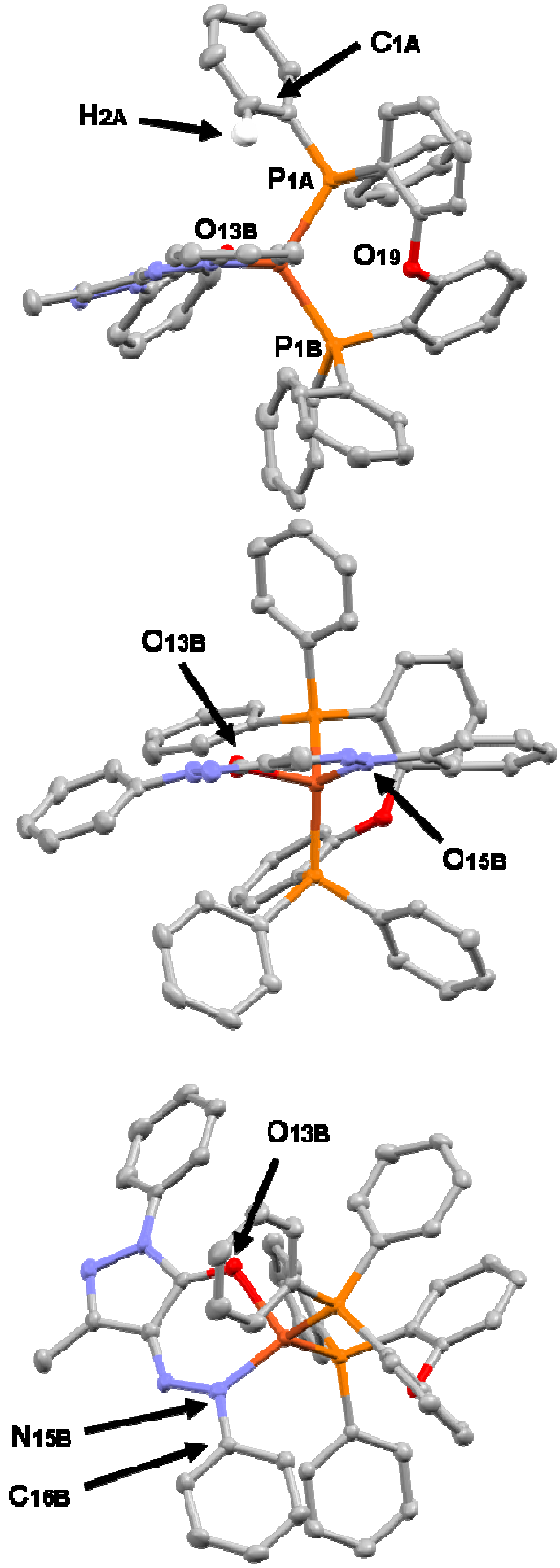


**Fig. 3** Mercury plots of **15**. Thermal ellipsoids are drawn at the 50% probability level.

**Table 1** Selected bond lengths (Å) and angles (deg) for single crystal X-ray crystallography data for **15**.

| (i) | **15** |
|---|---|
| Cu-N(15B) | 2.0293(15) |
| Cu-O(13B) | 2.0864(12) |
| Cu-P(1A) | 2.2596(5) |
| Cu-P(2A) | 2.2552(5) |
| N(15B)-Cu-O(13B) | 94.66(5) |
| N(15B)-Cu-P(1A) | 115.29(4) |
| O(13B)-Cu-P(1A) | 101.38(4) |
| N(15B)-Cu-P(2A) | 120.26(4) |
| O(13B)-Cu-P(2A) | 107.70(4) |
| P(1A)-Cu-P(2A) | 113.305(18) |
| O-C-C-N-N plane-P-Cu-P plane | 86.60 |
| Cu-P(2A)-C(1A) | 113.47(6) |
| Cu-N(15B)-C(16B) | 120.59(11) |

| (ii) | **15** |
|---|---|
| O-C-C-N-N plane – H(2A) | 2.655 |
| a† | 117.22(5) |
| b† | 119.68(13) |
| c† | 119.62(14) |
| d† | 119.30(12) |
| e† | 115.32(14) |
| f† | 117.85(13) |
| g† | 109.75(6) |

† Chapter Three Figure 6 for angle definitions

The ligand pmppT and pmppO are being considered in this work as being predominately π-donating in nature and it is being suggested this donation is going to the other ligand (bpy or POP). This assignment has been made after comparison with crystal structures of our complex (**15)**, pmppO,[14] and selected homoleptic Cu(II)- and Zn(II)-(X^N) complexes,[2, 15] (Table 2 and Figure 4). The O-C1 and N1-N2 bond distances (Table 2) of uncoordinated pmppO suggests that the hydrazono-thione(ketone) tautomer is preferred (Figure 5).[14] Dr Smith reported that [Zn(II)(pmppT)$_2$], due to the significant reduction in the N1-N2 bond length, adopts more of an imino-thiol tautomeric conformation (Table 2 and Figure 5),[2] and that the hydrazono-N is more π-accepting in character than it was in the free ligand. The N1-N2 bond length in **15** shortens to the same extent as the analogous Zn(II) and Cu(II) complexes (Table 2) suggesting that despite the hydrazono-N becoming more π-accepting in nature it is not the dominant ligand characteristic.

**Table 2** Selected bond lengths (Å) for single crystal X-ray crystallography data for free pmppO[14], **15** and [Cu(II)(pmppO)$_2$],[15] [Zn(II)(pmppO)$_2$],[15] and [Zn(pmppT)$_2$].[2] Atom numbers defined in Figure 4.

| Bond distance / Å | pmppO | **15** | [Cu(II)(pmppO)$_2$] | [Zn(II)(pmppO)$_2$] | [Zu(II)(pmppT)$_2$] |
|---|---|---|---|---|---|
| E – C1 | 1.230(3) | 1.278(2) | 1.281(6) | 1.256(2) | 1.711(4) |
| C1 – C2 | 1.468(4) | 1.414(5) | 1.422(8) | 1.432(2) | 1.426(6) |
| C2 – N1 | 1.307(3) | 1.344(5) | 1.338(7) | 1.355(2) | 1.351(5) |
| N1 – N2 | 1.318(3) | 1.297(2) | 1.295(6) | 1.292(2) | 1.288(5) |

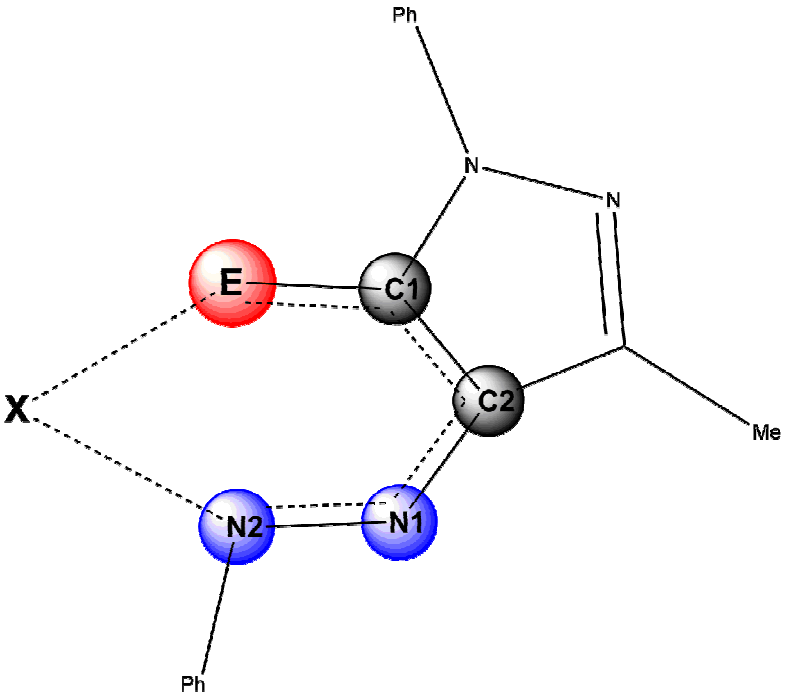


**Fig. 4** Schematic of the pmppE chelate ring.

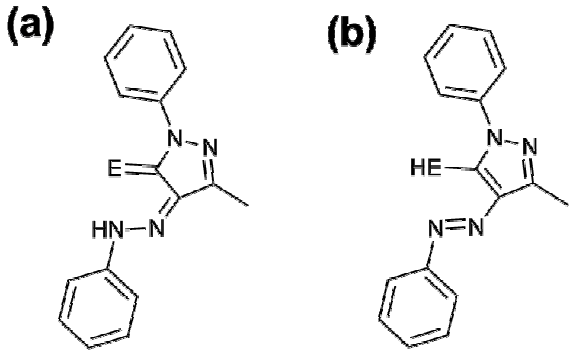


**Fig. 5** The tautomeric forms of the pmppE ligands;
(a) hydrazono-thione(ketone) tautomer; and (b) imino-thiol tautomer

## 5.2.3 UV/Vis Absorption Spectroscopy

The experimental UV-Vis absorption spectra for **12** – **15** are shown in Figures 6 and 7 alongside their appropriate pmppE ligand. The main absorption bands and related extinction coefficients for all species investigated are given in Table 3.

From previous work,[16] it is known that the absorption peak of the $\pi \rightarrow \pi^*$ intra-bipyridine transition occurs between 300-320nm. Figure 6 (a) and (b) clearly show that there is no peak in this region for the free pmppO ligands but that both **12** and **13** exhibit absorption peaks between 300 and 320 nm, consistent with the successful synthesis of a bipyridyl containing complex. Previous characterisation of the precursor $[Cu(POP)(MeCN)_2][BF_4]$ (Chapter Three; section 3.3.4) demonstrates POP is present in **14** and **15** by the presence of an absorption peak at ~290 nm which corresponds to a $\pi \rightarrow \pi^*$ intra-POP transition (Table 3).

**Table 3** Absorbance Measurements for all Complexes.

| Complex | Absorption / $\lambda_{max}$ (nm) ($\varepsilon_{max}$(x$10^3$$M^{-1}$$cm^{-1}$)) | | | | | |
|---|---|---|---|---|---|---|
| | Intraligand Transitions | | | | | MLCT |
| pmppT | 255 (16.7) | | | 399 (21.2) | 491 (4.0) | |
| pmppO | 252 (19.1) | | | 393 (20.9) | | |
| $[CuPOP(MeCN)_2]^+$ | | 272 (14.2) | | | | |
| **12** | 251 (22.1) | | 302 (22.4) | 370 (19.2) | 459 (5.5) | 560 (2.6) |
| **13** | 251 (27.5) | | 303 (12.3), 316 (12.7) | 390 (23.0) | | |
| **14** | 252 (29.4) | 288 (18.5) | | 357 (14.6) | 445 (6.3) | |
| **15** | 251 (31.5) | 289 (21.0) | | 345 (19.2) | | 465 (9.3) |

pmppT,pmppO and **12** - **15** carried out in DCM; $[CuPOP(MeCN)_2]^+$ carried out in MeCN

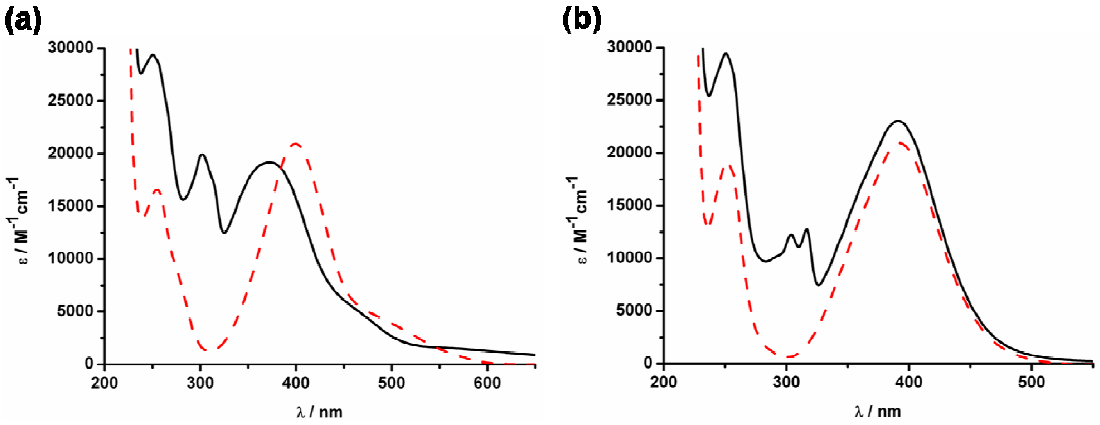


**Fig. 6** Absorbance Spectra for (a) Solid black line = **12** and red dashed line = pmppT;
(b) Solid black line = **13** and red dashed line = pmppO; in DCM

The absorption spectra of **12** and **13** are dominated by the ligand absorptions, in particular the pmppE peak at ~380 nm (Figure 6 and Table 3) which shifts little upon complexation. The most likely explanation for this behaviour is that the frontier orbitals of the π-donor pmppE ligands do not overlap well with the Cu(I) d-orbitals. This would result in limited orbital mixing between the closed shell Cu(I) metal atom and the π-donor pmppE ligand and the interaction possibly being only electrostatic in nature. This effect is more pronounced in the case of **13** where there is little variation from the absorption spectrum of pmppO, suggesting the oxygen orbitals mix to a lesser extent with the soft Cu(I) orbitals than those of the softer sulphur present in **12**. A lower energy transition is observed for **12** which has been assigned as a MLCT absorption as the peak position ($\lambda_{max}$ = 560 nm) does not correspond to any ligand based transitions (Table 3).

Inspection of the spectra for **14** and **15** suggests that there is increased mixing of the pmppE frontier orbitals and the Cu(I) d-orbitals as there is significant shifting of the pmppE absorption peaks upon complexation, and in the case of **15**, the introduction of a peak at 465 nm which could be assigned as MLCT.

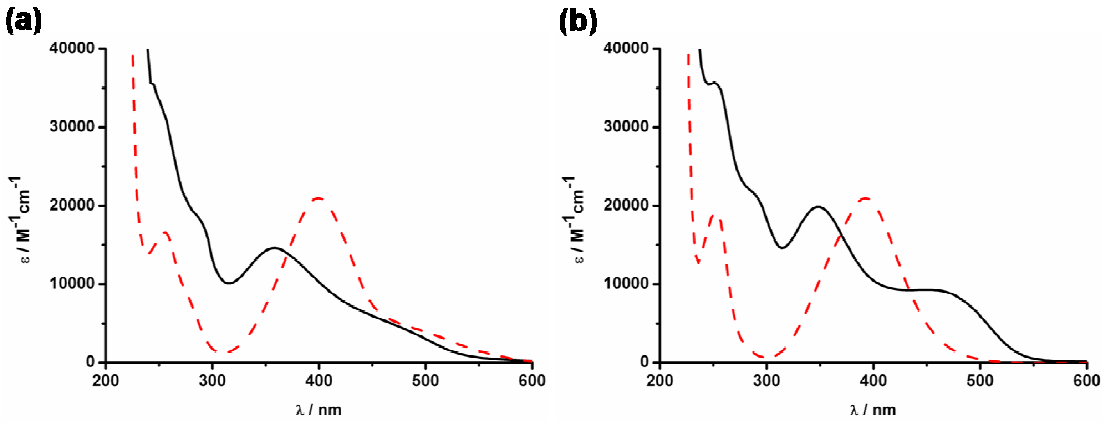


**Fig. 7** Absorbance Spectra for (a) Solid black line = **14** and red dashed line = pmppT; (b) Solid black line = **15** and red dashed line = pmppO; in DCM

## 5.2.4 Electrochemistry

The redox potentials for all complexes are shown in Table 4 with selected cyclic voltammograms shown in Figures 8, 9 and 10. For **12** and **13** the redox processes at ~+0.1 V that exhibit reduced currents compared to subsequent peaks, have been assigned to small quantities of impurities.

**Table 4** Oxidation and Reduction Potentials for all Complexes. pmppT, pmppO and **12 – 15** in solutions of 0.3M $TBABF_4$/DCM

| Complex | $E_{½}$ (V vs. Ag/AgCl) | | | | | |
|---|---|---|---|---|---|---|
| | $E_{Red.2}$ | $E_{Red.\ 1}$ | $E_{Ox.1}$ | $E_{Ox\ 2}$ | $E_{Ox.3}$ | $E_{Ox.4}$ |
| pmppT | -1.173 | -0.865 | | | +1.103 | +1.526 |
| pmppO | | -1.143 | | | +1.610 | +1.965 |
| **12** | | -1.648 | +0.485 | +0.817 | +1.063 | +1.396 |
| **13** | | | +0.373[a] | +0.838 | | |
| **14** | | -0.751 | +0.690 | | +1.124 | +1.507 |
| **15** | | -1.015 | +0.706 | | +1.166 | +1.569 |

All potentials vs. Ag/AgCl; recorded at 298K; All peaks are electrochemically irreversible and values shown represent peak potential except from; a = Peaks are electrochemically reversible and values shown represent E½;

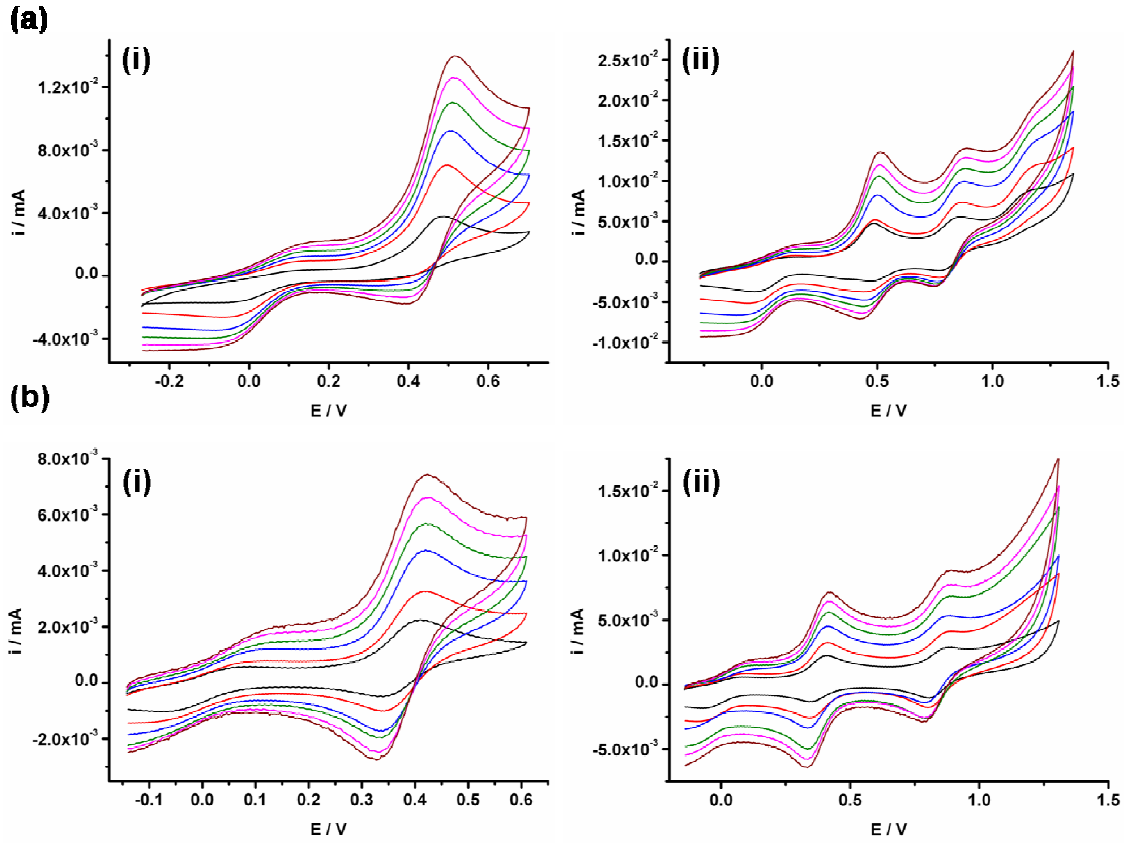


**Fig. 8** Cyclic Voltammogram of (a) **12** and (b) **13** showing oxidation peaks with scan rates of 0.1 (black line), 0.2 (red line), 0.4 (blue line), 0.6 (green line), 0.8 (magenta line) and 1.0 (wine line) $Vs^{-1}$ in 0.3M $TBABF_4$/DCM at 298K

The first oxidation potential for the [Cu(pmppO)(tmbpy)] complexes; **12** and **13**, occurs at ~+0.4 V and has been assigned as a Cu(I)/Cu(II) redox process (Table 4 and Figure 8). This process for **13** is electrochemically and chemically reversible (see Chapter Two; section 2.1 for definition) and for **12** the process suggests chemical reversibility. This behaviour would suggest that there is little geometric change and that the complex does not degrade upon oxidation to Cu(II). Our explanation for this is that the π-donating effect of pmppE ligand is acting to stabilise the Cu(II) oxidation state. If our description is accurate the inclusion of π-donors could be explored in more detail as for long-term DSSC operation sensitisers should ideally exhibit chemically reversible oxidations.

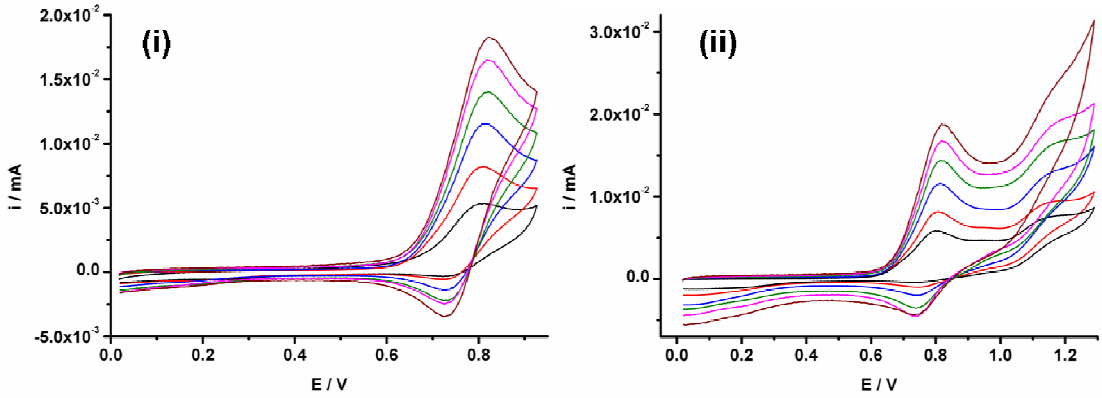


**Fig. 9** Cyclic Voltammogram of **15** showing oxidation peaks with scan rates of 0.1 (black line), 0.2 (red line), 0.4(blue line), 0.6 (green line), 0.8 (magenta line) and 1.0 (wine line) $Vs^{-1}$ in 0.3M $TBABF_4$/DCM at 298K

The corresponding Cu(I)/Cu(II) oxidation for the POP containing complexes (**14** and **15**) occurs at around +0.7 V (Figure 9 and Table 4). This increase in Cu(I) oxidation potential compared to **12** and **13** is due to the orbital interaction with the electron withdrawing POP ligand.[17] It has been concluded from Chapter Three that the POP ligand is more electron withdrawing than tmbpy as it is harder to oxidise $[Cu(POP)(tmbpy)][BF_4]$ than $[Cu(tmbpy)_2][BF_4]$; +1.41 V versus +0.77 V. The lower oxidation peak potential seen for **14** and **15** further suggests that the pmppE ligands are good donors as the oxidation potential is less positive than that required to oxidise the $[Cu(POP)(bpy)][BF_4]$ series presented in Chapter Three; ~+0.7 V versus ~1.4 V respectively. This is a positive outcome as the oxidation potentials seen for the $[Cu(POP)(bpy)][BF_4]$ complexes was significantly too positive for an optimised DSSC sensitiser.

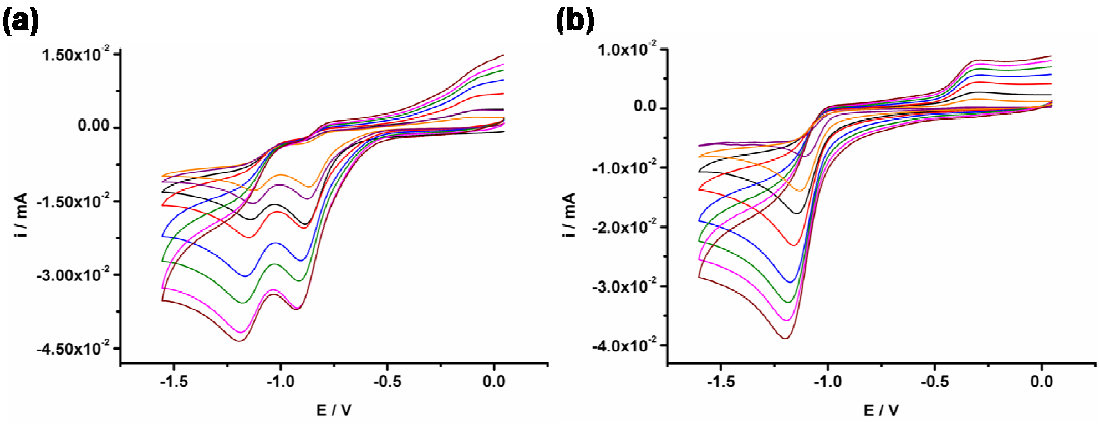


**Fig. 10** Cyclic Voltammogram of (a) pmppT and (b) pmppO showing reduction peaks with scan rates of 0.1 (black line), 0.2 (red line), 0.4(blue line), 0.6 (green line), 0.8 (magenta line) and 1.0 (wine line) $Vs^{-1}$ in 0.3M $TBABF_4$/DCM at 298K

Upon comparison with literature,[16] and with the reduction potentials for the free ligands (Table 4 and Figure 10), the reductions exhibited by **12** and **13** have been assigned as being bipyridyl-ligand based, while those of **14** and **15** are being assigned as being pmppE-based reductions (Table 4). These electrochemical results support the expectation that the charge transfer transition will have directionality in the desired direction; towards the carboxylate groups (on the bipyridyl ligand) that bind to $TiO_2$.

## 5.2.5 Emission Spectroscopy

Excitation and emission spectra were investigated for **12** – **15** in ethanol at 77 K and for comparison, for the free ligands pmppT and pmppO. pmppT and pmppT were found to be emissive only at 77 K and not at room temperature maxima values are given in Table 5. **12**, **13**, **14** and **15** were found to be non-emissive at room temperature and 77 K.

**Table 5** Excitation and Emission Measurements for pmppT and pmppO. In EtOH at 77 K

| Compound | Excitation Maxima $\lambda_{max}$ / nm | Emission Maxima $\lambda_{max}$ / nm |
|---|---|---|
| pmppT | 464[a] | 560[a] |
| pmppO | 450[a] | 576[a] |

[a]weakly emissive relative to other peaks shown in this table.

As discussed throughout this work, to function as a DSSC sensitiser, a complex must possess a sufficiently long excited-state lifetime to enable charge injection into the semiconductor conduction band and the observation of photoluminescence is generally taken as an indication that the excited-state lifetime will be sufficiently long. As none of these complexes exhibit emission we are concluding that when pmppE ligands are not as successful "blocking" ligands as POP. They do not provide the same extent of structural rigidity to the complex as the POP ligand as both [Cu(POP)(dmbpy][$BF_4$] and [Cu(POP)(tmbpy)][$BF_4$] exhibited emissive behaviour at room temperature (**5** and **8**; Chapters Three and Four).

Complexes **14** and **15** were synthesised in the hope of achieving highly emissive Cu(I) complexes but as can be seen from by the lack of emission, this was not the result. This is in sharp contrast with the emissive behaviour of [Cu(POP)(tmbpy)][$BF_4$] (**8**; Chapters Three and Four). We cannot completely explain this observation but suggest one possibility may be the increase from a 5-membered chelate ring for Cu(I)tmbpy, to a 6-membered one for Cu(I)(pmppE). We believe that this introduces an additional degree of flexibility into the ligand which can result in non-radiative decay of the excited state.

## 5.3 Conclusions

Shown here is the synthesis of four neutral complexes; two of the general formula [Cu(I)(pmppE)(tmbpy)] (**12** – **13**) and two of the general formula [Cu(I)(pmppE)(POP)] (**14** – **15**). Electrochemical and spectroscopic methods were used to understand the electronic characteristics of these complexes.

A key point of this work is that stable heteroleptic Cu(I)-sensitisers can be achieved using azo-derivative ligands but that the two investigated here are not ideal as a Cu(I) complex was only achievable using the synthetically demanding 4,4′,6,6′-tetramethyl-2,2′-bipyridine ligand (tmbpy). This limitation meant that the complex could not be developed for solar investigation as synthesis of the acid analogue of the [Cu(pmppE)(tmbpy)] complex was not possible due to the base required to deprotonate the pmppE ligand affecting the acid groups of the bipyridine ligand.

Investigation of the photoelectrochemical and photophysical properties of these complexes revealed that the inclusion of π-donor ligands could be beneficial for Cu(I) DSSC sensitisers. **13** exhibits an electrochemically and chemically reversible oxidation at +0.373 V that has been assigned to the Cu(I)/Cu(II) process. It has been proposed that the π-donor ligand is acting to stabilise the Cu(II) oxidation state allowing a reversible redox process. However despite this the π -donor ligands also creates undesirable properties when complexed to Cu(I). The frontier orbitals of the ligand do not mix well with the closed-shell metal d-orbitals meaning that MLCT is disfavoured and there is no shifting of the absorption spectrum into the visible region of the spectrum.

Emission experiments revealed that [Cu(POP)(pmppE)] complexes are significantly less emissive than the [Cu(POP)(tmbpy)][$BF_4$] analogues as we did not observe emission at room temperature for the prior while we did for the latter. We have suggested that an explanation for this may be that the increased chelate ring-size of the pmppE ligand with Cu(I) causes increased flexibility of the excited state complex and therefore creates more non-radative pathways for the decay of the excited state.

## 5.4 Experimental

### 5.4.1 General Procedures

The synthesis of bis[2-(diphenylphosphanyl)phenyl] ether (POP) (carried out by Dr Omar Moudam),[17] 4,4′,6,6′-tetramethyl-2,2′-bipyridine (tmbpy),[18] $[Cu(MeCN)_4][BF_4]$[19] and $[Cu(I)POP(MeCN)_2][BF_4]$ (carried out by Dr Omar Moudam)[17] were carried out according to literature procedures. Ligands pmppT and pmppO were synthesised by Dr Andrew Smith.[2] All other chemicals were purchased from Aldrich and used as received.

Electrochemistry was carried out using a Pt working electrode, Pt rod counter electrode and Ag/AgCl reference electrode. All electrochemical experiments were carried out in DCM and the supporting electrolyte used was $TBABF_4$ (0.3M). After each experiment the reference electrode was calibrated against the ferrocene/ferrocenium couple which was found to be at 0.55 V. The absorption spectra were recorded using a PerkinElmer Lambda 9 spectrophotometer controlled using the UV/Winlab software. Emission spectra were recorded at room temperature and using frozen samples, with ethanolic solutions of all samples and for ligands pmppT and pmppO, using a Fluoromax2 fluorimeter controlled by the ISAMain software.

#### 5.4.1.1 [Cu(pmppT)(tmbpy)] (12)

$[Cu(MeCN)_4][BF_4]$ (101 mg, 0.32 mmol), tmbpy (85 mg, 0.31 mmol) and pmppT (89mg, 0.30 mmol) were stirred in 20 mL degassed chloroform under nitrogen for 2 h. An excess of $NaOH_{(aq)}$ (1M) was added and the reaction mixture left to stir for an additional 3 hr. The organic layer was collected and magnesium sulphate added and left for 5 min before filtering under gravity. The solvent was removed under reduced pressure. Yield = 75 %, 136 mg. $\delta_H$ (DMSO, 500 MHz)/ppm = 8.27 (s, 2H, H-bpy), 7.86 (d, J = 7.85 Hz, 2H, H-pmppT), 7.48-7.28

(m, 5H, 2H-bpy, 8H-pmppT), 2.57 (s, 6H, $CH_3$-bpy), 2.44 (s, 6H, $CH_3$-bpy), 2.42 (s, 3H, $CH_3$-pmppT). MS (positive ESI); *m/z*: 567.01 $(M)^+$. Elemental analysis: calculated for $C_{30}H_{29}CuN_6S$: C 63.30, H 5.14, N 14.76. Found: C 63.18, H 5.24, N 14.69.

#### 5.4.1.2 [Cu(pmppO)(tmbpy)] (13)

$[Cu(MeCN)_4][BF_4]$ (101 mg, 0.32 mmol)in 5 mL degassed chloroform was added to tmbpy (67 mg, 0.32 mmol) and pmppO (89 mg, 0.32 mmol) in 20 mL degassed chloroform and the reaction mixture stirred, under nitrogen, for 2 h. An excess of $NaOH_{(aq)}$ (1M) was added and the reaction mixture left to stir for an additional 3 h. The organic layer was collected and magnesium sulphate added and left for 5 min before filtering under gravity. The solvent was removed under reduced pressure. Yield = 86 %, 150 mg. $\delta_H$ (DMSO, 400 MHz)/ppm = 8.37 (s, 2H, H-bpy), 7.93 (d, J = 7.96 Hz, 2H, H-pmppO), 7.62 (d, J = 7.92 Hz, 2H, H-pmppO), 7.46 (t, J = 7.60 Hz, 4H, H-pmppO), 7.43 (s, 2H-bpy), 7.23 (q, J = 6.80 and 6.94 Hz, 2H, H-pmppO), 2.47 (s, 6H, $CH_3$-bpy), 2.30 (s, 6H, $CH_3$-bpy), 2.13 (s, 3H, $CH_3$-pmppO). Elemental analysis: calculated for $C_{30}H_{29}CuN_6O$: C 65.14, H 5.28, N 15.19. Found: C 65.26, H 5.13, N 15.28.

#### 5.4.1.3 [Cu(pmppT)(POP)] (14)

$[Cu(POP)(MeCN)_2][BF_4]$ (153 mg, 0.20 mmol) and pmppT (59 mg, 0.20 mmol) were stirred in 20 mL degassed chloroform under nitrogen for 3 h. An excess of $NaOH_{(aq)}$ (1M) was added and the reaction mixture left to stir for an additional 3 hr. The organic layer was collected and magnesium sulphate added and left for 5 min before filtering under gravity. The solvent was removed under reduced pressure and the solid dissolved in acetone and left to stand for 30 min. The filtrate was collected and the solvent removed under reduced pressure. Yield = 87 %, 154 mg. $\delta_H$ (DMSO, 500 MHz)/ppm = 8.04 (d, 2H, H-pmppT), 7.73 (d, 2H, H-pmppT), 7.51-6.82 (m, 32H, 6H-pmppT, 26H-POP), 6.51 (m, 2H, H-POP), 2.27 (s, 3H, $CH_3$-pmppT). Elemental

analysis: calculated for $C_{52}H_{41}CuN_4OP_2S$: C 69.75, H 4.61, N 6.26. Found: C 69.57, H 4.51, N 6.19.

#### 5.4.1.4 [Cu(pmppO)(POP)] (15)

[Cu(POP)(MeCN)$_2$][$BF_4$] (100 mg, 0.13 mmol) and pmppO (36 mg, 0.17 mmol) were stirred in 20 mL degassed chloroform under nitrogen for 3 h. An excess of $NaOH_{(aq)}$ (1M) was added and the reaction mixture left to stir for an additional 3 hr. The organic layer was collected and magnesium sulphate added and left for 5 min before filtering under gravity. The solvent was removed under reduced pressure and the solid dissolved in acetone and left to stand for 30 min. The precipitate was collected and dried. Yield = 86 %, 98 mg. $\delta_H$ (DMSO, 500 MHz)/ppm = 8.03 (d, 2H, H-pmppO), 7.74 (d, 2H, H-pmppO), 7.52-6.83 (m, 32H, 6H-pmppO, 26H-POP), 6.52 (m, 2H, H-POP), 2.28 (s, 3H, $CH_3$-pmppO). Elemental analysis: calculated for $C_{52}H_{41}CuN_4O_2P_2$: C 71.02, H 4.70, N 6.37. Found: C 70.89, H 4.55, N 6.25.

## 5.4.2 X-ray Crystallography

Crystals of **15** were grown in acetone (solution open to air). Single crystal X-ray diffraction data is given in Table 6 and were collected using Mo-Kα radiation (λ = 0.71073 Å) on a Smart APEX CCD diffractometer equipped with an Oxford Cryosystems low-temperature device operating at 150 K. An absorption correction was applied using the multi-scan procedure SADABS.[20] The structures were solved by Direct methods (Shelx[21]) and refined by full-matrix least squares against $|F|^2$ using all data (Shelx[21]). Figures were prepared using the programme Mercury.[1] All non-H atoms were refined with anisotropic displacement parameters.

**Table 6** X-Ray crystallography data for **15**

| | **15** |
|---|---|
| Empirical Formula | $C_{52}H_{41}N_4CuO_2P_2.C_3H_6O$ |
| Formula weight | 937.45 |
| T / K | 100(2) |
| Crystal colour | red |
| Crystal dimensions | 0.84x0.42x0.19 |
| Crystal system | triclinic |
| Space group | P-1 |
| *a* / Å | 10.9230(2) |
| *b* / Å | 13.7220(3) |
| *c* / Å | 15.7389(3) |
| α / ° | 93.4340(10) |
| β / ° | 98.7880(10) |
| γ / ° | 95.4380(10) |
| *V* / Å$^3$ | 2314.20(8) |
| *Z* | 2 |
| $D_{calcd}$ / Mgm$^{-3}$ | 1.345 |
| Independent reflections | 9519 [$R_{int}$=0.0526] |
| Data / restraints / Parameters | 9519 / 0 / 551 |
| Absorption correction / mm$^{-1}$ | 0.591 |
| $R_1/wR_2$ (observed data: $F^2>2\sigma(F^2)$) | 0.0350/0.0850 |

## 5.5 References


1. C. F. Macrae, P. R. Edgington, P. McCabe, E. Pidcock, G. P. Shields, R. Taylor, M. Towler and J. van de Streek, *Journal of Applied Crystallography*, 2006, **39**, 453-457.
2. A. G. Smith, in *School of Chemistry*, University of Edinburgh, Edinburgh, 2000.
3. A. la Cour, M. Findeisen, K. Hansen, R. Hazell, L. Hennig, C. E. Olsen, L. Pedersen and O. Simonsen, *Journal of the Chemical Society, Dalton Transactions*, 1997, 2045-2058.
4. J. Gasparic and A. Sedmíková, *Journal of Chromatography A*, 1994, **665**, 197-202.
5. M. S. Lucas and J. A. Peres, *Dyes and Pigments*, 2006, **71**, 236-244.
6. M. Neamtu, A. Yediler, I. Siminiceanu and A. Kettrup, *Journal of Photochemistry and Photobiology A: Chemistry*, 2003, **161**, 87-93.
7. R. Jain, M. Bhargava and N. Sharma, *Industrial & Engineering Chemistry Research*, 2002, **42**, 243-247.
8. E. Razo-Flores, M. Luijten, B. Donlon, G. Lettinga and J. Field, *Water Science and Technology*, 1997, **36**, 65-72.
9. F. A. Snavely, W. C. Fernelius and B. P. Block, *Journal of the American Chemical Society*, 1957, **79**, 1028-1030.
10. F. A. Snavely and B. D. Krecker, *Journal of the American Chemical Society*, 1959, **81**, 4199-4200.
11. F. A. Snavely, B. D. Krecker and C. G. Clark, *Journal of the American Chemical Society*, 1959, **81**, 2337-2338.
12. S. Miyazaki, H. Mukai, S. Umetani, S. Kihara and M. Matsui, *Inorganic Chemistry*, 1989, **28**, 3014-3017.
13. S. Umetani, Y. Kawase, Q. T. H. Le and M. Matsui, *Inorganica Chimica Acta*, 1998, **267**, 201-207.
14. A. Whitaker, *Acta Crystallographica Section C*, 1988, **C44**, 1587.
15. L. C. Emeleus, D. C. Cupertino, S. G. Harris, S. Owens, S. Parsons, R. M. Swart, P. A. Tasker and D. J. White, *Journal of the Chemical Society, Dalton Transactions*, 2001, 1239-1245.
16. N. Armaroli, *Chemical Society Reviews*, 2001, **30**, 113-124.
17. N. Armaroli, G. Accorsi, M. Holler, O. Moudam, J. F. Nierengarten, Z. Zhou, R. T. Wegh and R. Welter, *Advanced Materials*, 2006, **18**, 1313.
18. P. Ghosh and T. G. Spiro, *Journal of the American Chemical Society*, 1980, **102**, 5543-5549.
19. O. Moudam, in *LCC-Toulouse*, LCC-Toulouse, Toulouse, 2007.
20. G. M. Sheldrick, University of Gottingen, Germany.
21. G. Sheldrick, *Acta Crystallographica Section A*, 2008, **64**, 112-122.

# 6. Chapter Six: [Ni(bipyridyl)(qdt)] Complexes

## 6.1 Introduction

The main topic under investigation throughout this work is the development of Cu(I) complexes for application in DSSC devices. In this chapter we branch out to look at another first row transition metal, nickel, and look at a Ni(II) sensitiser. The main focus for the design of this complex is the same as the previously discussed Cu(I) complexes, the extension of the excited state lifetime of the complex. Chapter One spoke of two design strategies that have been employed to develop DSSC applicable first row transition metal sensitisers; firstly complexes with a full d-subshell (Chapters 3, 4 and 5). The second is to have a strong crystal field, aimed at raising the energy of any d-d excited states, and it is this second method that will be explored in this chapter.

Research groups have already attempted implementing this technique of creating a strong ligand field in an attempt to extend the excited state lifetimes of first row transition metal complexes making them more suitable for DSSC application. Ferrere *et al.*[1-3] based their design of Fe(II) sensitiser (Figure 1) around obtaining a strong crystal field. They took their lead from successful, analogous Ru(II) sensitisers (Figure 1), that exhibit strong crystal-field splitting due in part to the inclusion of the high field $CN^-$ ligands.[4] The aim was that the excited state lifetime of the Fe(II) sensitisers would be long lived enough to allow sufficient charge injection into the $TiO_2$ conduction band.[1] Solar cell function was observed ($I_{SC}$ = 290 μA/cm$^2$ and $V_{OC}$ = 360 mV)[1] but it was significantly reduced compared to the analogous Ru(II) sensitiser ($I_{SC}$ = 19 mA/cm$^2$ and $V_{OC}$ = 600 mV).[5] These finding suggest that while charge injection does occur for Fe(II) complexes the timescale in which this takes place is comparable with the excited state decay time, resulting in low photocurrents.[6]

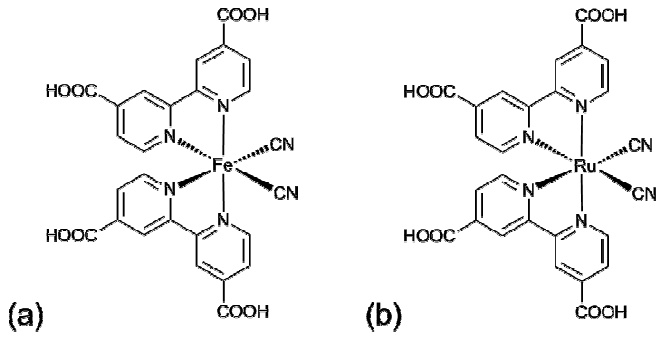


**Fig. 1** Structures of (a) $[Fe(II)(dcbpy)(CN)_2]$[1] and (b) $[Ru(II)(dcbpy)(CN)_2]$; **N3**[5]

The research presented here investigates the possible use of a Ni(II) complex as a DSSC sensitiser molecule. Ni(II) preferentially forms square planar complexes this achieves the lowest ground electronic configuration energy of a $d^8$, 4-coordinate complex as it is orbitally degenerate (Figure 2). This geometry has the beneficial characteristic of exhibiting strong crystal fields that are known to extend excited state lifetimes.[7] Based on this design rationale it is hoped that a Ni(II) square planer complex could display DSSC functionality.

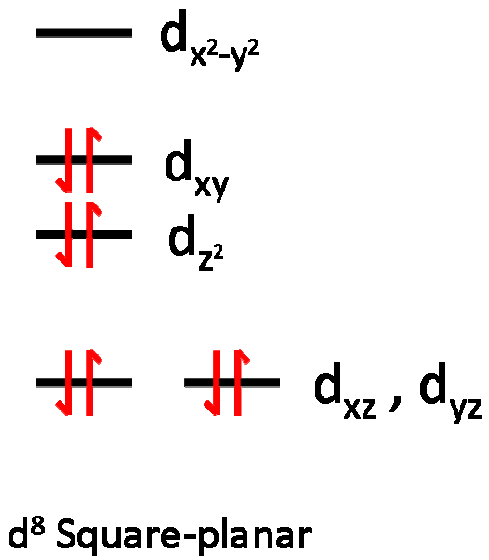


**Fig. 2** An Orbital Energy Level Diagram for a Ni(II) square planer complex.

Ligand selection for our Ni(II) sensitiser was based upon previous Pt(II) DSSC sensitiser research with the general formula [Pt(II)(NN)(SS)], as these have been shown in the literature to produce significant photocurrents, photovoltages and device efficiencies (Figure 3 and Table 1).[8-10] Aanalogous Pt(II) complexes were also synthesised where the bipryidine ligand had been replaced by a phenanthroline ligand, but reduced solar cell performance was observed in each case. The success of these complexes could arise in part from the inclusion of the dithiolate ligands which are high spin, π-donor ligands that are more easily oxidised than the bipyridyl ligand. This is believed to act to create charge directionality across the complex in the desired direction (see Chapter Three; section 3.1); the HOMO is located on the dithiolate ligand (with some possible metal character) and the LUMO on the bipyridyl ligand.

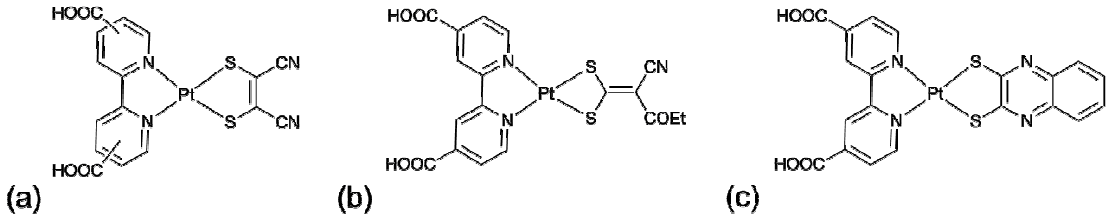


**Fig. 3** Structures of (a) [Pt(II)(dcbpy)(mnt)][8], (b) [Pt(II)(dcbpy)(ecda)][9] and (c) [Pt(II)(dcbpy)(qdt)][9]; where mnt = maleonitriledithiolate; ecda = ethyl-2-cyano-3,3-dimercaptoacrylate; qdt = quinoxaline-2,2-dithiolate.

**Table 1** Absorbance measurements and *IV* Characterisation Data for complexes shown in Figure 3

| Sensitiser | Absorption / nm (ε /$M^{-1}cm^{-1}x10^3$) | | | Solar Cell Data | | |
|---|---|---|---|---|---|---|
| | | | | $I_{SC}$ / mA | $V_{OC}$/ mV | η / % |
| [Pt(II)(dcbpy)(mnt)][8] | | | 537 (5.6)[(a)] † | 1.94 | 490 | 0.63 |
| [Pt(II)(dcbpy)(ecda)][9] | | 440 (13.0) ‡ | | 2.92 | 521 | 1.10 |
| [Pt(II)(dcbpy)(qdt)][9] | 425 (11.4) ‡ | 460 (10.3) ‡ | 495 (5.3) ‡ | 7.00 | 600 | 3.00 |

[(a)] data given for [Pt(decbpy)(mnt)]; † in DMF; ‡ in 4:1 EtOH:MeOH solution

Given in Table 1 are experimental values for key parameters upon which our ligand selection was directed. From these it is clear to see that the complex [Pt(II)(dcbpy)(qdt)][9] (Figure 3(c)) is the most successful and led to our synthesising the analogous Ni(II) complex shown in Figure 4. It should be noted that comparisons between these two sensitisers will be drawn during the following discussion of our results.

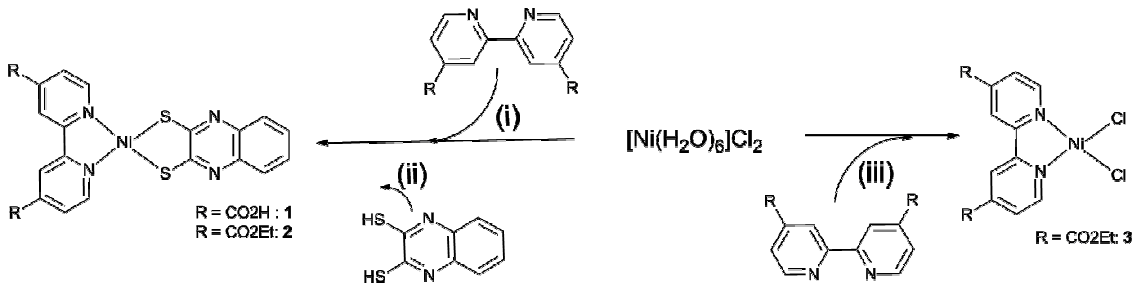


**Fig. 4** Synthetic Reaction Scheme for Complexes reported in this work.
(i) R = $CO_2H$: EtOH and 2eq. NaOH; R= $CO_2Et$: DCM (ii) EtOH and 2 eq. NaOH: (iii) THF.

Briefly before the research reported in this chapter is outlined in detail, it should be noted that there are no previous literature explorations into a [Ni(II)(qdt)] complex or any Ni(II) complex being used as a DSSC sensitiser, or indeed for any photoelectrochemical or photophysical application. Therefore in this chapter we report the first example of a Ni(II) complex that demonstrates sensitiser function in a DSSC. Complexes [Ni(dcbpy)(qdt)] (**16**), [Ni(decbpy)(qdt)] (**17**) and [Ni(decbpy)$Cl_2$] (**18**) (qdt = quinoxaline-2,3-dithiolate) have been prepared (Figure 4). The electrochemical and photophysical properties of the complexes and the qdt ligand were investigated using UV-Vis spectroscopy, electrochemistry and emission spectroscopic studies. **18** was synthesised to facilitate assignment of the electrochemical and spectroscopic properties of **16** and **17**. Solar cell function of **16** was investigated using *I-V* characterisation and Transient Absorption Decay (TAS) studies. Density Functional Theory (DFT) and Time-Dependent DFT (TDDFT) calculations were used to support and further investigate these properties.

## 6.2 Results and Discussion

### 6.2.1 Syntheses

The ligands 4,4'-dicarboxy-2,2'-bipyridine (dcbpy), 4,4'-di($CO_2$Et)-2,2'-bipyridine (decbpy) and 2,3-quinoxalinedithiol (qdt) were synthesised using modified literature method as described in the Experimental details. The reaction schemes outlined in Figure 4 demonstrate how the complexes were synthesised by simple addition, with stirring, of the relevant starting materials in stoichiometric amounts, to the appropriate solvent at room temperature. The ester analogue, **17**, has been synthesised alongside the acid, **16**, despite not being directly applicable for use in a DSSC, as the properties of ester are known to be similar to the acid, and are more convenient for detailed characterisation due to better solubility. The Ni(II) complexes were characterised by $^1$H NMR, ESI-MS, +FAB-MS and elemental analysis verifying the molecular structures.

### 6.2.2 DFT and TDDFT Calculations

Calculations were carried out for **16** using Gaussian 03[11] with B3PW91/6-31G(d,p)[12, 13] the functional and basis set with induced solvent effects. This level of theory was used in place of that quoted for the Cu(I) complex studies as it was found to produce reproducible data that predicted the experimental data reasonably well. It has also been used successfully in the literature to calculate the structural and electronic properties of a number of coordination complexes.[14, 15] The 6-31 G(d,p) basis set was used instead of the LANL2DZ basis set (used for the Cu(I) calculations), because despite the two being very similar, 6-31 G(d,p) is a larger basis set due to the inclusion of a polarisable function and having no effective core potential. This makes it more suitable for the smaller Ni(II) complexes than for the larger Cu(I) complexes which were found to be too computationally expensive to run with 6-31 G(d,p). Calculation details are outlined in full in the Experimental section. Time dependent density functional

theory (TDDFT), also at the B3PW91/6-31G(d,p) level of theory, was used to probe the electronic transitions that give rise to the visible and near-UV absorption of **16**. Although current TDDFT implementations have a tendency to underestimate the energy of charge-transfer interactions, the method has been shown to provide useful qualitative information on the electronic structure and photophysical behaviour of similar coordination complexes.[14, 15] Seventy singlet-singlet transitions were calculated with the solvent DMF.

**Table 2** TD-DFT calculated visible absorption wavelengths for **16**, indicating the molecular orbitals involved and their relative contribution to the absorption.

| Absorbance / nm | Main Charge Transitions | | Relative Contribution |
|---|---|---|---|
| | MO from | MO to | |
| 588 | HOMO-2 | LUMO | 32 % |
| | HOMO-2 | LUMO+4 | 16 % |
| | HOMO-1 | LUMO | 28 % |
| | HOMO | LUMO | 24 % |
| 582 | HOMO-2 | LUMO | 20 % |
| | HOMO-2 | LUMO+4 | 19 % |
| | HOMO-1 | LUMO | 32 % |
| | HOMO | LUMO | 29 % |
| 569 | HOMO-2 | LUMO | 50 % |
| | HOMO | LUMO | 50 % |
| 433 | HOMO | LUMO+1 | 100 % |
| 412 | HOMO-5 | LUMO | 25 % |
| | HOMO-4 | LUMO+1 | 9 % |
| | HOMO-1 | LUMO +1 | 57 % |
| | HOMO | LUMO | 9 % |
| 382 | HOMO-5 | LUMO | 44 % |
| | HOMO-2 | LUMO+1 | 9 % |
| | HOMO-1 | LUMO+1 | 19 % |
| | HOMO | LUMO+2 | 12 % |
| | HOMO | LUMO+3 | 16 % |
| 360 | HOMO-5 | LUMO | 12 % |
| | HOMO-2 | LUMO+2 | 13 % |
| | HOMO-1 | LUMO+5 | 12 % |
| | HOMO | LUMO+3 | 63 % |
| 308 | HOMO-8 | LUMO | 29 % |
| | HOMO-7 | LUMO | 10 % |
| | HOMO-6 | LUMO | 10 % |
| | HOMO-5 | LUMO+1 | 38 % |
| | HOMO-4 | LUMO+1 | 13 % |

**Table 3** Percentage contributions from component parts of **16** to selected molecular orbitals. Also quoted are the calculated energies for these molecular orbitals.

| MO | MO Energy / eV | % Contribution from Ni-based MOs | qdt-based MOs | bpy-based MOs |
|---|---|---|---|---|
| LUMO+5 | -0.577 | 0.18 | 61.58 | 38.24 |
| LUMO+4 | -1.713 | 36.90 | 33.25 | 29.85 |
| LUMO+3 | -1.776 | 1.26 | 93.98 | 4.76 |
| LUMO+2 | -2.011 | 0.44 | 3.07 | 96.49 |
| LUMO+1 | -2.325 | 1.76 | 0.30 | 97.94 |
| LUMO | -3.034 | 5.91 | 3.09 | 91.00 |
| HOMO | -5.723 | 24.41 | 67.80 | 7.79 |
| HOMO-1 | -5.893 | 32.75 | 63.86 | 3.39 |
| HOMO-2 | -6.316 | 90.21 | 3.95 | 5.84 |
| HOMO-3 | -6.695 | 8.69 | 88.99 | 2.32 |
| HOMO-4 | -6.735 | 37.08 | 57.12 | 5.80 |
| HOMO-5 | -6.897 | 59.51 | 33.40 | 7.09 |
| HOMO-6 | -7.460 | 12.68 | 61.49 | 25.84 |
| HOMO-7 | -7.540 | 10.87 | 55.62 | 33.51 |
| HOMO-8 | -7.620 | 21.67 | 38.63 | 39.70 |

Analysis of the components of the TDDFT expansion shows that the majority of predicted transitions are not well described by a single electron-promotion, but involve transitions between several different orbital pairs (Table 2). The nature of each electronic transition was determined by visual inspection (Argus Lab[16]) of each contributing molecular orbital as an isosurface map. Many of the calculated occupied and virtual orbitals were seen to be of mixed character, with electron density simultaneously present on both the ligand and metal. However, the electronic transitions could broadly be classified into three distinct types; metal-to-ligand-charge-transfer (MLCT), where the occupied orbital is predominantly metal based and the virtual orbital ligand based, either on the qdt or dcbpy; ligand-ligand (LL), where the transition involves occupied and virtual orbitals on the same ligand; and ligand-to-ligand-charge-transfer (LLCT), where the transition involves occupied and virtual orbitals on different ligands. These are discussed further in the context of the experimental results below.

## 6.2.3 UV-Vis Absorption Spectroscopy

The experimental UV-Vis absorption spectra of **16** and **17** are shown in Figure 5, and in Figure 6 alongside the experimental spectrum for **16** the computational spectrum is shown for comparison. The main absorption bands and molar extinction coefficients for all species investigated experimentally are given in Table 4, and it should be noted that both show absorption in the visible region between 530nm and 560nm.

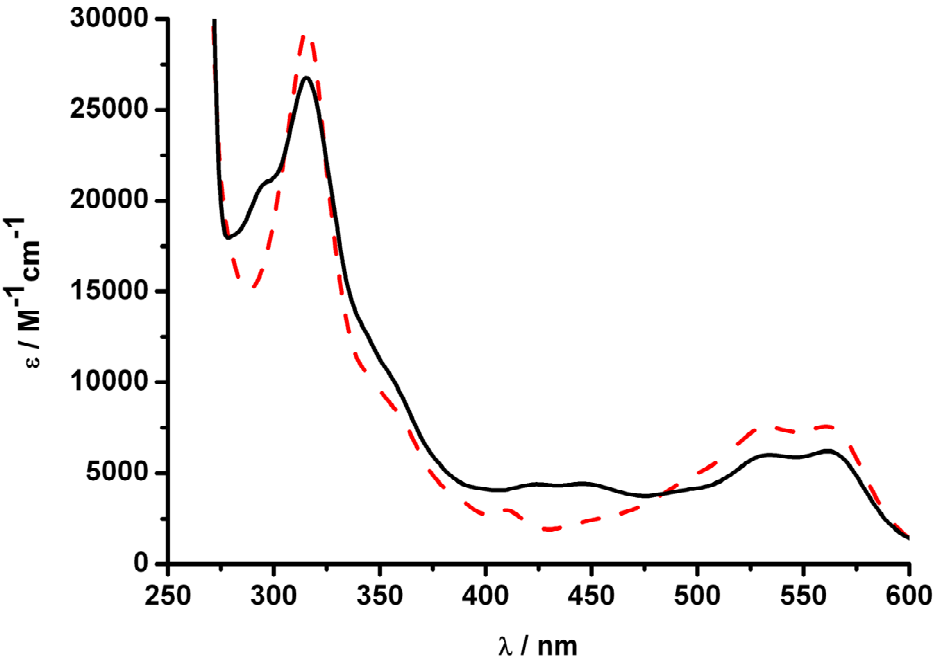


**Fig. 5** Absorbance Spectra for **16** (Black solid line) and **17** (Red dashed line). Y axis refers to results for **17**. Spectrum shown for **16** is normalised against **17** as accurate molar extinction coefficients could not be calculated for **16** due to poor solubility.

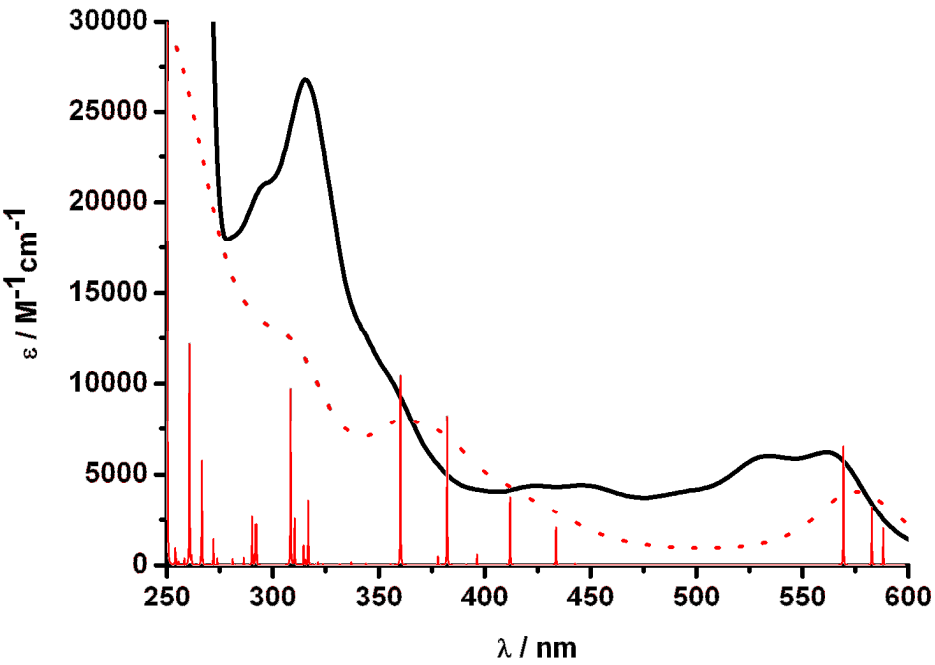


**Fig. 6** UV-Vis Absorption Spectra; Where red solid columns = calculated electronic transisiton; red dotted line = calculated spectra; black solid line = solution spectrum of **16** in DMF.

**Table 4** Absorbance measurements for **16, 17** and qdt carried out in DMF; **18** carried out in DCM; [Pt(decbpy)(qdt)] in 4:1 EtOH:MeOH solution.[9]

| Complex | Absorption / nm (ε /$M^{-1}cm^{-1}$ x$10^{3}$) | | |
|---|---|---|---|
| | π-π* intra-bpy | π-π* intra-qdt | LLCT |
| **16** | 315 | 424, 445 | 534, 561 |
| **17** | 316 (29.0) | 410 (2.9) | 533 (7.3), 561 (7.3) |
| **18** | 323 (13.3) | | |
| qdt | | 409 (18.9), 432 (19.1) 459 (11.3) | |
| [Pt(decbpy)(qdt)] | 305 (13.4) | 425 (11.4) 460 (10.3) | 495 (5.3) |

Assignment of LLCT has been proposed for the visible absorption based upon comparison with the Pt(II) analogues,[8, 9] however inspection of the TDDFT calculations suggests that a combination of LLCT (qdt-based to dcbpy-based) and MLCT (Ni-based to dcbpy-based) results in these absorptions (Tables 2 and 3). This assignment is also supported by comparison with the absorption data collected for **18** and the free qdt ligand; **18** lacks an absorption peak above 400nm and free qdt above 459 nm indicating the low-energy peak seen for **16** and **17** is MLCT or LLCT (Table 4).

A visible absorption at this wavelength and of this magnitude ($\lambda_{max}$ = 533 - 561 nm, and $\varepsilon$ = 7.3 $M^{-1}cm^{-1}$ $x10^3$ respectively) is well within the acceptable range required for a DSSC sensitiser. Also of positive note is that the absorption is red-shifted compared to the analogous Pt(II) sensitiser and has an increased molar extinction cooefficient for this charge transfer (Table 4).

## 6.2.4 Electrochemistry

The redox potentials of complexes **16** and **17** are shown in Table 5 along with the redox potentials for **18**, qdt and the Pt analogue[9] for comparison. As outlined in the introduction, the discussion will focus on the data collected for **17** due to the poorer solubility of **16**.

**17** exhibits two reduction potentials at -1.23 V and -0.72 V as can be seen in Figure 7, that have been assigned as bpy-based reductions upon comparison with **18** that has reduction potentials at -1.36 and-0.81 V (Table 5). This is consistent with bpy-based reduction potentials quoted in the literature for similar co-ordination complexes.[17] Both reduction processes have oxidation-reduction peak separations indicating electrochemical reversibility, although the second reduction has limited chemical reversibility (see Chapter Two, section 2.1 for definition).

**Table 5** Oxidation and Reduction Potentials for; **16**, **17** and qdt in solutions of 0.1M TBABF4/DMF; **18** in 0.3M $TBABF_4$/DCM; and [Pt(decbpy)(qdt)][9]

| **Sensitiser** | **$E_{½}$ (V vs. Ag/AgCl)** | | | |
|---|---|---|---|---|
| | **$E_{Red.2}$** | **$E_{Red.1}$** | **$E_{Ox.1}$** | **$E_{Ox.2}$** |
| **16** | -1.17[a] | | 0.53[a] | 1.15[a] |
| **17** | -1.23[a] | -0.72[a] | 0.86[b] | 1.08[b] |
| **18** | -1.36[b] | -0.81[b] | | |
| qdt | -1.12[b] | | | 1.12[b] |
| [Pt(decbpy)(qdt)] | -1.06[b] | | 0.90[b] | |

All potentials vs. Ag/AgCl; recorded at 298K; a = Peaks are electrochemically reversible and values shown represent E½; b = Peaks are electrochemically irreversible and values shown represent peak potential.

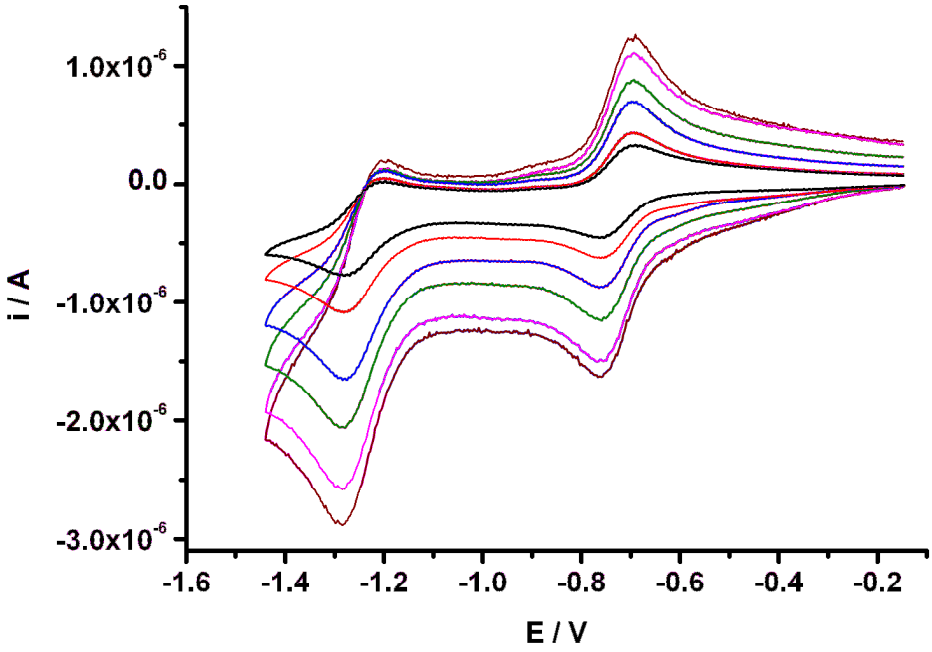


**Fig. 7** Cyclic Voltammogram of **17** showing reduction peaks with scan rates of 0.1 (black line), 0.2 (red line), 0.4(blue line), 0.6 (green line), 0.8 (magenta line) and 1.0 (wine line) $Vs^{-1}$ in 0.1M $TBABF_4$/DMF at 298K

The multiple oxidation processes observed for **17** have been assigned as qdt-based by comparison with the oxidation potentials seen for both free qdt and the Pt complex. This is supported by the lack of any oxidation processes for **18**. This demonstrates that the first oxidation of **17** is suitably located for a DSSC sensitizer, and this is confirmed by the TDDFT calculation that places the majority of the HOMO on the qdt and the LUMO on the bpy ligand (Table 3 and Figure 8).

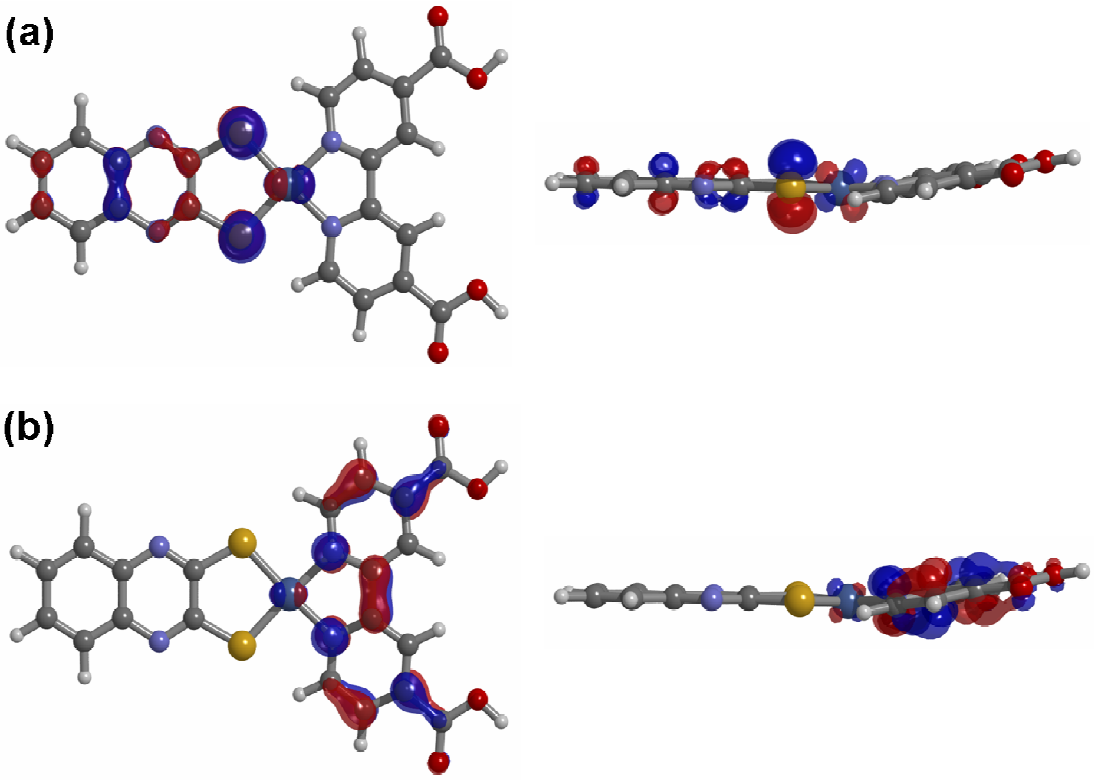


**Fig. 8** DFT Calculated Geometry Optimisation for **16** including (a) HOMO and (b) LUMO Isosurfaces.

The oxidation takes place on the dithiolate and reduction on the diimine, therefore implying that charge transfer transitions across the molecule will likely have directionality towards the carboxylate groups that bind to the $TiO_2$. The location of the HOMO also means that when the sensitiser is oxidised the positive charge density is placed further from the $TiO_2$. Charge recombination from the $TiO_2$ back to the dye is expected to be minimised by this physical separation. In addition the similarity of the reduction potential for the Ni(II) complex with the Pt(II) complex suggests that the LUMO of **16** is at an energy suitable to allow charge injection into the $TiO_2$ conduction band with a band edge at -0.81 V vs. Ag/AgCl.[4]

## 6.2.5 Transient Absorption Decay Studies

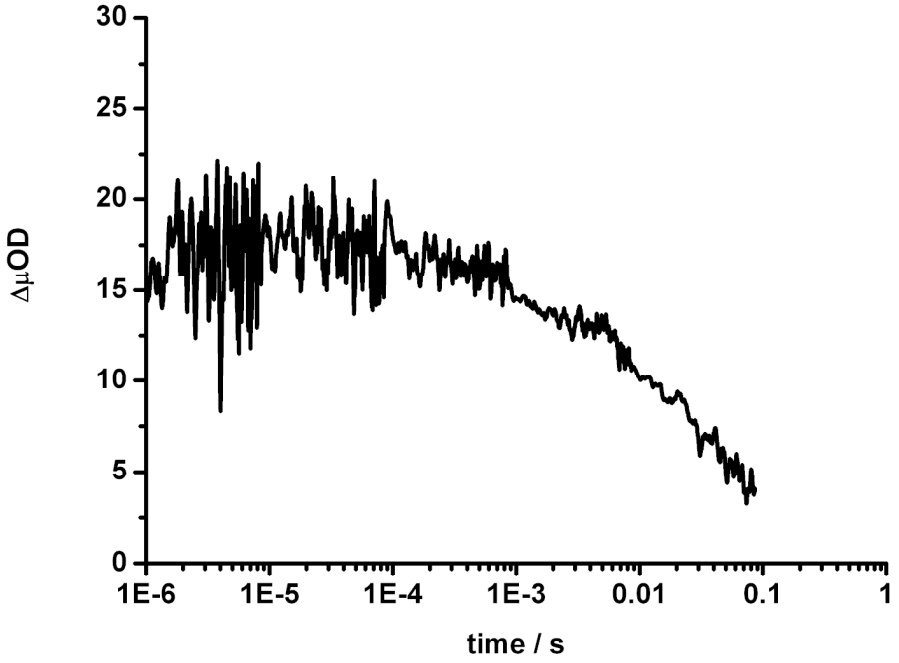


**Fig. 9** Transient Absorption Decay Trace for **17** adsorbed on $TiO_2$; Excitation wavelength = 520 nm; Probe = 995 nm.

Transient absorption spectroscopy was used to investigate the electron-transfer kinetics of the dye-sensitised $TiO_2$ system. Sensitisation of the $TiO_2$ was achieved by treating a freshly prepared $TiO_2$ film with pH 12 NaOH (aq) solution for 1 h, and then removing and drying the film (110ºC, 5 minutes). The film was then placed into a dye bath (a solution of **17** in DCM), and left for 48 h before removal and air drying. The excitation wavelength was set at 520 nm, previously identified as the light harvesting absorption. Photoinduced absorption was monitored at a probe wavelength of 995 nm, and assigned primarily to absorbed electrons injected into the $TiO_2$ conduction band/trap states. Figure 9 illustrates that the Ni(II) sensitiser does inject electrons into the conduction band of $TiO_2$ upon excitation at 520nm. The half time recorded for the electron recombination with the sensitiser was around 0.01 s which is comparable with other effective sensitisers.[18] A recombination time of this length indicates that this loss mechanism is not a limiting factor in this system and is consistent with the assignment of significant charge separation in the LLCT excited state.

## 6.2.6 Solar Cell Measurements

*I-V* characterisation was carried out on solar cells made using **16** adsorbed onto the $TiO_2$ film. Cell construction and treatments are outlined in the Experimental section. Overall cell efficiency was determined via *I-V* characterisation while irradiating under AM 1.5 light (100 $mWcm^{-1}$). Cell efficiencies ($\eta$) were calculated using the resulting values of $I_{sc}$ = short circuit current (mA), $V_{oc}$ = open circuit voltage (mV) and ff = fill factor.

In order to obtain the optimum coverage of the $TiO_2$ surface with our Ni(II) sensitiser, adsorption studies were carried out. A range of dye bath solvents and dye concentrations were explored, with a 2 mM complex in MeCN/t-butanol dye bath yielding the best $TiO_2$ coverage by **16**. Determination of $TiO_2$ surface coverage was carried out in an approximate fashion using UV-Vis spectroscopy. This method also allowed confirmation that the dye bound without degradation by comparison with the absorption spectrum of **16** in solution.

**Table 6** *IV* Characterisation Data for **16**.

| Sensitiser | Concentration of Cheno | $TiCl_4$ treated | Isc / mA | Voc / mV | ff | $\eta$ (%) |
|---|---|---|---|---|---|---|
| **16** | N/A | No | 0.090 | 389 | 0.41 | 0.006 |
| **16** | 1 mM | No | 0.172 | 485 | 0.52 | 0.043 |
| **16** | 50 mM | No | 0.122 | 476 | 0.54 | 0.031 |
| **16** | 50 mM | Yes | 0.293 | 521 | 0.55 | 0.084 |
| [Pt(dcbpy)(qdt)]: 0.05mM | 30 mmol | No | 7.00 | 600 | 0.77 | 3.000 |

Dye bath 2mM MeCN/t-butanol. Adsorption time 24 h. [Pt(qdt)(dcbpy)] 0.05mM in an ethanoic dye bath.[9]

### 6.2.6.1 Chenodeoxycholate Acid Studies

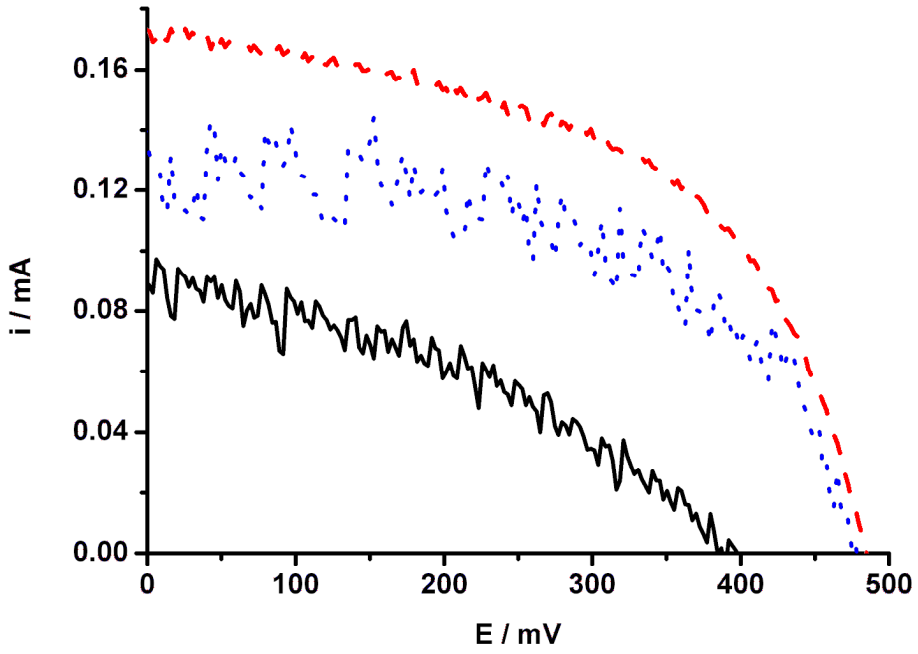


**Fig. 10** *I-V* Curve for **16**. Black solid line = no Cheno additive;
red dashed line = Dye:Cheno 2:1; Blue dotted line = Dye:Cheno 1:25

The planar geometry of complex **16** suggests that aggregation of the molecule may occur through π–π stacking as Islam *et al.*, found for their Pt(II) complexes in 2001.[9] In terms of DSSC device function, dye aggregation can be a significant hindrance as it can limit the number of sensitisers bound to the $TiO_2$ surface and may also lead to intermolecular quenching.[19] Here we have investigated a method outlined in the literature implemented to reduce dye aggregation that involve the use of an additive in the dye bath that acts as a spacer group on the $TiO_2$ surface. The additive investigated in this work was Chenodeoxycholate acid (Cheno) which has been shown to improve the short circuit currents produced in some systems.[19-23] A range of dye:Cheno concentration ratios were tried for **16** with representative examples and the results they yielded given in Figure 10 and Table 6. Improved solar cell function for the dye:Cheno cells over the non-Cheno cells was observed in every case, although further increase in the quantity of cheno beyond 1 mM led to no further improvement. The Cheno is believed to bind preferentially to $TiO_2$ over the dye sensitisers, forming a co-adsorption of the two species on the

surface. Once enough Cheno is present to prevent aggregation no further benefit is obtained from having excess quantities.

### 6.2.6.2 Titanium tetra-chloride Post-treatment Studies

A $TiCl_4$ post-treatment of the $TiO_2$ film prior to adsorption of the sensitiser has been discussed widely in the literature as a method of improving photocurrents obtained from a DSSC.[4, 24] When the $TiCl_4$ post-treatment was introduced into our work alongside the use of the Cheno-additive, the DSSC function of **16** improves dramatically (Figure 11). The photocurrent produced by **16** doubles (0.122 mA to 0.293 mA respectively), which is consistent with the results described by Sommeling *et al.* in 2006. It was proposed that the $TiCl_4$ post-treatment acts to improve dye adsorption onto $TiO_2$, but that it also, more importantly, increases charge injection into the $TiO_2$ by causing a downward shift in the conduction band edge of the $TiO_2$. There were concerns that a downward shift of the $TiO_2$ conduction band edge may reduce the $V_{oc}$ produced by the cell. However, as can be seen in Figure 11 and Table 6, the produced $V_{oc}$ increases by 50mV compared to a non-$TiCl_4$ post-treated cell which had the same dye:Cheno ratio. It is believed by Sommeling *et al.*,[25] that the increased charge injection caused by the $TiCl_4$ creates a greater charge density build up in the $TiO_2$, therefore maintaining, and perhaps even improving, the $V_{oc}$ of the cell.

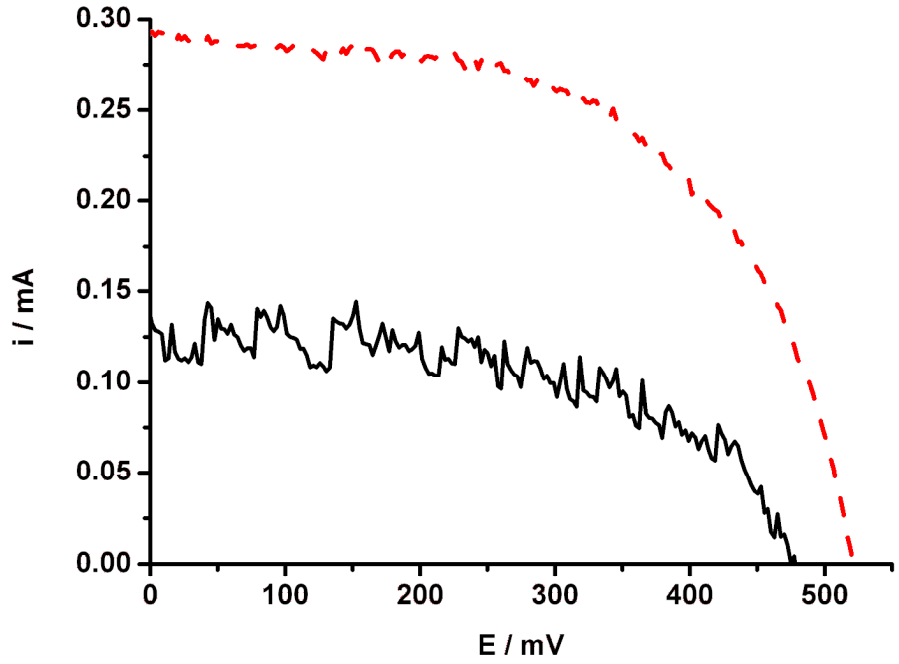


**Fig. 11** *I-V* Curve for **16**. Dye:Cheno = 1:25. Black line = no $TiCl_4$ Post-Treatment; Red dashed line = $TiCl_4$ post-treatment.

In order to compare our results with those of the Pt(II) analogue[9] it should be taken into account that the Pt(II) cells had an active area of 0.25cm$^2$ whereas our cells had an active area of 1cm$^2$. A reduced active area is known to produce higher cell efficiencies due to an increase in fill factor. Taking this into account our cells produce $V_{oc}$ potentials that are similar to those of the Pt(II) sensitiser but the photocurrents produced by our Ni(II) sensitiser are significantly reduced. Even with the inclusion of the $TiCl_4$ post-treatment the photocurrents produced by the Pt(II) sensitiser are around twenty times greater than those produced by the Ni(II) sensitiser (0.293mA and 7.000mA respectively).

### 6.2.7 Emission Spectroscopy

In order to rationalise our solar cell measurements, and in particular the $I_{sc}$ values recorded we investigated the emissive properties of **17.** These studies were carried out to give an indication of the excited state lifetimes of the Ni(II) complex. Spectra of **17** and free qdt were recorded in ethanol. Upon excitation between 350 and 500 nm both species emitted only very weakly at room temperature. No emission was observed when **17** was excited at 550nm, which is of note as this is where the LLCT is believed to take place. We propose that non-radiative decay pathways are competing with any emissive pathways suggesting the excited lifetime is likely to be short.

## 6.3 Conclusions

Shown here is the synthesis of the first example of a Ni(II)(diimine)(dithiolate) with an acid substituents attached to the diimine: [Ni(4,4'-dicarboxy-2,2'-dipyridyl)(2,3-quinoxalinedithiol)]; **16**, and its ester analogue, **17**. Electrochemical, spectroscopic and computational methods were used to understand the electronic characteristics of the complexes. In particular, this work demonstrates the first example of a Ni(II) complex that functions as a sensitiser in a dye-sensitised solar cell.

From the results obtained in solar testing we propose that our system is affected by dye-aggregation, with performance improving upon addition of cheno. In comparison with the analogous Pt(II) complex it is apparent that the limiting factor is the amount of photocurrent produced even after Cheno additives and $TiCl_4$ post-treatments ($I_{sc}$ = 0.293 mA and 7.000 mA for the Ni and analogous Pt complexes respectively). The satisfactory light harvesting, appropriate redox potentials and sufficient charge-separated lifetime suggest that the origin of the low photocurrents is the short lived excited state of the Ni(II) complex. This is also supported by the lack of emission observed upon photoexcitation. Although Ni complexes with long-lived excited states are uncommon, excited state lifetimes as long as 1-3 ns are known,[7] suggesting that higher-efficiency Ni-complex sensitisers are possible if this can be achieved in a complex also possessing the appropriate electrochemical and spectroscopic characteristics.

## 6.4 Experimental

### 6.4.1 General Procedures

The synthesis of 4,4'-dicarboxy-2,2'-bipyridine (dcbpy),[26] 4,4'-di($CO_2Et$)-2,2'-bipyridine (decbpy)[27] and 2,3-quinoxalinedithiol (qdt)[28] were carried out according to literature procedures. Full synthetic details for dcbpy and decbpy are given in Chapter Three, section 3.5.1. Ni(dcbpybpy)(qdt) and Ni(decbpy)(qdt) are novel complexes and have been synthesised using methods described below. 4,4'-Dimethyl-2,2'-bipyridine (dmbpy), $[Ni(H_2O)_6]Cl_2$ and all other chemicals were purchased from Aldrich and used as received. Electrochemistry was carried out using a Pt working electrode, Pt rod counter electrode and Ag/AgCl reference electrode. All electrochemical experiments were carried out in DMF and the supporting electrolyte used was $TBABF_4$ (0.1M). After each experiment the reference electrode was calibrated against the ferrocene/ferrocenium couple which was found to be at 0.55 V.

Density functional theory calculations were performed using the Gaussian 03 program[11] with the starting structure for **16** inputted using the builder program ArgusLab.[16] All calculations were carried out using the Becke three parameters hybrid exchange and the Perdew–Wang 1991 correlation functionals (B3PW91) level of theory were used.[12, 13] Frequency calculations were carried out to ensure that optimised geometries were minima on the potential energy surface. Solvent effects were included via the self-consistent reaction field (SCRF) method using the polarised continuum model (PCM).[29] Time-dependent density functional theory (TDDFT) was performed in a DMF polarizable continuum model,[29] with the first 70 singlet transitions calculated. ArgusLab[16] was used to generate the orbital isosurface maps.

Transient absorption spectroscopy was carried out by with Dr. Keri McCall from University of Edinburgh in collaboration with Dr. Ana Morandoria-Lopez from Prof. James Durrent's group at Imperial College London.

#### 6.4.1.1 2,3-quinoxalinedithiol (qdt)

Adopted literature method used.[28] *O*-phenylenediamine (2.2 g, 20.6 mmol) in 4N HCl (80 ml) was refluxed, under a nitrogen atmosphere, until fully dissolved. Oxalic acid dehydrate (2.6 g, 20.6 mmol) was added and the solution refluxed, under a nitrogen atmosphere, overnight. The precipitate was collected by hot filtration, washed with water and dried under vacuum (140 ºC). The solid was ground carefully with phosphorous pentachloride (7.1 g, 34 mmol), and refluxed (160 ºC) for 2 h at which temperature the reaction mixture is a think oily liquid. Once cooled, excess phosphorous pentachloride was quenched by adding crushed ice, and the solution returned to room temperature slowly. The precipitate was collected by filtration, washed with water and dried. Thiourea (3.7 g, 48 mmol) dissolved in ethanol (45 ml) was added to the product and refluxed for 2 h. Once cool, aqueous sodium hydroxide (11.3 g, 281.9 mmol) in 90 ml water was added slowly and the solution refluxed for1 h. The resulting solution was acidified using glacial acetic acid until a dark orange precipitate formed which was collected by filtration, washed with water and dried. Yield = 3 %, 106.8 mg. $\delta_H$ (250 MHz, DMSO) = 7.49 – 7.69 (ten line symmetrical second order pattern over the given range that can be assigned to the aromatic protons). Elemental analysis: Calculated for $C_8H_6N_4S_2$: C 49.47, H 3.11, N 14.43. Found: C 46.31, H 2.24, N 13.26.

#### 6.4.1.2 [Ni(dcbpy)(qdt)] (16)

$[Ni(H_2O)_6]Cl_2$ (243.4 mg, 1.02 mmol) in 20 mL ethanol and dcbpy (252.7 mg, 1.04 mmol) in 6 mL ethanol with NaOH (100 mg, 2.50 mmol) were stirred for 1 min, before addition of qdt (201.7 mg, 1.05 mmol) in 5 mL ethanol with NaOH (84.39 mg, 2.11 mmol). The resulting purple reaction mixture yielded a red/purple precipitate which was collected by filtration. Yield

= 54.3 %. $\delta_H$(solvent, 250 MHz)/ppm: 7.45 (m, 2H-qdt), 7.70 (m, 2H, H-qdt), 7.95 (d, J = 3.93 Hz, 2H, H-bpy), 8.86 (d, J = 4.83 Hz, 2H, H-bpy), 8.99 (s, 2H, H-bpy). MS (positive ESI): *m/z:* 468 $M^+$.

### 6.4.1.3 [Ni(decbpy)(qdt)] (17)

$[Ni(H_2O)_6]Cl_2$ (48.5 mg, 0.20 mmol) in 5 mL ethanol and decbpy (61.8 mg, 0.21 mmol) in 6 mL DCM were stirred for 2 min before addition of qdt (39.2 mg, 0.20 mmol) in 5 mL ethanol and 5 mL aqueous sodium hydroxide (0.1M). The reaction was left to stir for 30 min, concentrated to a minimum volume and the product obtained as a solid precipitate by addition of excess ethanol. Precipitate was collected by centrifugation and washed with 10 mL ethanol. Yield = 35 %. $\delta_H$(DMSO, 250 MHz)/ppm: 1.61 (b, 6H, $-CH_2-CH_3$), 4.65 (b, 4H, $-CH_2-CH_3$), 7.45 (b, 2H, H-qdt), 7.69 (b, 2H, H-qdt), 8.22 (b, 2H, H-bpy), 9.09 (b, 2H, H-bpy), 9.22 (b, 2H, H-bpy). MS (positive FAB); *m/z*: 551 $M^+$. Elemental analysis: calculated for $C_{24}H_{28}N_4O_8S_2Ni$: C 42.24, H 4.53, N 9.00. Found: C 45.06, H 3.70, N 8.75

### 6.4.1.4 [Ni(decbpy)$Cl_2$] (18)

$[Ni(H_2O)_6]Cl_2$ (100.8mg, 0.42 mmol) in 5 mL THF had a suspension of decbpy (76.9mg, 0.26 mmol) in THF (5ml) added over 3mins and the solution stirred for 2.5h. The precipitate was collected by filtration, washed with THF and dried. Yield: 117.0mg (64%). Found: C, 44.67; H, 3.82; N, 6.19. Calc. for $C_{16}H_{16}O_4N_2NiCl_2$: C, 44.73; H, 3.73; N, 6.52. +FAB-MS; *m/z*: 393 $M^+$(-Cl).

## 6.5 References


1. S. Ferrere and B. A. Gregg, *Journal of the American Chemical Society*, 1998, **120**, 843-844.
2. S. Ferrere, *Chemistry of Materials*, 2000, **12**, 1083-1089.
3. S. Ferrere, *Inorganica Chimica Acta*, 2002, **329**, 79-92.
4. M. K. Nazeeruddin, A. Kay, I. Rodicio, R. Humphry-Baker, E. Mueller, P. Liska, N. Vlachopoulos and M. Graetzel, *Journal of the American Chemical Society*, 1993, **115**, 6382-6390.
5. M. K. Nazeeruddin, R. Humphry-Baker, P. Liska and M. Graetzel, *The Journal of Physical Chemistry B*, 2003, **107**, 8981-8987.
6. S. E. Koops, B. C. O'Regan, P. R. F. Barnes and J. R. Durrant, *Journal of the American Chemical Society*, 2009, **131**, 4808-4818.
7. S. M. Kuebler and R. G. Denning, *Chemical Physics Letters*, 1996, **250**, 120-127.
8. E. A. M. Geary, L. J. Yellowlees, L. A. Jack, I. D. H. Oswald, S. Parsons, N. Hirata, J. R. Durrant and N. Robertson, *Inorganic Chemistry*, 2004, **44**, 242-250.
9. A. Islam, H. Sugihara, K. Hara, L. P. Singh, R. Katoh, M. Yanagida, Y. Takahashi, S. Murata, H. Arakawa and G. Fujihashi, *Inorganic Chemistry*, 2001, **40**, 5371-5380.
10. A. Islam, H. Sugihara, K. Hara, L. P. Singh, K. Ryuzi, M. Yanagida, Y. Takahashi, S. Murata and H. Arakawa, *New Journal of Chemistry*, 2000, **24**, 343.
11. M. J. Frisch, G. W. Trucks, H. B. Schlegel, G. E. Scuseria, M. A. Robb, J. R. Cheeseman, J. A. M. Jr., T. Vreven, K. N. Kudin, J. C. Burant, J. M. Millam, S.S.Iyengar, T. J., V. Barone, B. Mennucci, M. Cossi, G. Scalmani, N. Rega, G. A. Petersson, H. Nakatsuji, M. Hada, M. Ehara, K. Toyota, R. Fukuda, J. Hasegawa, M. Ishida, T. Nakajima, Y. Honda, O. Kitao, H. Nakai, M. Klene, X. Li, J. E. Knox, H. P. Hratchian, J. B. Cross, V. Bakken, A. C., J. Jaramillo, R. Gomperts, R. E. Stratmann, O. Yazyev, A. J. Austin, R. Cammi, C. Pomelli, J. W. Ochterski, P. Y. Ayala, K. Morokuma, G. A. Voth, P. Salvador, J. J. Dannenberg, V. G. Zakrzewski, S. Dapprich, A. D. Daniels, M. C. Strain, O. Farkas, D. K. Malick, A. D. Rabuck, K. Raghavachari, J. B. Foresman, J. V. Ortiz, Q. Cui, A. G. Baboul, S. Clifford, C. J., B. B. Stefanov, G. Liu, A. Liashenko, P. Piskorz, I. Komaromi, R. L. Martin, D. J. Fox, T. Keith, M. A. Al-Laham, C. Y. Peng, A. Nanayakkara, M. Challacombe, P. M. W. Gill, B. Johnson, W. Chen, M. W. Wong, C. Gonzalez and J. A. Pople, *Gaussian 03, Revised C.02, Gaussian, Inc., Wallingford, CT*, 2004.
12. J. P. Perdew, J. A. Chevary, S. H. Vosko, K. A. Jackson, M. R. Pederson, D. J. Singh and C. Fiolhais, *Physical Review B*, 1992, **46**, 6671.
13. J. P. Perdew, K. Burke and Y. Wang, *Physical Review B*, 1996, **54**, 16533.
14. K. L. McCall, J. R. Jennings, H. Wang, A. Morandeira, L. M. Peter, J. R. Durrant, L. J. Yellowlees, J. D. Woollins and N. Robertson, *Journal of Photochemistry and Photobiology A: Chemistry*, 2009, **202**, 196-204.
15. L. Yang, J.-K. Feng, A.-M. Ren, M. Zhang, Y.-G. Ma and X.-D. Liu, *European Journal of Inorganic Chemistry*, 2005, **2005**, 1867-1879.
16. M. A. Thompson, http://www.arguslab.com.
17. N. Armaroli, *Chemical Society Reviews*, 2001, **30**, 113-124.
18. J. N. Clifford, E. Palomares, M. K. Nazeeruddin, M. Grätzel and J. R. Durrant, *The Journal of Physical Chemistry C*, 2007, **111**, 6561-6567.
19. S. Ito, H. Miura, S. Uchida, M. Takata, K. Sumioka, P. Liska, P. Comte, P. Pechy and M. Gratzel, *Chemical Communications*, 2008, 5194-5196.
20. R. Chen, X. Yang, H. Tian, X. Wang, A. Hagfeldt and L. Sun, *Chemistry of Materials*, 2007, **19**, 4007-4015.
21. H. Choi, J. K. Lee, K. H. Song, K. Song, S. O. Kang and J. Ko, *Tetrahedron*, 2007, **63**, 1553-1559.

22. K. Sayama, S. Tsukagoshi, T. Mori, K. Hara, Y. Ohga, A. Shinpou, Y. Abe, S. Suga and H. Arakawa, *Solar Energy Materials and Solar Cells*, 2003, **80**, 47-71.
23. J. H. Yum, S. Moon, R. Humphry-Baker, P. Walter, T. Geiger, F. Nuesch, M. Gratzel and M. K. Nazeeruddin, *Nanotechnology*, 2008, **19**, 424005.
24. S. Ito, P. Liska, P. Comte, R. Charvet, P. Pechy, U. Bach, L. Schmidt-Mende, S. M. Zakeeruddin, A. Kay, M. K. Nazeeruddin and M. Gratzel, *Chemical Communications*, 2005, 4351-4353.
25. P. M. Sommeling, B. C. O'Regan, R. R. Haswell, H. J. P. Smit, N. J. Bakker, J. J. T. Smits, J. M. Kroon and J. A. M. van Roosmalen, *The Journal of Physical Chemistry B*, 2006, **110**, 19191-19197.
26. P. G. Hoertz, A. Staniszewski, A. Marton, G. T. Higgins, C. D. Incarvito, A. L. Rheingold and G. J. Meyer, *Journal of the American Chemical Society*, 2006, **128**, 8234-8245.
27. F. H. Case, *Journal of the American Chemical Society*, 1946, **68**, 2574-2577.
28. L. J. Theriot, K. K. Ganguli, S. Kavarnos and I. Bernal, *Journal of Inorganic and Nuclear Chemistry*, 1969, **31**, 3133-3140.
29. E. S. Böes, P. R. Livotto and H. Stassen, *Chemical Physics*, 2006, **331**, 142-158.
30. N. Papageorgiou, W. F. Maier and M. Gratzel, *Journal of The Electrochemical Society*, 1997, **144**, 876-884.

# 7. Chapter Seven:

# *In situ* Sensitisation

## 7.1 Introduction

The manufacture of a DSSC involves many processes, with the focus of this thesis being the synthesis of the sensitiser complexes and subsequent adsorption of them onto the surface of the $TiO_2$, as outlined in detail in Chapter Two section 2.4. This generally involves three main steps; (i) synthesis and isolation of ligands; (ii) synthesis and isolation of the sensitiser complex; and (iii) sensitisation of the $TiO_2$ surface. The work outlined in this chapter aims to make the first step as synthetically simple as is possible, and to eliminate the second step entirely. The Latin phrase *in situ* translates into English to mean *in the place*, and when used within the context of chemistry, *in situ* has come to typically mean "in the reaction mixture". The idea behind this work is to utilise the method of *in situ* sensitisation and carry out complex formation and $TiO_2$ sensitisation simultaneously.

The possibility of *in situ* sensitisation is available for Cu(I) complexes and not Ru(II) complexes due to the high lability of the former compared to inertness of the latter at ambient conditions. These characteristics arise due to their vastly different ligand field stabilisation energies (LFSE); Cu(I) LFSE = 0, and Ru(II) LFSE = -2.4 $\Delta_O$ (strong-field for bipyridyl containing species). The increased LFSE means that the Ru(II) complexes have stronger metal-ligand binding, therefore making them more inert. The metal-ligand binding is further strengthened by the improved ligand orbital overlap with the larger 4d orbitals of ruthenium compared to that of the 3d orbitals of copper. To gain an idea of the difference in the reaction kinetics: the timescale of ligand exchange for an inert complex typically ranges from ~$10^2$ to 60 s, while for labile complex the rate of ligand exchange is much faster, ranging from 1 ms – 1 ns.[1]

Another possible beneficial outcome from the use of *in situ* sensitisation comes as there is both a high financial and time cost associated with the methods currently employed. The synthesis

of the sensitisers takes additional time and skill, not to mention the environmental cost associated with the solvents used and by-product disposal. One of the main contributors to these is the high level of purity desired in the final product. Application of an *in situ* method may mean that there could be a reduction in the time and resources required to make a Cu(I) sensitised DSSC.

Here we look to explore *in situ* sensitisation, which to the best of our knowledge, has not been reported in the peer-reviewed published literature. There has been a previous study carried out and reported in the Thesis of Ana Hernández Redondo.[2] The work looked to utilise the technique to obtain $TiO_2$ sensitised with heteroleptic $[Cu(bipyridyl)_2]^+$ complexes.

Our work looks to explore the wider application of this technique, and so includes multiple systems for differing experimental reasons. Each system is made up of several component parts: the $TiO_2$ anchoring ligand shown in Figure 1 (a); the central Cu(I) atom; and the co-ligand, shown in Figure 1 (b-d); and finally the sensitisation solvent system. The exact details of these will be discussed later in this work. The main drawback to this technique is that the identification of which species, if anything, has adsorbed onto the surface of the $TiO_2$ is not qualitative. We have attempted to address this in some way by manufacturing a control cell for each different co-ligand series; a cell which will not be soaked in the anchoring ligand dye bath, but will be soaked in any subsequent Cu(I) and co-ligand dye bath(s). Comparisons can then be drawn against the control cell which may provide an insight into the chemical nature of the adsorbed species.

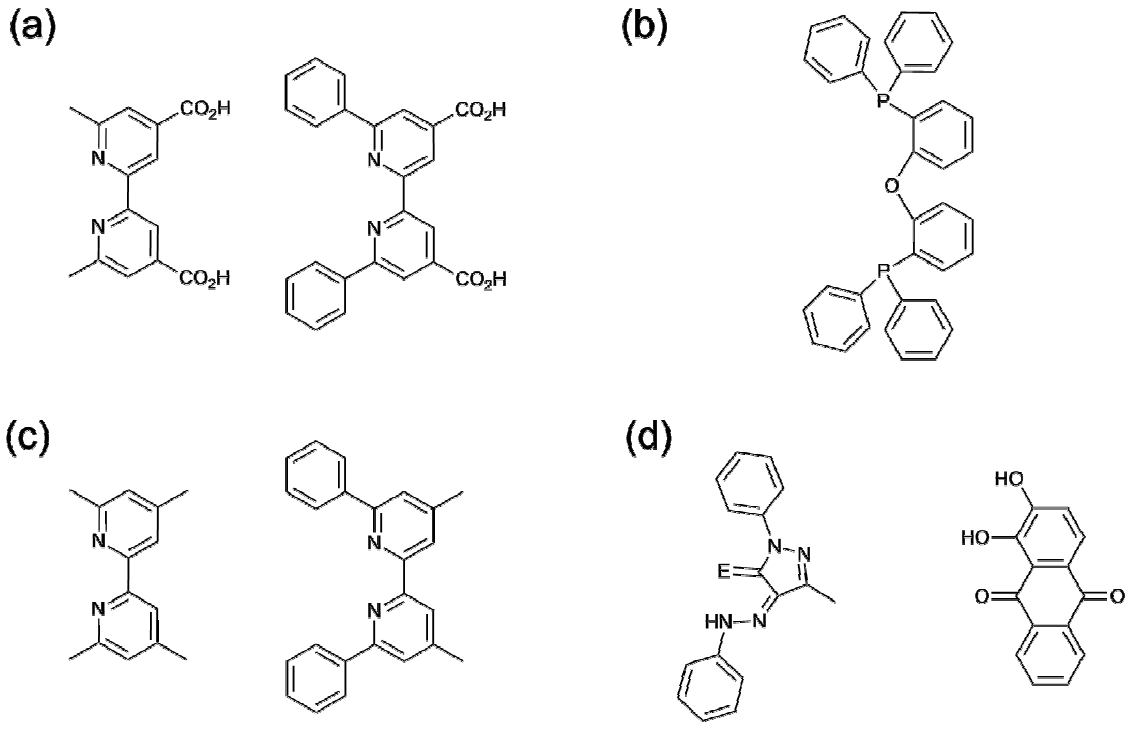


**Fig. 1** Structures of the Ligands used in this work: (a) Anchoring ligand; and Co-Ligands (b) POP; (c) tmbpy and dpdmby; and (d) pmppE (where E=S, O), and alizarine (1,2-dihydroxyanthraquinone).

## 7.2 Results and Discussion

### 7.2.1 Syntheses

The ligands 4,4′-dicarboxy-2,2′-bipyridine (dcbpy), 4,4′,6,6′-tetramethyl-2,2′-bipyridine (tmbpy), 4,4′-dimethyl-6,6′-diphenyl-2,2′-bipyridine (dpdmbpy) and 4,4′-dicarboxy-6,6′-diphenyl-2,2′-bipyridine (dpdmbpy), and the starting complexes $[Cu(MeCN)_4][BF_4]$ were synthesised using modified literature methods as described in the Experimental section of Chapter Three. The ligand bis[2-(diphenylphosphanyl)phenyl] ether (POP) and the starting material $[Cu(POP)(MeCN)_2][BF_4]$ was synthesised by Dr Omar Moudam. Ligands pmppT and pmppO were synthesised by Dr Andrew Smith.[3] Alizarine and all other chemicals were purchased from Aldrich and used as received.

### 7.2.2 *In situ* Sensitisation General Procedure

The procedure for the manufacture of a standard solar cell followed during this work is outlined in Chapter Two (section 2.4). The methods used in this chapter for the sensitisation of $TiO_2$ coated cells takes its lead from the sensitisation techniques utilised in Chapter Three; section 3.3.7. Figure 2 contains a schematic of the different methods used including the contents and order of the dye baths used in each method. Further details of the *in situ* sensitisation processes carried out for each system investigated will be given in the relevant subsection of the Experimental details (section 7.4.2).

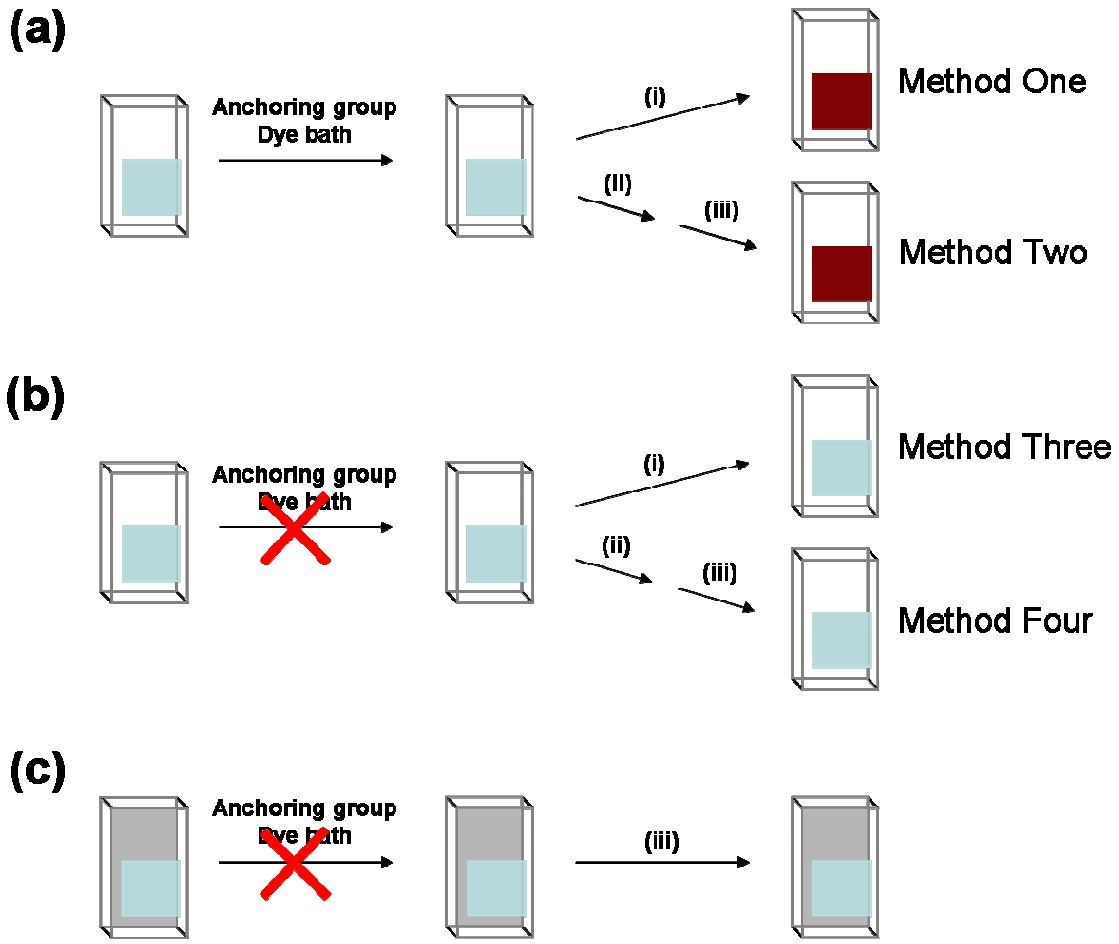


**Fig. 2** Schematic showing in situ sensitisation methods used for (a) Full Sensitisation; (b) Control One; and (c) Control Two; where (i) Cu(I) and co-ligand Dye Bath; (ii) Cu(I) Dye Bath; and (iii) Co-ligand Dye Bath.

Absorption studies have been used to approximate the relative $TiO_2$ surface coverage achieved by each sensitisation technique. An initial absorbance measurement was taken after soaking in the anchoring group dye bath for the cells undergoing full sensitisation, and prior to any soaking of the control cells. A final absorbance measurement was taken after all soaking processes had been completed. This method of analysis can suggest whether the dye has formed on the $TiO_2$ *in situ*, and in the case of the [Cu(POP)(dcbpy)][$BF_4$], allow confirmation by comparison with the absorption spectra of **6** in solution (Chapter Three).

*I-V* characterisation was carried out on all solar cells made using our *in situ* sensitisation method and power-conversion efficiencies were determined while irradiating under AM 1.5 light (100 $mWcm^{-2}$). Cell efficiencies (η) were calculated using the resulting values of $I_{SC}$ = short circuit current (mA), $V_{OC}$ = open circuit voltage (mV) and ff = fill factor as described in Chapter Two.

## 7.2.3 $[Cu(POP)(bipyridyl)]^+$ System

In order to get a proof of concept a system was required that could be directly compared to a cell made in the usual manner; isolation of the sensitiser complex and then adsorption onto the $TiO_2$. For this reason we selected the $[Cu(POP)(bpy)][BF_4]$ system to be our model system as absorption and *IV* characterisation data can be compared to the results given in Chapter Three, section 3.3.7 The *in situ* sensitisation procedure is given in detail in section 7.4.2.1, of note is that sensitisation Method One was followed for the Full Sensitisation and Method Three for the Control (One) Sensitisation (Figure 2). Diethyl ether was used as the dye bath solvent in accordance with our previous work with [Cu(POP)(bpy)][BF4] systems as it was shown to produce the best $TiO_2$ surface coverage by the sensitiser (Chapter Three). Absorption and IV characterisation data are given in Table 1, with selected absorption spectra *IV* curves shown in Figures 3 and 4 respectively.

**Table 1** Absorption Studies and *IV* Characterisation Data for the $[Cu(POP)(bpy)]^+$ series.

| anchoring ligand | UV-Vis | | $I_{SC}$ / mA | $V_{OC}$ / mV | ff | η |
|---|---|---|---|---|---|---|
| | Initial Absorbance at 404 nm | Final Absorbance at 404 nm | | | | |
| none | 0.009 | 0.066 | [a] | [a] | [a] | [a] |
| dcbpy | 0.193 | 0.691 | 0.240 | 355 | 0.56 | 0.048 |
| dpdcbpy | 0.005 | 0.592 | 0.146 | 420 | 0.40 | 0.025 |

[a]not measured. All dye bath concentrations 2 mM; $V_{OC}$ = open circuit potential, $I_{SC}$ = short circuit current, ff = fill factor, η = power conversion efficiency.

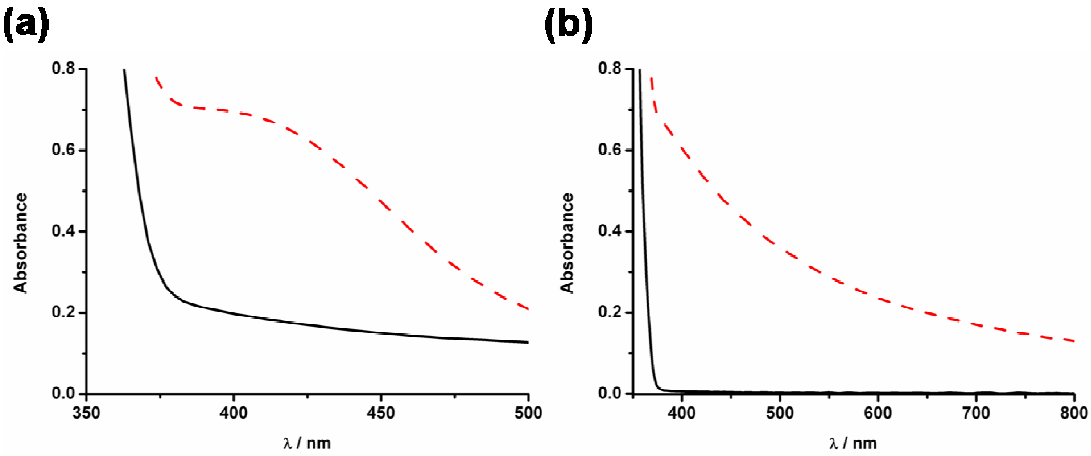


**Fig. 3** UV/Vis Absorption Spectrum for (a) [Cu(POP)(dcbpy)][$BF_4$] and (b) [Cu(POP)(dpdcbpy)][$BF_4$]; where black solid lines = Initial Absorbance, red dashed lines = Final Absorbance.

There is minimal increase in the absorption of the Control Cell at the wavelength of interest: initial absorbance = 0.009, to final absorbance = 0.066 (Table 1), and so subsequent *IV* characterisation was not carried out. This is in sharp contrast to the cells that underwent full sensitisation, whereby the absorption has increased significantly (Figure 3 and Table 1). Absorption of both these $TiO_2$ sensitised cells occurs at 404 nm (Figure 3 and Table 1), which strongly suggests that the same species is present as that reported in Chapter Three section 3.3.7: $\lambda_{max}$ = 403 nm (A = 0.39). Inspection of the absorption spectra suggests that a higher concentration of the dcbpy analogue has adsorbed onto the surface compared to the dpdcbpy analogue. It also suggests that the formation of a [Cu(POP)(dpdcbpy)][$BF_4$] species is possible using this *in situ* method, while it was not possible to synthesis as an isolated product (Chapter Three).

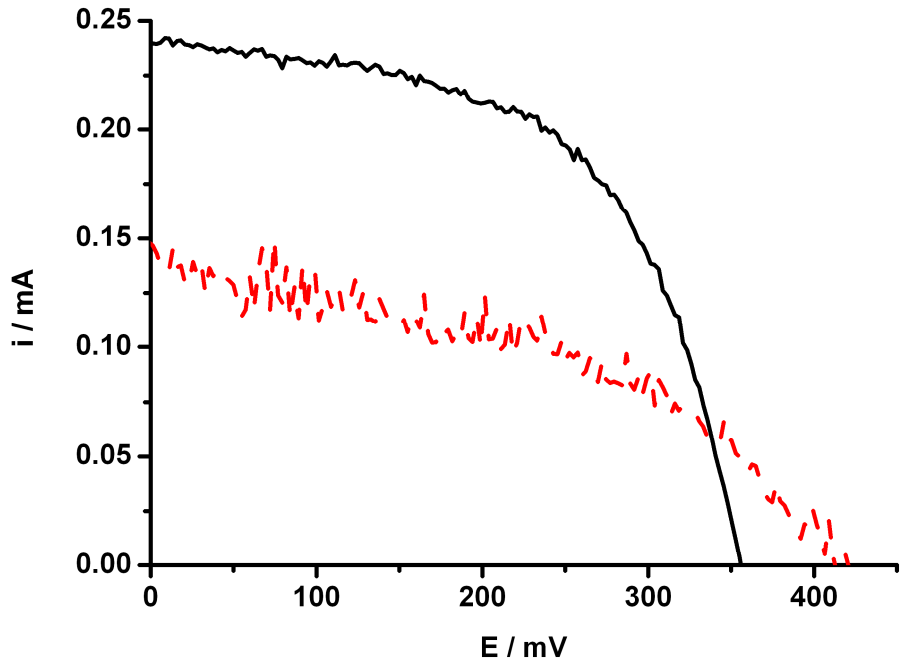


**Fig. 4** *I-V* Curve for [Cu(POP)(dcbpy)][$BF_4$] (black solid line); and [Cu(POP)(dpdcbpy)][$BF_4$] (red dashed line).

The photocurrent and photovoltage produced by the *in situ* method for the [Cu(POP)(dcbpy)][$BF_4$] species are comparable with those quoted for **6** in Chapter Three; 0.240 mA and 355 mV, and 0.233 mA and 347 mV respectively (Figure 4 and Table 1). The *in situ* method does not appear to affect the fill factor achievable by this system, which generally ranges from 0.4 to 0.6 for all of our solar cells. The photovoltage and fill factor observed for the *in situ* [Cu(POP)(dpdcbpy)][$BF_4$] species is also comparable with those of **6**, however there is a reduced photocurrent; 0.146 mA compared to 0.233 mA (Figure 4 and Table 1).

Based upon these results for the *in situ* sensitisation of [Cu(POP)(dcbpy)][$BF_4$] showing no variation from those reported in Chapter Three, we have extended this work to cover a wider range of systems to begin to explore the possibilities of *in situ* sensitisation.

## 7.2.4 Heteroleptic bis-bipyridyl Systems

The next series of co-ligands attempted was based on sensitiers related to the homoleptic $[Cu(I)(bipyridyl)_2]^+$ DSSC sensitisers synthesised by Constable *et al*. in 2009.[4] This strategy was adopted to allow comparisons to be drawn against structurally similar sensitisers. In our attempts the complexes were not homoleptic; with one carboxyl-substituted bipyridly (Figure 1 (a)), and the co-ligand as a methyl or phenyl-substituted bipyridyl (Figure 1 (c)). Two different *in situ* conditions were tried for these sensitisations: A and B, the details of which will be discussed in sections 7.2.4.1 and 7.2.4.2 respectively. For both *in situ* conditions tried for these heteroleptic bis-bipyridyl systems, sensitisation Method Two was used for the Full Sensitisation and Method Four for the Control (One) Sensitisation (Figure 2).

### 7.2.4.1 *In situ* Conditions A

The *in situ* sensitisation procedure for Conditions A are given in detail in section 7.4.2.2.1. Of note is that as for our model system, diethyl ether was used as the dye bath solvent. Absorption and IV characterisation data is given in Table 2, with absorption spectra for Conditions A shown in Figures 5.

When tmbpy was used as the co-ligand a minimal increase in the absorption of the control cell was observed at the wavelength of interest, however the same is not true when the dpdmbpy was used in the role of co-ligand (Figure 5 and Table 2). Absorption of the fully sensitised cells occurs at similar wavelengths for this cell and the control cell (Figure 5 and Table 2), perhaps suggesting formation of the bis-homoleptic complex $[Cu(dpdmbpy)_2][BF_4]$.

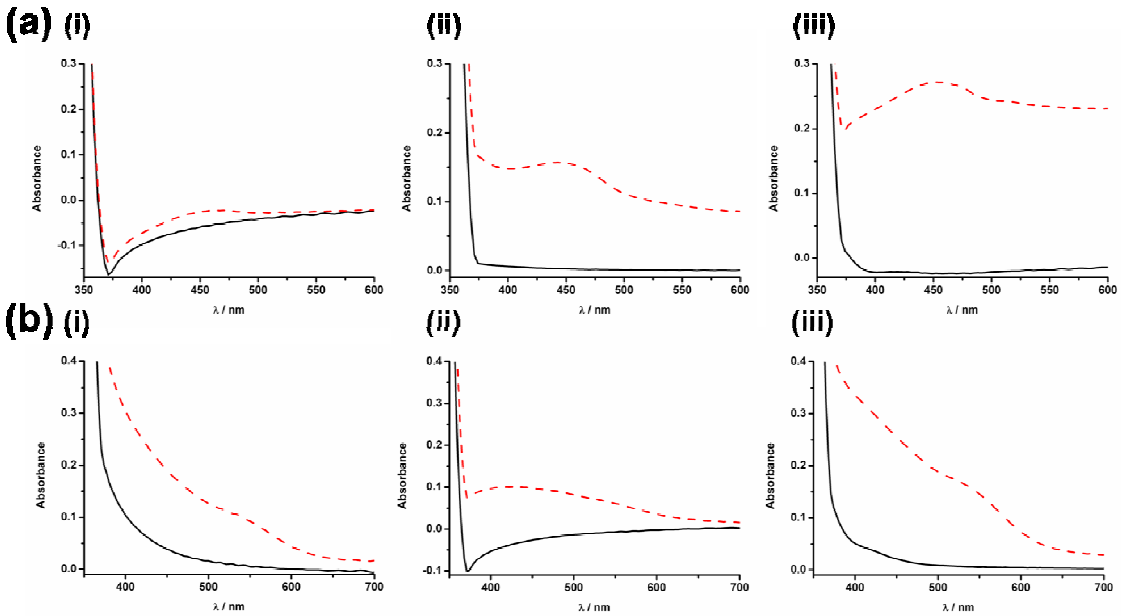


**Fig. 5** UV/Vis Absorption Spectrum for Conditions A; (a) [Cu(tmbpy)(anchoring ligand)][$BF_4$], and (b) [Cu(dpdmbpy)(anchoring ligand)][$BF_4$], where the anchoring ligand is (i) no anchoring ligand; (ii) dcbpy and (iii) dpdcbpy; black solid lines = Initial Absorbance, red dashed lines = Final Absorbance.

Inspection of the final absorption spectra for the tmbpy series shows a high base-line (Figure 5 (a)(ii) and (iii)). This is the result of a small quantity of unknown red solid on the $TiO_2$ surface. The cause of this red solid could be unbound [$Cu(MeCN)_4$][$BF_4$] (left on the surface of the $TiO_2$ after soaking in the Cu(I) Dye Bath), that, when placed into the Co-ligand Dye Bath, reacts with the tmbpy to form [$Cu(tmbpy)_2$][$BF_4$]. Section 7.2.4.1 goes on to address this behaviour by outlining research into alternative *in situ* conditions.

The photocurrents and photovoltages produced by cells manufactured following Conditions A for both co-ligands do not appear to follow a trend that can be easily explained. Furthermore the values are considerably poorer than similar homoleptic bis-bipyridyl systems quoted by Constable *et al.*;[4] methyl: 1.15 mA and 530 mV, and phenyl 0.69 mA and 484 mV; where sensitisation followed isolation of the sensitiser complex.

**Table 2** Absorption Studies and *IV* Characterisation Data for the heteroleptic bis-bipyridyl series.

| co-ligand | soaking conditions | anchoring ligand | UV-Vis | | | $I_{SC}$ / mA | $V_{OC}$ / mV | ff | η |
|---|---|---|---|---|---|---|---|---|---|
| | | | λ / nm | Initial Absorbance | Final Absorbance | | | | |
| tmbpy | A | none | [a] | [a] | [a] | [a] | [a] | [a] | [a] |
| | A | dcbpy | 447 | 0.003 | 0.157 | 0.055 | 216 | 0.29 | 0.003 |
| | A | dpdcbpy | 454 | 0.000 | 0.272 | 0.102 | 432 | 0.39 | 0.017 |
| tmbpy | B | none | 454 | 0.008 | 0.111 | 0.078 | 243 | 0.40 | 0.008 |
| | B | dcbpy | 447 | 0.026 | 0.084 | [a] | [a] | [a] | [a] |
| | B | dpdcbpy | 454 | 0.015 | 0.068 | 0.074 | 270 | 0.40 | 0.008 |
| dpdmbpy | A | none | 415 | 0.075 | 0.261 | 0.149 | 432 | 0.37 | 0.024 |
| | | | 530 | 0.008 | 0.107 | | | | |
| | A | dcbpy | 425 | 0.000 | 0.101 | 0.033 | 61 | 0.26 | 0.005 |
| | A | dpdcbpy | 415 | 0.042 | 0.313 | 0.071 | 273 | 0.40 | 0.008 |
| | | | 530 | 0.006 | 0.167 | | | | |
| dpdmbpy | B | none | 415 | 0.087 | 0.265 | 0.130 | 264 | 0.33 | 0.011 |
| | | | 530 | 0.032 | 0.101 | | | | |
| | B | dcbpy | 425 | 0.000 | 0.311 | [a] | [a] | [a] | [a] |
| | | | 530 | 0.000 | 0.201 | | | | |
| | B | dpdcbpy | 405 | 0.000 | 0.129 | 0.076 | 243 | 0.40 | 0.007 |
| | | | 530 | 0.000 | 0.056 | | | | |

[a]not measured. All dye bath concentrations 2 mM; $V_{OC}$ = open circuit potential, $I_{SC}$ = short circuit current, ff = fill factor, η = power conversion efficiency.

### 7.2.4.2 *In situ* Conditions B

The possible formation of homoleptic $[Cu(I)(bpy)]^+$ species on the $TiO_2$ is undesirable and we looked here to overcome this by adjustment of the solvent system used for the $[Cu(MeCN)_4][BF_4]$ and co-ligand dye baths. The *in situ* sensitisation procedure for Conditions B are given in detail in section 7.4.2.2.2 and of note is that a solvent system of diethyl ether:chloroform (2:1) was used to improve the solubility of the species in the hope of allowing more successful adsorption. Absorption and IV characterisation data are given in Table 2, with absorption spectra for conditions B shown in Figure 6.

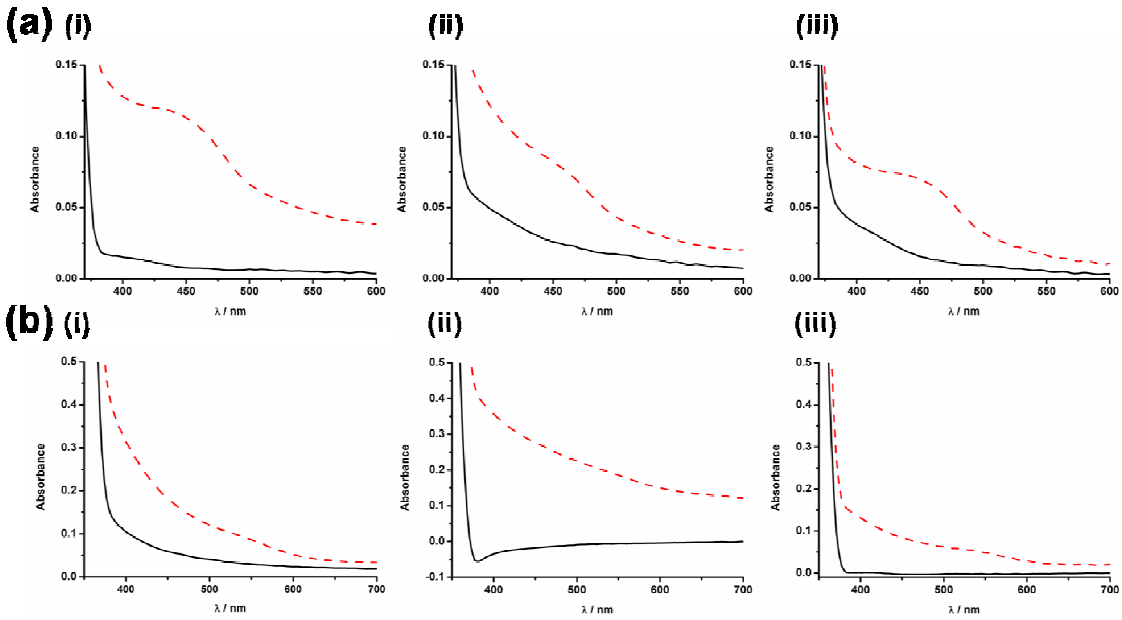


**Fig. 6** UV/Vis Absorption Spectrum for Conditions B; (a) [Cu(tmbpy)(anchoring ligand)][$BF_4$], and (b) [Cu(dpdmbpy)(anchoring ligand)][$BF_4$], where the anchoring ligand is (i) no anchoring ligand; (ii) dcbpy and (iii) dpdcbpy; black solid lines = Initial Absorbance, red dashed lines = Final Absorbance.

Our adaptation of the solvent system worked in that no solid was observed on the $TiO_2$ surface, however, the desired result was not completely observed. The absorption studies carried out on both sets of $TiO_2$ sensitised cells (co-ligand = tmbpy or dpdmbpy) show that adsorption occurs without the presence of an anchoring ligand (Figure 6(i) and Table 2), behaviour that did not occur for the [Cu(POP)(bpy)][$BF_4$] series. For both co-ligands, absorption studies suggest that the control and dpdcbpy cells have the same species present on the $TiO_2$ surface (Figure 6 and Table 2). This species was not identified but could perhaps be the bis-homoleptic species; [$Cu(tmbpy)_2$][$BF_4$] and [$Cu(dpdmbpy)_2$][$BF_4$].

As for Conditions A (section 7.2.4.1), *IV* characterisation yielded poor values for photocurrent, photovolage and fill factor with no explainable trend.

## 7.2.5 Novel Heteroleptic Systems

### 7.2.5.1 pmppE Systems

The work reported here carries on from the work presented in Chapter Five where it was not possible to syntheses a pmppE containing complex suitable as a DSSC sensitiser as an isolated product. The *in situ* sensitisation procedure followed Method One for the Full Sensitisation and Method Three for the Control (One) Sensitisation (Figure 2) and is given in detail in section 7.4.2.3.1, of note is that as for the [Cu(POP)bpy)][$BF_4$] system, the diethyl ether was used as the dye bath solvent. Absorption and IV characterisation data are given in Table 3, with absorption spectra shown in Figures 7. There is minimal increase in the absorption of the control cell for both co-ligands (pmppT and pmppO) at the wavelength of interest (Table 3) and so subsequent *IV* characterisation was carried out.

**Table 3** Absorption Studies and *IV* Characterisation Data for the [Cu(pmppE)(anchoring ligand)]$^+$ series.

| co-ligand | anchoring ligand | UV-Vis | | | $I_{SC}$ / mA | $V_{OC}$ / mV | ff | η |
|---|---|---|---|---|---|---|---|---|
| | | λ / nm | Initial Absorbance | Final Absorbance | | | | |
| pmppT | none | 390 | 0.101 | 0.144 | [a] | [a] | [a] | [a] |
| | | 480 | 0.042 | 0.056 | | | | |
| | dcbpy | 390 | 0.005 | 0.551 | 0.055 | 264 | 0.29 | 0.004 |
| | | 480 | 0.006 | 0.232 | | | | |
| | dpdcbpy | 390 | 0.071 | 0.045 | 0.137 | 423 | 0.39 | 0.022 |
| | | 480 | 0.029 | 0.015 | | | | |
| pmppO | none | 385 | 0.000 | 0.000 | [a] | [a] | [a] | [a] |
| | dcbpy | 385 | 0.126 | 0.541 | 0.068 | 87 | 0.27 | 0.002 |
| | dpdcbpy | 401 | 0.081 | 0.139 | 0.176 | 523 | 0.41 | 0.038 |
| | | 470 | 0.038 | 0.075 | | | | |

[a]not measured. All dye bath concentrations 2 mM; $V_{OC}$ = open circuit potential, $I_{SC}$ = short circuit current, ff = fill factor, η = power conversion efficiency.

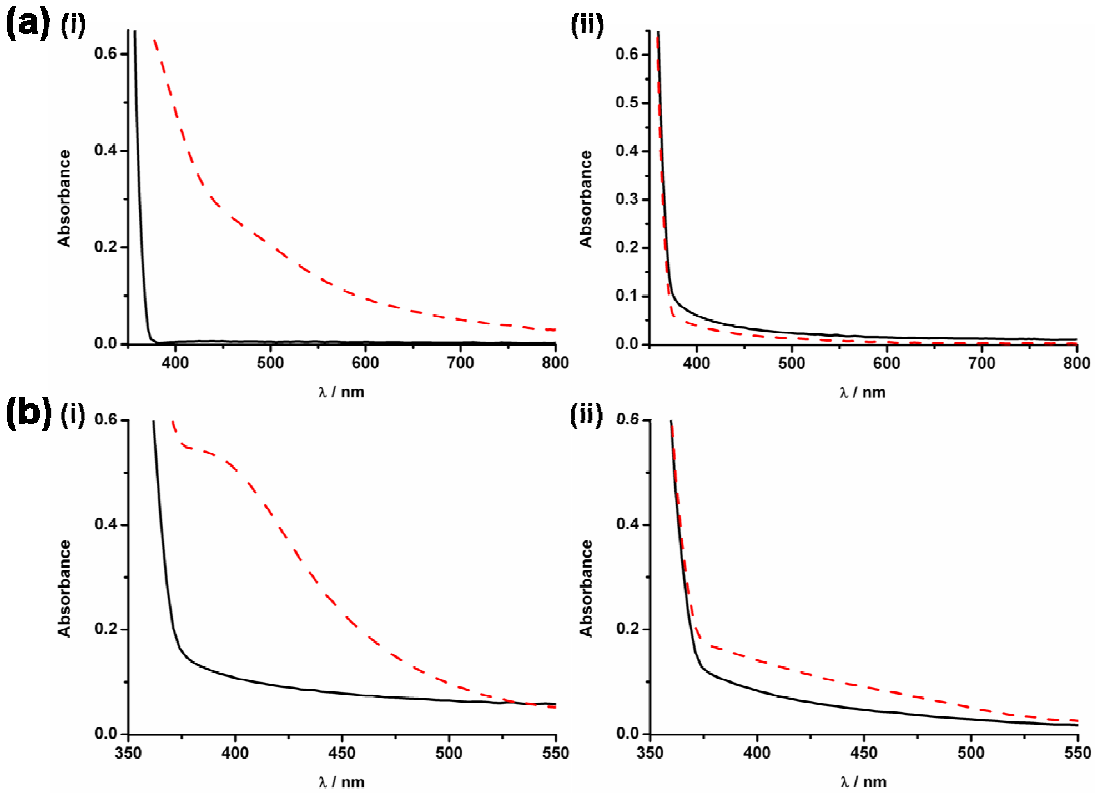


**Fig. 7** UV/Vis Absorption Spectrum for (a) [Cu(pmppT)(anchoring ligand)] and (b) [Cu(pmppO)(anchoring ligand)], where the anchoring ligand is (i) dcbpy and (ii) dpdcbpy; black solid lines = Initial Absorbance, red dashed lines = Finial Absorbance.

The key observation from these absorption studies is that for the dcbpy containing systems there is a noticeable increase in absorption after the sensitisation process which is not seen for the dpdcbpy containing cells (Figure 7 and Table 3). This would therefore suggest that there is a higher concentration of the dcbpy analogue adsorbed onto the $TiO_2$ surface. However *IV* characterisation showed that the dpdcbpy-containing attempt produced the larger photocurrents and photovoltages. One plausible explanation for this could be indicating that the dcbpy-containing attempt might have led to the adsorption of a Cu(II) species as there was not adequate steric constraint placed upon the complex by the co-ligand. This theory is supported by the failure to obtain the analogous methyl complex; [Cu(pmppE)(dmbpy)], as an isolated complex (Chapter Five).

The photovoltages produced by the *in situ* method for the $[Cu(pmppE)(dpdcbpy)]^+$ species are comparable with those seen for our $[Cu(POP)(bpy)]^+$ sensitised cells, however the photocurrents are reduced (Table 3). At this time it is not possible to identify the cause of the reduction in photocurrent.

### 7.2.5.2 Alizarine Systems

Our final system uses the red dye compound Alizarine (1,2-dihydroxyanthraquinone) as the co-ligand as not only does it absorb in the visible, it is capable of coordinating to Cu(I).[5, 6]

The *in situ* sensitisation procedure follows Method Two for the Full Sensitisation, Method Four for the Control One Sensitisation (Figure 2), which are given in detail in section 7.4.2.3.2. Of note is that a solvent system of diethyl ether:chloroform (2:1) was used to increase the solubility of the species in the hope of allowing more successful adsorption. Absorption and IV characterisation data are given in Table 1, with selected absorption spectra *IV* curves shown in Figures 8 and 9 respectively. There was an additional sensitisation carried out for this co-ligand as alizarine can undergo reversible redox processes,[7, 8] to allowed investigation of the nature of the species adsorbed onto the surface of the $TiO_2$ and also the source of any subsequent photocurrents produced. A second control cell was manufactured (procedure outlined in Figure 2) and underwent absorption studies and IV characterisation.

**Table 4** Absorption Studies and *IV* Characterisation Data for the $[Cu(Alizarine)(anchoring\ ligand)]^+$ series.

| anchoring ligand | UV-Vis | | | $I_{SC}$ / mA | $V_{OC}$ / mV | ff | η |
|---|---|---|---|---|---|---|---|
| | λ / nm | Initial Absorbance | Final Absorbance | | | | |
| none | 470 | 0.011 | 1.153 | 0.381 | 423 | 0.30 | 0.016 |
| dcbpy | 477 | 0.013 | 0.818 | 0.208 | 260 | 0.30 | 0.016 |
| dpdcbpy | 500 | 0.000 | 0.581 | 0.364 | 432 | 0.42 | 0.066 |
| none[a] | 450 | 0.000 | 1.455 | 0.199 | 404 | 0.52 | 0.042 |

[a] Not soaked in second dye bath. .All dye bath concentrations 2 mM; $V_{OC}$ = open circuit potential, $I_{SC}$ = short circuit current, ff = fill factor, η = power conversion efficiency.

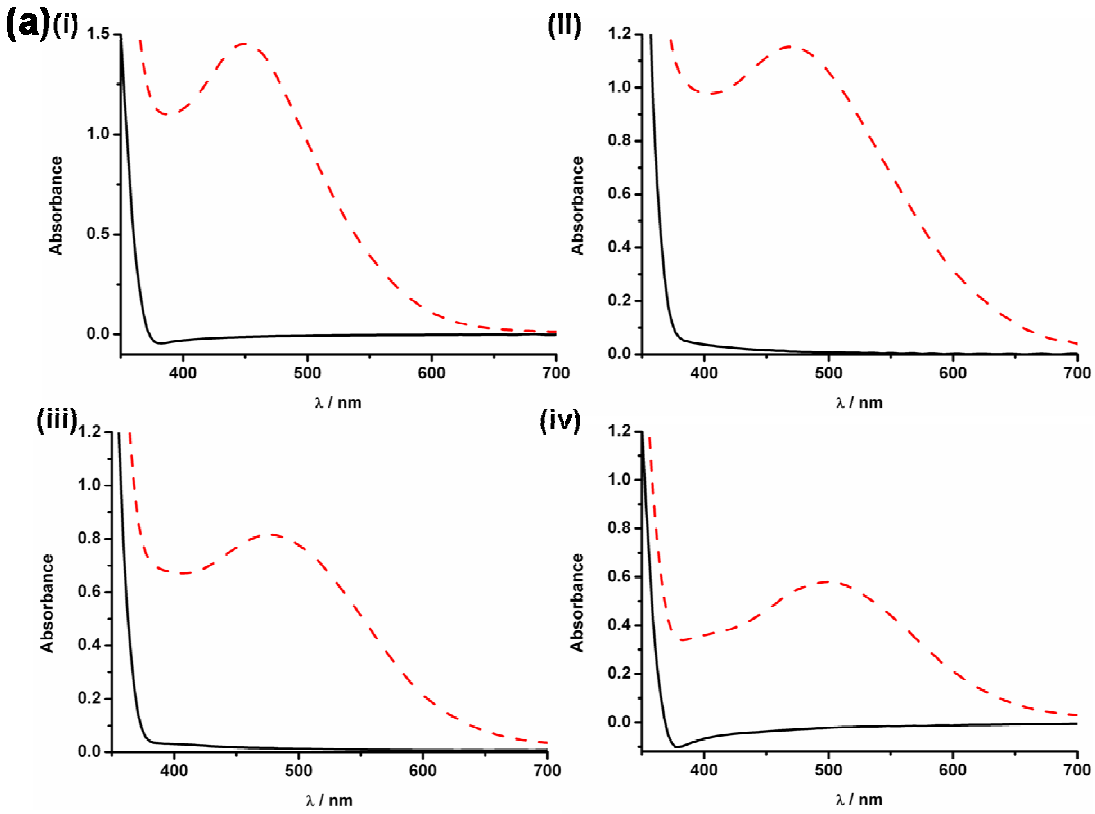


**Fig. 8** UV/Vis Absorption Spectrum for (a) [Cu(Alizarine)(anchoring ligand)], where the anchoring ligand is (i) no anchoring ligand and no $[Cu(I)(MeCN)]^+$; (ii) no anchoring ligand; (iii) dcbpy; and (iv) dpdcbpy; black solid lines = Initial Absorbance, red dashed lines = Final Absorbance.

Control Cell Two (Figure 8(i)) produced a blue shifted absorption peak; $\lambda_{max}$ = 450 nm compared to the Cu(I) containing attempts (Figure 8(ii)-(iv) and Table 4) which suggests that the alizarine has bound to the Cu(I) in these attempts. Comparison of the absorption profile of the Control Cell One (Figure 8 (ii)) with that of the dcbpy containing attempt (Figure 8 (iii)) reveals them to exhibit similar absorption maxima; $\lambda_{max}$ = 470 nm and 477 nm respectively. This may suggest the presence of a bis-alizarine Cu(I) species, and not the desired [Cu(alizarine)(dcbpy)]. The dpdcbpy-containing attempt produces the most red-shifted absorption; $\lambda_{max}$ = 500 nm perhaps indicating the formation of a [Cu(alizarine)(dpdcbpy)] species adsorbed onto the $TiO_2$.

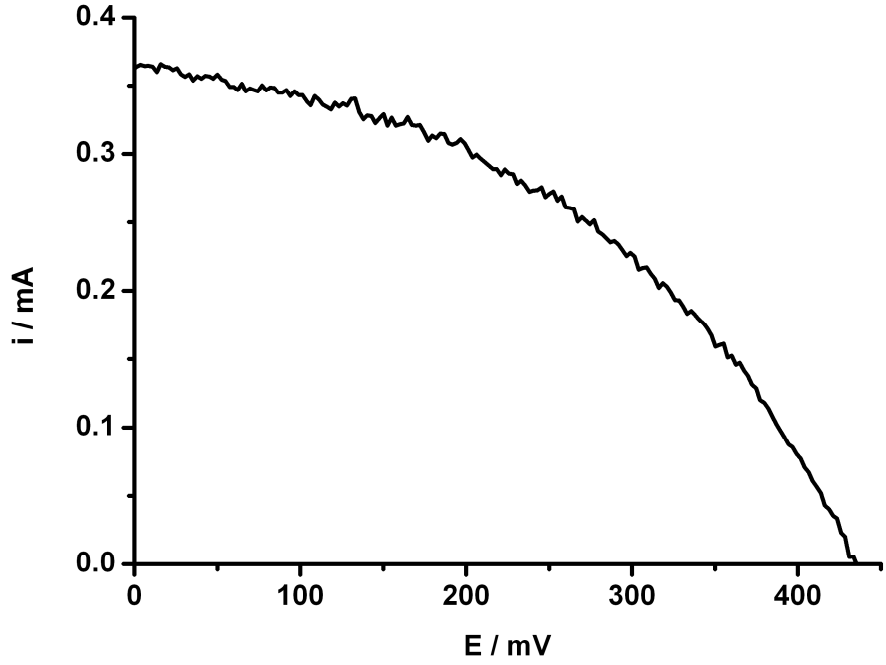


**Fig. 9** *I-V* Curve for [Cu(Alizarine)(dpdcbpy)]$^{+}$.

Inspection of the IV characterisation data for the dpdcbpy attempt and the two control cells (one and two), reveals all three produce similar photovolatges, and that Control Cell One (Figure 8 (ii)) and the dpdcbpy-containing cell (Figure 8 (iv)) produce similar photocurrents (Table 4). Based on this evidence it is not possible to conclude with complete certainty the nature of the adsorbed species. The dcbpy-containing attempt demonstrates a lower photocurrent compared to the dpdcbpy analogue, but one that is comparable to the POP system reported in section 7.2.3. At this stage in this research it is not possible to state any explanation for this, just to say that further analytical experiments are required to obtain a clearer understanding of the nature of the adsorbed species.

## 7.3 Conclusions

Shown here is the *in situ* sensitisation of $TiO_2$ with what we have shown preliminary evidence to be heteroleptic Cu(I) species. There were two anchoring ligands used throughout this work; dcbpy (4,4′-dicarboxy-2,2′-bipyridine) and dpdcbpy (4,4′-dicarboxy-6,6′-diphenyl-2,2′-bipyridine). Variation of the co-ligand alongside both these anchoring ligands was carried out with; POP, tmbpy, dpdmbpy, pmppE and alizarine.

Investigation of the model system [Cu(POP)(bipyridyl)][$BF_4$] suggested that no Cu(I) species adsorbed without the presence of an anchoring group as no absorption was observed for the control cell. This supports our assumption that the attempts containing an anchoring group do contain Cu(I) as both exhibited an absorption peak at $\lambda_{max}$ = 404 nm. Further support for this identification is that in Chapter Three section 3.3.7: [Cu(POP)(dcbpy)][$BF_4$] is reported to exhibit an absorption at $\lambda_{max}$ = 403 nm (A = 0.39). The results also suggest that the *in situ* method allows the formation of the dpdcbpy analogue which was not achieved by synthesis and isolation of the pure product. When compared to the photocurrents and photovoltages produced for **6** in Chapter Three our *in situ* results for [Cu(POP)(dcbpy)][$BF_4$] show little variation; 0.233 mA and 347 mV, and 0.240 mA and 355 mV respectively. The fill factors produced by the *in situ* sensitisation method are also within the same range as those quoted in Chapter Three; 0.4 to 0.6.

The heteroleptic bis-bipyridyl systems investigated produced photocurrents and photovoltages for both co-ligands that did not appear to follow any identifiable trend that could be easily explained. Furthermore, the values are considerably poorer than those seen for the [Cu(POP)(dcbpy)][$BF_4$] system.

When the pmppE ligands were used in the co-ligand role the results although interesting have presented a few questions. The [Cu(pmppE)(dcbpy)] containing systems exhibited a noticeable increase in absorption after the sensitisation process compared to that for the [Cu(pmppE)(dpdcbpy)] containing systems. However *IV* characterisation showed that the dpdcbpy containing attempt produced the larger photocurrents and photovoltages. The exact cause of this in unknown but may be that the [Cu(pmppE)(dcbpy)] species contains a Cu(II) central metal atom as there was not adequate steric constraint placed upon the complex by the co-ligand. This theory is supported by the failure to obtain the analogous methyl complex; [Cu(pmppE)(dmbpy)], as an isolated complex (Chapter Five).

It has proven hard to drawn conclusions from the work carried out on the alizarine co-ligand systems due to the redox behaviour of the free ligand alizarine. However it is believed there is evidence to say that due to the red shift in the absorption peak of the Cu containing attempts; $\lambda_{max}$ = 450 nm to $\lambda_{max}$ > 470 nm, the alizarine has bound to the Cu(I) in these attempts. The photocurrents and photovoltages produced are higher than those seen for the model [Cu(POP)(bpy)][$BF_4$] system, however the cause of them cannot be identified without further investigation.

These initial studies demonstrate that *in situ* sensitisation has been achieved, and cells produced in this manner can produce results comparable with those obtained from cells sensitised with an isolated product. Despite *IV* characterisation revealing low efficiencies there is every expectation that if a better heteroleptic system were identified, it may be transferred to an *in situ* sensitisation procedure.

## 7.4 Experimental

### 7.4.1 General Procedures

The synthesis of bis[2-(diphenylphosphanyl)phenyl] ether (POP),[9] 4,4′-dicarboxy-2,2′-bipyridine (dcbpy),[10] 4,4′,6,6′-tetramethyl-2,2′-bipyridine (tmbpy),[11] 4,4′-dimethyl-6,6′-diphenyl-bipyridine (dpdmbpy),[12] 4,4′-dicarboxy-6,6′-diphenyl-2,2′-bipyridine (dpdcbpy),[10] $[Cu(MeCN)_4][BF_4]$[13] and $[Cu(I)POP(MeCN)_2][BF_4]$[9] were carried out according to literature procedures. The full synthetic details for the ligands dcbpy, tmbpy, dpdmbpy and dpdcbpy are given in Chapter Three, section 3.5.1. The ligand POP and complex $[Cu(I)POP(MeCN)_2][BF_4]$ were synthesised by Dr Omar Moudam. Ligands pmppT and pmppO were synthesised by Dr Andrew Smith.[3] Alizarine (1,2-dihydroxyanthraquinone) and all other chemicals were purchased from Aldrich and used as received.

### 7.4.2 *In situ* Sensitisation Procedures

In all instances the dye bath concentrations were 2 mM as this was found to yield the best $TiO_2$ coverage for our Cu(I) complexes previously reported in Chapter Three. The $TiO_2$ coated cells were heated (100 ºC) for 15 mins before soaking in the anchoring ligand dye bath only and not prior to any other soaking condition. The anchoring ligand dye bath solvent system of MeCN:t-butanol (1:1) and the soaking time of 24 h were used as this provided significant adsorption when used for our previous N719-$TiO_2$ sensitisations.

#### 7.4.2.1 Model [Cu(POP)(bipyridyl)]$^+$ System

Sensitisation Method One followed for the Full Sensitisation and Method Three for the Control (One) sensitisation (Figure 2). The $TiO_2$ coated cells were heated at 100 ºC for 15 mins before soaking in an MeCN:t-butanol (1:1) anchoring ligand dye bath (2 mM) for 24 h (not carried out for Control Cells). The cells were then removed, washed in MeCN and dried in air before having their absorption spectrum recorded (Initial Absorbance). The cells were then soaked in a diethyl ether $[Cu(I)(POP)(MeCN)_2][BF_4]$ dye bath (2 mM) for 24 h, removed, washed in diethyl ether and dried in air before having their absorption spectrum recorded (Final Absorbance).

#### 7.4.2.2 Heteroleptic bis-bipyridyl Systems

##### 7.4.2.2.1 *In situ* Conditions A

Sensitisation Method Two followed for the Full Sensitisation and Method Four for the Control (One) sensitisation (Figure 2). The $TiO_2$ coated cells were heated at 100 ºC for 15 mins before soaking in an MeCN:t-butanol (1:1) anchoring ligand dye bath (2 mM) for 24 h (not carried out for Control Cells) . The cells were then removed, washed in MeCN and dried in air before having their absorption spectrum recorded (Initial Absorbance). The cells were then soaked in a diethyl ether $[Cu(I)(MeCN)_4][BF_4]$ dye bath (2 mM), removed after 5 h and soaked in the appropriate co-ligand diethyl ether dye bath (2 mM) for 22 h. The cells were then washed in diethyl ether and dried in air before having their absorption spectrum recorded (Final Absorbance).

#### 7.4.2.2.2 *In situ* Conditions B

Sensitisation Method Two followed for the Full Sensitisation and Method Four for the Control (One) sensitisation (Figure 2). The $TiO_2$ coated cells were heated at 100 ºC for 15 mins before soaking in an MeCN:t-butanol (1:1) anchoring ligand dye bath (2 mM) for 24 h (not carried out for Control Cells). The cells were then removed, washed in MeCN and dried in air before having their absorption spectrum recorded (Initial Absorbance). The cells were then soaked in a diethyl ether:chloroform (2:1) $[Cu(I)(MeCN)_4][BF_4]$ dye bath (2 mM), removed after 5 h and soaked in the appropriate co-ligand diethyl ether:chloroform (2:1) dye bath (2 mM) for 24 h. The cells were then washed in diethyl ether:chloroform (2:1) and dried in air before having their absorption spectrum recorded (Final Absorbance).

### 7.4.2.3 Heteroleptic Systems

#### 7.4.2.3.1 pmppE Systems

Sensitisation Method One followed for the Full Sensitisation and Method Three for the Control (One) sensitisation (Figure 2). The $TiO_2$ coated cells were heated at 100 ºC for 15 mins before soaking in an MeCN:t-butanol (1:1) anchoring ligand dye bath (2 mM) for 24 h (not carried out for Control Cells) . The cells were then removed, washed in MeCN and dried in air before having their absorption spectrum recorded (Initial Absorbance). The cells were then soaked in a diethyl ether, $[Cu(I)(MeCN)_4][BF_4]$ and pmmE dye bath (2 mM) for 24 h, removed, washed in diethyl ether and dried in air before having their absorption spectrum recorded (Final Absorbance).

#### 7.4.2.3.2 Alizarine Systems

Sensitisation Method One followed for the Full Sensitisation and Method Three for the Control (One) sensitisation (Figure 2). The $TiO_2$ coated cells were heated at 100 ºC for 15 mins before soaking in an MeCN:t-butanol (1:1) anchoring ligand dye bath (2 mM) for 24 h (not carried out for Control Cells). The cells were then removed, washed in MeCN and dried in air before having their absorption spectrum recorded (Initial Absorbance). The cells were then soaked in a diethyl ether:chloroform (2:1) $[Cu(I)(MeCN)_4][BF_4]$ dye bath (2 mM) and removed after 5 h (not carried out for Control Two). The cells were then soaked in a diethyl ether:chloroform (2:1) alizarine dye bath (2 mM) for 24 h. The cells were then washed in diethyl ether:chloroform (2:1) and dried in air before having their absorption spectrum recorded (Final Absorbance).

## 7.5 References


1. D. Shriver and P. Atkins, *Inorganic Chemistry*, Oxford University Press, 1999.
2. A. H. Redondo, University of Basel, Basel, 2009.
3. A. G. Smith, in *School of chemistry*, University of Edinburgh, Edinburgh, 2000.
4. E. C. Constable, A. H. Redondo, C. E. Housecroft, M. Neuburger and S. Schaffner, *Dalton Transactions*, 2009, 6634-6644.
5. S. Das, P. C. Mandal, M. C. Rath and T. Mukherjee, *Research on Chemical Intermediates*, 1999, **25**, 379-391.
6. M. Doskocz, K. Kubas, A. Frackowiak and R. Gancerz, *Polyhedron*, 2009, **28**, 2201-2205.
7. T. Komura, S. Isogai, T. Yamaguchi and K. Takahashi, *Journal of Electroanalytical Chemistry*, 2000, **490**, 70-78.
8. Ŝ. Komorsky-Lovrić, *Fresenius' Journal of Analytical Chemistry*, 1996, **356**, 306-309.
9. N. Armaroli, G. Accorsi, M. Holler, O. Moudam, J. F. Nierengarten, Z. Zhou, R. T. Wegh and R. Welter, *Advanced Materials*, 2006, **18**, 1313.
10. P. G. Hoertz, A. Staniszewski, A. Marton, G. T. Higgins, C. D. Incarvito, A. L. Rheingold and G. J. Meyer, *Journal of the American Chemical Society*, 2006, **128**, 8234-8245.
11. P. Ghosh and T. G. Spiro, *Journal of the American Chemical Society*, 1980, **102**, 5543-5549.
12. R. M. Williams, L. D. Cola, F. Hartl, J.-J. Lagref, J.-M. Planeix, A. D. Cian and M. W. Hosseini, *Coordination Chemistry Reviews*, 2002, **230**, 253-261.
13. O. Moudam, in *LCC-Toulouse*, LCC-Toulouse, Toulouse, 2007.

# 8. Chapter Eight:

# Conclusions

Shown in this thesis is the synthesis and subsequent photoelectrochemical and photophysical characterisation of Cu(I) and Ni(II) complexes of the general formula [M(bpy)(E^E)][$BF_4$] and [M(bpy)(E^E)]. The main driving force behind this work is the development of first row transition metal dye complexes suitable for application in a DSSC device, and the main focus of the thesis being the Cu(I) complexes.

The most extensively investigated series of complexes for this work was that with the general formula [Cu(POP)(bpy)][($BF_4$)] (Chapters Three, Four and Seven). This work reports the first series of heteroleptic Cu(I) complexes applied to DSSC technology in the literature. Chapter Three demonstrates that the blocking ligand, POP, can impart the required level of steric constraint on the geometry of the complex to prevent a Cu(II) complex being formed. However, the photoelectrochemical behaviour displayed by these complexes is not ideal for a DSSC sensitiser as there is not significant quantities of visible light absorbed. Despite this behaviour being expected, the complexes were synthesised as a model system from which to learn about the blocking function required to prevent decomposition of a complex to Cu(II). The possibilities of the [Cu(I)(POP)(bpy)][($BF_4$)] system for use as a DSSC sensitiser have been exhausted and yielded key insights into the connection between structural behaviour and photoeleectrochemical and photophysical behaviour.

The work then progressed to investigate the replacement of the POP ligand with another blocking ligand designed to benefit the photoelectrochemical behaviour of the complex. This led to the exploration of several novel Cu(I) complexes (Chapters Five and Seven), however, the results observed for these were not promising due to synthetic difficulties. To continue the development of this field further, design adaptations need to be made to the blocking ligand to explore the possibilities.

Reported also is the photophysical and computational investigation of two complexes; [Cu(POP)(dmbpy)][($BF_4$)] (**5**) and [Cu(POP)(tmbpy)][($BF_4$)] (**8**). This study highlighted the link between structural rigidity and photophysical behaviour, with the computational calculations providing insight into the nature of structural rearrangement involved.

The final chapter presents preliminary experiments into *in situ* preparation of a DSSC with promising results yielded. In order to expand upon this work a second dye complex needs to be characterised following both the traditional and in situ preparation methods. This would allow additional conformation that it is the desired species which is active and not a by-product.

# Appendix A

## Crystallographic Information

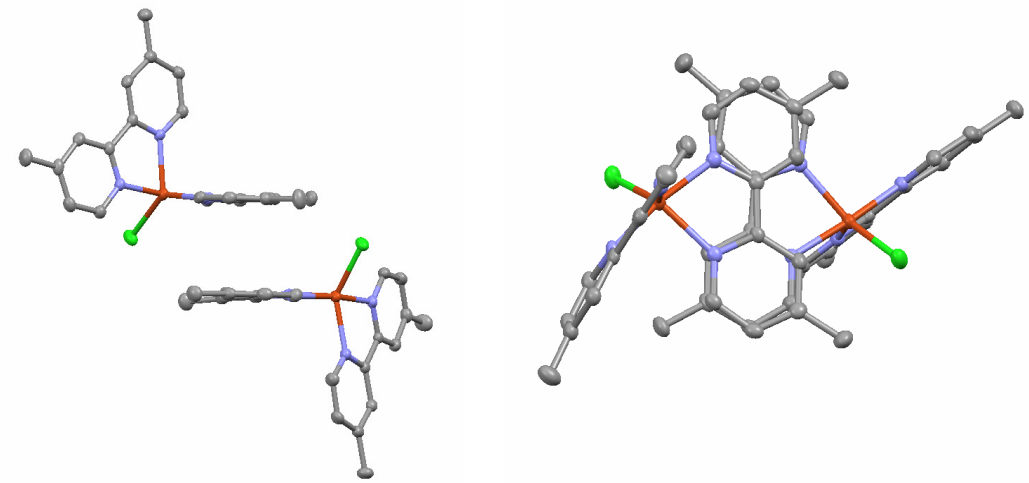

**Fig. A** Mercury plots of $[Cu(dmbpy)_2Cl][BF_4]$ demonstrating π–stacking interactions. Thermal ellipsoids are drawn at the 50% probability level. $[BF_4]$ counter ion omitted for clarity.

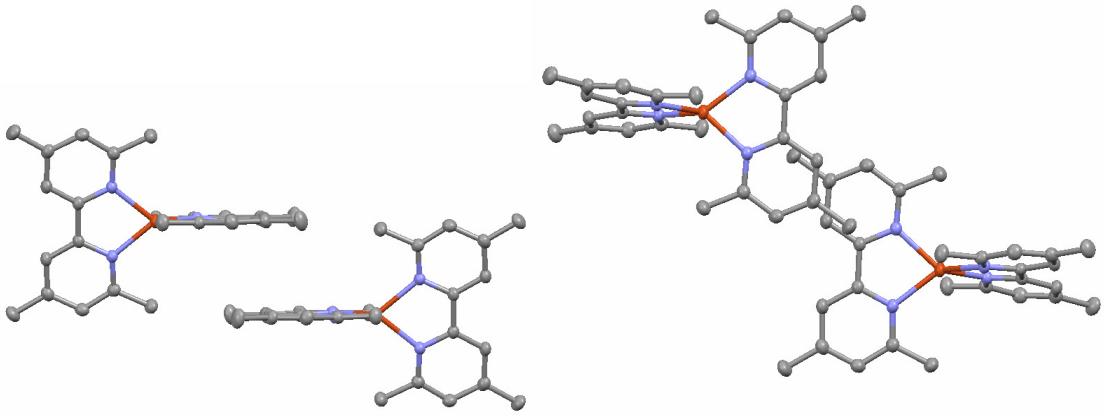

**Fig. B** Mercury plots of **1** demonstrating no π–stacking interactions. Thermal ellipsoids are drawn at the 50% probability level. $[BF_4]$ counter ion omitted for clarity.

## UV-Vis Absorption Spectroscopy

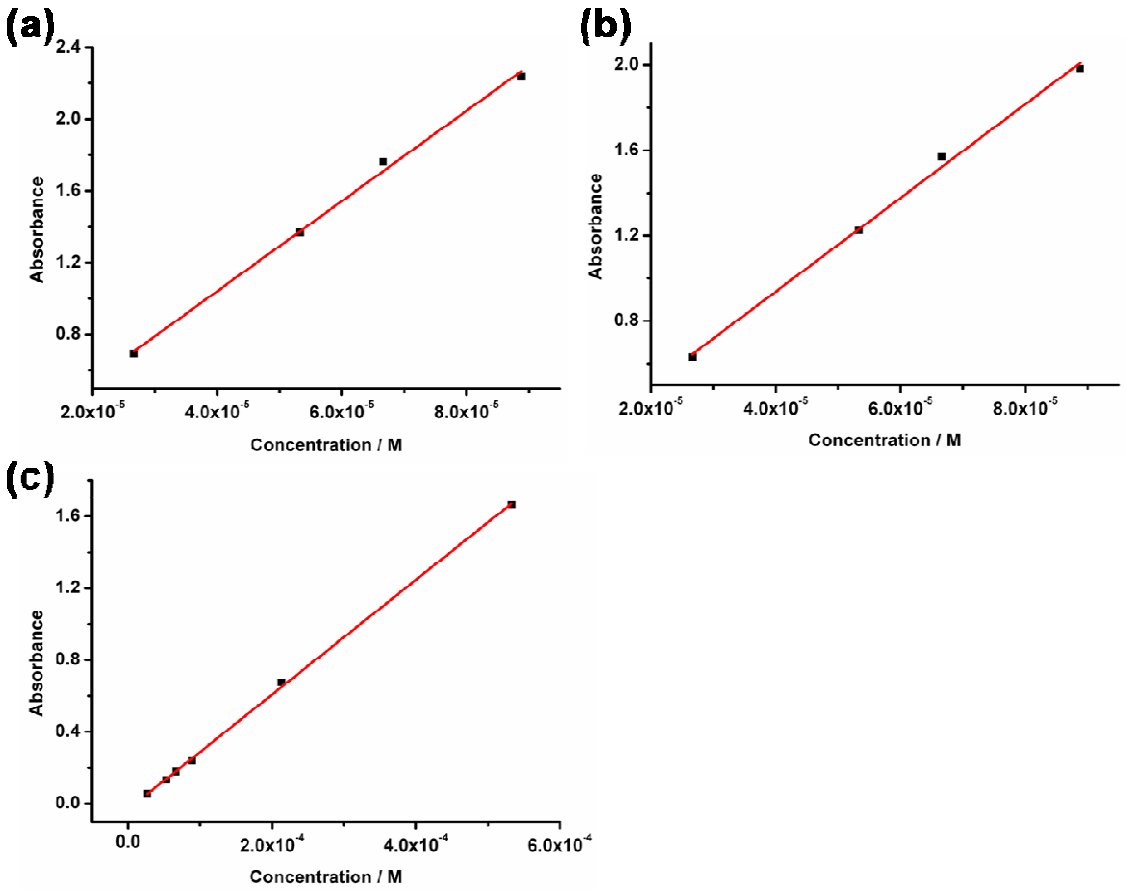


**Fig. C** Absorbance versus Concentration plots for **5** at (a) 248 nm (ε = 25.1 x$10^3$$M^{-1}$$cm^{-1}$), (b) 282 nm (ε = 22.6 x$10^3$$M^{-1}$$cm^{-1}$), and (c) 369 nm (ε = 3.2 x$10^3$$M^{-1}$$cm^{-1}$). Where ε = gradient of the linear fit.

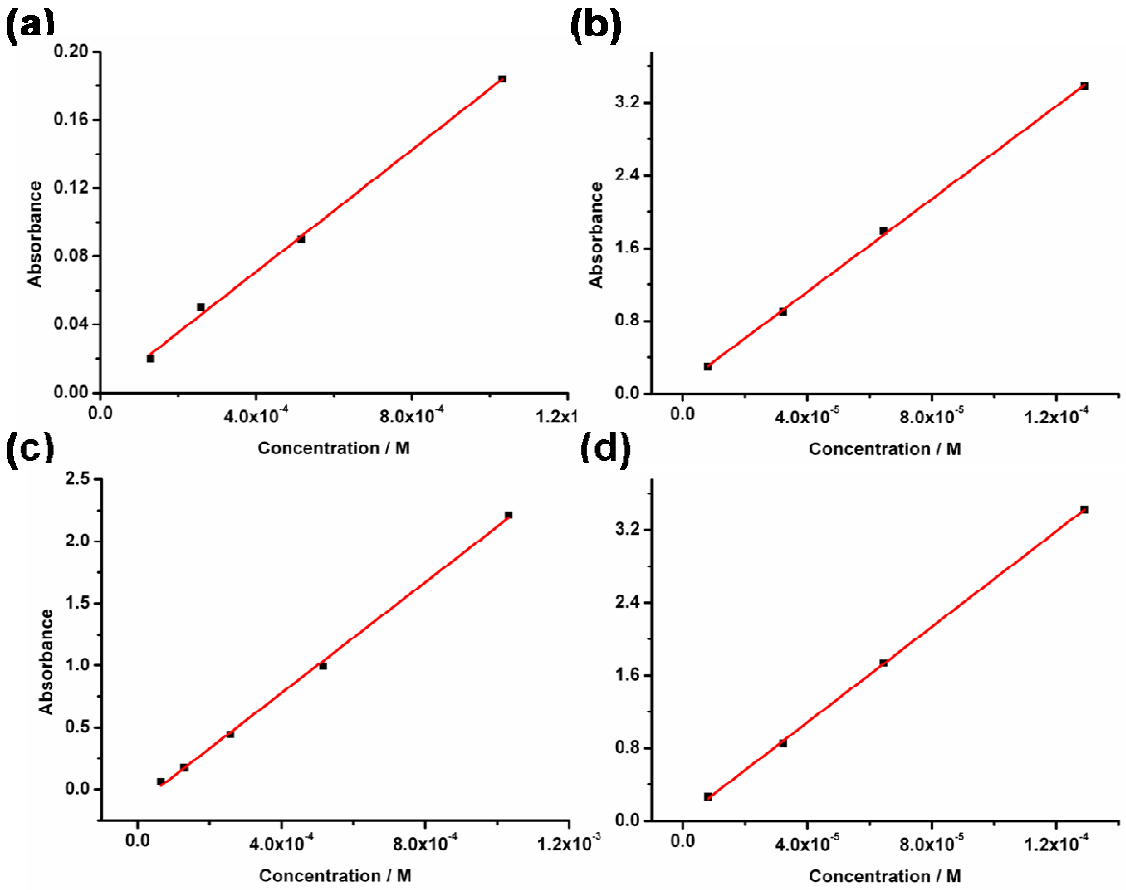


**Fig. D** Absorbance versus Concentration plots for **8** at (a) 250 nm (ε = 26.3 x10$^3$M$^{-1}$cm$^{-1}$), (b) 288 nm (ε = 25.5 x10$^3$M$^{-1}$cm$^{-1}$), (c) 358 nm (ε = 2.2 x10$^3$M$^{-1}$cm$^{-1}$), and (c) 460 nm (ε = 0.2 x10$^3$M$^{-1}$cm$^{-1}$). Where ε = gradient of the linear fit.

## DFT and TDDFT calculations

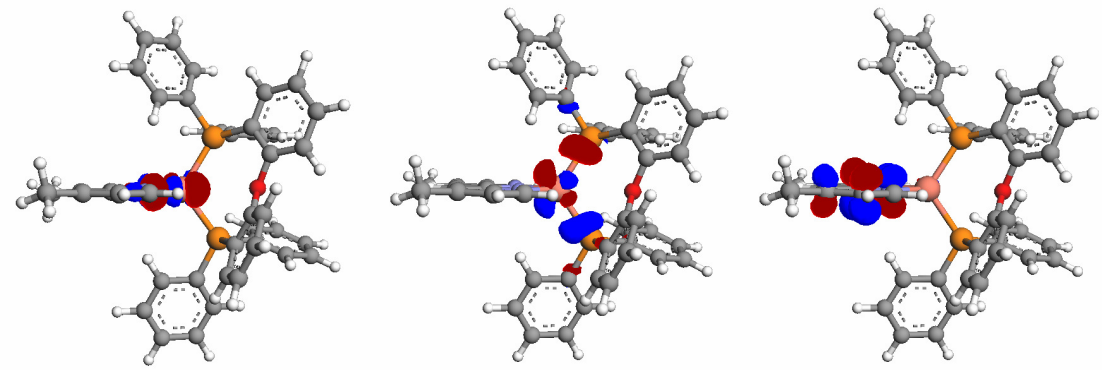


**Fig. E** Selected Molecular Orbital Images for **5**

| MO | Energy / eV | % Contribution from Cu-based MOs | % Contribution from POP-based MOs | % Contribution from bpy-based MOs |
|---|---|---|---|---|
| LUMO+10 | -0.567 | 3.25 | 95.33 | 1.42 |
| LUMO+9 | -0.634 | 1.93 | 97.10 | 0.97 |
| LUMO+8 | -0.718 | 2.70 | 94.82 | 2.48 |
| LUMO+7 | -0.821 | 0.34 | 98.37 | 1.29 |
| LUMO+6 | -0.870 | 0.33 | 98.87 | 0.80 |
| LUMO+5 | -0.995 | 1.30 | 97.73 | 0.97 |
| LUMO+4 | -1.045 | 1.00 | 97.21 | 1.79 |
| LUMO+3 | -1.139 | 0.33 | 5.62 | 94.05 |
| LUMO+2 | -1.168 | 0.42 | 97.87 | 1.71 |
| LUMO+1 | -1.474 | 2.27 | 4.23 | 93.50 |
| LUMO | -2.268 | 1.48 | 5.68 | 92.84 |
| HOMO | -5.873 | 44.34 | 50.38 | 5.28 |
| HOMO-1 | -5.993 | 63.78 | 8.80 | 27.42 |
| HOMO-2 | -6.232 | 51.66 | 38.83 | 9.51 |
| HOMO-3 | -6.511 | 8.33 | 90.36 | 1.31 |
| HOMO-4 | -6.961 | 72.64 | 11.99 | 15.37 |
| HOMO-5 | -6.989 | 63.63 | 33.40 | 2.97 |
| HOMO-6 | -7.019 | 33.20 | 65.23 | 1.57 |
| HOMO-7 | -7.091 | 18.43 | 78.77 | 2.80 |
| HOMO-8 | -7.142 | 14.75 | 84.14 | 1.11 |
| HOMO-9 | -7.177 | 8.47 | 87.58 | 3.95 |
| HOMO-10 | -7.189 | 11.26 | 84.84 | 3.90 |
| HOMO-11 | -7.202 | 5.48 | 93.22 | 1.30 |
| HOMO-12 | -7.219 | 13.47 | 18.32 | 68.21 |

**Table A** Percentage contributions from component parts of **5** to selected molecular orbitals. Also quoted are the calculated energies for these molecular orbitals.

| Absorbance / nm | Main Charge Transitions | | Relative Contribution |
|---|---|---|---|
| | MO from | MO to | |
| 416 | HOMO-1 | LUMO | 16 % |
| | HOMO | LUMO | 84 % |
| 392 | HOMO-3 | LUMO | 14 % |
| | HOMO-2 | LUMO | 86 % |
| 340 | HOMO-1 | LUMO+1 | 82 % |
| | HOMO | LUMO+1 | 18 % |
| 328 | HOMO-6 | LUMO | 8 % |
| | HOMO-5 | LUMO | 14 % |
| | HOMO-4 | LUMO | 18 % |
| | HOMO-1 | LUMO+1 | 11 % |
| | HOMO | LUMO+1 | 49 % |
| 280 | HOMO-12 | LUMO | 33 % |
| | HOMO-10 | LUMO | 10 % |
| | HOMO-9 | LUMO | 11 % |
| | HOMO-8 | LUMO | 11 % |
| | HOMO-4 | LUMO+1 | 14 % |
| | HOMO-2 | LUMO+2 | 13 % |
| | HOMO-2 | LUMO+4 | 8 % |

**Table B** TD-DFT calculated visible absorption wavelengths for **5**, indicating the molecular orbitals involved and their relative contribution to the absorption.

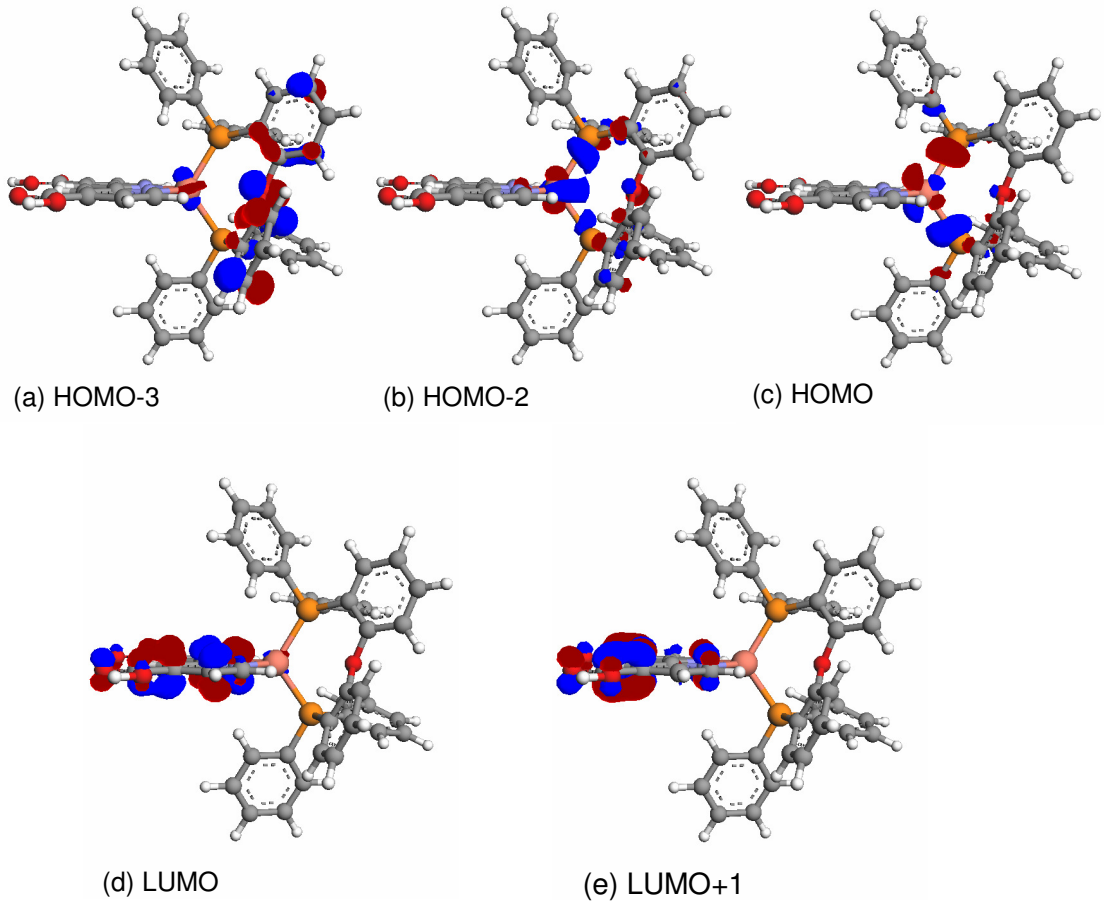


**Fig. F** Selected Molecular Orbital Images for **6**

| MO | Energy / eV | % Contribution from Cu-based MOs | % Contribution from POP-based MOs | % Contribution from bpy-based MOs |
|---|---|---|---|---|
| LUMO+4 | -1.108 | 0.98 | 96.59 | 2.43 |
| LUMO+3 | -1.232 | 0.50 | 98.35 | 1.15 |
| LUMO+2 | -2.223 | 0.40 | 1.13 | 98.47 |
| LUMO+1 | -2.604 | 0.40 | 0.53 | 99.07 |
| LUMO | -3.158 | 2.57 | 4.25 | 93.18 |
| HOMO | -6.083 | 36.98 | 58.41 | 4.61 |
| HOMO-1 | -6.347 | 65.77 | 7.37 | 26.86 |
| HOMO-2 | -6.424 | 38.48 | 54.01 | 7.51 |
| HOMO-3 | -6.595 | 14.09 | 83.47 | 2.44 |
| HOMO-4 | -7.042 | 1.26 | 98.47 | 0.27 |
| HOMO-5 | -7.176 | 11.88 | 87.18 | 0.94 |
| HOMO-6 | -7.198 | 7.77 | 91.73 | 0.50 |
| HOMO-7 | -7.226 | 1.81 | 97.67 | 0.52 |
| HOMO-8 | -7.269 | 20.74 | 77.43 | 1.83 |
| HOMO-9 | -7.234 | 28.29 | 69.38 | 2.33 |
| HOMO-10 | -7.309 | 69.95 | 22.78 | 7.27 |
| HOMO-11 | -7.331 | 54.99 | 42.99 | 2.02 |
| HOMO-12 | -7.359 | 39.89 | 57.20 | 2.91 |
| HOMO-13 | -7.383 | 5.67 | 93.85 | 0.48 |
| HOMO-14 | -7.487 | 4.45 | 94.40 | 1.15 |
| HOMO-15 | -7.537 | 16.79 | 81.94 | 1.27 |
| HOMO-16 | -7.622 | 4.05 | 90.70 | 5.25 |
| HOMO-17 | -7.653 | 6.61 | 6.22 | 87.17 |

**Table C** Percentage contributions from component parts of **6** to selected molecular orbitals. Also quoted are the calculated energies for these molecular orbitals.

| Absorbance λ / nm | Main Charge Transitions | | Relative Contribution |
|---|---|---|---|
| | MO from | MO to | |
| 509 | HOMO | LUMO | 100 % |
| 481 | HOMO-3 | LUMO | 25 % |
| | HOMO-2 | LUMO | 75 % |
| 440 | HOMO-3 | LUMO | 29 % |
| | HOMO-2 | LUMO | 10 % |
| | HOMO | LUMO+1 | 61 % |
| 383 | HOMO-17 | LUMO | 64 % |
| | HOMO-16 | LUMO | 22 % |
| | HOMO-10 | LUOM+2 | 14 % |
| 281 | HOMO | LUMO+4 | 100 % |

**Table D** TD-DFT calculated visible absorption wavelengths for **6**, indicating the molecular orbitals involved and their relative contribution to the absorption.

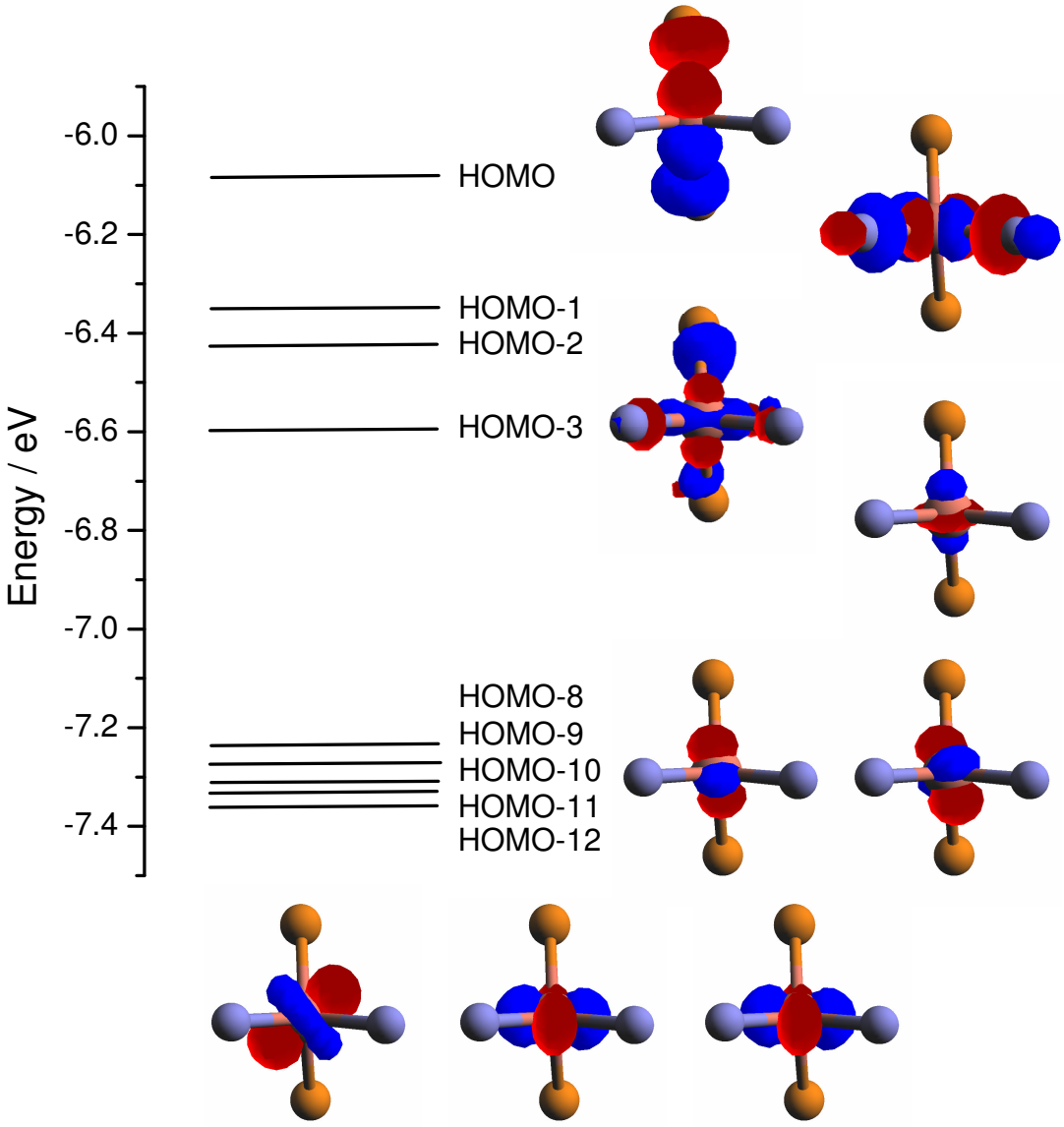


**Fig. G** Molecular Orbital Diagram for **6**

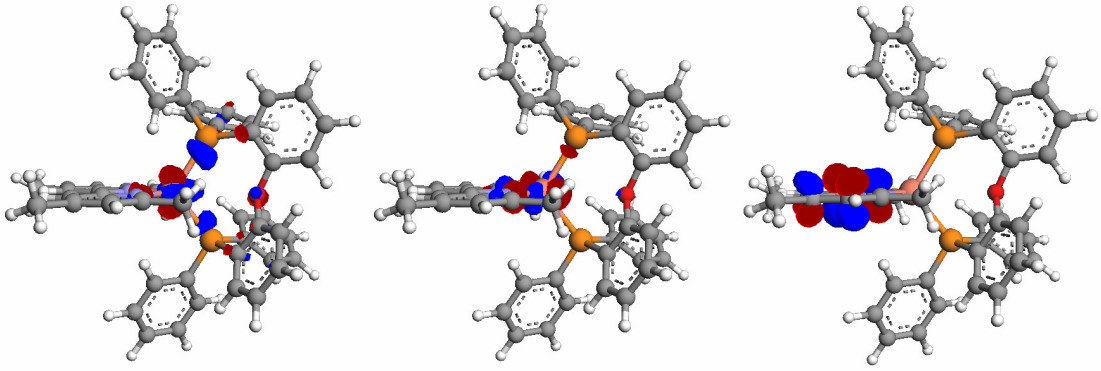

(a) HOMO-2 (a) HOMO-1 (a) LUMO

**Fig. H** Selected Molecular Orbital Images for **8**

| MO | Energy / eV | % Contribution from Cu-based MOs | % Contribution from POP-based MOs | % Contribution from bpy-based MOs |
|---|---|---|---|---|
| LUMO+6 | -0.850 | 0.34 | 97.53 | 2.13 |
| LUMO+5 | -0.944 | 1.04 | 62.54 | 36.42 |
| LUMO+4 | -0.993 | 1.16 | 85.05 | 13.79 |
| LUMO+3 | -1.124 | 0.63 | 69.93 | 29.44 |
| LUMO+2 | -1.237 | 0.40 | 96.04 | 3.56 |
| LUMO+1 | -1.252 | 1.22 | 4.93 | 93.85 |
| LUMO | -2.117 | 1.44 | 4.24 | 94.32 |
| HOMO | -5.903 | 51.16 | 36.34 | 12.50 |
| HOMO-1 | -6.033 | 61.10 | 18.98 | 19.92 |
| HOMO-2 | -6.268 | 51.93 | 38.80 | 9.27 |
| HOMO-3 | -6.413 | 12.69 | 85.30 | 2.01 |
| HOMO-4 | -6.547 | 51.80 | 7.38 | 40.82 |
| HOMO-5 | -7.009 | 86.10 | 10.02 | 3.88 |
| HOMO-6 | -7.022 | 34.96 | 28.18 | 36.86 |

**Table D** Percentage contributions from component parts of **8** to selected molecular orbitals. Also quoted are the calculated energies for these molecular orbitals.

| Absorbance λ / nm | Main Charge Transitions | | Relative Contribution |
|---|---|---|---|
| | MO from | MO to | |
| 446 | HOMO-1 | LUMO | 42 % |
| | HOMO | LUMO | 58 % |
| 402 | HOMO-1 | LUMO | 59 % |
| | HOMO-2 | LUMO | 41 % |
| 378 | HOMO-3 | LUMO | 21 % |
| | HOMO-2 | LUMO | 79 % |
| 293 | HOMO-6 | LUMO | 18 % |
| | HOMO-4 | LUMO | 11 % |
| | HOMO-2 | LUMO+1 | 16 % |
| | HOMO-1 | LUMO+2 | 37 % |
| | HOMO-1 | LUOM+3 | 11 % |
| | HOMO-1 | LUMO+5 | 7 % |
| 288 | HOMO-6 | LUMO | 13 % |
| | HOMO-1 | LUMO+3 | 16 % |
| | HOMO-1 | LUMO+5 | 8 % |
| | HOMO | LUMO+3 | 9 % |
| | HOMO | LUMO+4 | 11 % |
| | HOMO | LUMO+6 | 43 % |

**Table E** TD-DFT calculated visible absorption wavelengths for **8**, indicating the molecular orbitals involved and their relative contribution to the absorption.

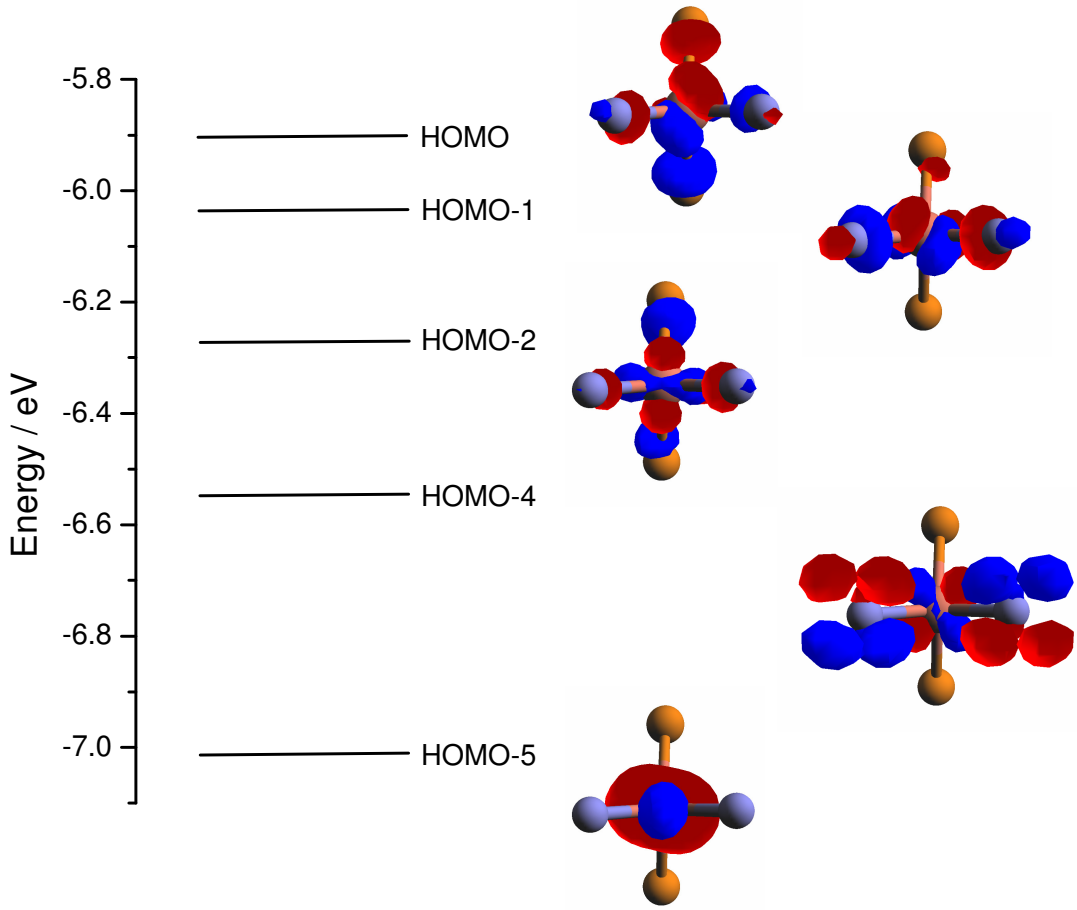


**Fig. I** Molecular Orbital Diagram for **8**

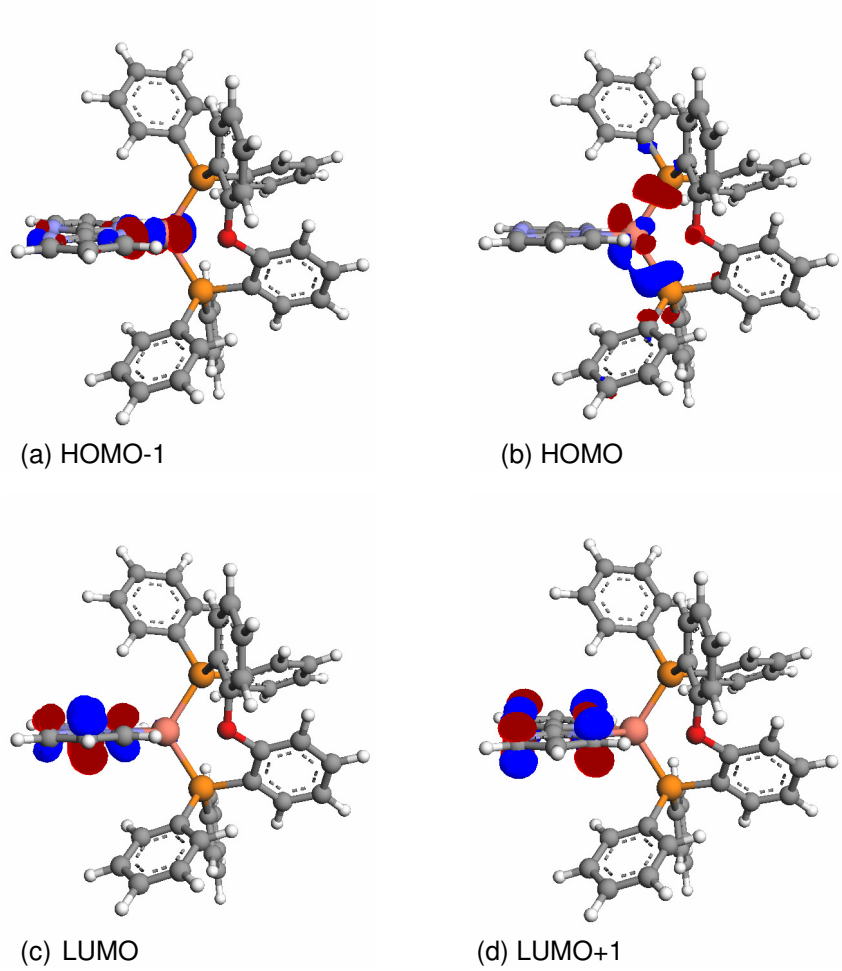


**Fig. J** Selected Molecular Orbital Images for **10**

| MO | Energy / eV | % Contribution from Cu-based MOs | % Contribution from POP-based MOs | % Contribution from bpy-based MOs |
|---|---|---|---|---|
| LUMO+5 | -1.037 | 0.36 | 99.05 | 0.59 |
| LUMO+4 | -1.173 | 0.33 | 98.93 | 0.74 |
| LUMO+3 | -1.238 | 0.75 | 98.18 | 1.07 |
| LUMO+2 | -2.015 | 0.35 | 1.81 | 97.84 |
| LUMO+1 | -2.273 | 1.97 | 3.41 | 94.62 |
| LUMO | -2.921 | 1.47 | 3.80 | 94.73 |
| HOMO | -6.067 | 38.12 | 56.37 | 5.51 |
| HOMO-1 | -6.333 | 59.87 | 12.00 | 28.13 |
| HOMO-2 | -6.498 | 48.57 | 42.12 | 9.31 |
| HOMO-3 | -6.784 | 4.63 | 94.22 | 1.15 |
| HOMO-4 | -7.166 | 8.35 | 90.47 | 1.18 |
| HOMO-5 | -7.187 | 3.07 | 96.66 | 0.27 |
| HOMO-6 | -7.227 | 5.71 | 93.94 | 0.35 |

**Table F** Percentage contributions from component parts of **10** to selected molecular orbitals. Also quoted are the calculated energies for these molecular orbitals.

| Absorbance λ / nm | Main Charge Transitions | | Relative Contribution |
|---|---|---|---|
| | MO from | MO to | |
| 516 | HOMO-1 | LUMO | 63 % |
| | HOMO | LUMO | 37 % |
| 481 | HOMO-1 | LUMO | 37 % |
| | HOMO | LUMO | 63 % |
| 447 | HOMO-2 | LUMO | 100 % |
| 400 | HOMO-1 | LUMO+1 | 54 % |
| | HOMO | LUMO+1 | 46% |
| 383 | HOMO-1 | LUMO+1 | 46 % |
| | HOMO | LUMO+1 | 54 % |
| 291 | HOMO | LUMO+4 | 100 % |
| 281 | HOMO-6 | LUMO+1 | 13 % |
| | HOMO-1 | LUMO+3 | 69 % |
| | HOMO | LUMO+5 | 18 % |

**Table G** TD-DFT calculated visible absorption wavelengths for **10**, indicating the molecular orbitals involved and their relative contribution to the absorption.

# Appendix B

## DFT and TDDFT Calculations

| MO | Energy / eV | % Contribution from Cu-based MOs | % Contribution from POP-based MOs | % Contribution from bpy-based MOs |
|---|---|---|---|---|
| LUMO+12 | -0.429 | 0.35 | 98.66 | 0.99 |
| LUMO+11 | -0.571 | 0.80 | 98.12 | 1.08 |
| LUMO+10 | -0.607 | 3.61 | 95.04 | 1.35 |
| LUMO+9 | -0.652 | 1.95 | 97.01 | 1.04 |
| LUMO+8 | -0.736 | 2.70 | 94.87 | 2.43 |
| LUMO+7 | -0.835 | 0.31 | 98.42 | 1.27 |
| LUMO+6 | -0.889 | 0.31 | 98.89 | 0.80 |
| LUMO+5 | -1.014 | 1.32 | 97.77 | 0.91 |
| LUMO+4 | -1.084 | 0.97 | 97.37 | 1.66 |
| LUMO+3 | -1.197 | 0.37 | 15.92 | 83.71 |
| LUMO+2 | -1.212 | 0.41 | 92.68 | 6.91 |
| LUMO+1 | -1.534 | 2.21 | 4.09 | 93.70 |
| LUMO | -2.333 | 1.47 | 4.89 | 93.64 |
| HOMO | -5.914 | 43.50 | 51.62 | 4.88 |
| HOMO-1 | -6.032 | 64.32 | 8.16 | 27.52 |
| HOMO-2 | -6.271 | 51.05 | 39.51 | 9.44 |
| HOMO-3 | -6.567 | 7.88 | 90.84 | 1.28 |
| HOMO-4 | -7.003 | 73.53 | 12.52 | 13.95 |
| HOMO-5 | -7.026 | 42.81 | 54.74 | 2.45 |
| HOMO-6 | -7.051 | 53.98 | 43.68 | 2.34 |
| HOMO-7 | -7.100 | 20.06 | 76.95 | 2.90 |
| HOMO-8 | -7.155 | 13.30 | 85.69 | 1.01 |
| HOMO-9 | -7.194 | 16.13 | 82.19 | 1.68 |
| HOMO-10 | -7.202 | 5.77 | 91.54 | 2.69 |
| HOMO-11 | -7.223 | 6.36 | 92.26 | 1.38 |
| HOMO-12 | -7.275 | 12.99 | 7.92 | 79.09 |

**Table A** Percentage contributions from component parts of **5** (in ethanol) to selected molecular orbitals. Also quoted are the calculated energies for these molecular orbitals.

| Absorbance / nm | Main Charge Transitions | | Relative Contribution |
|---|---|---|---|
| | MO from | MO to | |
| 419 | HOMO | LUMO | 100 % |
| 394 | HOMO-3 | LUMO | 14 % |
| | HOMO-2 | LUMO | 86 % |
| 331 | HOMO-6 | LUMO | 14 % |
| | HOMO-5 | LUMO | 11 % |
| | HOMO-4 | LUMO | 31 % |
| | HOMO | LUMO+1 | 44 % |
| 330 | HOMO-6 | LUMO | 18 % |
| | HOMO-5 | LUMO | 15 % |
| | HOMO-4 | LUMO | 33 % |
| | HOMO | LUMO+1 | 34 % |
| 298 | HOMO | LUMO+4 | 100 % |
| 280 | HOMO-12 | LUMO | 23 % |
| | HOMO-11 | LUMO | 9 % |
| | HOMO-9 | LUMO | 10 % |
| | HOMO-8 | LUMO | 15 % |
| | HOMO-4 | LUMO+1 | 12 % |
| | HOMO-2 | LUMO+2 | 13 % |
| | HOMO-2 | LUMO+4 | 6 % |
| | HOMO-1 | LUMO+5 | 12 % |

**Table B** TDDFT calculated visible absorption wavelengths for **5** (in ethanol), indicating the molecular orbitals involved and their relative contribution to the absorption.

| MO | Energy / eV | % Contribution from Cu-based MOs | % Contribution from POP-based MOs | % Contribution from bpy-based MOs |
|---|---|---|---|---|
| LUMO+6 | -0.949 | 0.37 | 98.43 | 1.20 |
| LUMO+5 | -1.017 | 1.02 | 67.72 | 31.26 |
| LUMO+4 | -1.039 | 1.17 | 91.07 | 7.76 |
| LUMO+3 | -1.085 | 0.60 | 57.63 | 41.77 |
| LUMO+2 | -1.244 | 0.40 | 95.85 | 3.75 |
| LUMO+1 | -1.371 | 1.21 | 4.46 | 94.33 |
| LUMO | -2.261 | 1.44 | 4.17 | 94.39 |
| HOMO | -5.863 | 50.89 | 36.87 | 12.24 |
| HOMO-1 | -6.100 | 61.15 | 19.32 | 19.53 |
| HOMO-2 | -6.328 | 51.88 | 38.93 | 9.19 |
| HOMO-3 | -6.502 | 12.61 | 85.39 | 2.00 |
| HOMO-4 | -6.913 | 53.86 | 7.58 | 38.56 |
| HOMO-5 | -6.960 | 85.99 | 10.54 | 3.47 |
| HOMO-6 | -7.019 | 33.39 | 26.58 | 40.03 |
| HOMO-7 | -7.070 | 7.75 | 77.74 | 14.51 |
| HOMO-8 | -7.137 | 15.94 | 82.27 | 1.79 |
| HOMO-9 | -7.152 | 20.09 | 76.13 | 3.78 |

**Table C** Percentage contributions from component parts of **8** (in ethanol) to selected molecular orbitals. Also quoted are the calculated energies for these molecular orbitals.

| Absorbance / nm | Main Charge Transitions | | Relative Contribution |
|---|---|---|---|
| | MO from | MO to | |
| 447 | HOMO-1 | LUMO | 41 % |
| | HOMO | LUMO | 59 % |
| 403 | HOMO-1 | LUMO | 59 % |
| | HOMO | LUMO | 41 % |
| 380 | HOMO-3 | LUMO | 20 % |
| | HOMO-2 | LUMO | 80 % |
| 331 | HOMO-5 | LUMO | 14 % |
| | HOMO-3 | LUMO | 18 % |
| | HOMO-1 | LUMO+1 | 23 % |
| | HOMO | LUMO +1 | 45 % |
| 310 | HOMO-1 | LUMO+1 | 52 % |
| | HOMO | LUMO+1 | 26 % |
| | HOMO | LUMO+2 | 12 % |
| | HOMO | LUMO+3 | 10 % |
| 297 | HOMO-7 | LUMO | 6 % |
| | HOMO-6 | LUMO | 16 % |
| | HOMO-4 | LUMO | 9 % |
| | HOMO-1 | LUMO+2 | 19 % |
| | HOMO-1 | LUMO+3 | 11 % |
| | HOMO-1 | LUMO+5 | 6 % |
| | HOMO | LUMO+4 | 19 % |
| | HOMO | LUMO+5 | 14 % |
| 288 | HOMO-9 | LUMO | 10 % |
| | HOMO-6 | LUMO | 15 % |
| | HOMO-4 | LUMO | 7 % |
| | HOMO-2 | LUMO +2 | 6 % |
| | HOMO-1 | LUMO+3 | 22 % |
| | HOMO-1 | LUMO+5 | 8 % |
| | HOMO | LUMO+3 | 7 % |
| | HOMO | LUMO+5 | 9 % |
| | HOMO | LUMO+6 | 16 % |

**Table D** TD-DFT calculated visible absorption wavelengths for **8** (in ethanol), indicating the molecular orbitals involved and their relative contribution to the absorption.

## Emission Spectroscopy

### Decay Curves

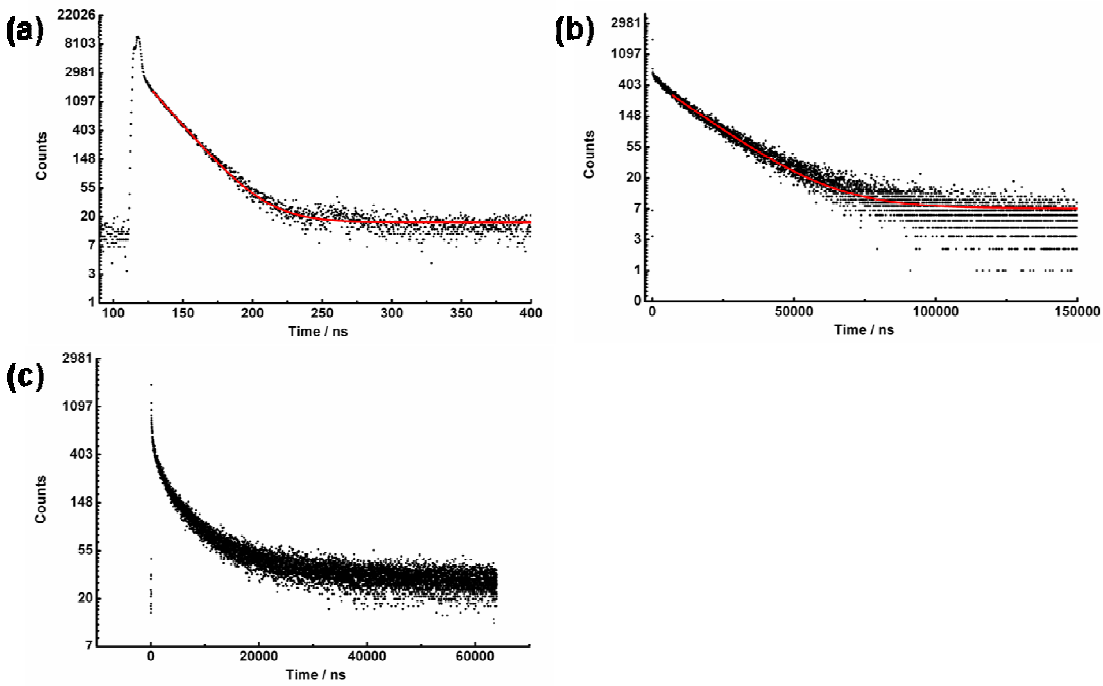


**Fig. A** Decay curves for **5** in (a) de-aerated ethanol at 300 K; (b) ethanol at 77 K; and (c) PMMA at 300 K

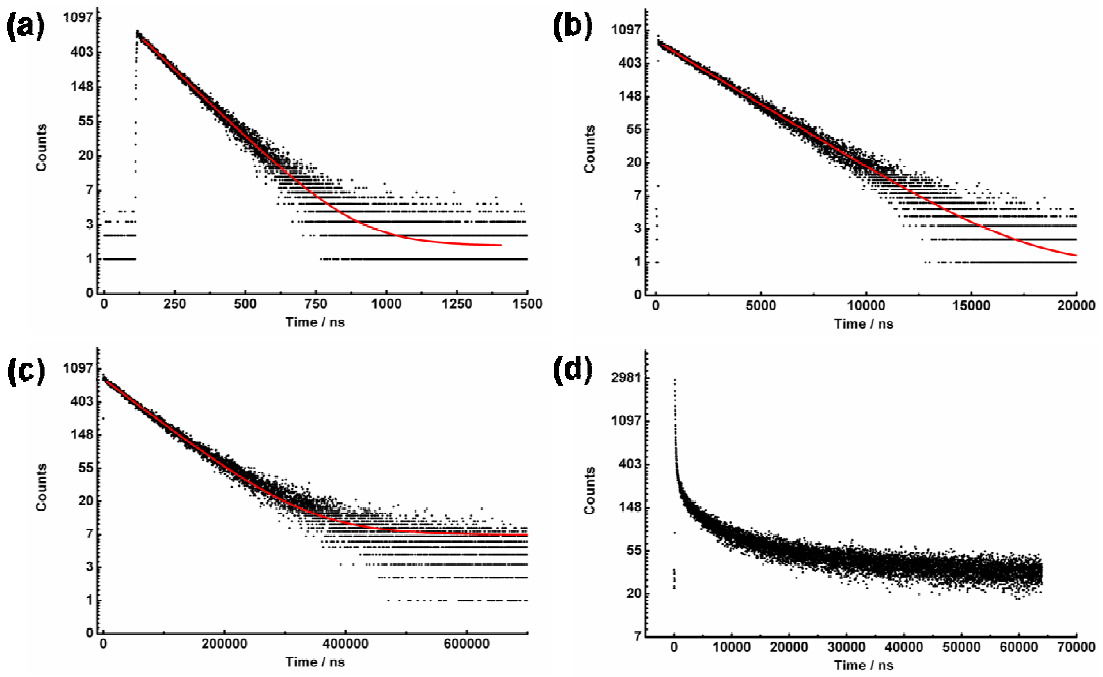


**Fig. B** Decay Curves for **8** in (a) air saturated ethanol at 300 K; (b) de-aerated ethanol at 300 K; (c) ethanol at 77 K; and (d) PMMA at 300 K

# Substituted [Cu(I)(POP)(bipyridyl)] and related complexes: Synthesis, structure, properties and applications to dye-sensitised solar cells†‡

**Charlotte L. Linfoot, Patricia Richardson, Tracy E. Hewat, Omar Moudam, Michael M. Forde, Anna Collins, Fraser White and Neil Robertson***

***Received 23rd March 2010, Accepted 8th July 2010***
**DOI: 10.1039/c0dt00190b**

The synthesis and subsequent spectroscopic, electrochemical, photophysical and computational characterisation of a series of heteroleptic Cu(I) complexes of general formula: [CuPOP{*4,4′*(R)-bipyridyl}][$BF_4$] and [CuPOP{*4,4′,6,6′*(R)-bipyridyl}][$BF_4$] is described (POP = bis{2-(diphenylphosphanyl)phenyl} ether; R = Me, $CO_2H$, $CO_2Et$. The steric constraint imposed by the POP ligand can impede distortion towards square planar geometry upon MLCT excitation or oxidation and this is explored in the context of varying substituents on the bipyridyl ligand. The insight gained opens new avenues for design of functional Cu(I) systems suitable for photophysical and photoelectrochemical applications such as sensitisers for dye-sensitised solar cells (DSSCs).



## Introduction

Recent research into the electrochemical and photophysical properties of phenanthroline- and bipyridine-based Cu(I) complexes[1–4] has revealed their potential for application in dye-sensitised solar cells (DSSCs),[2,3,5–7] organic light emitting diodes (OLEDs)[4,8] and light-emitting electrochemical cells (LECs).[4,8] The most successful DSSCs developed to date are based on Ru(II) containing sensitiser molecules,[9] some of which are being commercially developed for niche markets.[10] Lower efficiency DSSCs have also been constructed using transition metal complexes of Os(II), Pt(II), Re(I), Cu(I), Fe(II)[11] and Ni(II).[12] The use of third row transition metal sensitisers has been particularly successful due to their ability to display long-lived excited states following MLCT absorption in the visible. However low abundance, and toxicity considerations could present detrimental practical implications in the long term. Research into the field of first row transition metals has been limited due to their often extremely short-lived excited states compared to 2nd and 3rd row transition metal complexes, arising from the low lying metal d-d excited states which allow non-radiative decay of the MLCT excited state. This is a limiting factor in terms of DSSC functionality as charge injection from the dye is not efficiently achieved.[13,14]

To overcome this problem, complexes with a strong crystal field have been studied, aimed at raising the energy of any d-d excited states. This strategy has been explored by Ferrere[13,15,16] with work on Fe(II) sensitiser molecules analogous to known Ru(II) sensitisers that exhibit strong crystal-field splitting.[9] Solar cell function was observed but it was significantly reduced compared to the corresponding Ru(II) sensitiser. Similarly low efficiencies using Ni(II)(dithiolate)(diimine) complexes as DSSC sensitiser molecules has recently been presented by our group, with limited solar cell function being observed,[12] also attributed to short excited state lifetimes.

In contrast, Cu(I) complexes can display longer excited-state lifetimes due to their $d^{10}$ configuration, leading to a power-conversion efficiency of 2.6%.[17] To date however, Cu(I) DSSC research has been limited to homoleptic sensitisers,[2,3,5,7] and in this work we extend this to an initial investigation of heteroleptic Cu(I) complexes. In analogous Ru(II) dyes, the heteroleptic ligands control directionality of the MLCT transition to minimise recombination losses and also allow tuning of the HOMO energy.[18] During the redox process; Cu(I)/Cu(II),[19,20] a conformational geometry change typically occurs from distorted tetrahedral to tetragonally-flattened, respectively.[21] Research investigating Cu(I) bis-phenanthroline complexes[1,8,20–22] has revealed that substituents in the 2- and 9-positions of the phenanthroline ligand acts as "blocking groups" to sterically constrain the molecule.[1,20,21] A similar approach has been utilised for DSSC Cu(I) sensitisers by including substituents groups in the 6,6′positions of the bipyridine, however this leads to increased synthetic complexity of the bipyridine ligands which must also be 4,4′-substituted with acid groups to bind to $TiO_2$.[2,3,5–7] In this work, we

*School of Chemistry and EaStChem, University of Edinburgh, King's Buildings, Edinburgh, UK. E-mail: neil.robertson@ed.ac.uk; Fax: +44 131 6504743; Tel: +44 131 650 4755*

†

‡ Electronic supplementary information (ESI) available: Figure A. Schematic of the POP chelate ring; Figure B. Mercury plots of [Cu(dmbpy)$_2$Cl][$BF_4$] demonstrating π–stacking interactions; Figure C. Mercury plots of **1** demonstrating no π–stacking interactions; Figure D. (a) Absorbance Spectra for **1** and **3**; (b) Absorbance Spectra for **4**, **6**, **7** and **9**; Figure E. Excitation and Emission Spectra; Figure F. Selected Molecular Orbital Images for **4**; Figure G. Selected Molecular Orbital Images for **5**; Figure H. Selected Molecular Orbital Images for **7**; Figure I. Selected Molecular Orbital Images for **9**; Figure J. Molecular Orbital Diagram for **4**; Figure K. Molecular Orbital Diagram for **7**; Figure L. Molecular Orbital Diagram for **5**; Figure M. *I–V* Curve for **5**; Figure N. *I–V* Curve for **5** with Cheno treatment; Figure O. *I–V* Curve for **5** with $TiCl_4$ treatment; Table A. Crystallographic data for complexes **6**, **9** and **10**; Table B. Percentage contributions from component parts of **4** to selected molecular orbitals; Table C. TDDFT calculated visible absorption wavelengths for **4**; Table D. Percentage contributions from component parts of **5** to selected molecular orbitals; Table E. TDDFT calculated visible absorption wavelengths for **5**; Table F. Percentage contributions from component parts of **7** to selected molecular orbitals; Table G. TDDFT calculated visible absorption wavelengths for **7**; Table H. Percentage contributions from component parts of **9** to selected molecular orbitals; Table I. TDDFT calculated visible absorption wavelengths for **9**. CCDC reference numbers 771439–771443. For ESI and crystallographic data in CIF or other electronic format see DOI: 10.1039/c0dt00190b

explore the use of a geometrically inflexible co-ligand bis{2-(diphenylphosphanyl)phenyl} ether (POP), enabling the simpler 4,4′-$(CO_2H)_2$-bipyridine to be used as the $TiO_2$-binding ligand, without requiring 6,6′-substitution and therefore simplifying the intensive bipyridine synthesis required for previous Cu(I)-based sensitisers. POP has been used effectively in OLED studies due to this rigid and inflexible geometry it can impose on the complex.[13,23,24]

The work outlined here reports the synthesis and subsequent electrochemical and photophysical characterisation of a series of homo- and heteroleptic Cu(I)(bipyridine) complexes (Fig. 1 and 2), enabling a comparison of structural rigidity imposed by the POP and variously-substituted bipyridine ligands. Included is the first example of a heteroleptic Cu(I) complex investigated as a DSSC sensitiser.

## Results and discussion

### Syntheses

The ligands 4,4′-dicarboxy-2,2′-bipyridine (dcbpy), 4,4′-di($CO_2Et$)-2,2′-bipyridine (decbpy), 4,4′,6,6′-tetramethyl-2,2′-bipyridine (tmbpy) and bis{2-(diphenylphosphanyl)phenyl} ether (POP), and the starting complexes $[Cu(MeCN)_4][BF_4]$ and $[Cu(POP)(MeCN)_2][BF_4]$ were synthesised using modified literature methods as described in the Experimental section. 4,4′,6,6′-tetracarboxy-2,2′-bipyridine (tcbpy) and 4,4′,6,6′-tetra($CO_2Et$)-2,2′-bipyridine (tecbpy) are novel ligands that were synthesised *via* oxidation of the tmbpy ligand. The reaction schemes shown in Fig. 1 and 2 demonstrate how the Cu(I) complexes were synthesised by simple addition, with stirring, of the relevant starting materials in stoichiometric amounts, to the appropriate solvent at room temperature. It should be noted that $[Cu(tcbpy)_2][BF_4]$ **2**, and $[Cu(POP)(tcbpy)][BF_4]$ **8** were synthesised and characterised by $^1H$ NMR under nitrogen, but were not air stable and so were not further investigated. The methyl and ester analogues have been synthesised alongside the acids, despite not being directly applicable for use in a DSSC, as they can give insight into the properties of the acid complexes while being more convenient for detailed characterisation due to better solubility. The Cu(I) complexes **1**, **3**–**7** and **9** were characterised by $^1H$ NMR, ESI-MS, +FAB-MS and elemental analysis, verifying molecular structures.

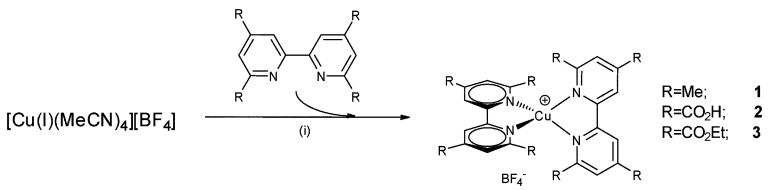


**Fig. 1** Synthetic reaction scheme for homoleptic complexes reported in this work. All procedures carried out under a nitrogen atmosphere. (i) **1** degassed chloroform; **2** dry, degassed MeOH; **3** dry, degassed DCM.

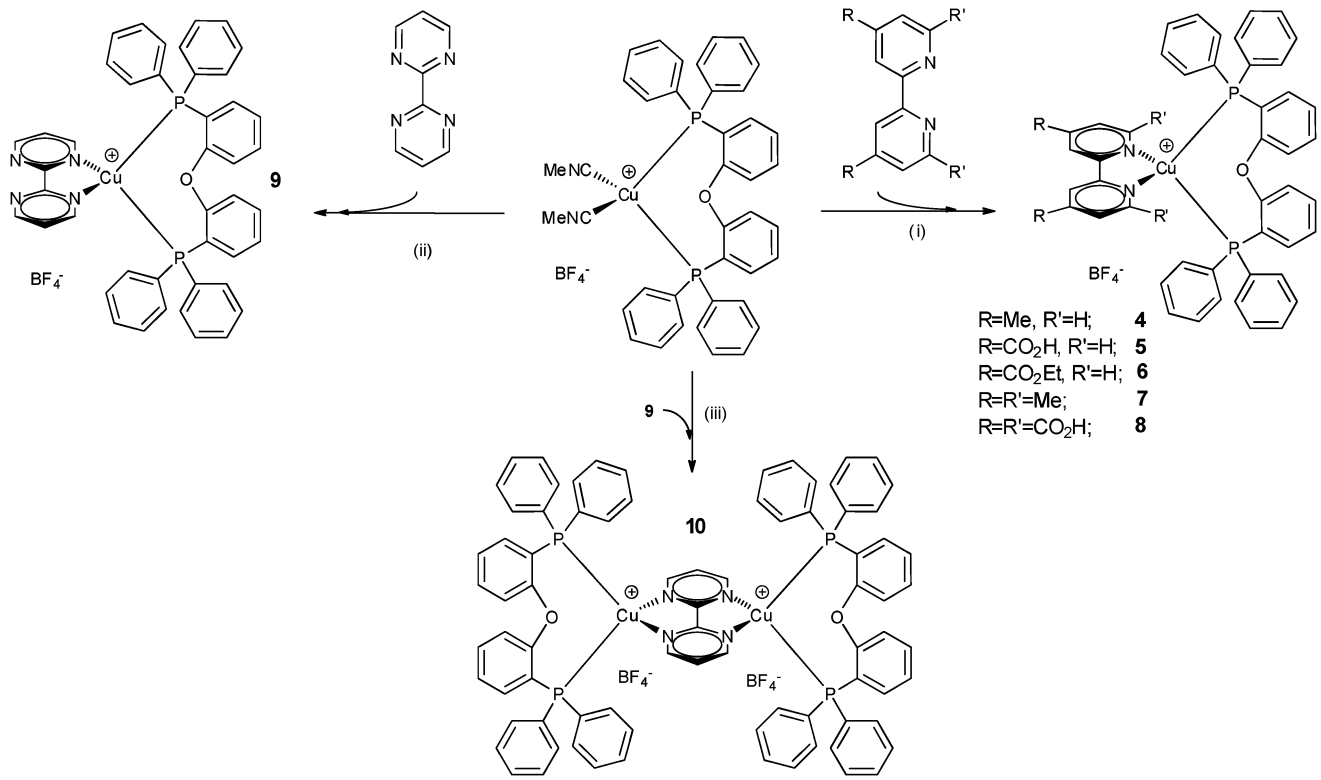


**Fig. 2** Synthetic reaction scheme for heteroleptic complexes reported in this work. (**1**) **4**, **5**, **6**, **8** acetone; **7** anhydrous acetonitrile (ii) DCM (iii) acetone.

 

**Table 1** Selected bond lengths (Å) and bond angles (deg) of complexes $[Cu(dmbpy)_2Cl][BF_4]$ and **1**

| | $[Cu(dmbpy)_2Cl][BF_4]$ | **1** |
|---|---|---|
| Cu–N(1A) | 2.154(2) | 2.055(2) |
| Cu–N(1B) | 2.082(2) | 2.056(2) |
| Cu–N(2A) | 2.001(2) | 2.055(2) |
| Cu–N(2B) | 1.981(2) | 2.056(2) |
| N(1A)–Cu–N(1B) | 100.97(8) | 117.63(9) |
| N(2A)–Cu–N(2B) | 169.34(8) | 117.63(9) |
| N(1A)–Cu–N(2B) | 91.78(8) | 134.37(9) |
| N(2A)–Cu–N(1B) | 96.60(8) | 134.37(9) |
| N(1A)–Cu–N(2A) | 79.07(8) | 80.60(13) |
| N(1B)–Cu–N(2B) | 79.64(8) | 80.63(13) |

## Structure analysis

The single crystal structures of $[Cu(II)(dmbpy)_2Cl][BF_4]$ and compounds **1**, **6**, **9** and **10** have been determined allowing insight into the structural features of these complexes (Table 1 and 2), in particular the blocking group effects. All crystals were grown from solutions open to air. Despite obtaining a crystal structure of **10**, we were unable to isolate the complex in a pure form and therefore further characterisation was not carried out. In attempting to crystallise the 4,4′-dimethyl-2,2′-bipyridine analogue of **1**, the complex oxidised in air along with coordination of chlorine to give $[Cu(II)(dmbpy)_2Cl][BF_4]$ (Fig. 3a). In contrast, the structure of complex **1** (Fig. 3b) illustrates the stabilisation of the Cu(I) oxidation state by addition of methyl groups in the 6,6′-positions of the bipyridine. The angle between the planes of the two bipyridyls is 72.18° giving a pseudo-tetrahedral geometry and suggesting considerable flexibility of this geometric parameter.

The crystal structures of the heterolpetic complexes (**6**, **9** and **10**) shown in Fig. 4 illustrate the role of POP in stabilisation in air of a Cu(I) oxidation state over Cu(II) as the complexes are forced to adopt distorted tetrahedral conformations with reduced structural flexibility. The angles between the bipyridyl plane and the P–Cu–P plane for these complexes range from 84.05 to 88.61° indicating a geometry closer to tetrahedral than that of **1** (Table 2). Additionally, the bite angle of POP in each case remains comparatively close to that expected for an ideal tetrahedron (Table 2). The blocking functionality of POP arises as one of

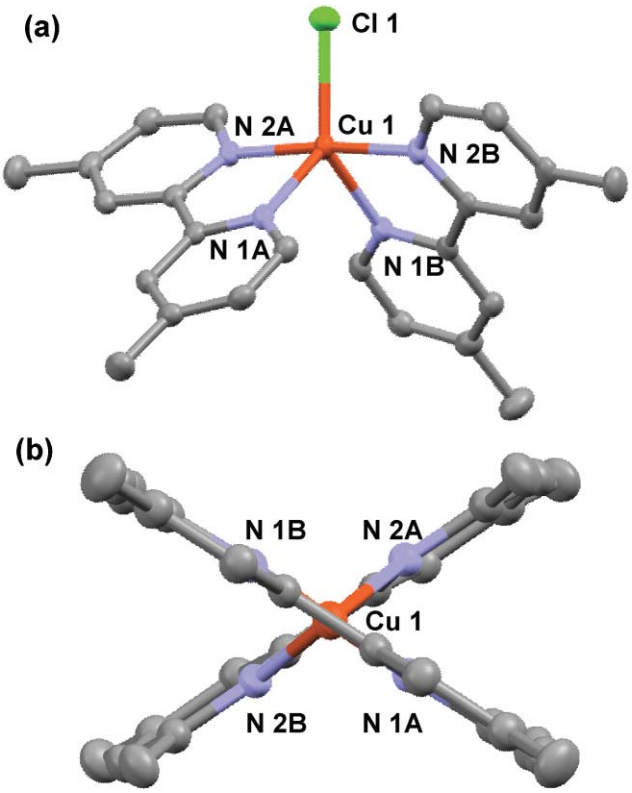


**Fig. 3** Mercury plots of (a) $[Cu(dmbpy)_2Cl][BF_4]$; and (b) **1**. Thermal ellipsoids are drawn at the 50% probability level. $[BF_4]$ counter ion omitted for clarity. Selected bond lengths and bond angles for $[Cu(dmbpy)_2Cl][BF_4]$ involving the chloride atom: Cu–Cl: 2.2770(7) Å; Cl–Cu–N(1A) 123.54(6)°; Cl–Cu–N(2A) 93.08(6)°; Cl–Cu–N(1B) 135.48(6)°; Cl–Cu–N–(2B) 96.57 (6)°.

the phenyl rings attached to the phosphorus atoms is constrained to be over the bipyridyl ligand resulting in H-phenyl-to-bipyridyl plane distances of 2.891 Å, 2.941 Å, 2.790 Å for **6**, **9** and **10** respectively that prevent structural distortion. This geometrical arrangement is caused by the rigid nature of the chelating ring (Cu–P–C–C–O–C–C–P). Among the three structures presented here (see supplementary information) and also those reported

**Table 2** Selected bond lengths (Å) and bond angles (deg) from single crystal X-ray crystallography for **6**, **9** and **10**.; and from solvated DFT calculations for **9**

X

| | **6** | **9**: single crystal X-ray structure | **9**: DFT geometry optimisation | **10** |
|---|---|---|---|---|
| Cu–N(1) | 2.037 (2) | 2.068(2) | 2.105 | 2.103(2) |
| Cu–N(2) | 2.0621(19) | 2.093(2) | 2.107 | 2.070(2) |
| Cu–P(1) | 2.2213(6) | 2.2482(7) | 2.400 | 2.2158(7) |
| Cu–P(2) | 2.2465 (6) | 2.2756(7) | 2.411 | 2.2851(7) |
| N(1)–Cu–N(2) | 80.30(8) | 79.74(8) | 79.64 | 80.16(8) |
| N(1)–Cu–P(1) | 128.87(6) | 121.08(6) | 121.96 | 128.91(6) |
| N(2)–Cu–P(1) | 111.47(5) | 118.49(6) | 115.30 | 119.24(6) |
| N(1)–Cu–P(2) | 109.74(6) | 108.47(6) | 106.85 | 102.14(6) |
| N(2)–Cu–P(2) | 112.26(5) | 113.65(6) | 112.25 | 102.75(6) |
| P(1)–Cu–P(2) | 110.40(2) | 111.77(2) | 114.50 | 116.30(3) |
| bpy plane–PCuP plane[a] | 84.05 | 85.77 | N/A | 88.61 |
| Cu–P(2)–C[b] | 114.38(8) | 115.58(8) | 115.89 | 107.54(9) |

[a] for **6** C═C17; for **9** C═C9; for **10** C═C35.

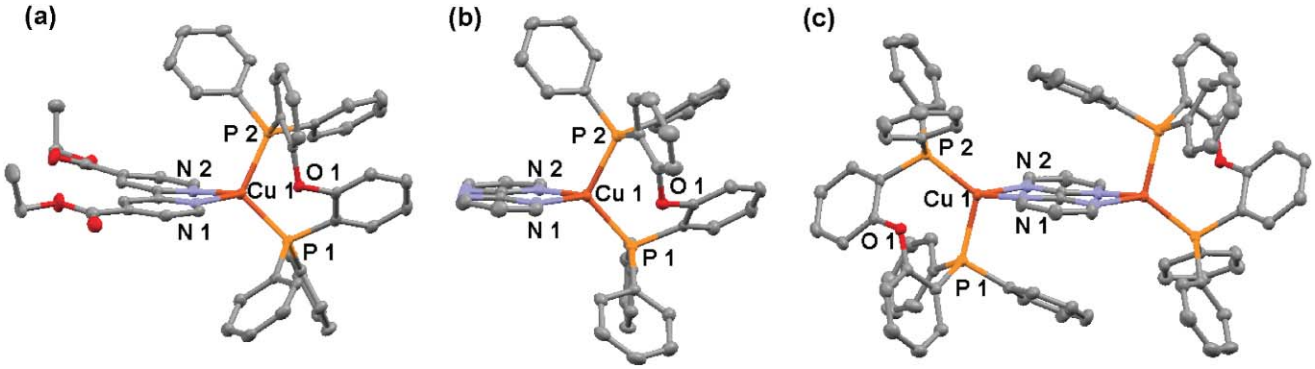


**Fig. 4** Mercury plots of (a) **6**; (b) **9** and (c) **10**. Thermal ellipsoids are drawn at the 50% probability level. **10** lies on an inversion centre. The [$BF_4$] counter ions are omitted for clarity.



previously, there is little variation between the angles within the chelate ring providing strong support for the lack of flexibility in the POP coordination geometry and hence the rigidity of the whole molecule. In general, the structures shows little geometric deviation compared with eleven POP containing Cu(I)-structures described in the literature.[14,24–28] Furthermore, the structures of **6** and **9** clearly demonstrate that in a heteroleptic complex with an appropriate co-ligand, 6,6′-substituted bipyridine ligands are not required to maintain an air-stable Cu(I)-complex. This enables the use in Cu(I) DSSC sensitisers of the straightforward dcbpy ligand widely exploited in Ru sensitisers and bypassing the need for more complex multiply substituted bipyridyl ligands.

## DFT and TDDFT calculations

All calculations were carried out using Gaussian 03[29] with the B3LYP/LANL2DZ[30–33] functional and basis set with induced solvent effects. This level of theory has been used successfully in the literature to calculate the structural and electronic properties of a number of coordination complexes.[25] Calculation details are outlined in full in the Experimental section. The optimised geometry for **9** is in very good agreement with the structure obtained crystallographically (Table 2), but as expected the DFT calculated solvated bond lengths are longer than those in the crystal structure. Packing forces present in the calculated liquid-phase are weaker than those in the solid-phase. The DFT calculated gas-phase and solution-phase structures for **4**, **5**, **7** and **9** produce identical overall structure energies and comparable bond distances and angles.

Time dependent density functional theory (TDDFT), also at the B3LYP/LANL2DZ level of theory, was used to probe the electronic transitions that give rise to the visible and near-UV absorption of each complex. Although current TDDFT implementations have a tendency to underestimate the energy of charge-transfer interactions, the method has been shown to provide useful qualitative information on the electronic structure and photophysical behaviour of similar coordination complexes.[25] Seventy singlet-singlet transitions were calculated with solvent, for each complex. Analysis of the components of the TDDFT expansion shows that the majority of predicted transitions are not well described by a single electron-promotion, but involve transitions between several different orbital pairs.

The nature of each electronic transition was determined by visual inspection (Argus Lab[34]) of each contributing molecular orbital as an isosurface map. Many of the calculated occupied and virtual orbitals were seen to be of mixed character, with electron density simultaneously present on both the ligand and metal. However, the electronic transitions could broadly be

classified into three distinct types; metal-to-ligand-charge-transfer (MLCT), where the occupied orbital is predominantly metal based and the virtual orbital ligand based, either on the POP or bpy; ligand-ligand (LL), where the transition involves occupied and virtual orbitals on the same ligand; and ligand-to-ligand-charge-transfer (LLCT), where the transition involves occupied and virtual orbitals on different ligands. These are discussed further in the context of the experimental results below.

## UV/Vis absorption spectroscopy

The experimental and calculated UV-Vis absorption spectra are shown in Fig. 5, with the main absorption bands and related extinction coefficients given in Table 3. For each complex the experimental spectra show two distinct groupings; very strong absorption in the near uv and weaker absorption bands in the visible that are sensitive to the nature of the biypridine substituents. From previous work,[1] it is known that the absorption peak of the $\pi \rightarrow \pi^*$ intra-bipyridine transition occurs between 300–320 nm. Each complex in the homoleptic series exhibits an absorption peak in this range (Table 3), however this absorption peak cannot be resolved for the heteroleptic series as it is believed to be masked by the stronger POP ligand UV absorption band. In the absorbance spectra collected for **4** and **7** the shoulder present at 320 nm may possibly be attributed to the bipryidyl absorption.

The TDDFT calculations reproduce the experimental spectra reasonably well in the UV region, predicting a large number of transitions with significant oscillator strength (Fig. 5). Examination of the molecular orbitals involved in each transition shows that the UV absorption bands are dominated by $\pi \rightarrow \pi^*$ transitions on both the bipyridine and the POP ligands (see supplementary information‡).

The longer wavelength bands have been assigned as Cu(I) to bipyridyl MLCT transfer bands based upon comparison with literature. This assignment is supported by the calculated energies and deduced characters of the frontier orbitals (Table 4) and the percentage contribution to the lowest energy MLCT bands, of

 

**Table 3** Absorbance measurements for all complexes. **1** and **4 - 9** carried out in MeCN; **3** carried out in DCM

| | | Absorption/$\lambda_{max}$/nm ($\varepsilon_{max}$($\times 10^3$ $M^{-1}cm^{-1}$)) | | | | |
|---|---|---|---|---|---|---|
| Complex | | Intraligand transitions | | | MLCT | |
| [Cu(tmbpy)$_2$] | **1** | | | 300 (25.8) | 358 (1.4) | 449 (3.5) |
| [Cu(tecbpy)$_2$] | **3** | | | 315 (32.0) | 477 (4.9) | 594 (7.4) |
| [CuPOP(MeCN)2] | — | | 272 (14.2) | | | |
| [CuPOP(dmbpy)] | **4** | 248 (25.1) | 282 (22.6) | | 369 (3.2) | |
| [CuPOP(dcbpy)] | **5** | | 276 | | 416 | |
| [CuPOP(decbpy)] | **6** | 246 (26.6) | 290 (19.7) | | 424 (2.4) | |
| [CuPOP(tmbpy)] | **7** | 250 (26.3) | 288 (25.5) | | 358 (2.2) | 460 (0.2) |
| [CuPOP(bpym)] | **9** | 247 (35.5) | 294 (16.1) | | 403 (2.0) | |

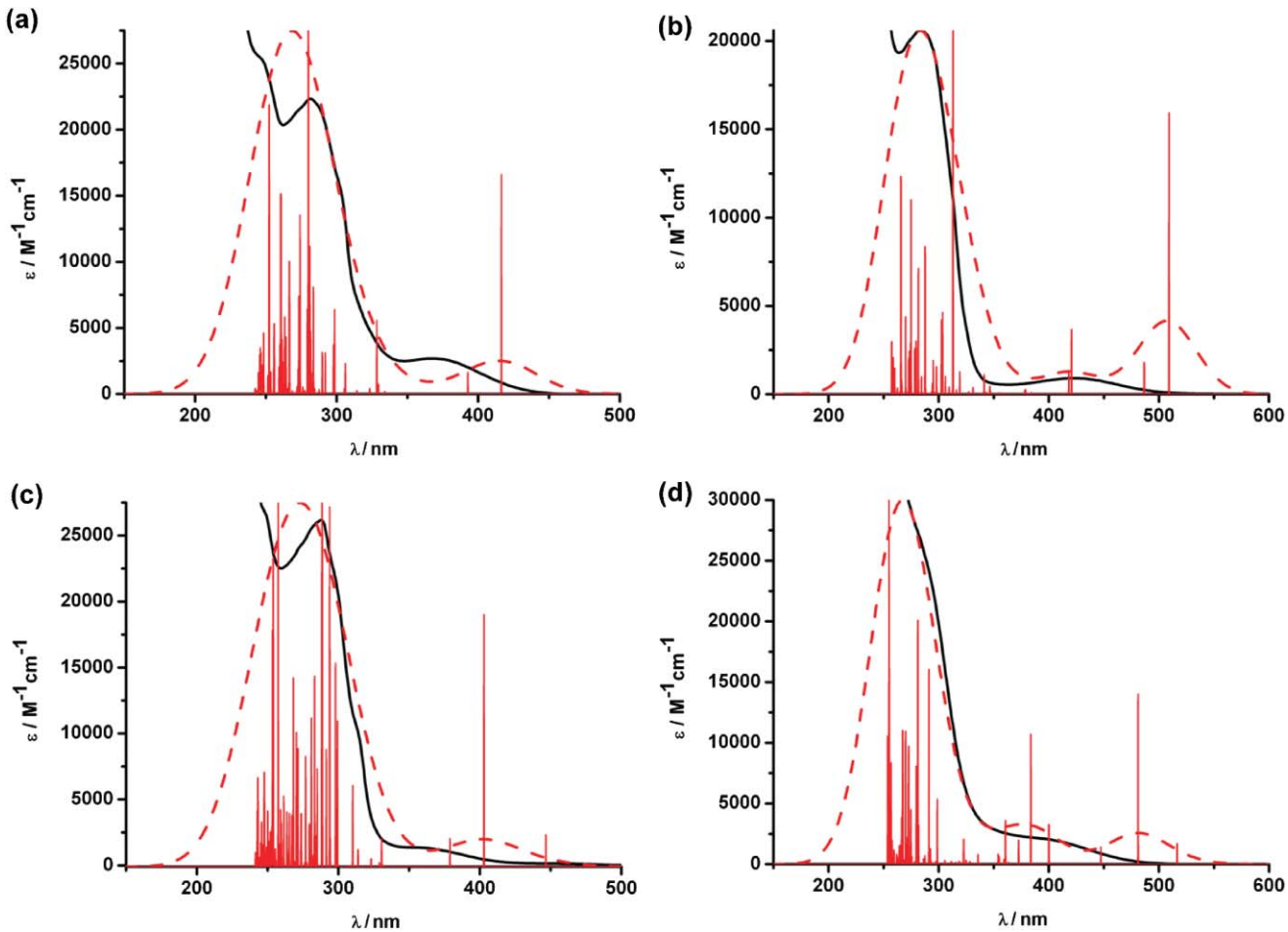


**Fig. 5** Theoretical UV/Vis absorption spectra against experimental absorption spectra for (a) **4**; (b) **5**; (c) **7**; (d) **9**.Where red solid columns = calculated electronic transition; red dotted line = calculated spectra; black solid line = solution spectrum of (a) **4**, (b) **6**, (c) **7** and (d) **9** in MeCN.

each orbital pair (Table 5) in the TDDFT expansion. It must be noted that TDDFT has a tendency to over stabilise, and indeed the calculated MLCT absorptions are consistently predicted at lower energy than those seen experimentally.[35]

For the 4,4′-disubstituted complexes the TDDFT calculations agree with experimental data in placing the MLCT absorption for **5** at lower energy than that of **4**. The proposed explanation for this, based upon the previous experimental data, is that **5** has a lower lying LUMO as a result of the electron-withdrawing acid substituents. This proposal can be further confirmed upon inspection of the TDDFT results with Fig. 6 showing molecular orbital images for the LUMO of **4** and **5**. **5** displays increased delocalisation and therefore a lower energy LUMO (Table 4) which subsequently reduces the required MLCT energy, causing the absorption to take place at longer wavelength.

The MO diagram for **4** looks almost as expected for a pseudo-tetrahedral complex (see supplementary information‡). Three MOs are close in energy (HOMO,

HOMO-1 and HOMO-2) and approximate as $t_2$ ($d_{xy}$, $d_{xz}$ and $d_{yz}$), and another two MOs at lower energy (HOMO-4 and HOMO-5) which approximate as e ($d_{x2-y2}$ and $d_{z2}$). The MLCT transition can therefore be said to be $t_2$ to π* (bipyridine) in

**Table 4** Percentage contributions from component parts of **4**, **5**, **7** and **9** to selected molecular orbitals. Also quoted are the calculated energies for these molecular orbitals

| | | | | % Contribution from | | |
|---|---|---|---|---|---|---|
| Complex | MO | MO character | MO energy/eV | Cu-based orbitals | POP-based orbitals | Bpy-based orbitals |
| **4** | HOMO-1 | $d_{xz}$ or $d_{yz}$ | –5.99 | 63.78 | 8.80 | 27.42 |
| | HOMO | $d_{xz}$,or $d_{yz}$ | –5.87 | 44.34 | 50.38 | 5.28 |
| | LUMO | π*-bpy | –2.27 | 1.48 | 5.68 | 92.84 |
| **5** | HOMO-3 | | –6.60 | 14.09 | 83.47 | 2.44 |
| | HOMO-2 | | –6.42 | 38.48 | 54.01 | 7.51 |
| | HOMO | | –6.08 | 36.98 | 58.41 | 4.61 |
| | LUMO | π*-bpy | –3.16 | 2.57 | 4.25 | 93.18 |
| | LUMO+1 | π*-bpy | –2.60 | 0.40 | 0.53 | 99.07 |
| **7** | HOMO-2 | $d_{xy}$ | –6.27 | 51.93 | 38.80 | 9.27 |
| | HOMO-1 | $d_{xz}$,or $d_{yz}$ | –6.03 | 61.10 | 18.98 | 19.92 |
| | LUMO | π*-bpy | –2.12 | 1.44 | 4.24 | 94.32 |
| **9** | HOMO-1 | | –6.33 | 59.87 | 12.00 | 28.13 |
| | HOMO | | –6.07 | 38.12 | 56.37 | 5.51 |
| | LUMO | π*-bpy | –2.92 | 1.47 | 3.80 | 94.73 |
| | LUMO+1 | π*-bpy | –2.27 | 1.97 | 3.41 | 94.62 |

**Table 5** TD-DFT calculated visible absorption wavelengths for **4**, **5**, **7** and **9**, indicating the molecular orbitals involved and their relative contribution to the absorption

| | | Main charge transitions | | |
|---|---|---|---|---|
| Complex | Main visible absorbance/nm | Mo from | MO to | Relative contribution |
| **4** | 416 | HOMO-1 | LUMO | 16% |
| | | HOMO | LUMO | 84% |
| **5** | 509 | HOMO | LUMO | 100% |
| | 420 | HOMO-3 | LUMO | 29% |
| | | HOMO-2 | LUMO | 10% |
| | | HOMO | LUMO+1 | 61% |
| **7** | 402 | HOMO-1 | LUMO | 59% |
| | | HOMO-2 | LUMO | 41% |
| **9** | 481 | HOMO-1 | LUMO | 37% |
| | | HOMO | LUMO | 63% |
| | 383 | HOMO-1 | LUMO+1 | 46% |
| | | HOMO | LUMO+1 | 54% |

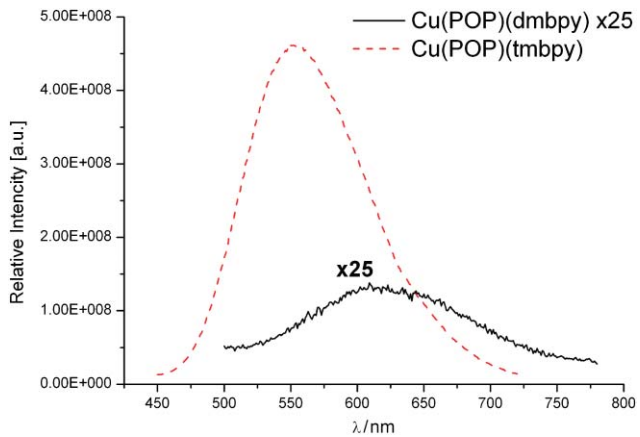


**Fig. 6** Isosurface images generated from DFT calculations of (a) LUMO for **4**; (b) LUMO for **5**.

nature. Despite the lowest energy MLCT transition taking place in **5**, **7** and **9** being of the same character, their MO diagrams vary more from the ideal pseudo-tetrahedral model due to increased interactions with the ligand-based orbitals. Inspection of Table 5 demonstrates that the LUMO and LUMO+1 orbitals for all four of the complexes are bpy-based, and that the HOMO to HOMO-3 orbitals are Cu(I)- and POP-based, as predicted.

This is of importance as the main charge-transfer transitions occur between these orbitals (see Table 5), indicating MLCT across the molecule in the desired direction for DSSC function of the acid analogous: towards the acid groups bound to the $TiO_2$.

## Emission spectroscopy

Excitation and emission spectra were investigated for **4**, **7** and **9** in ethanol at room temperature and in a frozen glass at 77 K. For comparison, data were also collected for the uncomplexed dmbpy and tmbpy ligands, and the precursor complex $[CuPOP(MeCN)_2][BF_4]$ (Table 6).Maxima values are given in Table 6 with full spectra given in the supplementary information. Complex **9** was found to be emissive only at 77 K and not at room temperature. Complexes **4** and **7** both showed room-temperature emission with a significant increase in intensity upon freezing accompanied by some shifting of the absorption and emission maxima (Fig. 7). This behaviour is consistent with emission from a triplet MLCT state in keeping with characteristic behaviour of related Cu(I) polypyridyl complexes.[8]

Fig. 8 shows a comparison of the emission intensity for **4** and **7**, where the excitation wavelengths used for both complexes have comparable molar absorption coefficients. The role of the 6,6′-methyl groups on the bipyridine ligand is apparent in providing additional steric constraint to the complex leading to the significantly greater emission intensity of **7**. Nevertheless, the observation of emission from **4**, **7** and **9**, all of which lack 6,6′-substituents on the bipyridyl, demonstrates the role of the ancilliary POP ligand in providing structural rigidity to the complex. To function as a sensitiser in a DSSC, a complex must possess a sufficiently long excited-state lifetime to enable charge injection into the semiconductor condution band and the observation of photoluminescence is generally taken as an indication that the excited-state lifetime will be sufficiently long. Alonside the structural studies, the observed emission from **4**, **7** and **9** demonstrates the suitability of using the dcbpy ligand in conjuction with a sterically-blocking co-ligand

 

**Table 6** Excitation and emission measurements for dmby, tmbpy, [CuPOP(MeCN)$_2$][BF$_4$], **4**, **7**, and **9**

| | Room-temperature EtOH | | 77 K rigid matrix (EtOH) | |
|---|---|---|---|---|
| Compound | Excitation maxima $\lambda_{max}$/nm | Emission maxima $\lambda_{max}$/nm | Excitation maxima $\lambda_{max}$/nm | Emission maxima $\lambda_{max}$/nm |
| dmbpy | 300, 330 | 410 | Not recorded | Not recorded |
| tmbpy | 264, 304 | 373 | Not recorded | Not recorded |
| CuPOP(MeCN)$_2$ | 324 | 457 | Not recorded | Not recorded |
| **4** | 408 | 618 | 340 | 592 |
| **7** | 369 | 554 | 369 | 527 |
| **9** | Not observed | Not observed | 328, 356 | 515 |



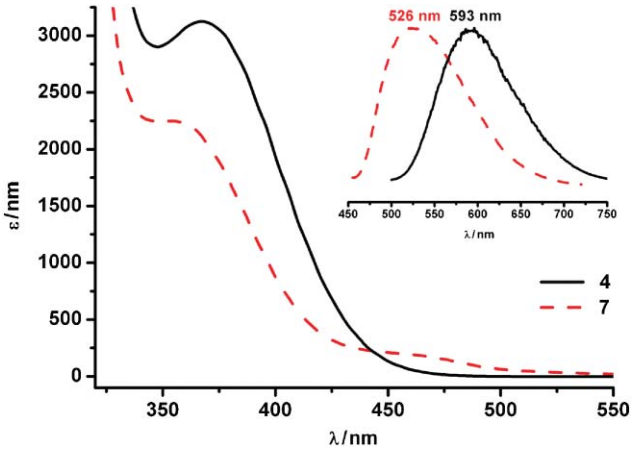


**Fig. 7** Absorbance and emission spectra for heteroleptic complexes **4** and **7**. Absorbance spectrum carried out in MeCN; fluorescence emission spectrum recorded in a rigid matrix of EtOH.

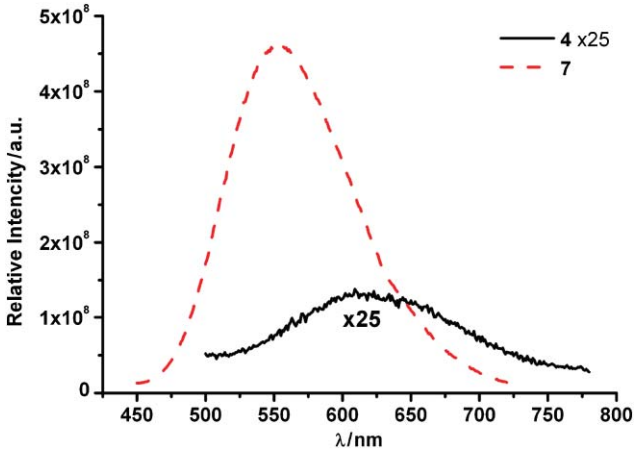


**Fig. 8** Emission spectra for **4** and **7** recorded in EtOH at 300 K. The spectra have been normalised against concentration of solution used.

to design Cu(I) DSSC sensitisers. Due to the qualitatively large photoluminescence observed for **7**, the photophysical properties of complexes **4** and **7** are currently under further investigation in a variety of media and a range of temperatures along with computational studies of structural rigidity in the excited state. This work will be reported elsewhere.

## Electrochemistry

The redox potentials for all complexes are shown in Table 7. The first oxidation potential for the homoleptic complexes occurs within the range +0.75 to +0.91 V and can be assigned as an irreversible Cu(I)/Cu(II) redox process. The corresponding Cu(I)/Cu(II) oxidation for the heteroleptic complexes (**4**–**7**) occurs at more positive potentials, around +1.4 V (Table 7). This increase in Cu(I) oxidation potential is due to the orbital interaction with the electron withdrawing POP ligand.[8] The oxidation potentials vary little across **4**–**7**, suggesting the HOMO is largely Cu(I)/POP in character as this feature is invariant across the series. This is also consistent with the TDDFT results shown in Tables 4 and 5 and is appropriate for use of **5** as a DSSC sensitiser since positive charge density on the oxidised sensitiser will be located away from the semiconductor. For long-term DSSC operation, it would clearly be preferable to develop sensitisers that exhibit chemically reversible oxidations, however the acid analogue, **5**, is still viable for study as model sensitiser since cyclic voltammetry experiments occur on a far longer timescale relative to those taking place in a DSSC device.

**Table 7** Oxidation and reduction potentials for all complexes; **1**, **4**–**7** and **9** = 0.3M TBABF$_4$/MeCN; **3** = 0.3M TBABF$_4$/DCM

| | | $E_{\frac{1}{2}}$ (V *vs.* Ag/AgCl) | | | | | | | |
|---|---|---|---|---|---|---|---|---|---|
| Complex | | $E_{Red.4}$ | $E_{Red.3}$ | $E_{Red.2}$ | $E_{Red.1}$ | $E_{Ox.1}$ | $E_{Ox.2}$ | $E_{Ox.3}$ | $E_{Ox.4}$ |
| [Cu(tmbpy)$_2$] | **1** | | | −1.68 | −1.34 | +0.77 | | | |
| [Cu(tecbpy)$_2$] | **3** | | | −1.27 | −0.87 | +0.91* | | | |
| [CuPOP(dmbpy)] | **4** | | | | −1.60 | +1.44 | +1.73 | | |
| [CuPOP(dcbpy)] | **5** | | | −1.61 | −1.40 | +1.41 | +1.64 | | |
| [CuPOP(decbpy)] | **6** | | | −1.52 | −0.91 | +1.42 | +1.68 | | |
| [CuPOP(tmbpy)] | **7** | | | | −1.66 | +1.41 | +1.65 | | |
| [CuPOP(bpym)] | **9** | −1.63 | −1.44 | −1.08 | −0.78* | +0.55* | +1.24 | +1.44 | +1.75 |

All potentials *vs.* Ag/AgCl (saturated solution); recorded at 298 K; Peaks are chemically and electrochemically irreversible and values shown represent peak potential, except; * = Peaks are chemically reversible and electrochemically irreversible, and values shown represent $E_{\frac{1}{2}}$.

**Table 8** *I–V* Characterisation data for **5**. Dye Bath diethyl ether. Adsorption time 24 h. $V_{OC}$ = open circuit potential, $I_{SC}$ = short circuit current, ff = fill factor, $\eta$ = power conversion efficiency. N719 measure $I_{SC}$ = 7.96 mA; $V_{OC}$ = 753 mV; ff = 0.51 and $\eta$ = 3.05%

| Dye concentration/mM | Cheno concentration/mM | Post-treated with $TiCl_4$ | $I_{SC}$/mA | $V_{OC}$/mV | ff | $\eta$/% |
|---|---|---|---|---|---|---|
| 1 | N/A | N | 0.176 | 361 | 0.51 | 0.032 |
| 2 | N/A | N | 0.233 | 347 | 0.65 | 0.053 |
| 1 | 1 | N | 0.198 | 333 | 0.48 | 0.030 |
| 2 | 2 | N | 0.300 | 373 | 0.45 | 0.050 |
| 1 | N/A | Y | 0.210 | 388 | 0.47 | 0.038 |
| 2 | N/A | Y | 0.230 | 345 | 0.58 | 0.046 |



Upon comparison with literature,[1] the reductions exhibited by all the complexes can be assigned as bipyridyl-ligand based, which is consistent with the predictions from TDDFT. The variation in reduction potential seen for the complexes is consistent with their calculated LUMO energies, with the acid and ester analogues requiring a less negative reduction potential due to the extended conjugation. These electrochemical results support the expectation that the charge transfer transition will have directionality in the desired direction; towards the carboxylate groups (on the bipyridyl ligand) that bind to $TiO_2$.

### Solar cell measurements

*I–V* characterisation was carried out on solar cells made using **5** adsorbed onto $TiO_2$ films. Cell construction and treatments are outlined in the Experimental section and power-conversion efficiency was determined while irradiating under AM 1.5 light (100 $mWcm^{-2}$). Cell efficiencies ($\eta$) were calculated using the resulting values of $I_{SC}$ = short circuit current (mA), $V_{OC}$ = open circuit voltage (mV) and ff = fill factor.

Adsorption studies revealed the dye bath conditions yielding the optimum $TiO_2$ surface coverage of **5** to be a sensitiser concentration of 2 mM in diethyl ether. The results for 1 mM diethyl ether dye baths have also been quoted for completeness. Approximate relative $TiO_2$ surface coverage was determined using UV/Vis spectroscopy. This method also allowed confirmation that the dye bound without degradation by comparison with the absorption spectra of **5** in solution. Results for a selected range of these cells are shown in Table 8 and for comparative reasons, N719 DSSCs were constructed and tested following the same procedures.

The observed photovoltages for cells using complex **5** were consistently around 350 mV, lower than that observed for N719 (753 mV), and lower than the best homoleptic Cu(I) sensitisers quoted in the literature (around 550 mV),[2,3,5–7] The photocurrents were also significantly lower than those recorded for our N719 cells and for existing homoleptic

Cu(I) sensitisers (up to 0.3 mA compared to 8.0 and 5.0 mA respectively). This however is as expected due to the blue shift of the MLCT absorption caused by the electron-accepting POP ligand such that the complex only just absorbs in the visible region ($\lambda_{max}$ = 394 nm). The low photocurrents may also play a role in the reduced photovoltages displayed using this sensitiser.

The studies reported in Table 8 include two additional DSSC fabrication procedures outlined in the literature. Firstly, the inclusion of Chenodeoxycholic acid (Cheno) in the dye baths was carried out as it has been shown to dramatically improve the short circuit currents produced in some systems[36–40] by acting as a spacer group on the $TiO_2$ surface, limiting the extent of dye aggregation. A range of dye:Cheno concentration ratios were tried for **5** with representative examples in Table 8. Improved photocurrents for the dye:Cheno cells over the non-Cheno cells was observed in every case, with an optimum ratio of 1 : 1, although no improvement to the photovoltage was seen. Secondly, a $TiCl_4$ post-treatment of the $TiO_2$ film prior to adsorption of the sensitiser was applied as a potential method for improving photocurrents.[9,40] No improvement to photocurrent was recorded upon the introduction of the $TiCl_4$ post-treatment, and photovoltages remained within the same range seen throughout this work (Table 8).

Despite the low power-conversion efficiency of cells sensitised with **5**, the key feature of the work is the demonstration of sensitiser function for a dye of this design. The POP ligand was chosen for its known steric rigidity and successfully demonstrates that simple dcbpy ligands can be used in heteroleptic Cu(I) DSSC sensitisers due to the chemical stability and sufficiently-long excited-state lifetime imposed by the POP. The low power-conversion efficiency is largely the result of poor harvesting of the solar spectrum by the dye leading to low $I_{SC}$. Our future work is now focused on the development of sterically-constraining co-ligands that also impart more optimised spectroscopic characteristics on heteroleptic Cu(I) DSSC sensitisers.

## Conclusions

Shown here is the synthesis of a series of homoleptic complexes of general formula $[Cu(I)(diimine)_2][BF_4]$ (**1**–**3**), and a series of heteroleptic complexes of the general formula $[Cu(I)(POP)(diimine)][BF_4]$ (**4**–**9**). Electrochemical, spectroscopic and computational methods were used to understand the electronic characteristics of these complexes. In particular, this work demonstrates the first example of a heteroleptic Cu(I) complex; $[Cu(I)(POP)(dcbpy)][BF_4]$ (**5**), that functions as a sensitiser in a dye-sensitised solar cell. The photocurrents and photovoltages achievable by **5** are lower than existing Cu(I)-sensitisers[7] but this is a result of the dye absorbing weakly in the visible region ($\lambda_{max}$ = 394 nm and $\varepsilon_{max} = 3.3 \times 10^3$ $M^{-1}cm^{-1}$).

A key point of this work is that stable heteroleptic Cu(I)-sensitisers can be achieved with simple 4,4′($CO_2H$)-bipyridine, synthetically less intensive to produce than the 4,4′,6,6′-substituted analogues. Work is now moving towards replacing the POP ligand with a more suitable second ligand that can have a beneficial impact on the absorption properties of the sensitiser as well as providing the required steric constraint.

 

## Experimental

### General procedures

The synthesis of bis{2-(diphenylphosphanyl)phenyl} ether (POP),[8] 4,4′-dicarboxy-2,2′-bipyridine (dcbpy),[41] 4,4′-di($CO_2$Et)-2,2′-bipyridine (decbpy),[42] 4,4′,6,6′-tetramethyl-2,2′-bipyridine (tmbpy),[43] [Cu(MeCN)$_4$][$BF_4$][44] and [Cu(I)POP(MeCN)$_2$][$BF_4$][8] were carried out according to literature procedures. 4,4′,6,6′-tetracarboxy-2,2′-bipyridine (tcbpy) and 4,4′,6,6′-tetra($CO_2$Et)-2,2′-bipyridine (tecbpy) are novel complexes and have been synthesized using adapted literature methods.[42]

4,4′-dimethyl-2,2′-bipyridine (dmbpy), bipyrimidine (bpym) and all other chemicals were purchased from Aldrich and used as received.

Electrochemistry was carried out using a Pt working electrode, Pt rod counter electrode and Ag/AgCl reference electrode. All electrochemical experiments were carried out in either acetonitrile or DCM and the supporting electrolyte used was TBA$BF_4$ (0.3M). After each experiment the reference electrode was calibrated against the ferrocene/ferrocenium couple which was found to be at 0.55 V. The absorption spectra were recorded using a PerkinElmer Lambda 9 spectrophotometer controlled using the UV/Winlab software. Emission spectra were recorded at room temperature and using frozen samples, with ethanolic solutions of **4**, **7**, **9**, [CuPOP(MeCN)$_2$][$BF_4$], dmbpy and tmbpy (0.1–0.6 mM), using a Fluoromax2 fluorimeter controlled by the ISAMain software.

Density functional theory calculations were performed using the Gaussian 03 program[29] with the starting structures for **4**, **5** and **7** inputted using the builder program Arguslab and the crystal structure coordinates used as the starting point for **9**. All calculations were carried out using the Becke's three parameter exchange functional with the Lee–Yang–Parr for the correlation functional (B3LYP),[30] using the Los Alamos National Laboratory basis sets, known as LANL2DZ (developed by Hay and Wadt),[31–33] which comprises ECP + double zeta for copper, and the all-electron valence double zeta basis sets developed by Dunning (D95V) for light atoms.[45] Frequency calculations were carried out to ensure that optimised geometries were minima on the potential energy surface. Solvent effects were included *via* the self-consistent reaction field (SCRF) method using the polarised continuum model (PCM),[46] with slight modifications to the default cavity parameters to aid convergence. Time-dependent density functional theory (TDDFT) was performed in an acetonitrile polarizable continuum model, with the first 70 singlet transitions calculated. ArgusLab[34] was used to generate the orbital isosurface maps.

To make the DSSCs titanium dioxide paste (Dyesol, DSL-18NR-T) was deposited onto cleaned fluorine doped tin oxide conductive glass (TEC 8, Pilkington, UK) by doctor-blading. The film was dried at 100 °C for 15 min and then sintered at 450 °C for 30 min to remove the organics and to form a mesoporous film structure. The thickness of the film was about 18 μm. The films were sensitized with **5** using a solution of the dye in diethyl ether. The platinized counter electrode was fabricated following the previously reported procedure.[47] The cell was completed by sealing the dye coated $TiO_2$ electrode and Pt electrode of a cell together by a thermal plastics spacer (Surlyn 1702, 25 μm, Solaronix) at 120 °C. The electrolyte was introduced into the cell through the two holes which were drilled in the counter electrode. The holes were subsequently sealed using Kapton tape. The default electrolyte used was 0.6 M LiI, 0.03 M $I_2$, 0.1 M Guanidinium thiocyanate, 0.5 M 4-*tert*-butylpyridine, 15 : 85 Valeronitrile:Acetonitrile. The active area of the cell was 1 $cm^2$. The current–voltage characteristics of the cells were measured under simulated AM 1.5 illumination (100 $mWcm^{-2}$) provided by a solar simulator (1 kW Xe with AM 1.5 filter, Müller) calibrated using a Digital Solar Power Meter. The Cheno additive was dissolved in the Dye Baths at the same time as the sensitiser. The $TiCl_4$ post-treatment of the $TiO_2$ films was carried out prior to dye adsorption. The $TiO_2$ coated FTO cells were coated with a 40mM aqueous $TiCl_4$ solution and placed into a steam bath at 70 °C for 30 min. The cells were removed, washed with deionised water, dried at 100 °C for 15 min and then sintered at 500 °C for 30 min. Dye adsorption was then carried out as described above.

#### Cu(tmbpy)$_2$][$BF_4$] (1)

[Cu(MeCN)$_4$][$BF_4$] (140 mg, 0.45 mmol) and tmbpy (200 mg, 0.89 mmol) were stirred in 20 mL degassed chloroform under nitrogen for 30 min. The solvent was removed under reduced pressure and the solid obtained triturated in hexane. The product was obtained by filtration. Yield = 75%, 193 mg. $\delta_H$ (DMSO, 250 MHz)/ppm = 8.36 (s, 4H, H-bpy), 7.42 (s, 4H, H-bpy), 2.45 (s, 12H, $CH_3$), 2.11 (s, 12H, $CH_3$). MS (positive ESI); *m*/*z*: 487.10 (M–$BF_4^-$)$^+$. Elemental analysis: calculated for $C_{28}H_{32}BCuF_4N_4$: C 58.49, H 5.61, N 9.74. Found: C 57.78, H 5.46, N 9.57.

#### [Cu(tcbpy)$_2$][$BF_4$] (2)

[Cu(MeCN)$_4$][$BF_4$] (20.5 mg, 0.07 mmol) and tcbpy (42.3 mg, 0.13 mmol) were stirred in 5 mL degassed, dry MeOH under nitrogen for 2 h. A white solid (uncomplexed tcbpy) was removed by filtration. The pure product was then obtained by precipitation with isopropyl alcohol overnight. Yield = 32%, 17 mg. $\delta_H$(DMSO, 250 MHz)/ppm: 8.84 (s, 4H, H-bpy), 8.22 (s, 4H, H-bpy). MS (positive ESI): *m*/*z* = 725.31 (M–$BF_4^-$)$^+$. Elemental analysis: calculated for $C_{28}H_{16}BCuF_4N_4O_{16}$: C 41.27, H 1.98, N 6.88. Found: C 41.44, H 2.24, N 7.96.

#### [Cu(tecbpy)$_2$][$BF_4$] (3)

[Cu(MeCN)$_4$][$BF_4$] (14.2 mg, 0.05 mmol) and tecbpy (40 mg, 0.09 mmol) were stirred in 50 mL degassed, dry DCM under nitrogen for 30 min. The pure product was obtained by precipitation with isopropyl alcohol. Yield = 53%, 28 mg. $\delta_H$ ($CDCl_3$, 250 MHz)/ppm = 9.15 (s, 4H, H-bpy), 8.69 (s, 4H, H-bpy), 4.54 (q, *J* = 7.10 Hz, 8H, –C**H$_2$**–$CH_3$), 3.88 (q, *J* = 7.14 Hz, 8H, –C**H$_2$**–$CH_3$), 1.47 (t, *J* = 7.18 Hz, 12H, –$CH_2$–C**H$_3$**), 1.03 (t, *J* = 7.11 Hz, 12H, $CH_2$–C**H$_3$**). MS (positive ESI); *m*/*z*: 950 (M–$BF_4^-$)$^+$. Elemental analysis: calculated for $C_{44}H_{48}N_4O_{16}CuBF_4{\cdot}CH_2Cl_2$: C 48.08, H 4.48, N, 4.98. Found: C 47.60, H 4.33, N 4.79.

#### [Cu(POP)(dmbpy)][$BF_4$] (4)

[Cu(I)POP(MeCN)$_2$][$BF_4$] (201 mg, 0.26 mmol) and dmbpy (51 mg, 0.06 mmol) were stirred in 5 mL acetone for 3 h resulting in an orange solution. The solvent was removed under reduced pressure. The pure product was then obtained by reprecipitaiton

**Table 9** X-Ray crystallography data

| | [Cu(dmbpy)$_2$Cl] [BF$_4$] | **1** | **6** | **9** | **10** |
|---|---|---|---|---|---|
| CCDC deposition number | 771442 | 771443 | 771439 | 771440 | 771441 |
| Empirical Formula | $(C_{24}H_{24}N_4CuCl)_2$. $(BF_4)_2\cdot(CH_2Cl_2)$ | $C_{28}H_{32}N_4Cu\cdot BF_4$ | $C_{52}H_{44}N_2CuO_5P_2$ $BF_4\cdot C_2H_3N$ | $C_{44}H_{34}N_4OP_2Cu\cdot BF_4$ | $C_{80}H_{62}N_4O_2P_4Cu_2\cdot 2[BF_4]\cdot 2[C_3H_6O]$ |
| Formula weight | 1193.47 | 574.93 | 1030.24 | 847.08 | 1652.15 |
| $T$/K | 150(2) | 150(2) | 100(2) | 150(2) | 150(2) |
| Crystal colour | Cyan | Orange | Orange | Orange | Orange-Yellow |
| Crystal dimensions | 0.50 × 0.40 × 0.30 | 0.90 × 0.59 × 0.43 | 0.15 × 0.15 × 0.08 | 0.22 × 0.33 × 0.36 | 0.15 × 0.21 × 0.25 |
| Crystal system | Triclinic | Monoclinic | Triclinic | Monoclinic | Triclinic |
| Space group | $P\bar{1}$ | $C2/c$ | $P\bar{1}$ | $P2_1/c$ | $P\bar{1}$ |
| $a$/Å | 10.8528(3) | 13.8531(14) | 12.3345(3) | 9.5405(2) | 11.3321(3) |
| $b$/Å | 14.4072(4) | 16.4771(14) | 12.6111(3) | 19.8580(4) | 13.2821(3) |
| $c$/Å | 17.6085(5) | 13.5039(19) | 18.0200(4) | 20.4442(4) | 14.2188(3) |
| $\alpha$ (°) | 83.9868(16) | 90 | 98.4411(13) | 90 | 108.665(1) |
| $\beta$ (°) | 74.9744(14) | 119.730(7) | 100.4738(12) | 95.4810(10) | 105.605(1) |
| $\gamma$ (°) | 73.3850(14) | 90 | 113.2549(12) | 90 | 97.186(1) |
| $V$/Å$^3$ | 2546.69(12) | 2676.7(5) | 2457.18(10) | 3855.55(14) | 1899.81(7) |
| $Z$ | 4 | 4 | 2 | 4 | 1 |
| $D_c$/Mg m$^{-3}$ | 1.556 | 1.427 | 1.392 | 1.459 | 1.440 |
| Independent reflections | 8998 [$R_{int}$ = 0.0411] | 2747 [$R_{int}$ = 0.0492] | 10570 [$R_{int}$ = 0.0606] | 10239 [$R_{int}$ = 0.038] | 10287 [$R_{int}$ = 0.037] |
| All data/restraints/parameters | 36169/0/666 | 13995/184/190 | 49789/63/680 | 31367/0/514 | 27104/0/496 |
| Absorption correction/mm$^{-1}$ | 1.119 | 0.869 | 0.577 | 0.711 | 0.719 |
| $R_1$, w$R_2$ (observed data: $F^2>2\sigma(F^2)$) | 0.0366/0.0933 | 0.0526/0.1470 | 0.0422/0.0937 | 0.0485/0.1071 | 0.0537/0.1160 |

from acetonitrile upon addition of isopropyl alcohol and leaving overnight. Yield = 67%, 153 mg. $\delta_H$(DMSO, 250 MHz)/ppm:. 8.51 (s, 2H, H-bpy), 8.37 (d, 2H, H-bpy), 7.47-7.15 (m, 18H, H-POP), 7.09 (t, 2H, H-bpy), 6.98 (m, 8H, H-POP), 6.61 (m, 2H, H-POP), 2.47 (s, 6H, $CH_3$-bpy). MS (positive FAB): $m/z$ = 784.7 (M–BF$_4^-$)$^+$. Elemental analysis: calculated for $C_{48}H_{40}BCuF_4N_2OP_2$: C 66.03, H 4.62, N 3.21. Found: C 65.58, H 4.42, N 3.90.

### [Cu(POP)(dcbpy)][BF$_4$] (5)

[Cu(I)POP(MeCN)$_2$][BF$_4$] (100 mg, 0.13 mmol) and dcbpy (28 mg, 0.03 mmol) were stirred in 5 mL acetone for 3 h resulting in a yellow solution. The pure product was then obtained by reprecipitation upon addition of isopropyl alcohol and leaving overnight. Yield = 26%, 96 mg. $\delta_H$(DMSO, 250 MHz)/ppm: 9.17 (s, 2H, H-bpy), 8.91 (d, 2H, H-bpy), 8.07 (d, 2H, H-bpy), 7.4 (m, 28H, H-POP). MS (positive ESI): $m/z$ = 844.80 (M–BF$^-$)$^+$. Elemental analysis: calculated for $C_{48}H_{36}CuN_2O_5P_2.BF_4$: C 61.73, H 3.89, N 3.00. Found C 62.06, H 4.20, N 2.87.

### [Cu(POP)(decbpy)][BF$_4$] (6)

[Cu(I)POP(MeCN)$_2$][BF$_4$] (201 mg, 0.26 mmol) and decbpy (51 mg, 0.05 mmol) were stirred in 5 mL acetone for 3 h resulting in an orange solution. The solvent was removed under reduced pressure. The pure product was then obtained by reprecipitation upon addition of isopropyl alcohol and leaving overnight. Yield = 87%. 231 mg, $\delta_H$(DMSO, 250 MHz)/ppm: 8.79 (s, 2H, H-bpy), 8.75 (d, $J$ = 4.74 Hz, 2H, H,-bpy), 7.98 (dd, $J$ = 1.32 Hz, $J$ = 5.42 Hz, 2H, H-bpy), 7.10 (m, 28H, H-POP), 4.53 (dd, $J$ = 7.07 Hz, 4H, C**H$_2$**CH$_3$), 1.49 (t, $J$ = 7.13 Hz, 6H, CH$_2$C**H$_3$**). MS (positive ESI): $m/z$ = 784.87 (M–BF$^-$)$^+$. Elemental analysis: calculated for $C_{52}H_{44}CuN_2O_5P_2.BF_4$: C 63.14, H 4.48, N 2.83. Found C 62.71, H 4.36, N 2.11.

### [Cu(POP)(tmbpy)][BF$_4$] (7)

[Cu(I)POP(MeCN)$_2$][BF$_4$] (101 mg, 0.13 mmol) and tmbpy (25 mg, 0.03 mmol) were stirred in 10 mL anhydrous acetonitrile under N$_2$ for 3 h resulting in an orange solution. The volume of reaction mixture was reduced by half under reduced pressure. The pure product was then obtained upon addition of isopropyl alcohol and leaving overnight. The desired product remains in the filtrate and is obtained by solvent removal under reduced pressure. Yield = 75%, 90 mg. $\delta_H$(DMSO, 250 MHz)/ppm: 8.09 (s, 2H, H-bpy), 6.85-7.34 (m, 30H, H-bpy and POP), 2.37 (s, 6H, $CH_3$), 2.31 (s, 6H, $CH_3$). MS (positive FAB): $m/z$ (%) = 812.6 (M–BF$^-$)$^+$. Elemental analysis: calculated for $C_{50}H_{44}BCuF_4N_2OP_2$: C 66.64, H 4.92, N 3.11. Found C 66.40, H 4.76, N 3.00.

### [Cu(POP)(tcbpy)][BF$_4$] (8)

[Cu(I)POP(MeCN)$_2$][BF$_4$] (100 mg, 0.13 mmol) and tcbpy (45 mg, 0.04 mmol) were stirred in 5 mL acetone for 3 h resulting in a dark purple solution and white solid. The white solid was removed by filtration. The pure product was then obtained by reprecipitation upon addition of isopropyl alcohol and leaving overnight. The desired product remains in the filtrate and was obtained by solvent removal under reduced pressure. Yield = 53%, 72 mg. $\delta_H$(DMSO, 250 MHz)/ppm: 9.32 (s, 2H, H-bpy), 8.72 (s, 2H, H-bpy), 6.87-7.67 (m, 28H, POP). MS (positive FAB): $m/z$ (%) = 617.3 (CuPOP). Elemental analysis: calculated for $C_{50}H_{36}BCuF_4N_2O_9P_2$: C 58.81, H 3.55, N 2.74. Found C 59.10, H 3.88, N 2.86.

### [Cu(POP)(bpym)][BF4] (9)

[Cu(I)POP(MeCN)$_2$][BF4] (486 mg, 0.63 mmol) and bpym (100 mg, 0.63 mmol) were stirred in 20 mL DCM. The product was obtained by concentration of the reaction mixture then precipitation by the addition of ether. Yield = 64%.

 

$\delta_H$($CD_3OD$, 250 MHz)/ppm: 8.90 (s, 4H, H-bpym), 7.59–6.77 (m, 30H, H-bpym and H-POP). Elemental analysis: calculated for $C_{44}H_{34}BCuF_4N_4OP_2$: C 62.39, H 4.05, N 6.61. Found C 61.56, H 3.43, N 6.34

**[$Cu_2$(POP)$_2$(η4-bpym)][($BF_4$)$_2$] (10)**

[Cu(I)POP($MeCN$)$_2$][BF4] (33 mg, 0.04 mmol) and 11 (34 mg, 0.04 mmol) were stirred in 5 mL acetone for 30 h. The product was obtained by concentration of the reaction mixture then precipitation by the addition of ether. Despite obtaining a crystal structure we were unable to obtain a pure product with satisfactory elemental analysis. Yield = 48%, 32 mg. $\delta_H$(DMSO, 250 MHz)/ppm: 9.01 (s, 4H, H-bpym), 7.85-6.58 (m, 58H, H-bpym and H-POP). Elemental analysis: calculated for $C_{80}H_{62}B_2Cu_2F_8N_4O_2P_4$: C 62.56, H 4.07, N 3.65. Found C 59.06, H 3.96, N 3.01.

### X-ray crystallography

Crystals of [Cu(dmbpy)$_2$][$BF_4$] were grown by slow diffusion of diethyl ether into a saturated DCM solution of **4**. Crystals of **1** and **9** were grown by slow diffusion of diethyl ether into a saturated DCM solution of **1** or **9** respectively. Crystals of **6** were grown by slow diffusion of diethyl ether into a saturated solution of **6** in acetonitrile. Crystals of **10** was grown by slow diffusion of hexane into a saturated solution of **10** in acetone. Single crystal X-ray diffraction data are given in Table 9 and were collected using Mo-Kα radiation ($\lambda$ = 0.71073 Å) on a Smart APEX CCD diffractometer equipped with an Oxford Cryosystems low-temperature device operating at 150 K. An absorption correction was applied using the multi-scan procedure SADABS.[48] The structures were solved by Direct methods (Shelx[49] for [Cu(dmbpy)$_2$][$BF_4$], **1** and **6**; and SIR92[50] for **9** and **10**) and refined by full-matrix least squares against $|F|^2$ using all data (Shelx[49] for [Cu(dmbpy)$_2$][$BF_4$], **1** and **6**; and CRYSTALS[51] for **9** and **10**). Figures were prepared using the programme Mercury.[52] All non-H atoms were refined with anisotropic displacement parameters.



## Acknowledgements

We thank EaSTChem and the EPSRC Supergen Excitonic Solar Cell Consortium for funding. This work has made use of the resources provided by the EaStChem Research Computing Facility (http://www.eastchem.ac.uk/rcf). This facility is partially supported by the eDIKT initiative (heep://www.edikt.org).

## Notes and references

1 N. Armaroli, *Chem. Soc. Rev.*, 2001, **30**, 113.
2 N. Alonso-Vante, J.-F. Nierengarten and J.-P. Sauvage, *J. Chem. Soc., Dalton Trans.*, 1994, 1649.
3 S. Sakaki, T. Kuroki and T. Hamada, T., *J. Chem. Soc., Dalton Trans.*, 2002, 840.
4 A. Barbieri, G. Accorsi and N. Armaroli, *Chem. Commun.*, 2008, 2185.
5 T. Bessho, E. C. Constable, M. Graetzel, A. H. Redondo, C. E. Housecroft, W. Kylberg, Md. K. Nazeeruddin, M. Neuburger and S. Schaffner, *Chem. Commun.*, 2008, 3717.
6 A. Hernandez Redondo, E. C. Constable and C. E. Housecroft, *Chimia*, 2009, **63**, 205.
7 E. C. Constable, A. H. Redondo, C. E. Housecroft, M. Neuburger and S. Schaffner, *Dalton Trans.*, 2009, 6634.
8 N. Armaroli, G. Accorsi, M. Holler, O. Moudam, J.-F. Nierengarten, Z. Zhou, R. T. Wegh and R. Welter, *Adv. Mater.*, 2006, **18**, 1313.
9 M. K. Nazeeruddin, A. Kay, I. Rodicio, R. Humphry-Baker, E. Mueller, P. Liska, N. Vlachopoulos and M. Grätzel, *J. Am. Chem. Soc.*, 1993, **115**, 6382.
10 http://www.g24i.com/.
11 N. Robertson, *Angew. Chem., Int. Ed.*, 2006, **45**, 2338.
12 C. L. Linfoot, P. Richardson, K. L. McCall, J. R. Durrant, A. Morandeira and N. Robertson, *Solar Energy*, in press.
13 S. Ferrere and B. Gregg, *J. Am. Chem. Soc.*, 1998, **120**, 843.
14 S.-M. Kuang, D. G. Cuttell, D. R. Mcmillin, P. E. Fanwick and R. A. Walton, *Inorg. Chem.*, 2002, **41**, 3313.
15 S. Ferrere, *Chem. Mater.*, 2000, **12**, 1083.
16 S. Ferrere, *Inorg. Chim. Acta*, 2002, **329**, 79.
17 N. Robertson, *ChemSusChem*, 2008, **1**, 977.
18 L. Spiccia, G. B. Deacon and C. M. Kepert, *Coord. Chem. Rev.*, 2004, **248**, 1329.
19 R. M. Williams, L. D. Cola, F. Hartl, J.-J. Lagref, J.-M. Planeix, A. D. Cian and M. W. Hosseini, *Coord. Chem. Rev.*, 2002, **230**, 253.
20 N. Armaroli, G. Accorsi, F. Cardinali and A. Listorti, *Photochemistry and Photophysics of Coordination Compounds I*, 69, Springer, 2007.
21 M. Schmitted, C. Michel, S. -X. Liu, D. Schildbach and D. Fenske, *Eur. J. Inorg. Chem.*, 2005, **5**, 1155.
22 M. Ruthkosky, C. A. Kelly, F. N. Castellano and G. J. Meyer, *Coord. Chem. Rev.*, 1998, **171**, 309.
23 O. Moudam, A. Kaeser, B. Delavaux-Nicot, C. Duhayon, M. Holler, G. Accorsi, N. Armaroli, I. Séguy, J. Navarro, P. Destruel and J.-F. Nierengarten, *Chem. Commun.*, 2007, 3077.
24 T. McCormick, W. L. Jia and S. Wang, *Inorg. Chem.*, 2006, **45**, 147.
25 L. Yang, J.-K. Feng, A.-M. Ren, M. Zhang, Y.-G. Ma and X.-D. Liu, *Eur. J. Inorg. Chem.*, 2005, 1867.
26 Y.-M. Xie and J.-H. Wu, *Inorg. Chem. Commun.*, 2007, **10**, 1561.
27 U. Monkowius, Y. N. Svartsov, T. Fischer, M. Zabel and H. Yersin, *Inorg. Chem. Commun.*, 2007, **10**, 1473.
28 Q. Zhang, J. Ding, Y. Cheng, L. Wang, Z. Xie, X. Jing and F. Wang, *Adv. Funct. Mater.*, 2007, **17**, 2983.
29 M. J. Frisch, G. W. Trucks, H. B. Schlegel, G. E. Scuseria, M. A. Robb, J. R. Cheeseman, J. A. Montgomery Jr., T. Vreven, K. N. Kudin, J. C. Burant, J. M. Millam, S. S. Iyengar, J. Tomasi, V. Barone, B. Mennucci, M. Cossi, G. Scalmani, N. Rega, G. A. Petersson, H. Nakatsuji, M. Hada, M. Ehara, K. Toyota, R. Fukuda, J. Hasegawa, M. Ishida, T. Nakajima, Y. Honda, O. Kitao, H. Nakai, M. Klene, X. Li, J. E. Knox, H. P. Hratchian, J. B. Cross, V. Bakken, C. Adamo, J. Jaramillo, R. Gomperts, R. E. Stratmann, O. Yazyev, A. J. Austin, R. Cammi, C. Pomelli, J. W. Ochterski, P. Y. Ayala, K. Morokuma, G. A. Voth, P. Salvador, J. J. Dannenberg, V. G. Zakrzewski, S. Dapprich, A. D. Daniels, M. C. Strain, O. Farkas, D. K. Malick, A. D. Rabuck, K. Raghavachari, J. B. Foresman, J. V. Ortiz, Q. Cui, A. G. Baboul, S. Clifford, J. Cioslowski, B. B. Stefanov, G. Liu, A. Liashenko, P. Piskorz, I. Komaromi, R. L. Martin, D. J. Fox, T. Keith, M. A. Al-Laham, C. Y. Peng, A. Nanayakkara, M. Challacombe, P. M. W. Gill, B. Johnson, W. Chen, M. W. Wong, C. Gonzalez and J. A. Pople, 2004, *Gaussian 03, Revision C.02*, Gaussian, Inc., Wallingford, CT.
30 A. D. Becke, *J. Chem. Phys.*, 1993, **98**, 5648.
31 W. R. Wadt and P. J. Hay, *J. Chem. Phys.*, 1985, **82**, 270.
32 W. R. Wadt and P. J. Hay, *J. Chem. Phys.*, 1985, **82**, 284.
33 W. R. Wadt and P. J. Hay, *J. Chem. Phys.*, 1985, **82**, 299.
34 Arguslab 4.0, M. A. Thompson, *Planaria*, Software LLC, Seattle, http://www.arguslab.com.
35 K. L. McCall, J. R. Jennings, H. Wang, A. Morandeira, L. M. Peter, J. R. Durrant, L. J. Yellowlees, J. D. Woollins and N. Robertson, *J. Photochem. Photobiol. A–Chem.*, 2000, **202**, 196.
36 S. Ito, H. Miura, S. Uchida, M. Takata, K. Sumioka, P. Liska, P. Comte, P. Péchy and M. Grätzel, *Chem. Commun*, 2008, 5194.
37 R. Chen, X. Yang, H. Tian, X. Wang, A. Hagfeldt and L. Sun, *Chem. Mater.*, 2007, **19**, 4007.
38 H. Choi, J. K. Lee, K. H. Song, K. Song, S. O. Kanga and J. Koa, *Tetrahedron*, 2007, **63**, 1553.
39 K. Sayama, S. Tsukagoshi, T. Mori, K. Hara, Y. Ohga, A. Shinpou, Y. Abe, S. Suga and H. Arakawa, *Sol. Energy Mat. Sol. C.*, 2003, **80**, 47.
40 J. H. Yum, S. Moon, R. Humphry-Baker, P. Walter, T. Geiger, F. Nüesch, M. Grätzel and M. K. Nazeeruddin, *Nanotechnology*, 2008, **19**, 424005.

41 P. G. Hoertz, A. Staniszewski, A. Marton, G. T. Higgins, C. D. Incarvito, A. L. Rheingold and G. J. Meyer, *J. Am. Chem. Soc.*, 2006, **128**, 8234.
42 F. H. Case, *J. Am. Chem. Soc.*, 1946, **68**, 2574.
43 P. Ghosh and T. G. Spiro, *J. Am. Chem. Soc.*, 1980, **102**, 5543.
44 O. Moudam, *Thesis*, LCC-Toulouse, France, July 2007.
45 T. H. Dunning Jr. and P. J. Hay, in *Modern Theoretical Chemistry*, Ed. H. F. Schaefer III, Vol. 3 (Plenum, New York, 1976) 1–28.
46 A. Vleck and S. Zalis, *Coord. Chem. Rev.*, 2007, **251**, 258.
47 N. Papageorgiou, W. F. Maier and M. Grätzel, *J. Electrochem. Soc.*, 1997, **144**, 876.
48 G. M. Sheldrick, *SADABS*, Version 2004/1, University of Gottingen, Germany.
49 G. M. Sheldrick, *Acta Cryst.*, 2008, **A64**, 112.
50 A. Altomane, G. Cascarano, C. Giacovazzo, A. Guagliardi, M. C. Burla, G. Polidori and M. Carnalli, *J. Appl. Cryst*, 1994, **27**, 435.
51 P. W. Betteridge, J. R. Carruthers, R. I. Cooper, K. Prout and D. J. Watkin, *J. Appl. Cryst*, 2003, **36**, 1487.
52 C. F. Macrae, P. R. Edgington, P. McCabe, E. Pidcock, G. P. Shields, R. Taylor, M. Towler and J. van de Streek, *J. Appl. Cryst.*, 2006, **39**, 453.



 